Investigations on selected cobalt-based quaternary Heusler alloys for spintronic applications

A thesis submitted

by

Madhav Mohan Bhat

to

Indian Institute of Technology Guwahati

in

Partial fulfilment of the requirement for the award of the degree of

Doctor of Philosophy in Physics

Department of Physics

Indian Institute of Technology Guwahati

Guwahati 781 039, Assam, India

August 2025

Investigations on selected cobalt-based quaternary Heusler alloys for spintronic applications

A thesis submitted

by

Madhav Mohan Bhat

to

Indian Institute of Technology Guwahati

in

Partial fulfilment of the requirement for the award of the degree of

Doctor of Philosophy in Physics

Department of Physics

Indian Institute of Technology Guwahati

Guwahati 781 039, Assam, India

August 2025

Statement

The work contained in the thesis, entitled "**Investigations on selected cobalt-based quaternary Heusler alloys for spintronic applications**", has been carried out by me under the supervision of Prof. A. Srinivasan and Prof. A. Perumal at the Department of Physics, Indian Institute of Technology Guwahati and Dr. Y. Sakuraba, Research Center for Magnetic and Spintronic Materials, National Institute for Materials Science (NIMS), Japan. This work has not been submitted elsewhere for the award of any degree.

16 December 2025

(Madhav Mohan Bhat)

Roll No. 196121016

Department of Physics

Indian Institute of Technology Guwahati

Guwahati-781039

India

Certificate

It is certified that the work contained in this thesis, entitled "**Investigations on selected cobalt-based quaternary Heusler alloys for spintronic applications**" submitted by Madhav Mohan Bhat, a Ph.D. student of the Department of Physics, Indian Institute of Technology Guwahati for the award of the degree of Doctor of Philosophy, has been carried out under the supervision of Prof. A. Srinivasan, Prof. A. Perumal, and Dr. Y. Sakuraba. This work has not been submitted elsewhere for the award of any degree.

18 August 2025

(Prof. A. Srinivasan)

Department of Physics

Indian Institute of Technology Guwahati

Guwahati – 781039, India

(Prof. A. Perumal)

Department of Physics

Indian Institute of Technology Guwahati

Guwahati – 781039, India

(Dr. Y. Sakuraba)

Research Center for Magnetic and Spintronic Materials

National Institute for Materials Science (NIMS)

1-2-1 Sengen, Tsukuba, Ibaraki 305-0047, Japan.

Dedicated to

my parents

and teachers

Acknowledgments

I feel truly fortunate to have been surrounded by remarkable individuals who have consistently supported and encouraged me throughout my Ph.D. journey. This phase has been an enriching experience filled with personal and professional growth, made more memorable by the vibrant atmosphere of IIT Guwahati and the valuable one-year research stint at NIMS, Japan. Although every chapter must eventually close, the path I embarked upon as a researcher will continue well beyond this milestone. It brings me immense joy to finally express my heartfelt gratitude to everyone who has played a part in guiding me to this important juncture.

First and foremost, I extend my deepest respect and sincere gratitude to my thesis supervisors, Prof. A. Srinivasan, Prof. A. Perumal, Department of Physics, IIT Guwahati, for giving me the opportunity to carry out my research under their esteemed guidance. Their unwavering encouragement, insightful mentorship, and genuine care have been a pillar of strength during challenging times. Their dedication to research and humble nature have greatly influenced my own development as a scholar, something I will always treasure. The knowledge and wisdom I have gained from their experience and perspective have laid a strong foundation for my research career. I would also like to sincerely thank my host supervisor Dr. Y. Sakuraba at NIMS, Tsukuba, Japan, for his invaluable guidance, the opportunities he extended to me during my time at NIMS, and his continued support.

I am truly grateful to my Doctoral Committee members-Prof. Subhradip Ghosh, Dr. Binoy Krishna Hazra, Prof. Mohd. Qureshi-for their insightful feedback and suggestions, which significantly enhanced the quality of my research. With immense gratitude, I acknowledge Dr. H. Suto, whose mentorship fostered valuable discussions and laid the foundation for cultivating a scientific mindset. His insightful guidance and innovative ideas greatly broadened my understanding.

My heartfelt thanks go to the current Head of the Department of Physics, Prof. Bosanta R. Boruah, as well as the former Heads, Prof. Subhradip Ghosh and Prof. A. Perumal for their administrative support throughout this journey. I would also like to thank all the faculty and non-teaching staff in the department for their continuous help and encouragement during my Ph.D.

I extend my sincere appreciation to Dr. T. Nakatani, Dr. T. Sasaki, K. Simalaotao, Dr. Varun Kushwaha, Dr. Prabhanjan Kulkarni, Dr. Vineet Barwal, Dr. Dolly taparia,

Dr. Muralikrishnan, Dr. Ravi Goutam, S. Kuramochi and N. Kojima, from NIMS, Japan, for their guidance and support during my internship. I am also thankful for the financial assistance provided by NIMS through the ICGP internship program.

I am grateful to the Department of Physics, IIT Guwahati, for fostering a supportive environment that enabled me to pursue my academic goals with confidence and a sense of professionalism. I would like to extend my sincere thanks to Dr. S. Sarma and Dr. D. Gogoi, Scientific Officers, for their valuable assistance in operating sophisticated instruments. I also deeply appreciate the support of the heads, scientific officers, and technical staff of the Central Instruments Facility for their expertise and guidance throughout my research work.

I express my gratitude to the Ministry of Education, Government of India, for providing a fellowship. I would like to acknowledge the use of facilities at the Department of Physics, IIT Guwahati provided by the Department of Science and Technology, Government of India, under project no. SR/FST/PSII-037/2016, and the Central Instrument Facility at IIT Guwahati. I am also thankful for access to the PARAM-ISHAN and PARAM-KAMRUPA facility at the computer centre, IIT Guwahati. I extend my gratitude to the broader IIT Guwahati administration for offering such a beautiful and peaceful campus that became my home for five years-a place that offered comfort and calm after intense workdays.

I am deeply thankful to my seniors Dr. Rajkumar Modak, Dr. Manisha, Dr. Nitu, and Dr. Sananda Das for their support and guidance. My appreciation also goes to my lab mates Subrath, Pushpesh, Alok, Didwmsha, Dev, Aritra, Dinesh, Debraj, Harekrushna, Sourav, Tandrima, Nidhi, Pratibha, Abul, and Sanjay, for maintaining a positive and co-operative lab environment. A special thanks to my dear friends Dr. Akanshu, Dr. Sayan, Dr. Maruthi, Dr. Samik, Dr. Rajesh, Dr. Dilipan, Dr. Sunil Mohan, Amritava and Subrahmnya Hegde for always being there to listen, motivate, and uplift my spirits.

Finally, I express my heartfelt gratitude to my family for being my greatest source of strength and motivation. I am deeply thankful to my parents for their unconditional love and support, which have been the foundation of all my achievements. I also acknowledge everyone who has contributed to my journey, directly or indirectly. Above all, I thank the Almighty for granting me the strength and focus to persevere.

-Madhav Mohan Bhat

Preface

The growing demand for high-performance, and energy-efficient technologies has driven the search for advanced materials and design strategies beyond conventional systems. In this context, the emerging field of spintronics offers significant advantages over conventional electronics. In recent years, extensive research work is being pursued with zeal to identify potential materials for spintronics applications such as magnetic tunnel junctions and spin valves. However, achieving a high magnetoresistance (MR) ratio (MRR) in such device modules requires materials with high spin polarization (*P*). In this context, Heusler alloys have garnered attention owing to their excellent structural, magnetic, and electronic properties. Though many Heusler alloys exhibit 100% *P*, most of them retain high *P* only at cryogenic temperatures, with a significant drop in *P* at room temperature, which is reflected in a corresponding drop in MRR. This decline in *P* is due to the Fermi level (E_F) being located near edge of the minority conduction (or valence) spin band. This makes MRR highly sensitive to small shifts in E_F caused by thermally induced disorder. Therefore, wide bandgap half-metallic materials with E_F positioned near the center of the minority gap are in demand.

Among Heusler alloys, cobalt based compounds are especially appealing due to their high Curie temperature. In particular, Co_2MnAl and Co_2FeAl are promising material due their high saturation magnetization. However, E_F in both these alloys lies near the edge of the minority valence band, resulting in finite electronic states at E_F and hence a reduced *P*. Studies shows that 50 at.% substitution of V for Co in Co_2MnAl and Ti for Co in Co_2FeAl shifts E_F deeper into the minority gap, resulting in semiconducting CoMnVAl and CoFeTiAl alloys, respectively. This suggests the possibility of shifting E_F into the minority gap by partial substitution of V for Co in Co_2MnAl and Ti for Co in Co_2FeAl. Despite this potential, no systematic investigations reported on $Co_{2-x}MnV_xAl$ and $Co_{2-x}FeTi_xAl$ ($0 < x < 1$) alloys so far.

Beyond identifying half-metals with robust high *P*, low Gilbert damping constant (α) is crucial for energy-efficient magnetization switching of the free (or unpinned) ferromagnetic (FM) layer in MR devices. Since α is proportional to the total density of states at E_F, materials like $Co_2FeGa_{0.5}Ge_{0.5}$ (CFGG) alloy are promising due to their low α. However, stoichiometric CFGG has been found to exhibit reduced *P* due to Co-Fe anti-site disorder, which can be minimized by considering off-stoichiometric CFGG. Despite these insights, the relationship between α and *P* in off-stoichiometric CFGG thin films, remains unexplored. In addition to low α, spin-orbit torque enables efficient magnetization switching of the free FM layer in MR devices by injecting spin current from the adjacent non-magnetic (NM) to FM layer. The

efficiency of spin current injection is measured by spin mixing conductance ($g_{\text{eff}}^{\downarrow\uparrow}$), which depends strongly on the nature of the FM/NM interface. Several studies show that insertion layers (ILs) can significantly modify $g_{\text{eff}}^{\downarrow\uparrow}$. Although the reason behind $g_{\text{eff}}^{\downarrow\uparrow}$ modification has been understood from the viewpoints of proximity induced magnetization and interface spin current transparency, a detailed structural analysis of the NM overlayer at the FM/NM interface has not been conducted so far. Hence, careful evaluation of $g_{\text{eff}}^{\downarrow\uparrow}$ of the FM/IL/NM layers after eliminating the contribution from the IL induced structural changes in NM layer is required. This thesis work aims to address these gaps in the literature by focusing on the following aspects: (a) Perform experimental and theoretical investigations on bulk $Co_{2-x}MnV_xAl$ and $Co_{2-x}FeTi_xAl$ ($0 \leq x \leq 1$) alloys to obtain alloys with good magnetic properties, and half-metallic nature. (b) Investigate the correlation between α and P in off-stoichiometric CFGG Heusler alloy films. (c) Evaluate $g_{\text{eff}}^{\uparrow\downarrow}$ at CFGG/Pt bilayer interface with CFGG as FM and Pt as NM layer. (d) Study the effect of ultrathin Cu, Ni, Ru, Ta, and Cr insertion layers on $g_{\text{eff}}^{\uparrow\downarrow}$ of CFGG/IL/Pt layers after carefully eliminating any changes in the atomic structure of the Pt layer structure due to IL at the interface.

This thesis comprises eight chapters. Chapter 1 introduces the topics of spintronics and half-metals, with an emphasis on Heusler alloys, and provides a review of the relevant literature. This is followed by a discussion on tailoring Heusler alloys for spintronic applications. The chapter also outlines the motivation and objectives behind the thesis work, along with the brief overview of the content in the thesis. The second chapter outlines arc melting and magnetron sputtering techniques employed to prepare the samples and also provides details of the characterization techniques and data analysis procedures followed in the study. This chapter concludes with the details of the first-principles calculations performed. Chapters 3 to 7 present the core research work carried out in this thesis towards the objectives mentioned above. Chapter 8 provides a summary of the work done, highlighting the key findings and briefly outlining potential directions for future research in this area.

With respect to the objectives cited above, this thesis work has achieved the following: Demonstrated (a) strategies to enhance the half-metallic character in ternary Co_2MnAl and Co_2FeAl alloy by atomic substitution of V and Ti for Co, respectively. (b) Brought out the relationship between α and P, which revealed a decrease in α with increase in P of off-stoichiometric CFGG alloy film. (c) Demonstrated high $g_{\text{eff}}^{\uparrow\downarrow}$ at CFGG/Pt interface. (d) Revealed the effect of ultrathin Cu, Ni, Ru, Ta, and Cr ILs on $g_{\text{eff}}^{\uparrow\downarrow}$ of CFGG/IL/Pt layers and accounted for the observed changes in $g_{\text{eff}}^{\uparrow\downarrow}$ due to each of the five ILs.

Table of Contents

Chapter 1

Introduction

Human civilization has progressed alongside the materials it has utilized throughout different periods. The development of functional materials with superior properties plays a vital role in driving modern technological growth. Today, semiconductor devices play an integral role in our daily lives, powering a wide range of modern technologies. Among semiconductor technology advancements, digital data storage and retrieval technology, or simply memory technology, has been one of the main features over the past century. In 1965, Gordon Moore made a crucial observation known as Moore's law, predicting that the number of transistors in integrated circuit chips roughly doubles every 18 months, which was found true for more than two decades [MOOR1965]. However, the continuous miniaturization of transistors is constrained by inherent physical boundaries, and current technologies are nearing those limits as further downscaling becomes increasingly difficult [WALD2016]. As a result, rising demands for faster operation, greater energy efficiency, and sustainable solutions have led researchers to explore alternative functionalities and newer materials actively. This has led to growing interest in spintronics, a field that provides distinct advantages over conventional charge-based electronics by incorporating the electron's spin as an additional functional property [ZUTI2004]. Over the past few decades, spintronics research has focused on various phenomena such as giant magnetoresistance (GMR) and tunnel magnetoresistance (TMR) in an attempt to exploit this evolving field. Considering the growing industrial demand for spintronic technologies, exploring materials that meet the required criteria has become increasingly important. In this regard, Heusler alloys have emerged as strong contenders for spintronics applications, owing to their tunable electronic and magnetic properties [FELS2015].

This thesis presents the research work carried out on the spintronic properties of promising Heusler alloys in two parts. The first part focuses on enhancement of half-metallic character of some promising bulk Heusler alloys with 100 % spin-polarization (P), while the second explores the application oriented magneto-dynamic properties such as Gilbert damping constant (α) and spin mixing conductance ($g_{\mathrm{eff}}^{\uparrow\downarrow}$) in emerging multicomponent Heusler alloy films. The research begins by exploring a viable single-phase bulk Heusler alloy that exhibits

robust *P* at elevated temperatures, ideally suited for spintronic applications. Following this, the potential application of promising Heusler alloys as a magneto-dynamic material is examined using single- and multiple-layered films.

1.1. Spintronics

Spintronics is an emerging field that integrates concepts from solid state physics and electronics to enhance device functionality by utilizing both the charge and spin of electrons [WOLF2001]. Utilizing spin as an active component opens up new possibilities beyond the traditional charge-based electronics. In 1988, Baibich *et al*. [BAIB1988] and Binasch *et al*. [BINA1989] made independent discoveries and reported the large magnetoresistance, which greatly accelerated the progress of spintronic research. Further, in 1995, Miyazaki *et al*. [MIYA1995] and Moodera *et al*. [MOOD1995] discovered TMR in the magnetic tunnel junction (MTJ). The combined use of charge and spin offers several advantages, including non-volatile memory, high-density data storage with enhanced sensitivity, and lower power consumption [ZUTI2004].

Current research in spintronics, particularly in memory technologies involving GMR and TMR mechanisms, involves exploring novel materials to propel advancements in spintronics within modern solid state physics. The operation of spin valves (SVs) and MTJs follows mainly two mechanisms, *viz*., (1) the generation of spin-polarized current, and (2) the injection, transport, and detection of spin-polarized current.

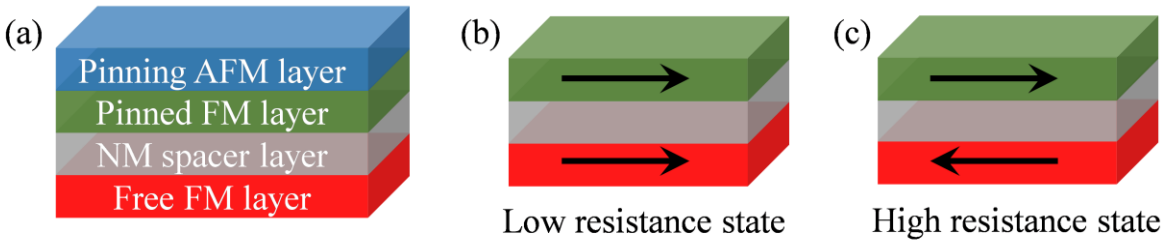

Figure 1.01. (a) Schematic illustration of a typical SV and MTJ. (b) A low resistance state is due to parallel alignment of magnetizations, and (c) a high resistance state results from antiparallel alignment of magnetizations of the two FM layers. The arrows in (b) and (c) indicate the magnetization direction in the FM layers.

A schematic representation of spintronic devices such as SVs and MTJs is displayed in Figure 1.01 (a). SVs and MTJs are composed of two ferromagnetic (FM) layers separated by a non-magnetic (NM) spacer layer, which can be either a conductor (in SVs) or an insulator (in MTJs) [CHAP2007]. Among the two FM layers, the pinned layer has a fixed magnetization

direction, stabilized through exchange bias by an adjacent antiferromagnetic (AFM) pinning layer, while the free layer has a switchable magnetization that changes direction with external aid [BHAT2017]. Electrons with spins aligned to the magnetization of the FM layer experience lower resistance due to a higher density of states (DOS) available for conduction. In contrast, electrons with opposite spin orientation encounter a reduced DOS, resulting in increased scattering and higher resistance [ZUTI2004]. Therefore, in SVs and MTJs, spin-polarized current encounters different electrical resistance depending on the relative alignment of magnetizations of FM layers, being lower for parallel alignment (*c.f.* Figure 1.01 (b)) and higher for antiparallel (*c.f.* Figure 1.01 (c)) configuration (The arrows in the figures indicate the magnetization direction) [ZUTI2004]. This variation in resistance between the two configurations leads to the magnetoresistance (MR) ratio. It is essential to use FM materials with high *P* for high MR ratios in SVs and MTJs (collectively referred to as MR devices).

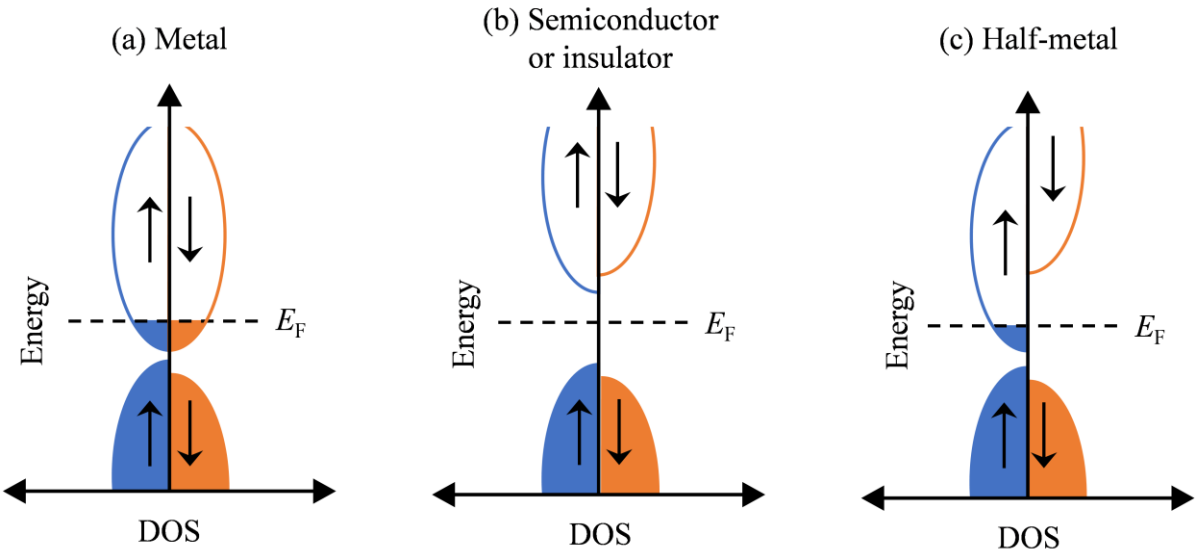

Figure 1.02. Schematic representation of DOS for a (a) metal, (b) semiconductor or insulator, and (c) half-metal (↑ and ↓ represent the up and down spin states, respectively).

1.1.1. Half-metal

Half-metals have emerged as highly promising candidates for spintronic applications, owing to their distinctive electronic configuration. The concept of half-metal was first introduced by de Groot *et al*. in 1983 through *ab initio* calculations performed on half Heusler alloys like NiMnSb and PtMnSb [DEGR1983]. Figures 1.02 (a-c) presents a schematic representation of DOS near the Fermi level (E_F) for conventional metals, semiconductors (or insulators), and half-metals. In a half-metal, one spin channel exhibits metallic behaviour with a non-zero DOS at E_F, while the opposite spin channel behaves like a semiconductor or an insulator, featuring

a bandgap at E_F. This asymmetry in the electronic structure gives rise to 100% P, which can be quantified using the following expression [TRUD2010],

$$P\ (\text{in}\ \%) = \left(\frac{D_\uparrow - D_\downarrow}{D_\uparrow + D_\downarrow}\right) \times 100 \qquad (1.01)$$

where $D_\uparrow$ and $D_\downarrow$ are the DOS for the spin up (↑) and spin down (↓) channels at E_F, respectively. In a perfect half-metal, P = 100% since $D_\downarrow$ is absent. As a result, the conduction electrons belong to a particular type of spin (either spin-up or spin-down).

1.2. Promising half-metallic materials for spintronics

It is evident from the preceding discussion that a high P FM material is crucial in MR devices. It is possible to achieve high P in various material classes, including Heusler alloys [DEGR1983], transition metal oxides [SZOT2004], zinc-blende-type compounds [ZHAN2008a], as well as perovskites and double perovskites [MIRS2020, TANG2022]. Among these, Heusler alloys attract more attention due to several advantages, including high thermal stability resulting from their elevated Curie temperature (T_C) [VARA2012], and tunable magnetic moment, magnetic anisotropy, and electronic bandgap through atomic substitution [BHAT2025a]. Additionally, Heusler alloys are well-suited for device integration, particularly due to their compatibility with MgO tunnel barriers in MTJs [WENZ2011], making them promising candidates for magnetoresistive random access memory (MRAM) production. Moreover, they offer excellent industrial scalability, as thin films can be readily fabricated using standard techniques like sputtering.

1.2.1. Heusler alloys

The discovery of Heusler alloys dates back to 1903, when Fritz Heusler identified a class of ternary compounds that exhibited ferromagnetism despite being composed of elements that are not FM [GRAF2011]. Heusler alloys have attracted significant interest in spintronics since de Groot *et al*. first predicted half-metallic behaviour in the half-Heusler alloy NiMnSb in 1983 [DEGR1983]. This finding drew considerable interest among theoretical and experimental material science researchers, since it opened up avenues to develop next-generation spin-based electronics and memory technologies.

Heusler alloys are classified into two groups based on their chemical formula: (1) full Heusler alloys with the formula X_2YZ, and (2) half Heusler alloys with the formula XYZ.

Where X and Y are transition elements and Z is a *p*-block element, forming a vast collection of compounds.

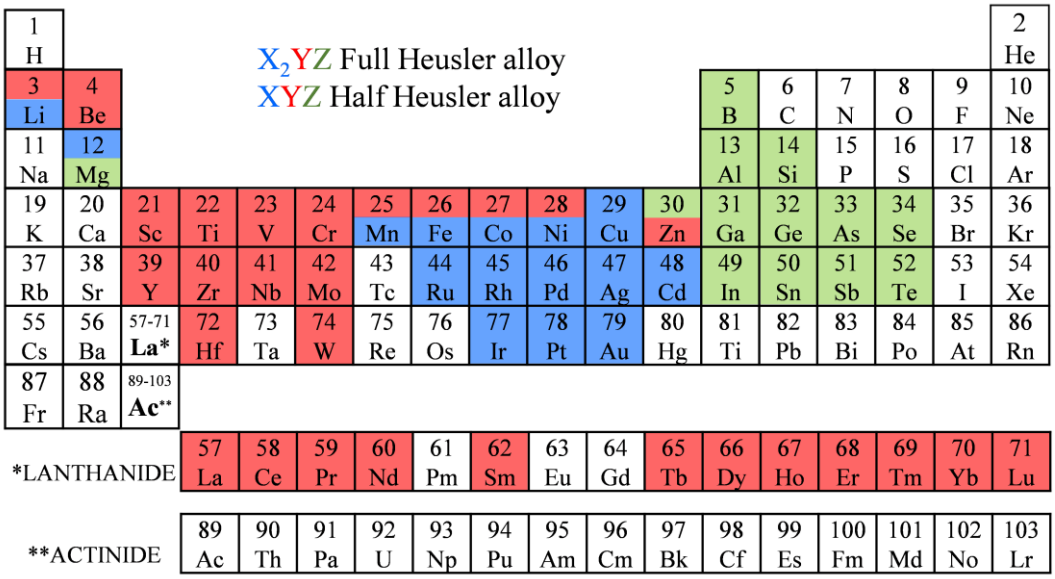

Figure 1.03. Periodic table showing possible X, Y, and Z elements used in Heusler alloys.

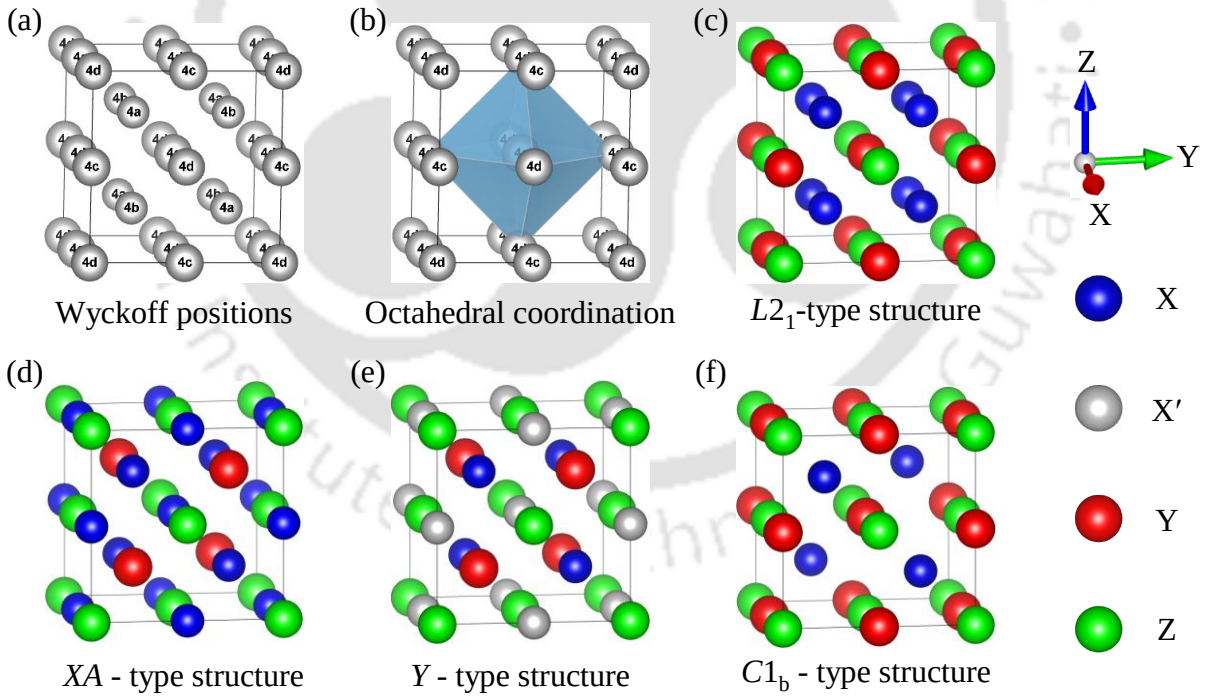

Figure 1.04. (a) Wyckoff positions in Heusler alloy unit cell. (b) Octahedral coordination of two atomic sites forming the rock-salt structure. Schematic diagram of (c) $L2_1$-type, (d) *XA*-type, (e) *Y*-type, and (f) $C1_b$-type ordered Heusler alloy structures.

1.2.1.1. Crystal structure

Stable (ordered) structures

The stable crystal structure of Heusler alloys comprises of four interpenetrating face centered cubic sub-lattices with Wyckoff positions 4*a* (0.25, 0.25, 0.25), 4*b* (0.75, 0.75, 0.75), 4*c* (0.5, 0.5, 0.5), and 4*d* (0, 0, 0) as shown in Figure 1.04 (a) [GRAF2009, MATS2017]. Here, 4*c* (0.5, 0.5, 0.5) and 4*d* (0, 0, 0) Wyckoff positions have octahedral coordination, as shown in Figure 1.04 (b). Atoms with the maximum difference in electronegativity prefer to occupy 4*c* (0.5, 0.5, 0.5) and 4*d* (0, 0, 0) sub-lattices, leading to the formation of a rock salt-type structure with ionic bonding [GRAF2011]. As a result, Z atoms, which belong to a *p*-block element, exhibit high electronegativity and tend to form a rock-salt-type structure with the most electropositive element among X and Y. In the case of normal Heusler alloys, the Y atoms with a low atomic number will show higher electropositivity. Therefore, Y and Z atoms will occupy the 4*c* (0.5, 0.5, 0.5) and 4*d* (0, 0, 0) Wyckoff positions, respectively. Additionally, the sites corresponding to the remaining 4*a* (0.25, 0.25, 0.25) and 4*b* (0.75, 0.75, 0.75) Wyckoff positions at the tetrahedral sites are occupied by the X atoms, forming the $L2_1$-type structure with a space group of $Fm\bar{3}m$ (space group no. 225) with a prototype structure of Cu_2MnAl as shown in Figure 1.04 (c) [WEDE2024]. On the other hand, in inverse Heusler alloys, the X atom possesses a lower atomic number than the Y atom, making the X atom more electropositive. Due to this, the X and Z atoms preferentially occupy the 4*c* (0.5, 0.5, 0.5) and 4*d* (0, 0, 0) Wyckoff positions, respectively. The remaining atomic sites, 4*a* (0.25, 0.25, 0.25) and 4*b* (0.75, 0.75, 0.75), which have tetrahedral coordination, are filled by the X and Y elements, respectively. This atomic arrangement results in the formation of *XA*-type structure, which crystallizes in $F\bar{4}3m$ space group (no. 216), with Hg_2CuTi serving as its structural prototype, as depicted in Figure 1.04 (d) [GRAF2011]. In the $L2_1$-type structure, if the atoms in the 4*a* (0.25, 0.25, 0.25) and 4*b* (0.75, 0.75, 0.75) Wyckoff positions are different, such as X and X′, then the resulting quaternary Heusler alloy is denoted as *Y*-type structure with chemical formula XX′YZ, as shown in Figure 1.04 (e). The crystal structure follows the prototype structure of LiMgPdSn with the space group of $F\bar{4}3m$ (space group no. 216) [WEDE2024]. In the $L2_1$-type structure, if one of the 4*a* (0.25, 0.25, 0.25) and 4*b* (0.75, 0.75, 0.75) Wyckoff positions is vacant, then the half Heusler structure results, which has the $C1_b$-type structure with chemical formula XYZ and $F\bar{4}3m$ space group (no. 216), as shown in Figure 1.04 (f). The prototype crystal structure of half Heusler alloys is the MgAgAs structure [GRAF2011].

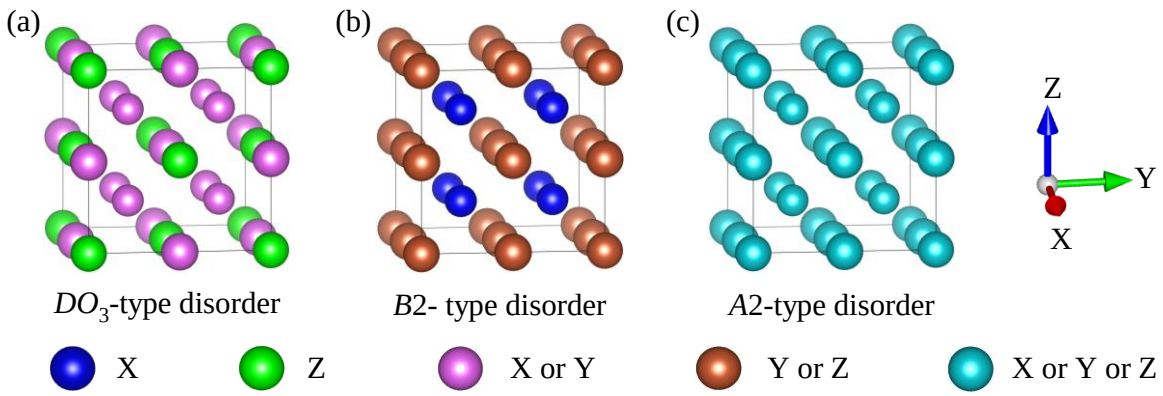

Figure 1.05. (a) Schematic representation of disordered Heusler alloy crystal structures of (a) DO_3-type, (b) *B*2-type, and (c) *A*2-type.

Disordered structures

Heusler alloys often exhibit atomic disorders in as-prepared samples due to the intermixing of constituent elements in Wyckoff positions defined for the stable (ordered) structures. The type of structural disorder depends on which atoms undergo intermixing. If X and Y atoms are intermixed in $L2_1$-type alloy, the resulting structure is said to have DO_3-type atomic disorder. The corresponding crystal structure is depicted in Figure 1.05 (a), which belongs to the $Fm\bar{3}m$ space group (no. 225) with the prototype structure of BiF_3 [GRAF2011]. On the other hand, an intermixing of Y and Z atoms in 4*c* (0.5, 0.5, 0.5) and 4*d* (0, 0, 0) Wyckoff positions results in *B*2-type partially disordered structure shown in Figure 1.05 (b) [GRAF2011], with the CsCl prototype structure having a space group of $Pm\bar{3}m$ (no. 221). Finally, if all the elements are equally distributed among all the Wyckoff positions in the $L2_1$-type structure, it results in *A*2-type fully disordered structure with a space group of $Im\bar{3}m$ (no. 229). The corresponding *A*2-type fully disordered structure is shown in Figure 1.05 (c) [GRAF2011].

Since the physical properties of Heusler alloys are highly sensitive to structural disorders, structural analysis is essential for understanding the relationship between atomic arrangement and material behaviour. X-ray diffraction (XRD) serves as a facile way to investigate structural characteristics and identify possible atomic disorders. In general, stable ordered Heusler alloys show the three superlattice reflections (111), (200), and (400), which are commonly used to assess the level of atomic ordering and detect deviations from the ideal structure. To evaluate the degree of *B*2 (S_{B2}) and $L2_1$ (S_{L2_1}) ordering in Heusler alloy structures, one can utilize the experimentally observed and theoretically simulated (or ideal) intensity ratios of the (111) and (200) superlattice reflections relative to the prominent (400) reflection as [MODA2021],

$$S_{B2} = \sqrt{\frac{(I_{200}/I_{400})_{exp}}{(I_{200}/I_{400})_{th}}} \quad (1.02)$$

$$S_{L2_1} = \frac{2}{3 - S_{B2}} \sqrt{\frac{(I_{111}/I_{400})_{exp}}{(I_{111}/I_{400})_{th}}} \quad (1.03)$$

Here, I_{200}, I_{400}, and I_{111} indicate the integrated intensities of the (200), (400), and (111) superlattice reflections, respectively, with the subscripts 'exp' and 'th' corresponding to the values obtained from experimental measurements and theoretical simulation. An ideal $L2_1$ fully ordered crystal structure is characterized by the order parameters S_{B2} and S_{L2_1} having values equal to unity. Any decrease in S_{L2_1} signifies a deviation from the $L2_1$-type atomic ordering. Likewise, a reduction in the S_{B2} value indicates a reduction in *B*2-type partial atomic disordering and the evolution of a completely disordered *A*2-type structure. However, certain types of structural disorder, such as DO_3, are not detectable using standard XRD measurements.

1.2.1.2. Physical properties

Heusler alloys are a class of intermetallic compounds known for their diverse properties, including high *P* [VARA2012], tuneable saturation magnetization (M_s) [SHAM2019], elevated T_C [AHMA2021], ultra-low α [ANDR2016, GUIL2019, PERI2020], shape memory effect [YUGH2015], magnetocaloric effect [SHAR2007], thermoelectric effect [MIZU2022], and topological properties [FELS2022]. The origin and underlying mechanisms behind some of these properties are explored in detail in the following sections.

1.2.1.2.1. Electronic properties

Heusler alloys exhibit a wide range of electronic properties, including metallic, insulating, half-metallic, semiconducting, semimetallic, *etc*. Among these, half-metallic property with 100% *P* is crucial for spintronics applications. Underlying mechanisms responsible for high *P* in full Heusler alloys with $L2_1$ and *XA*-type crystal structures, and half-Heusler alloys with $C1_b$-type structure are discussed with typical examples below.

The half-metallic gap in X_2YZ full Heusler alloys originates from the hybridization of *d*-orbitals of the X and Y elements [GRAF2011], since the energy level of *s* and *p*-orbitals of these elements, positioned well below E_F, can be disregarded. This allows us to focus on the *d*-*d* hybridization between the two X atoms (labelled as X^A and X^B in Figure 1.06) and a Y atom.

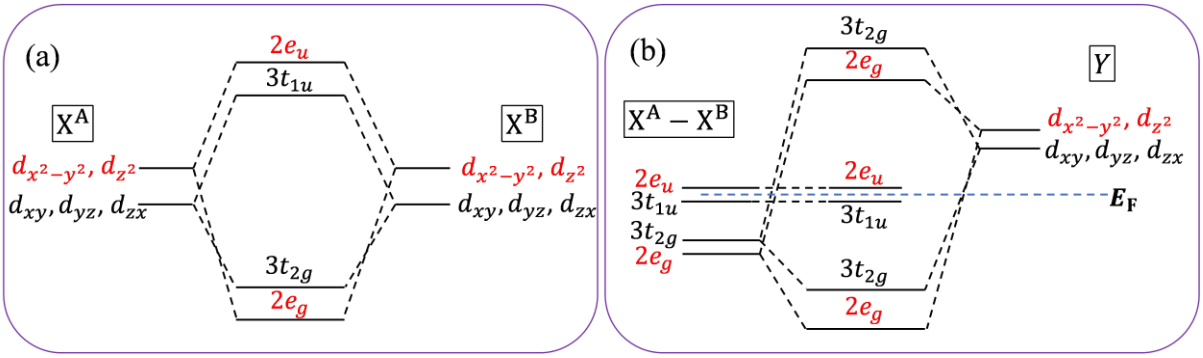

Figure 1.06. Schematic representation of possible hybridization in a full Heusler X_2YZ alloy with $L2_1$-type structure. (a) *d-d* hybridization between two X (X^A-X^B) atoms, and (b) hybridization of the newly formed X^A-X^B hybridized state with the *d*-orbitals of the Y atom.

The *d*-orbitals of the transition elements (*i.e.*, X and Y) are split into doubly degenerate e_g ($d_{x^2-y^2}$, d_{z^2}) and triply degenerate t_{2g} (d_{xy}, d_{yz}, and d_{zx}) energy states, respectively, due to the crystal field effect. Initially, the two X atoms (X^A and X^B) undergo hybridization, forming five bonding states ($2e_g$ and $3t_{2g}$) and five antibonding states ($3t_{1u}$ and $2e_u$) as depicted in Figure 1.06 (a) [GALA2002b]. The prefix in the hybridized states such as e_g, t_{2g}, t_{1u}, and e_u denotes the corresponding degeneracy of the state. In addition, the X^A-X^B bonding states such as $2e_g$ engage in further hybridization with the doubly degenerate e_g ($d_{x^2-y^2}$ and d_{z^2}) states of Y atoms, resulting in the formation of $2e_g$ states below E_F, along with the unoccupied anti-bonding states located above E_F. Similarly, hybridized $3t_{2g}$ states further hybridize with the triply degenerate t_{2g} (d_{xy}, d_{yz}, and d_{zx}) states of Y atoms, leading to the formation of $3t_{2g}$ occupied bonding and unoccupied anti-bonding states positioned below and above E_F, respectively. On the other hand, the X^A-X^B anti-bonding states, such as $3t_{1u}$ and $2e_u$, do not undergo further hybridization and are located below and above E_F, respectively.

So, in total, full Heusler alloys exhibit eight minority spin *d*-states per unit cell below E_F, comprising of $2e_g$+$3t_{2g}$+$3t_{1u}$. Additionally, there are seven minority spin *d*-states, including $2e_u$, $2e_g$, and $3t_{2g}$ above E_F. Apart from these hybridized states, the Z atom in the X_2YZ compound introduces deep-lying 1*s* and 3*p* states (not shown in the figure) below the hybridized *d*-states, which are located below E_F. Consequently, full Heusler alloys possess a total of 12 occupied minority-spin states per unit cell, originating from both hybridized *d*-orbitals of transition metals and non-hybridized *s* and *p* states of the main group element [GALA2002b].

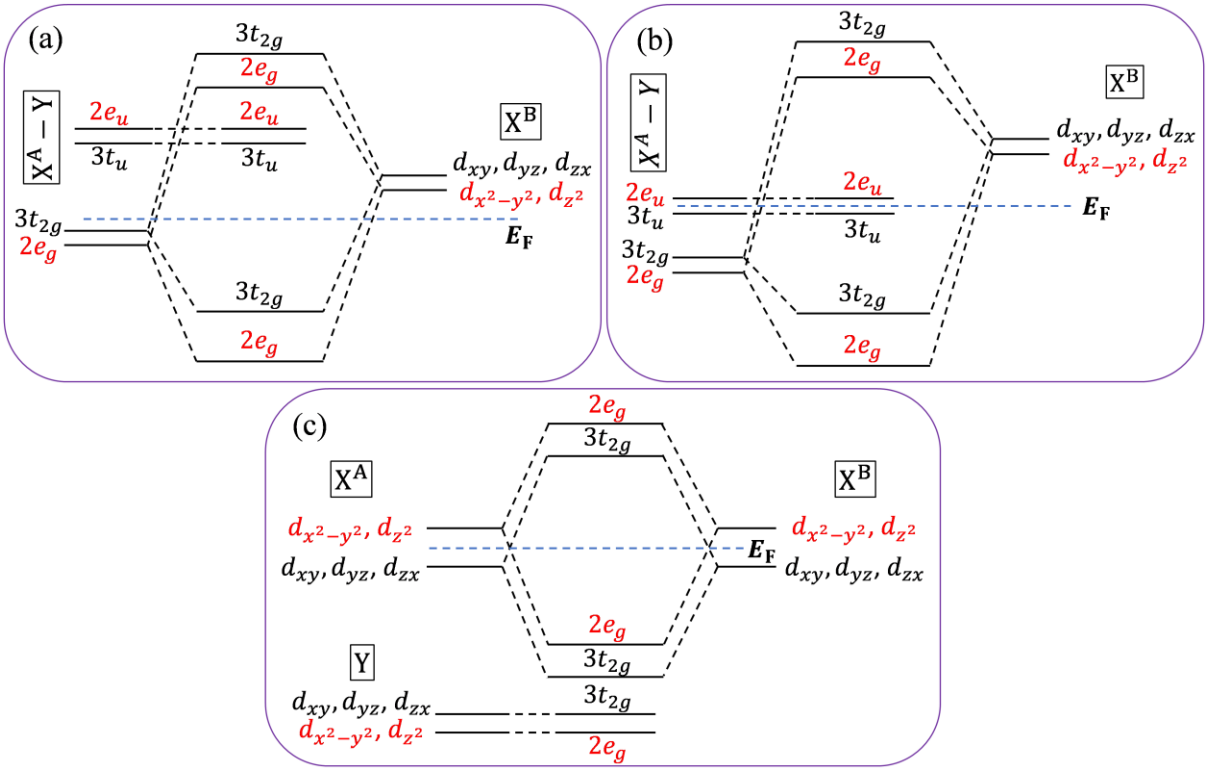

Figure 1.07. Schematic diagram of various hybridizations possible between different *d*-orbitals for inverse Heusler alloys with (a) 9, (b) 12, and (c) 14 minority spin states below E_F.

In the case of inverse Heusler alloys, X atoms (later denoted as X^B) occupying the Wyckoff position 4*b* (0.75, 0.75, 0.75) swap their position with the Y atoms located at the 4*c* (0.5, 0.5, 0.5) site, deviating from the conventional atomic arrangement seen in the $L2_1$-type structure [KOUS2024]. As a result, in the first step, the X^A atoms located at the 4*c* (0.25, 0.25, 0.25) Wyckoff sites interact with Y atoms at 4*b* (0.75, 0.75, 0.75), forming hybridized states. These states further undergo hybridization with the X^B atoms located at the 4*c* (0.5, 0.5, 0.5) Wyckoff sites. The variation in the splitting of these states following the hybridization process results (*c.f.* Figures 1.07 (a-b)) in differences in the occupancy of spin-down states. Consequently, inverse-Heusler alloys may possess either 9 or 12 occupied minority-spin states per unit cell, depending on the types of energy level splitting due to hybridizations [SKAF2013]. However, in certain inverse Heusler alloys, only X^A and X^B atoms undergo hybridization, forming bonding and antibonding hybrid states ($3t_{2g}$ and $2e_g$) below and above E_F, respectively. On the other hand, Y atoms do not participate in hybridization, and the corresponding states ($2e_g$ and $3t_{2g}$) lie below the hybridized *d*-states resulting from the X^A and X^B hybridization illustrated in Figure 1.07 (c). Therefore, including the deep-lying 1*s* and 3*p*-states from Z atoms, the inverse Heusler alloy may also possess 14 minority spin states below E_F [SKAF2013]. Like in full Heusler alloys, the *s* and *p* orbitals of the X and Y elements are

positioned well below the E_F in half-Heusler compounds, and hence the half-metallic gap primarily originates from the hybridization of their *d*-orbitals. Therefore, the focus is on the *d-d* hybridization between the X and Y atoms, which is schematically represented in Figure 1.08.

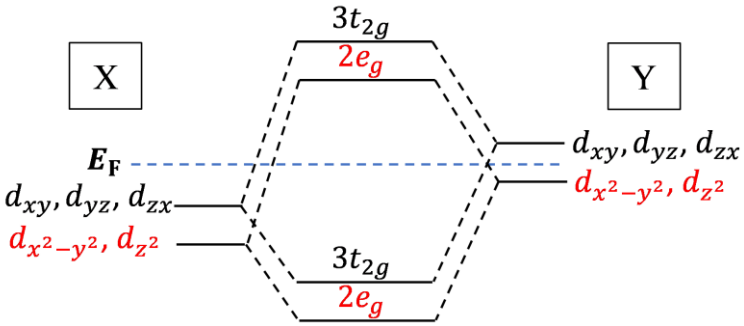

Figure 1.08. *d*-orbital hybridization scheme between X and Y atoms in half-Heusler alloys, resulting in the formation of bonding and antibonding states comprising of $3t_{2g}$ and $2e_g$ orbitals.

During hybridization, doubly degenerate e_g ($d_{x^2-y^2}$ and d_{z^2}) and triply degenerate t_{2g} (d_{xy}, d_{yz}, and d_{zx}) atomic orbitals of X and Y atoms hybridize to give bonding and antibonding $2e_g$ and $3t_{2g}$ orbitals, which are distributed below and above E_F, respectively. As discussed in full Heusler alloys, XYZ also possess 1*s* and 3*p* orbitals located (not shown in the figure) well below the hybridized *d*-orbitals. Consequently, half-Heusler alloys possess 9 minority-spin states per unit cell below E_F, originating from both transition-metal hybridizations ($2e_g$ and $3t_{2g}$) and the non-hybridized (1*s* and 3*p*) states of the main group element [GALA2006].

1.2.1.2.2. Magnetic properties

Heusler alloys are known for their diverse magnetic nature ranging from FM, ferrimagnetic, AFM, or even NM. This diversity comes from the vast range of elemental composition and structure achievable in X_2YZ alloys. A simple way for forecasting the magnetic moment of half-metallic Heusler alloys is through the empirical Slater-Pauling (S-P) rule [GALA2006, GALA2023]. This rule establishes a relationship between the total number of valence electrons (Z_t) and the total spin magnetic moment (M_t) in terms of μ_B/f.u. The relationship can be established by linking Z_t and M_t to the number of valence electrons in up ($N_\uparrow$) and down ($N_\downarrow$) spin states. The total number of valence electrons can be expressed as the sum of $N_\uparrow$ and $N_\downarrow$. Therefore,

$$Z_t = N_\uparrow + N_\downarrow \qquad (1.04)$$

The total magnetic moment M_t, resulting from the uncompensated magnetic moment between the two different (up and down) spin states, is given by,

$$M_t = N_\uparrow - N_\downarrow \tag{1.05}$$

Combining Equations (1.04) and (1.05), the total magnetic moment can be expressed as,

$$M_t = Z_t - 2N_\downarrow \tag{1.06}$$

As already discussed, half-metallic full Heusler alloys with $L2_1$-type structure exhibit a total of 12 states below E_F in the spin-down (minority) channel, which can accommodate 12 spin-down electrons, yielding [GALA2006].

$$M_t = Z_t - 24 \tag{1.07}$$

The linear variation of M_t as a function of Z_t for full Heusler alloys as per the S-P rule is depicted in Figure 1.09.

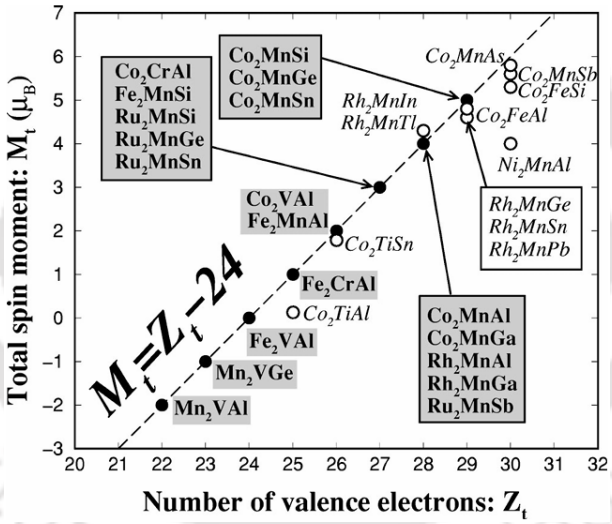

Figure 1.09. Variation of M_t with Z_t according to the S-P rule for full Heusler alloys [GALA2002b].

However, half-Heusler alloys possess only 9 minority-spin states below E_F, capable of accommodating 9 spin-down electrons, leading to [GALA2006],

$$M_t = Z_t - 18 \tag{1.08}$$

Similarly, inverse Heusler alloys possess either 9, 12, or 14 occupied minority states, depending on the specific electronic configuration and hybridization. Therefore, three possible distinct S-P rules for half-metallic inverse Heusler alloys are [SKAF2013],

$$\left.\begin{aligned} M_t &= Z_t - 18 \\ M_t &= Z_t - 24 \\ M_t &= Z_t - 28 \end{aligned}\right\} \qquad (1.09)$$

These are referred to as the generalized S-P rules for half-metallic Heusler alloys. Figure 1.10 shows the variation of M_t with respect to the change in Z_t for inverse Heusler alloys. According to these rules, full Heusler compounds with $Z_t < 24$ tend to be ferrimagnetic, those with $Z_t = 24$ are typically NM, and those with $Z_t > 24$ exhibit FM behaviour.

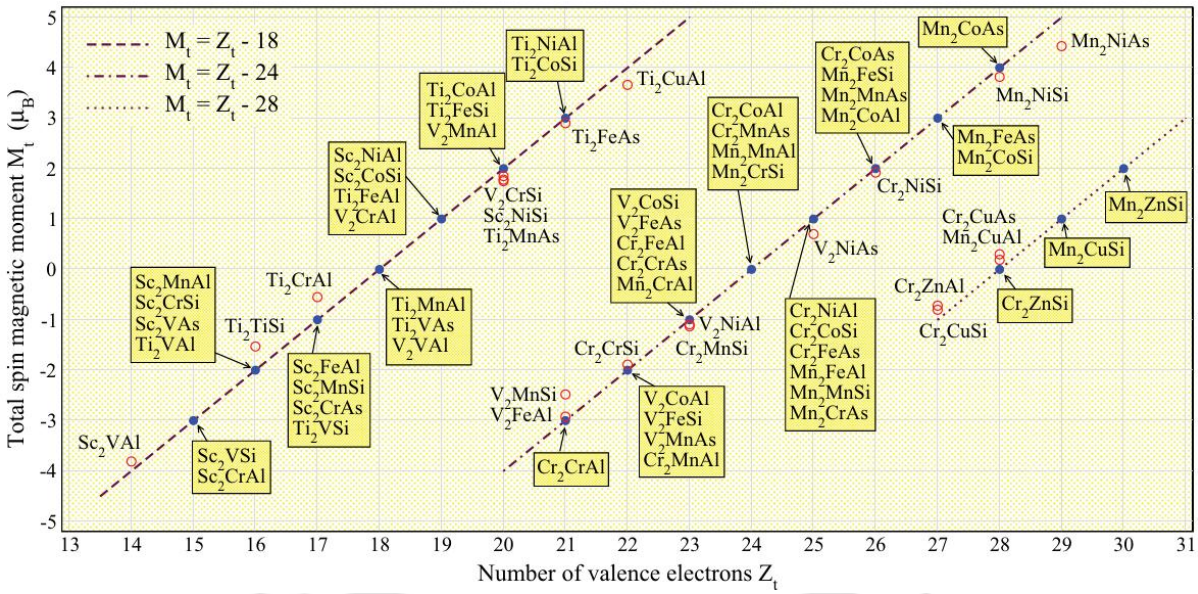

Figure 1.10. Variation of spin magnetic moment M_t with total number of valence electrons Z_t in inverse Heusler alloys, as described by the S-P rules in Equation (1.09) [SKAF2013].

1.2.1.2.3. Magnetization dynamics

FM materials exhibit spontaneous magnetization due to the collective alignment of individual spin moments in the same direction. When an FM material is exposed to an external magnetic field, the magnetization vectors gradually reorient along the field direction, typically through a precessional motion in a helical path. The time evolution of a spin can be described mathematically using an equation of motion [KAUF2006]. This dynamic behaviour is governed by the commutator of the spin operator **S** (or $S\hat{n}$, where $\hat{n}$ is the unit vector along S)

with the Hamiltonian operator *H*, providing a fundamental description of how the spin responds to the magnetic field. *i.e.*,

$$i\hbar \frac{d}{dt}\langle \boldsymbol{S} \rangle = [\boldsymbol{S}, H] \tag{1.10}$$

The interaction between the spin vector $\boldsymbol{S}$ and the magnetic field $\boldsymbol{B}$ ($B\hat{n}$, where $\hat{n}$ is unit vector along B) can be expressed as,

$$H = -\frac{g\mu_{\mathrm{B}}}{\hbar}\, \boldsymbol{S} \cdot \boldsymbol{B} \tag{1.11}$$

Using the commutation relations for spin operators [KAUF2006],

$$\left[S_i, S_j\right] = \mathrm{i}\hbar\varepsilon_{\mathrm{ijk}} S_{\mathrm{k}} \tag{1.12}$$

Now, using Equation (1.11), we can write,

$$[\boldsymbol{S}, H] = \mathrm{i}g\mu_{\mathrm{B}}(\boldsymbol{S} \times \boldsymbol{B}) \tag{1.13}$$

Substituting Equation (1.13) in (1.10), we get,

$$\frac{d}{dt}\langle \boldsymbol{S} \rangle = \frac{g\mu_{\mathrm{B}}}{\hbar}(\boldsymbol{S} \times \boldsymbol{B}) \tag{1.14}$$

The motion described above pertains to an individual spin. In the macro spin model, the magnetization $\boldsymbol{M}$ is spatially uniform throughout the entire sample. In this context, $\boldsymbol{M}$ is expressed as $M\hat{n}$, where M denotes the magnitude of the total magnetic moment, and $\hat{n}$ indicates its orientation. For clarity, the vector $\boldsymbol{M}$ will be used to represent directional magnetization, while the scalar M will refer to its scalar magnitude. Magnetization $\boldsymbol{M}$ is associated with the spin $\boldsymbol{S}$ through the relation,

$$\boldsymbol{M} = \frac{g\mu_{\mathrm{B}}}{\hbar}\, \langle \boldsymbol{S} \rangle \tag{1.15}$$

As a result, the dynamics of magnetization in an external magnetic field $\boldsymbol{H}$ (or $H\hat{n}$, where $\hat{n}$ is the unit vector along H) is described by the equation,

$$\frac{d\boldsymbol{M}}{dt} = -\frac{g\mu_{\mathrm{B}}}{\hbar}(\boldsymbol{M} \times \boldsymbol{H}) \tag{1.16}$$

or

$$\frac{d\boldsymbol{M}}{dt} = -\gamma\,(\boldsymbol{M} \times \boldsymbol{H}) \tag{1.17}$$

Where, $\gamma = {}^{g\mu_B}/_{\hbar}$ referred to as the gyromagnetic ratio, defined in terms of Lande's g factor (g), Bohr magneton (μ_B), and reduced Planck constant ($\hbar$).

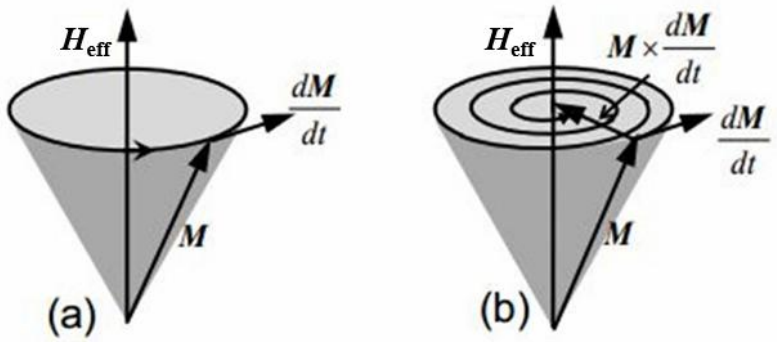

Figure 1.11. Schematic representation of magnetization vector ($\boldsymbol{M}$) precessing about the magnetic field ($\boldsymbol{H}$) (a) in the absence of damping and (b) in the presence of damping.

The equation presented above is known as the Landau-Lifshitz equation, which describes the motion of spins in the presence of a magnetic field without considering magnetic damping. Equation (1.17) can be extended to the effective magnetic field ($\boldsymbol{H}_{\text{eff}}$) by replacing $\boldsymbol{H}$ by $\boldsymbol{H}_{\text{eff}}$. Then, the modified expression suggests that the tip of the magnetization vector precesses in a circular orbit around the $\boldsymbol{H}_{\text{eff}}$, as depicted in Figure 1.11 (a), by maintaining a steady angular frequency of $\omega = \gamma \boldsymbol{H}_{\text{eff}}$ for the ideal undamped case. However, in reality, the precession amplitude of the magnetization gradually diminishes over the time, causing the tip of the magnetization vector to trace a spiral path as shown in Figure 1.11 (b).
Consequently, a damping or relaxation term (denoted as R) must be introduced into the Landau-Lifshitz equation [GURE1996].

$$\frac{d\boldsymbol{M}}{dt} = -\gamma\,(\boldsymbol{M} \times \boldsymbol{H}_{\text{eff}}) + R\,(\boldsymbol{M}, \boldsymbol{H}_{\text{eff}}) \tag{1.18}$$

Landau and Lifshitz proposed [LAND1935],

$$R = -\frac{\lambda}{M_s^2}\,\boldsymbol{M} \times (\boldsymbol{M} \times \boldsymbol{H}_{\text{eff}}) \tag{1.19}$$

In the above expression, λ will change depending on $\boldsymbol{H}_{\text{eff}}$, which is physically inconsistent. To fix this, Gilbert proposed a model where the relaxation term is linked to the rate of change of the magnetization vector [GILB2004], *i.e.*,

$$R = \frac{\alpha}{M_s}\left(\boldsymbol{M} \times \frac{d\boldsymbol{M}}{dt}\right) \tag{1.20}$$

By substituting Equation (1.20) for the relaxation term in Equation (1.18), the equation of motion of the magnetization vector can be formulated as,

$$\frac{d\boldsymbol{M}}{dt} = -\gamma\,(\boldsymbol{M} \times \boldsymbol{H}_{\text{eff}}) + \frac{\alpha}{M_s}\left(\boldsymbol{M} \times \frac{d\boldsymbol{M}}{dt}\right) \tag{1.21}$$

Equation (1.21) is commonly referred to as the Landau-Lifshitz-Gilbert (LLG) equation [LAND1935]. The term α is Gilbert damping, associated with the material's intrinsic relaxation rate. It plays a vital role in influencing the dynamic response of magnetic materials in spintronic applications, especially in the free FM layer of MR devices. In most transition metals, $\alpha \ll 1$, indicating that the magnetization vector precesses multiple times around $\boldsymbol{H}_{\text{eff}}$ before aligning with it. The approximate values of α for Co, Fe, Ni, permalloy, and $Co_2FeGa_{0.5}Ge_{0.5}$ Heusler alloy are 0.0035, 0.0024, 0.045, 0.0046, and 0.008, respectively [DONG2021, VARA2012, WALO2008, WEBE2019, WUSS2022].

1.2.2. Literature review on Co-based Heusler alloys

Heusler alloys exhibit diverse technological applications, with their functional properties being sensitive to their elemental constituents. Among the Heusler alloys family, Co-based Heusler alloys are the most extensively investigated alloys due to their exceptional magnetic, electric, and electronic properties [WOLL2017]. After the initial research on Cu_2MnAl and Cu_2MnSn alloys conducted by F. Heusler, Otto Heusler, and Bradley *et al*. [BRAD1933, HEUS1934], Co-based full Heusler alloys were first explored by Ziebeck and Webster [ZIEB1974]. Later, in 1978, Jaggi *et al*. investigated the distribution of atoms within Co_2FeGa synthesized by induction melting [JAGG1978]. Grover *et al*. in 1980 studied the magnetic properties of Co_2FeAl Heusler alloys [GROV1980]. Following this, Buschow *et al*. synthesized a series of Co_2YAl (Y = Fe, Mn, Cr, Ta) compounds, which demonstrated a wide range of magnetic moments from 1.50 to 4.96 μ_B/f.u. [BUSC1981]. In 1982, Ishida *et al*. performed first-principles calculations on Heusler compounds such as Co_2MnSn, Co_2TiSn, and Co_2TiAl to investigate their half-metallic ferromagnetism. However, their study did not reveal any

evidence of half-metallic ferromagnetism in these compounds [ISHI1982]. It was de Groot *et al*. in 1983 who first reported half-metallic electronic structure in the half-Heusler compound, NiMnSb. Later, Galanakis *et al*. supported this finding through theoretical studies [GALA2002a] and further extended their investigations to CoMnSb and FeMnSb, which were also predicted to exhibit half-metallic behavior [GALA2006]. In contrast to these predictions, Ksenofontov *et al*. demonstrated that bulk CoMnSb does not exhibit half-metallic behavior when its experimentally deduced crystal structure was taken into account [KSEN2006]. Through *ab initio* calculations, Wollmann *et al*. discovered half-metallic behavior in Co_2MnGe and Co_2MnSi [WOLL2017]. Galanakis *et al*.'s theoretical studies identified a half-metallic nature in Co_2MnGe, but not in Co_2MnZ (where Z = Al, Sn). They also proposed the S-P rule for full Heusler alloys [GALA2002b]. Marchenkov *et al*. [MARC2018a] synthesized bulk Co_2YZ (Y = Ti, V, Cr, Mn, Fe, Ni; Z = Al, Si, Ga, Ge, In, Sn, Sb) alloys and observed half-metallic behavior in Co_2FeSi Heusler alloy, and reported a T_C of 1100 K, which were consistent with the subsequent studies on Co_2FeSi compound. In addition to the above advancements in Co-based Heusler alloys, Co_2Fe- and Co_2Mn-based alloys have, in particular, drawn more attention due to their structural stability and desirable magnetic properties, including a wide range of M_s and high T_C, along with superior electronic properties like high *P*.

1.2.3. Tailoring Heusler alloys for spintronics

In recent years, extensive research has been conducted to identify potential materials for spintronics applications. In particular, high *P* is the key factor for achieving large MR output in devices like SVs and MTJs. Although many Heusler alloys have been reported to exhibit 100% *P*, most of them retain high *P* only at low temperatures, with a significant drop at room temperatures, as evidenced by the reduction in MR [ISHI2006, LIST2013, MARU2007, SAKU2010]. The decline in *P* in half-metallic Heusler alloys is because E_F is positioned near the edge of either the conduction or valence (minority spin) band, making *P* and consequently MR, highly sensitive to small shifts in E_F caused by thermally induced disorder. To address this drawback, materials should have a wide band gap in the minority spin channel with E_F positioned near the center of the minority gap. Elemental substitution in ternary Heusler alloys has proven to be effective for enhancing *P*, as it can shift E_F toward the center of the minority spin bandgap. In this context, it is worth pointing out certain reports, including that of Shambhu *et al*., which showed that *P* increases in $Co_{2-x}Ti_xFeGe$ ($0 \leq x \leq 1$) Heusler alloys with Ti substitution [SHAM2019]. Mahat *et al*. [MAHA2021b] studied $Co_{2-x}Cr_xFeGe$ ($0 \leq x \leq 1$) Heusler alloys and found that increasing Cr leads to an increase in *P* by widening the minority

gap and shifting E_F toward the center of the minority gap, along with an increase in majority spin density near E_F. In a related study, they also examined $Co_2Fe_{1-x}V_xGe$ ($0 \leq x \leq 1$) and predicted high P using *ab initio* calculations, which was subsequently supported by the resistivity measurements [MAHA2021a]. They also reported that M_s of arc-melted $Co_{2-x}V_xFeGe$ ($0 \leq x \leq 1$) alloys followed the S-P rule, indicating their half-metallic character and supported their findings with resistivity measurements [MAHA2023].

Apart from the studies focused on inducing half-metallicity in ternary Heusler alloys, Co_2FeAl and Co_2MnAl are the widely investigated Heusler alloys due to their high M_s and T_C. It is reported that E_F lies at the edge of the minority spin valence band in both these compounds, resulting in a small amount of states at E_F, which leads to a lower P [BALK2008, JUNG2009, RAMS2011]. Additionally, these alloys are known to exhibit a $B2$-type partially disordered structure. Miura *et al*. reported that this partial disorder in Co_2FeAl leads to a slight increase in the minority DOS, resulting in reduced P [MIUR2004]. Hence, to achieve high P at room temperature, E_F should be positioned close to the centre of the minority gap by appropriately modifying the alloy composition with a highly ordered $L2_1$-type structure. In line with this, Xiong *et al*. [XION2014] resorted to substituting 50 at.% Ti for Co in Co_2FeAl and reported shifting E_F to the centre of the minority gap of semiconducting Heusler alloy CoFeTiAl with zero magnetic moment. In a similar way, Marco *et al*. [MARC2018b] and Basit *et al*. [BASI2011] suggested that substituting 50 at.% of V for Co in Co_2MnAl results in the formation of a zero magnetic moment quaternary Heusler alloy, CoMnVAl. Furthermore, Basit *et al*. [BASI2011] confirmed the formation of the Y-type fully ordered structure in both CoFeTiAl and CoMnVAl. Based on these reports, it can be speculated that partial substitution of Ti and V atoms for Co in Co_2FeAl and Co_2MnAl, respectively, may shift E_F into the minority gap while simultaneously enhancing the order in the alloys. Although there are a significant number of reports on Co_2FeAl and Co_2MnAl, only limited studies are available on CoFeTiAl [BASI2011, LINT2016a, LINT2016b, LINT2018, XION2014] and CoMnVAl [BASI2011] alloys. Moreover, there is no systematic investigation on the effect of Ti and V on the properties of the $Co_{2-x}FeTi_xAl$ and $Co_{2-x}MnV_xAl$ (where $0 < x < 1$) alloys, respectively. Notably, from the report on zero magnetic moment CoFeTiAl and CoMnVAl, it is expected that the magnetic moment will decrease with an increase in Ti in $Co_{2-x}FeTi_xAl$ and V in $Co_{2-x}MnV_xAl$. Because of the reduction in magnetic moment, the T_C is also expected to decrease with Ti and V substitution. Since achieving high P and T_C along with an optimized magnetic moment of the alloy are important for spintronic applications, systematic investigations of the structural,

magnetic, and electronic properties of $Co_{2-x}FeTi_xAl$ and $Co_{2-x}MnV_xAl$ ($0 \leq x \leq 1$) Heusler alloys are crucial.

In addition to identifying robust half-metallic materials with high *P* to achieve large MR ratio, it is equally important to assess their compatibility for spintronic applications. Specifically, for employing an FM material as the free layer in MR devices, low α is important for energy efficiency [FANY2024]. Low α can be related to high *P* of the material. Because, α is considered to be proportional to the DOS at E_F, the presence of only one type of electronic spin (either up or down) DOS at E_F in a half-metallic material can result in a small DOS at E_F, leading to low α [KUBO2009, MIZU2009, SHAW2018]. Furthermore, spin-flip scattering is forbidden in half-metallic materials [SHAW2018], leading to a further reduction in α. Although materials like Fe, Co, Ni, and their alloys (NiFe and CoFe) demonstrate low α values [DONG2021, WALO2008, WEBE2019, WUSS2022], Heusler alloys like Co_2MnSi [ANDR2016], Co_2MnZ (Z = Si, Ge, Sn, Al, Ga, and Sb) [GUIL2019], and $Co_{2-x}Mn_{1+x}Si$ (x = 0.1) [OOGA2018] exhibit even lower α due to their half-metallic property. However, the finite solubility of Mn of these alloys in the Ag spacer used in the SVs reduces the MR [INOU2019, SAKU2011]. These findings have focused research interest on the more extensively studied stable $Co_2FeGa_{0.5}Ge_{0.5}$ (CFGG) alloy with low α. However, Goto *et al*. [GOTO2020] have shown a reduced *P* in stoichiometric CFGG due to Co-Fe anti-site disorder arising from Co atoms occupying Fe sites. To overcome this drawback, Chen *et al*. [CHEN2022] proposed that *P* can be enhanced in Co-deficient and Fe-rich off-stoichiometric CFGG through suppression of Co-Fe disorder. Despite these insights, α of the CFGG alloy thin film has not yet been reported, with only the bulk value (~0.008) [VARA2012] available in the literature. Moreover, for spintronic applications, it is important to understand the correlation between α and *P*, which in turn depends on the atomic order. Surprisingly, the same has not been investigated in Co-deficient and Fe-rich off-stoichiometric CFGG films.

Besides low α, the development of high-performance MR devices requires an effective mechanism for efficient switching of the free FM layer. This has led to the use of the spin-orbit torque (SOT) mechanism, which involves placing an additional heavy metal (HM) layer adjacent to the free FM layer, as shown in Figure 1.12 [KRIZ2022, LIUT2024, SONG2021, WORL2024].

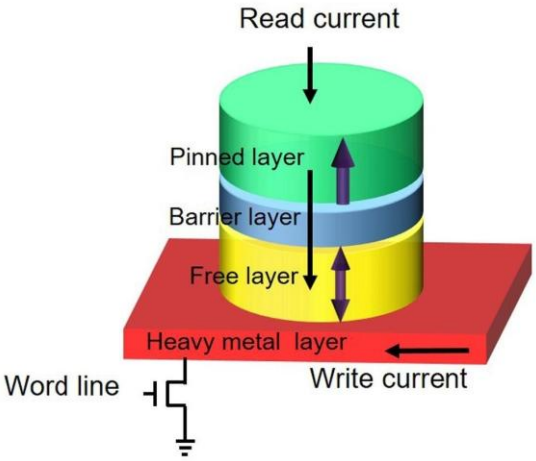

Figure 1.12. Schematic representation of SOT-based MR device. An in-plane current in the heavy metal (HM) layer is used to switch the magnetization of the free layer by the SOT mechanism [SONG2021].

An in-plane charge current in the HM layer generates a spin current via the spin Hall effect. This spin current is injected into the adjacent FM free layer, where it exerts a SOT that switches the magnetization of this FM layer. The efficiency of spin current injection is quantified by $g_{\mathrm{eff}}^{\downarrow\uparrow}$ across the free FM/HM interface [AKAN2018, KUMA2019, SING2021]. For efficient SOT-driven magnetization switching, a large $g_{\mathrm{eff}}^{\downarrow\uparrow}$ (~ 10^{19} to 10^{20}) is required. $g_{\mathrm{eff}}^{\downarrow\uparrow}$ depends on the HM layer, and materials such as Pt, Ta, W, Ir, or Hf as a HM layer have been reported to achieve high $g_{\mathrm{eff}}^{\downarrow\uparrow}$ due to large spin-orbit coupling. In addition to HM layer materials, $g_{\mathrm{eff}}^{\downarrow\uparrow}$ depends on the properties at the FM/HM interface. Zhang *et al*. theoretically showed that an increase in interface roughness enhanced $g_{\mathrm{eff}}^{\downarrow\uparrow}$ in the permalloy/Pt bilayer [ZHAN2011]. Tokaç *et al*. experimentally observed the effect of FM and NM crystal structure at the interface in Ta/Cu/Co/Cu(or Ir)/Ta multilayers and found that $g_{\mathrm{eff}}^{\downarrow\uparrow}$ increases when the FM layer and NM overlayers have the same crystal structure [TOKA2015]. The impact on $g_{\mathrm{eff}}^{\downarrow\uparrow}$ by modifying the FM/HM interface with insertion layers have been reported in several studies. For example, Kumar *et al*. [KUMA2019] studied the effect of Cu insertion layer (thickness = 0 - 10 nm) on $g_{\mathrm{eff}}^{\downarrow\uparrow}$ in Co_2FeAl/β -Ta bilayer, and Swindells *et al*. studied the effect of Au insertion layer (0 - 3 nm) in $Co_{25}Fe_{75}$/Pt and $Ni_{80}Fe_{20}$/Pt bilayers, which demonstrated a modification in $g_{\mathrm{eff}}^{\downarrow\uparrow}$ by the insertion layer [SWIN2021, SWIN2022]. Although the mechanism underlying $g_{\mathrm{eff}}^{\downarrow\uparrow}$ modification has been discussed from the viewpoints of proximity induced magnetization and interface transparency of spin current, a detailed structural analysis of the HM overlayer at the FM/HM interface has not been conducted so far. Therefore, it is important to investigate the

changes in $g_{\text{eff}}^{\uparrow\downarrow}$ solely due to the insertion layers, by separating the possible contributions arising from structural modifications in the Pt overlayer caused by the insertion layers.

1.3. Motivation and objectives of the thesis

Though Co_2FeAl and Co_2MnAl have high M_s and elevated T_C, the presence of a small amount of minority DOS at E_F reduces the P of these alloys, thereby limiting their performance as a FM layer in MR devices. On the other hand, quaternary Heusler alloys, such as CoFeTiAl and CoMnVAl, have been found to be semiconducting with zero net magnetization and exhibiting zero minority DOS at E_F [BASI2011, MARC2018b, XION2014]. Therefore, it is speculated that partial substitution of Ti and V for Co in Co_2FeAl and Co_2MnAl, respectively, could enhance P by shifting the E_F from the valence band edge toward the center of the minority bandgap.

In addition to achieving the high P, the impact of P on α is equally important for determining the compatibility of free FM layers in MR devices. In this regard, CFGG is a noteworthy choice as an FM layer for such investigations due to its reported high MR ratio [TAPA2024]. However, the presence of Co-Fe disorder in CFGG reduces its P [GOTO2020]. To overcome this, it is proposed to investigate the impact of P on α in Co-deficient and Fe-rich off-stoichiometric CFGG alloy film in this thesis work.

Furthermore, the utilization of the SOT mechanism to switch the free FM layer magnetization in MR devices requires high $g_{\text{eff}}^{\uparrow\downarrow}$ (~ 10^{19} to 10^{20}) across the FM/HM interface. Since $g_{\text{eff}}^{\uparrow\downarrow}$ depends on the spin orbit coupling of HM layer, and Pt has high spin orbit coupling, it is proposed to investigate Pt as a HM layer in this thesis work. Additionally, several studies have shown that the $g_{\text{eff}}^{\uparrow\downarrow}$ depends on the FM/HM interface properties. In this regard, the impact on $g_{\text{eff}}^{\uparrow\downarrow}$ by modifying the FM/HM interface with insertion layers have been reported. However, none of the studies discuss the impact of structural modifications induced in the HM overlayer by the insertion layer. Therefore, it is important to investigate the changes in $g_{\text{eff}}^{\uparrow\downarrow}$ solely due to the insertion layers, by separating the possible contributions arising from structural modifications in the Pt overlayer structure caused by the insertion layers.

Motivated by the above discussions and gap in the literature, the main objective of this thesis was to identify suitable single-phase and highly ordered Co-Fe-Ti-Al and Co-Mn-V-Al quaternary Heusler alloy compositions with high P for spintronic applications. The next objective was to study the influence of P on α in CFGG thin films and investigate its potential

for spintronic applications by evaluating the $g_{\text{eff}}^{\downarrow\uparrow}$ across CFGG/Pt bilayer and examine the effect of insertion layers on $g_{\text{eff}}^{\downarrow\uparrow}$.

This thesis work was carried out with the above objectives. The contents of the remaining part of the thesis are outlined below:

- Chapter 2 presents the experimental methodologies employed for sample preparation and characterization, along with details of theoretical calculations performed to estimate their magnetic and electronic properties.
- Chapter 3 of the thesis focuses on the increasing *P* and enhancing the structural order in Co_2MnAl Heusler alloy bulk sample by the partial substitution of V for Co and provides a detailed study of structural, magnetic, and electronic properties of the alloys.
- Chapter 4 presents a comprehensive study on enhancing *P* and promoting fully ordered structure in bulk Co_2FeAl Heusler alloys through partial substitution of Ti for Co. This study offers an in-depth examination of the resulting changes in structural, magnetic, electronic, and electrical characteristics of the alloys.
- Chapter 5 of the thesis explores the variation of α with the change in *P* by improving the atomic order in off-stoichiometric CFGG alloy films.
- Chapter 6 of the thesis focuses on evaluating the $g_{\text{eff}}^{\downarrow\uparrow}$ in CFGG/Pt bilayer structures.
- Chapter 7 investigates the changes in $g_{\text{eff}}^{\downarrow\uparrow}$ due to modifications at the interface solely from Cu, Ni, Ru, Ta, or Cr insertion layers.
- Chapter 8 summarizes the main findings of the thesis and outlines possible directions for future research in these areas.
- The thesis concludes with a list of collated references cited in the thesis and a list of publications emanating from the thesis work.

Chapter 2

Experimental and theoretical methodologies

This chapter serves as a foundational element of the thesis by providing a comprehensive description of the methodologies used in synthesizing and characterizing bulk Heusler alloys and Heusler alloy-based thin films. It highlights the importance of selecting a particular synthesis method, as it directly influences material properties, structure, and performance in many applications. Following the discussion on material synthesis, the chapter describes the characterization techniques utilized to evaluate the structural, magnetic, and electronic properties of the prepared samples. To complement the experimental approach, theoretical calculations carried out on the alloys are then explained. These calculations were used to predict material behaviour and provide theoretical support for interpreting the experimental results. The experimental and theoretical approaches outlined in this chapter establish the framework for the analyses and discussions presented in the subsequent chapters of the thesis.

2.1. Sample preparation

2.1.1. Arc melting

Arc melting is a widely used method for preparing bulk alloy ingots of specific composition by melting constituent elements under an inert atmosphere. This method involves the generation of an electric arc between a tungsten electrode (anode) and the copper hearth (cathode) to produce intense heat to melt the pieces of high-purity elemental constituents of the proposed alloy. Figure 2.01 (a) depicts a schematic diagram of a conventional arc melting furnace. The arc melting process begins with loading high-purity (> 99.97%) constituent elements into the copper hearth inside the melting chamber. Here, copper was chosen as a hearth for its excellent thermal and electrical conductivity, facilitating efficient heat dissipation during melting and serving as a cathode in the arc generation process. To ensure an inert atmosphere and prevent contamination during melting, the chamber is first evacuated to 10^{-3} Pa using a high vacuum pumping station consisting of a combination of oil-based diffusion and rotary pumps. Subsequently, the chamber is purged with Ar gas 2-3 times, and finally, filled with Ar gas up to a residual pressure of ~101 kPa. In this condition, an electric current of 180-200 A is passed through the tungsten electrode to generate an electric arc between the anode and cathode. This arc creates a high local temperature of ~3000 °C, which melts the elements

placed in the copper hearth and forms the alloy ingot. To accomplish homogeneity in the composition throughout the alloy ingot, it is remelted 5-6 times by flipping it after each melt. Throughout the melting process, a continuous flow of water beneath the copper hearth is maintained to dissipate the heat flawlessly and prevent overheating of the hearth and chamber. The photograph of the experimental setup (Vacuum Technique Pvt. Ltd.) used in the present study for melting the samples is shown in Figure 2.01 (b) along with the associated instruments.

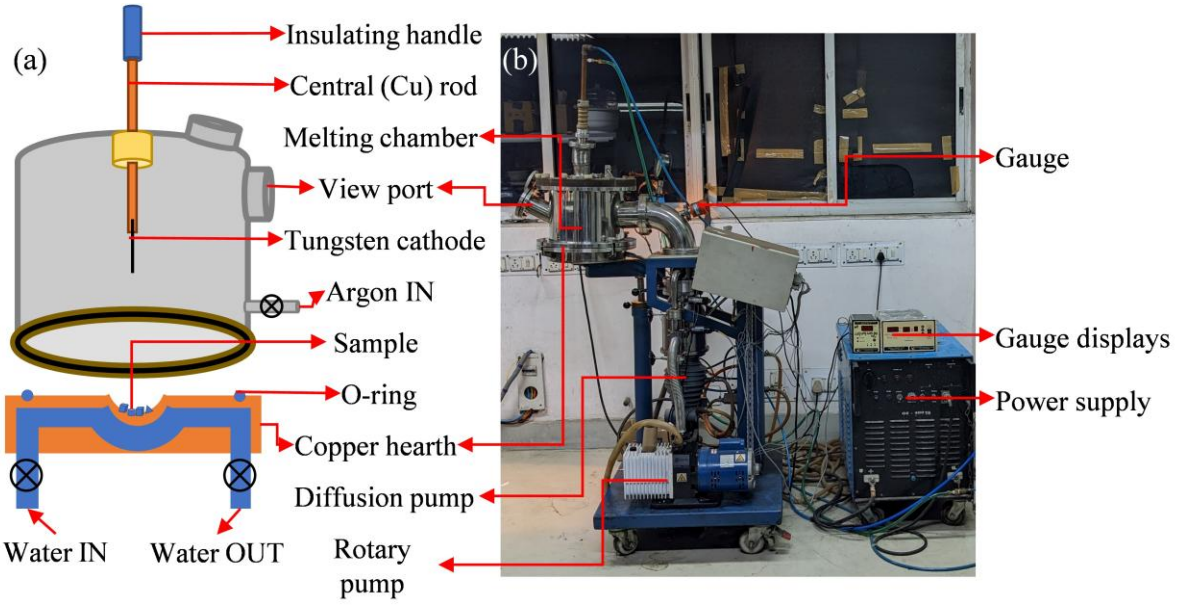

Figure 2.01. (a) Schematic representation of an arc melting furnace. (b) Experimental setup used in this study for arc melting.

In order to improve the compositional homogeneity and promote atomic ordering, as-melted bulk alloy ingots were subjected to heat treatment. This process involves placing the sample inside a fused silica ampoule, which is then evacuated to a low pressure of approximately 10^{-3} Pa using a high vacuum pumping station consisting of a combination of diffusion and rotary pumps (Vacuum Technique Pvt. Ltd.). The ampoule containing the sample is then flame-sealed at this low pressure to prevent oxidation during subsequent heat treatment. The sealed ampoule is heat treated in a rising-hearth electric furnace (OKAY, Model 70R4) for a selected time at a chosen temperature, followed by rapid quenching in ice water. The experimental arrangement of the vacuum sealing setup and the raising-hearth furnace is shown in Figure 2.02 (a and b), respectively. Finally, heat-treated samples are either gently ground into fine powder or sliced into flat specimens with a low-speed saw, depending on the requirements for further characterization.

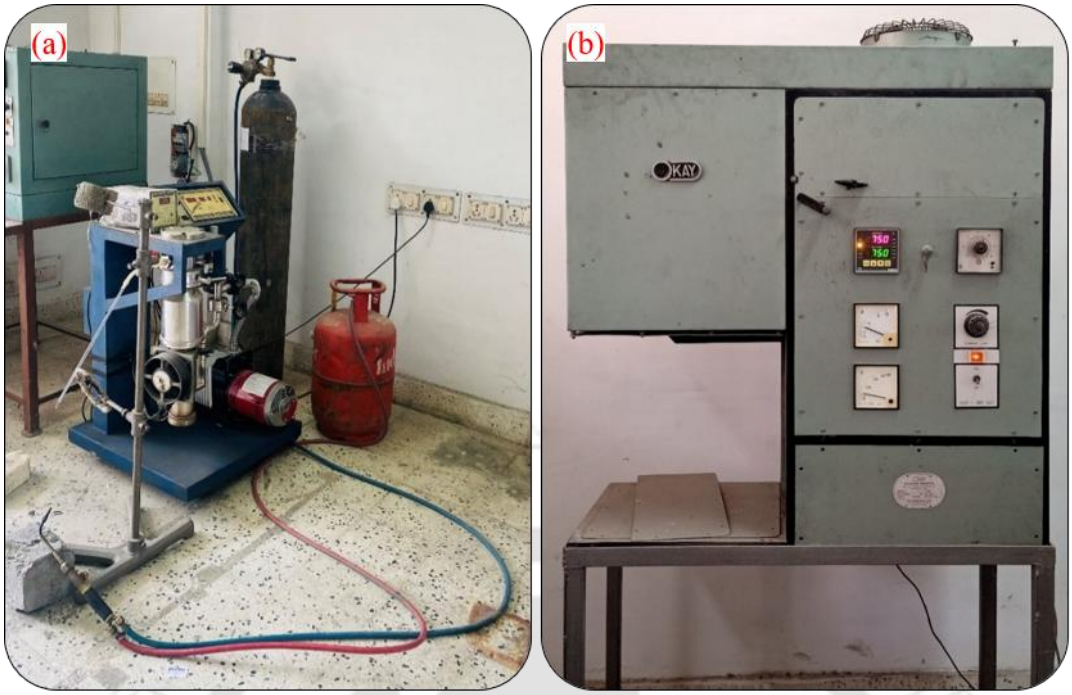

Figure 2.02. (a) Set-up for vacuum sealing of fused silica ampoule containing the as-melted ingot, and (b) raising-hearth furnace for heat treatment of the alloy sealed inside the ampoule.

2.1.2. Magnetron sputtering

Sputtering is a widely used technique for the deposition of thin films. Sputtering involves the ejection of atoms from the surface of a target material by the impact of energetic positive ions of noble gases (helium, argon, neon, and krypton) [KRIS2002], followed by the deposition of ejected atoms onto the substrate. Figure 2.03 (a) shows the schematic diagram of the sputtering process, which mainly involves three steps. First, the generation of positive ion plasma is achieved by applying a large potential difference between the target material (which acts as a cathode) and the anode. Second, generated positive ions in the plasma move at a large velocity toward the cathode, transferring their momentum to atoms on the cathode target surface, resulting in the ejection of atoms. Finally, the ejected energized atoms from the target surface are deposited onto the substrate. The deposited atoms undergo nucleation on the substrate, forming the initial atomic structure of the thin film. A schematic of a typical vacuum chamber arrangement for the sputtering process, with its main components are shown in Figure 2.03 (b).

During the deposition of thin film, to maintain a self-sustained plasma, a minimum Ar gas pressure is required to ensure a sufficient number of Ar ions. As the pressure increases, electrons collide more frequently with Ar atoms, enhancing ionization and increasing plasma density. However, excessively high Ar pressure can cause Ar^+ ions to lose energy through collisions with neutral Ar atoms. This energy loss reduces the ions' ability to effectively

bombard the target surface, thereby decreasing the sputtering efficiency and ultimately lowering the deposition rate. This limitation can be overcome by using the magnetron sputtering process in which magnets are placed behind the target to generate a magnetic field in the vicinity of the target. This magnetic field traps electrons near the target surface, thereby enhancing ionization efficiency at relatively lower Ar pressure. Achieving a high ionization rate at lower pressure enhances the probability of Ar^+ ion bombardment on the target with high speed and facilitates efficient transport of sputtered atoms to the substrate, resulting in an increased deposition rate.

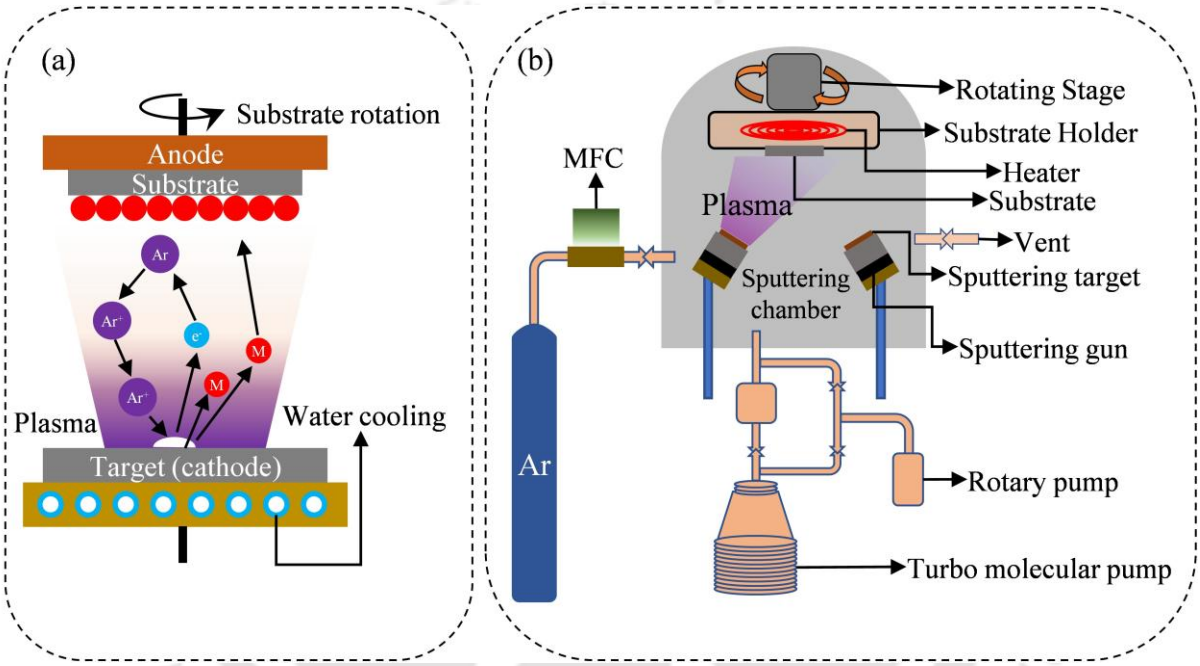

Figure 2.03. (a) Schematic illustration of the sputtering process. (b) Main components of a typical sputtering system.

The process of deposition of thin films starts with evacuating the sputtering chamber to a base pressure of ~10^{-7} Pa, followed by purging it with Ar gas 2-3 times to remove any residual gas molecules. Then, the chamber is filled with Ar at the desired deposition pressure, typically around 10^{-1} Pa. Under these conditions, electric power is applied to initiate and sustain the Ar ion plasma for the sputtering of the target. Based on the type of applied electric power, the sputtering technique is primarily classified into two types: direct current (DC) and radio frequency (RF) sputtering. DC magnetron sputtering offers the advantage of a higher deposition rate, making it ideal for applications requiring conducting films. Despite these advantages, DC magnetron sputtering is limited to the deposition of conducting materials. Since insulators do not conduct electricity, the continuous bombardment of positive (Ar^+) ions leads to the accumulation of charges on the insulating target. This causes instability in the

plasma and failure of the Ar ions to sputter the atoms from the surface of the target effectively. To overcome this, RF magnetron sputtering is used for insulating target materials, as it allows an alternating current of 13.56 MHz frequency to neutralize the surface charge and ensure continuous sputtering. In addition to insulators, RF sputtering is also suitable for depositing conducting materials, offering broader versatility in thin film deposition. It operates under similar conditions as DC magnetron sputtering, using inert gases like Ar to generate and maintain the plasma.

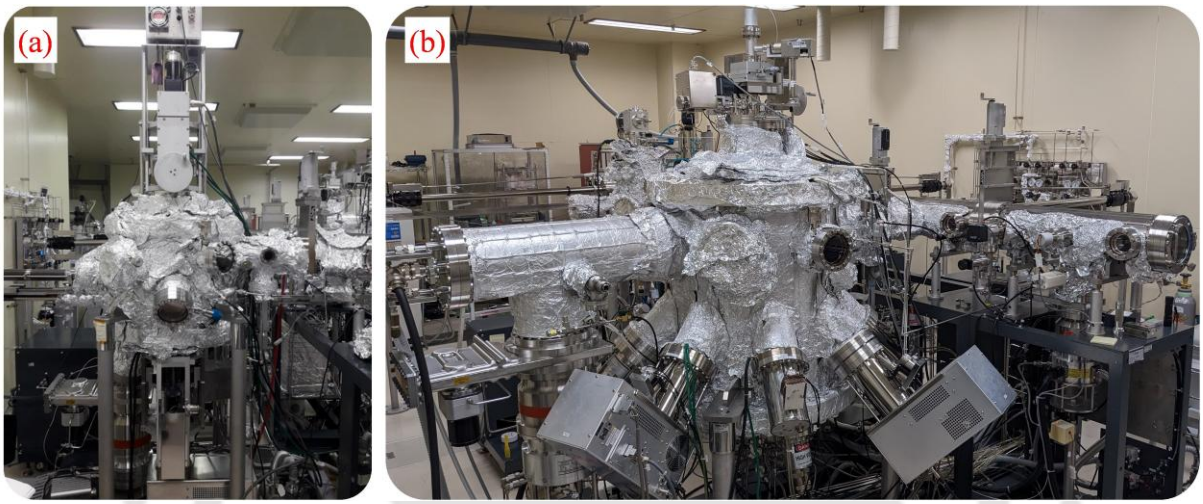

Figure 2.04. Photograph of ultra-high vacuum magnetron sputtering system comprising of two chambers, *viz*., (a) CH1, and (b) CH2.

Taking all these aspects into account, both DC and RF magnetron sputtering are employed in the deposition of uniform single and multilayer thin films with precise control over thickness and composition. The ultrahigh vacuum magnetron sputtering system (Eiko ES-350) comprising two sputtering chambers (CH1 and CH2) is shown in Figure 2.04 (a and b), respectively. This sputtering system is equipped with a load lock chamber and a robotic arm that facilitates the transfer of the sample holder between the two sputtering chambers and the load lock chamber. The two deposition chambers, CH1 and CH2, collectively have 9 sputtering guns, comprising both DC and RF magnetron sources. Each deposition chamber and load lock chamber is fitted with a turbo molecular pump and backed by a rotary pump to maintain a high vacuum (~10^{-7} Pa) environment. Both deposition chambers are equipped with substrate heaters to maintain a constant substrate temperature during the deposition and to enable *in situ* annealing after deposition. CH2 includes an Ar^{+} milling facility that enables substrate cleaning by surface etching to promote epitaxial growth of thin films. This system is designed to seamlessly integrate substrate cleaning, film deposition, and *in situ* annealing processes in a single workflow. To ensure uniform deposition, the substrate is rotated about its vertical axis

during the deposition process. The deposition rate depends on various parameters, such as the electrical power, target-to-substrate distance, and Ar gas pressure.

2.1.2.1. Film thickness control

The properties of thin films are highly sensitive to their thickness. So, it is essential to control the film thickness by calibrating the deposition rate accurately for a chosen target and deposition conditions. Once the deposition rate is calibrated, a desired film thickness can be achieved by merely controlling the deposition time without changing the other process parameters. The thickness of the deposited films was measured *ex situ* using a surface profilometer (KLTA-Tencor D-120), shown in Figure 2.05 (a).

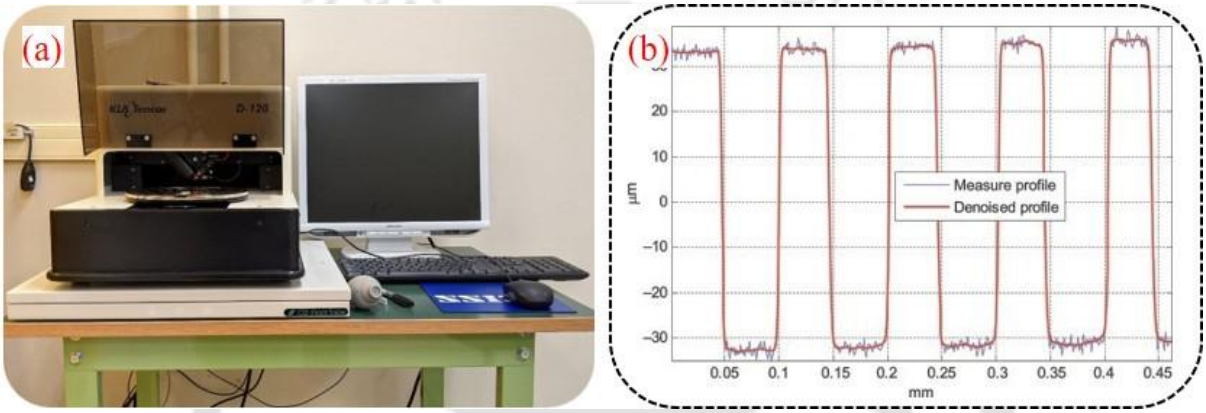

Figure 2.05. (a) Photograph of stylus profilometer (KLA-Tencor D-120). (b) A representative scan profile, obtained using the stylus profilometer, shows the surface topography and step height measurements.

To measure the thickness of the thin film, the substrate was initially cleaned, and a fine line was drawn on it using a permanent ink marker pen prior to deposition. The thin film is then deposited on this substrate as explained above. After deposition, the film was gently cleaned with ethanol and then sonicated in acetone to remove the permanent marker ink along with the material deposited on top of it. This process creates distinct step heights and trench depths. While measuring the sample thickness, the stylus of the profilometer moves linearly, and as it encounters the sample surface, it moves vertically to record the nature of the surface and measures the film thickness and surface irregularities. A typical scan profile, obtained using the stylus profilometer, is depicted in Figure 2.05 (b), showing the surface topography and step height. This helps to determine the thickness of the thin film deposited. To minimize the error, the sample thickness was measured at multiple positions, and the average value was taken. During sputtering, by keeping all controllable deposition parameters constant, a nearly uniform deposition rate can be achieved throughout the deposition. The average deposition rate

was calculated by dividing the measured average film thickness by the total deposition time (say, 15 minutes). Using this deposition rate as a reference, thin films with different thicknesses were deposited by varying the deposition time, while maintaining identical sputtering conditions. The same procedure was consistently followed while depositing various thin films under different sputtering conditions.

2.1.2.2. Lithographic patterning of the films

Lithography is one of the most widely used techniques for patterning thin films into desirable structures at micrometer or sub-micrometer scales. The ability to design complex devices at various scales, down to a few micrometers, along with the integration of multiple components, cost-effectiveness, and high precision in electrode fabrication, makes this process highly advantageous. The lithography process employed in this work includes several steps, outlined in Figure 2.06, and described below:

i. Cleaning of the film

The lithography process begins with cleaning of the thin film by sonicating it in butanone for 10 minutes to remove any organic or inorganic contaminants from its surface. This is followed by sonication for 10 minutes in isopropyl alcohol, then gently drying using a spray of nitrogen gas over it using an N_2 air gun.

ii. Resist coating

Resist coating is a process of applying a thin layer of radiation-sensitive material on top of the sample surface. These resists are generally highly viscous organic polymers and are classified into mainly two types, namely, positive and negative, based on their response to ultraviolet (UV) radiation [BRAT2006]. In positive resists, exposure to UV light degrades the polymer and makes it soluble in the developer solution, causing it to be removed, while the unexposed regions remain intact. Conversely, in negative resists, UV exposure hardens the polymer, making it resistant to solubility in the developer solution. The choice of resist material determines different forms of exposure, enabling various lithographic techniques, such as electron-beam lithography, ion-beam lithography, photolithography, X-ray lithography, *etc*. The choice of radiation primarily depends on the specific application requirements and the dimensions of the device. In this thesis work, photolithography was employed to fabricate device patterns for magnetoresistance studies on the thin film samples.

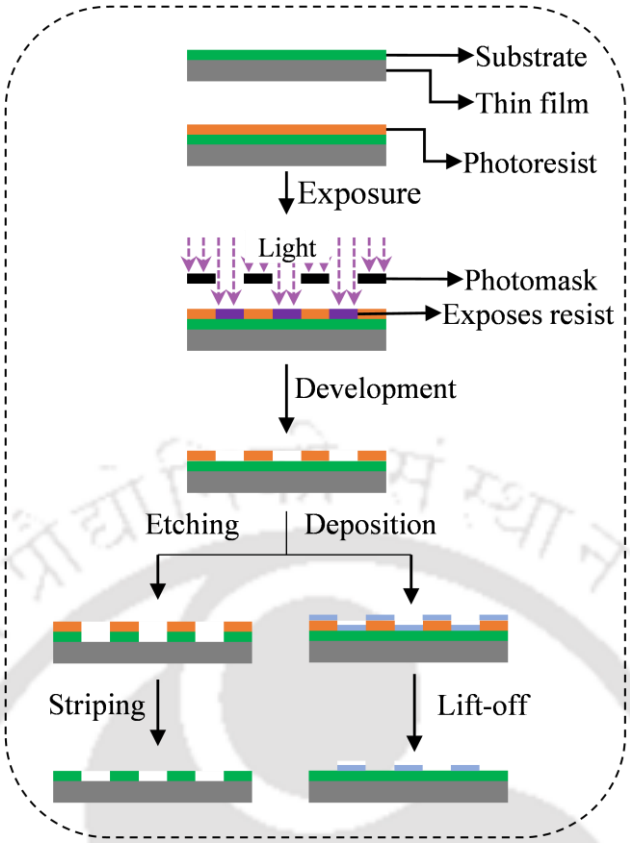

Figure 2.06. Steps involved in the lithographic patterning process.

Once the film surface is cleaned, an organosilicon compound hexamethyldisilazane ($[(CH_3)_3Si]_2NH$) is spin-coated onto the sample at 3000 rpm for 45 seconds. To remove residual solvents, the coated sample is subjected to a prebake process on a hot plate at 100 °C for 2 minutes. A uniform coating of either the positive photoresist AZ5214E or the negative photoresist Ma N140 is applied using spin coating at 5000 rpm. This is followed by baking at 100 °C for 90 seconds to stabilize the resist layer. To prevent unintended exposure to ambient light, the sample is kept in a lightproof container. All these processes were carried out in a clean room environment.

iii. Exposure and development of the pattern on films

A physical photomask was used to transfer the desired pattern onto the photoresist-coated film through UV exposure. The underlying mechanism relies on the selective solubility of the photoresist in the developer, where exposed and unexposed regions dissolve at different rates, allowing a patterned mask to emerge. Following UV exposure, the photoresist pattern is developed by submerging the sample in AZ developer with mild agitation for 90 seconds. It is then quickly rinsed with distilled water for 30 seconds to remove any residual chemicals. Finally, the film is dried by purging with N_2 gas.

iv. Etching and removal of the resist

Once the photoresist pattern is developed, the pattern has to be transferred onto the underlying film. This is achieved by selectively removing the exposed regions of the film (those not protected by the photoresist) by etching. The regions of the film covered by UV-exposed negative photoresist serve as a protective mask during the etching process, shielding them from material removal. Etching can be carried out using chemical or physical approaches. One commonly employed physical method is ion milling, where inert gas ions (typically Ar^+) are directed at the film surface under high vacuum conditions to sputter away unprotected material. By this method, the exposed areas of the film are etched to a controlled depth, thereby transferring the intended pattern onto the film surface. The Ar ion milling system used in this thesis work is illustrated in Figure 2.07.

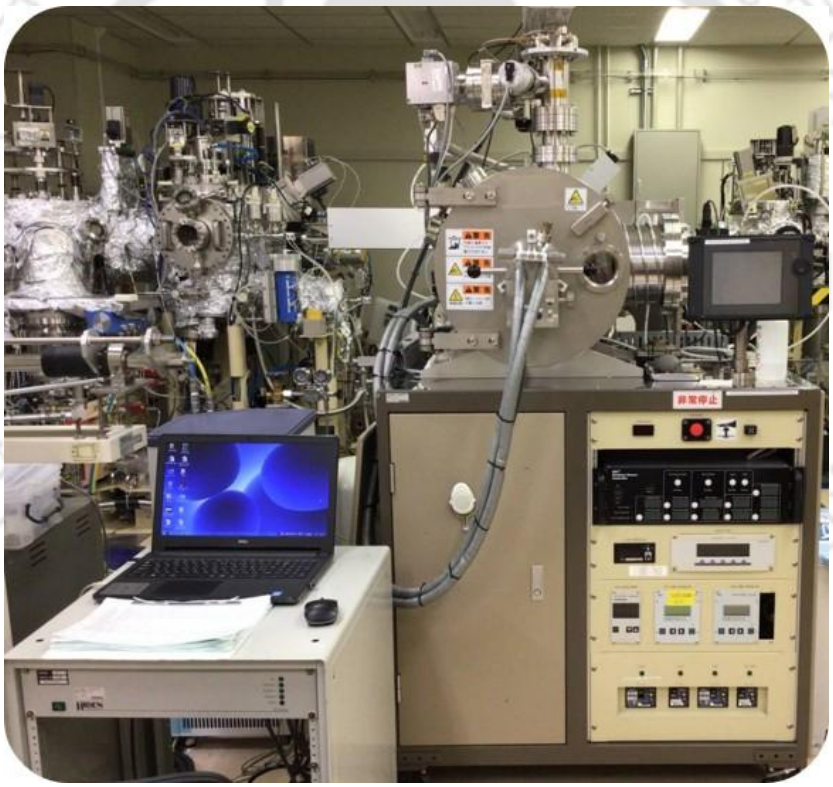

Figure 2.07. An Ar ion milling setup is used to etch and deposit thin film devices.

Once the photoresist has served its purpose, it is removed from the film surface. This sequence of steps is repeated multiple times, with different layers being deposited and patterned in succession to build intricate 3-dimensional designs. To form the contact pads, a 100 nm thick layer of gold is deposited over the patterned film surface. Following deposition, the remaining photoresist is removed by sonicating first in N-methylpyrrolidone (NMP) for 10-15 minutes, and then in acetone.

2.2. Characterization techniques

Characterization of materials is a fundamental step in understanding their structure, properties, and compatibility for various applications. This process involves using a range of probing techniques employing X-rays, photons, electrons, atoms, or ions, each capable of revealing different aspects of a material's behaviour. When these probes interact with a sample, they generate measurable signals that can be analyzed to reveal detailed information about the material's composition, crystal structure, microstructure, electronic states, magnetic properties, *etc*. The selection of characterization techniques depends on both the nature of the probe and the specific property being investigated. In this study, a combination of different techniques has been employed to systematically investigate the characteristic properties of the synthesized Heusler alloy samples. A detailed discussion of the properties examined, along with the experimental approaches and tools utilized, is presented in the following sections.

2.2.1. Determination of elemental composition

2.2.1.1. Energy dispersive X-ray spectroscopy

Energy dispersive X-ray spectroscopy (EDS or EDX) is an analytical technique used for the qualitative and quantitative determination of the elemental composition of materials. EDS operates on the principle of characteristic X-ray emission induced by a high-energy electron beam interaction with the atoms in the sample. When a focused electron beam strikes the sample surface, it imparts energy to the atoms. This will cause the electrons in the inner shells of the atoms to be ejected, creating electron vacancies. Electrons from higher energy levels then fall into the vacant lower energy states, releasing energy in the form of characteristic X-rays as shown in Figure 2.08 (a). The energy of these X-rays is unique to each element, and by measuring this energy, the elements present in the sample can be identified. The energy dispersive X-ray spectrometer is commonly mounted on a scanning electron microscope (SEM), so that it can exploit the advantages of the SEM and use its functions. The schematic of a typical SEM is shown in Figure 2.08 (b). An SEM mainly consists of an electron source (electron gun), condenser lenses, objective lenses, scan coils, and detectors.

The electrons in the SEM are typically generated using either thermionic or field emission sources [ZHAN2008b]. In this study, a field emission source was used to generate an electron beam. So, the instrument is named as a field emission scanning electron microscope (FESEM). In FESEM, the condenser lens with a larger focal length is used to focus the electron beam onto the sample, while the objective lens, having a shorter focal length, is used to magnify and project the image onto the image plane [ZHAN2008b]. Both of these lenses are

electromagnetic lenses, in which the focal length of each can be precisely adjusted by changing the current passing through the respective solenoid coil [ZHAN2008b]. The scan coils are responsible for directing the electron beam towards the sample as required. When the incident electron beam strikes the sample, electrons may undergo scattering, absorption, or transmission, depending on their interaction with the material. In FESEM, multiple detectors are employed depending on the type of information required from the sample, such as surface morphology, elemental composition, or internal structure. For compositional analysis, the FESEM with EDS detector (Zeiss, Σigma) operated at an acceleration voltage of 20 kV was used. The photograph of instrument used in the present work is shown in the Figure 2.09.

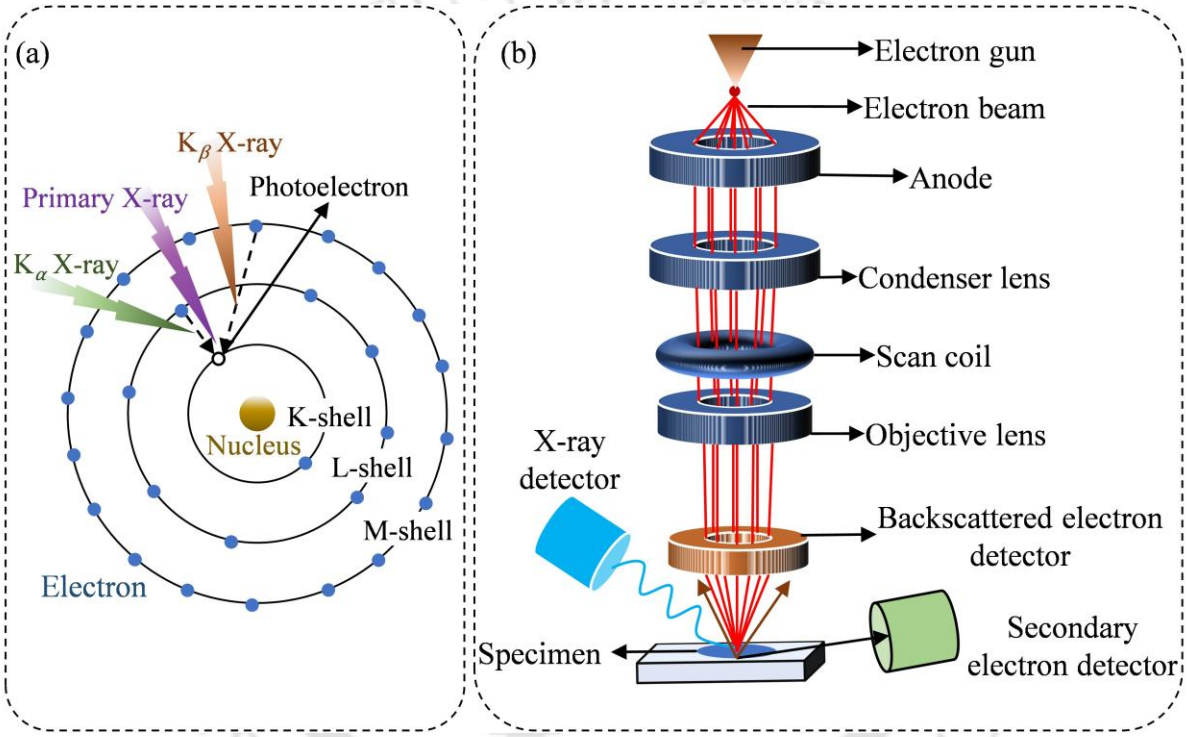

Figure 2.08. (a) Schematic of the characteristic X-ray generation process by the incident electrons. (b) Schematic diagram of a typical SEM setup.

Analysis of an EDS spectrum can provide elemental concentration in both weight percentage (wt.%) and atomic percentage (at.%). At.% data have been used in the present studies as they are more relevant to metallic alloys. The actual atomic percentages were obtained by excluding the carbon content from the mounting tape and the gold content from the applied surface coating. Figure 2.10 displays an EDS spectrum of the $Co_{1.5}FeTi_{0.5}Al$ bulk Heusler alloy, where the intensity of X-rays is plotted as a function of energy. Each distinct peak corresponds to a characteristic element present in the sample. The spectrum reveals Co, Fe, Ti, and Al as the constituent elements with atomic percentages of 37.5, 25.3, 12.8, and 24.5,

respectively. The elemental compositions were evaluated by taking the average of 10-15 such individual spectral scans from different parts of the same sample.

Figure 2.09. Field emission scanning electron microscope (Zeiss, Σigma) with EDS unit.

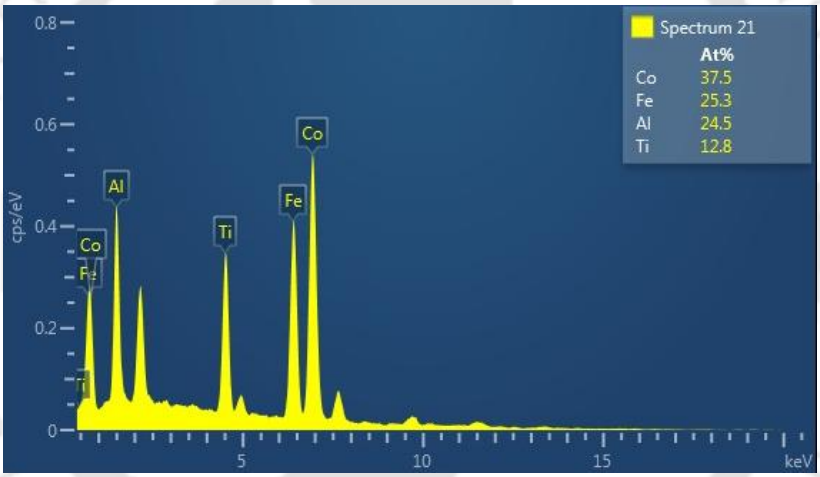

Figure 2.10. Typical reduced EDS spectrum of $Co_{1.5}FeTi_{0.5}Al$ Heusler alloy.

2.2.1.2. X-ray fluorescence spectroscopy

X-ray fluorescence (XRF) spectroscopy is a non-destructive technique used to identify and quantify the elements present in the sample by detecting characteristic X-rays emitted from the material upon excitation. In this thesis, the XRF technique is employed to analyse the elemental composition of thin films. Its fundamental principles are similar to those of FESEM-EDS. The technique involves exciting the material under investigation with high-energy X-rays to ionize the atoms in the sample by dislodging the tightly held inner shell electrons. The vacancies created by the dislodged inner shell electrons are occupied by the outer shell electrons, accompanied by the emission of secondary X-rays (fluorescence) as shown in Figure 2.08 (a). These X-rays are characteristic of each element, allowing for qualitative identification through

Moseley's law. Additionally, the intensity of photon count at each energy level enables accurate quantitative analysis of the elemental composition.

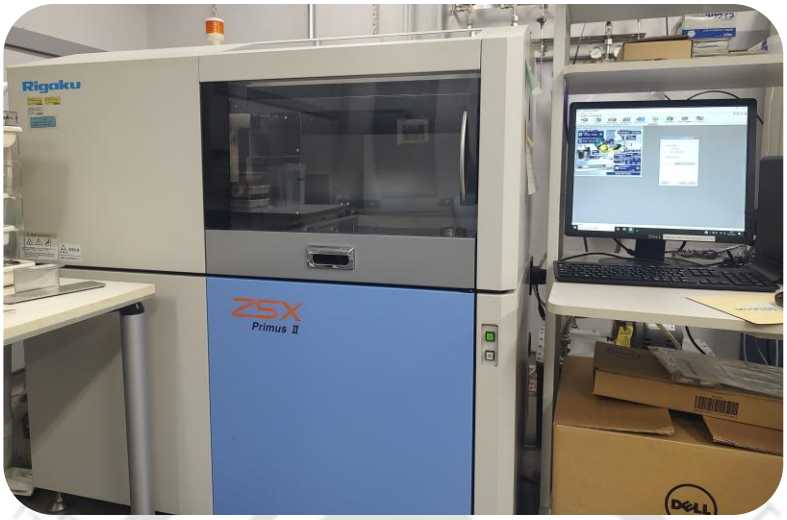

Figure 2.11. Photograph of the XRF instrument used for elemental analysis of thin film.

Although FESEM-EDS and XRF operate on similar principles, they differ in their sampling areas. FESEM-EDS provides compositional information from a highly localized region, typically spanning only a few tens of μm^2 due to the focused electron beam. In comparison, XRF analyses a much larger area of the sample, making it more suitable for determining the average overall composition of a thin film sample. In this study, XRF measurements were performed using a Rigaku ZSX Primus II spectrometer (Figure 2.11).

2.2.2. Crystal structure determination

2.2.2.1. X-ray diffraction

X-ray Diffraction (XRD) is a widely used non-destructive analytical technique employed to determine the crystallographic structural parameters such as lattice constants a, b, and c and the angles α, β, and γ between the crystallographic axes, average crystallite size, *etc*. It plays a crucial role in materials science, especially in crystal phase identification and its quantitative analysis. It is well known that the crystals are characterized by a periodic arrangement of atoms, and each with several allowed atomic planes. When the atoms in these atomic planes interact with the incoming X-rays and elastically scatter them, diffraction is said to take place. The constructive interference of these diffracted X-rays from different atomic planes gives rise to the distinct diffraction peaks, corresponding to each set of atomic planes present in the crystal. The condition for the constructive interference of the diffracted X-rays is that the path length from the two consecutive atomic planes should be equal to an integral multiple of the wavelength λ. This condition is known as Bragg's law given by [CULL2014],

$$2d \sin\theta = n\lambda \qquad (2.01)$$

Here, d is the interplanar spacing between 2 consecutive atomic planes (labelled as 1 and 2), and θ denotes the diffraction angle, corresponds to the angle of incidence of X-rays relative to atomic planes as shown in Figure 2.12.

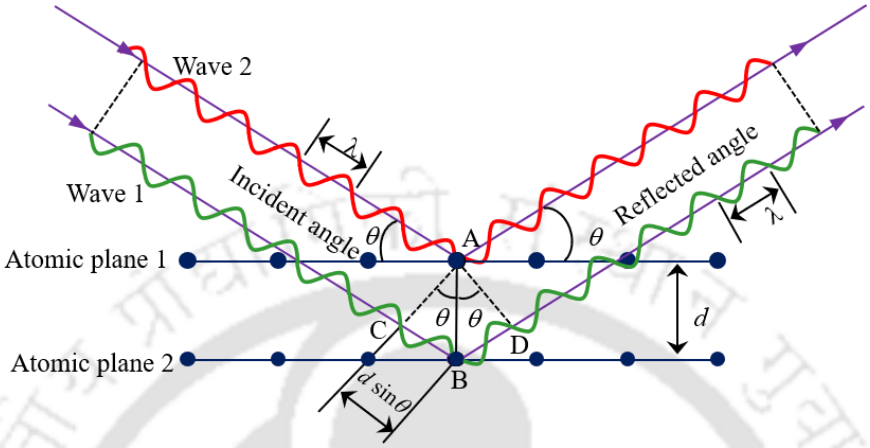

Figure 2.12. Schematic diagram of Bragg's law.

In crystallography, Miller indices ($h\ k\ l$) are used to designate set of parallel planes in a crystal lattice as well as the orientation of the planes. They provide a concise and systematic way to describe the geometry of atomic arrangements, which is essential for understanding the physical and chemical properties of crystalline materials. For a given set of crystallographic planes in a crystal, the Miller indices ($h\ k\ l$) are defined by the smallest set of integers representing the reciprocal of the fractional intercepts that the plane makes with the crystallographic axes. For a lattice with a unit cell defined by lattice constants a, b, and c, along the x, y, and z axes, the Miller indices h, k, and l can be expressed as:

$$h = a/\mathrm{x}, \qquad k = b/\mathrm{y}, \qquad l = c/\mathrm{z} \qquad (2.02)$$

The perpendicular distance between two adjacent and parallel crystallographic planes (interplanar spacing), denoted as d_{hkl} is characterized by a common set of Miller indices ($h\ k\ l$). This interplanar spacing d_{hkl} can be related to the lattice constants a, b, and c through the relation [CULL2014],

$$\frac{1}{d_{\mathrm{hkl}}^2} = \frac{h^2}{a^2} + \frac{k^2}{b^2} + \frac{l^2}{c^2} \qquad (2.03)$$

Since Heusler alloys crystallize in a cubic structure, their unit cell is characterized by $a = b = c$ (and, $\alpha = \beta = \gamma = 90°$). As a result, the general expression for interplanar spacing simplifies to [CULL2014],

$$\frac{1}{d_{hkl}^2} = \frac{h^2 + k^2 + l^2}{a^2} \tag{2.04}$$

On combining Equations (2.01) and (2.04),

$$\frac{sin^2\theta}{h^2 + k^2 + l^2} = \frac{\lambda^2}{4\,a^2} \tag{2.05}$$

The right-hand side of the equation remains constant for a fixed X-ray wavelength and given lattice constant. This indicates that planes corresponding to specific Miller indices (*h k l*) will produce diffraction at a distinct angle θ (θ_{hkl}), such that the left-hand side of the equation equals the constant right-hand side. Hence, the diffraction pattern observed at θ_{hkl} is indexed with the corresponding (*h k l*) values and used to evaluate the lattice constant.

To determine the degree of atomic order, it is essential to evaluate the relative intensities of reflections corresponding to different atomic planes. Since the intensity of these reflections are directly proportional to the square of the magnitude of the structure factor (F_{hkl}), it is important to evaluate F_{hkl}, which is defined as [CULL2014]:

$$F_{hkl} = \sum_{i=1}^{N_{total}} f_n\, e^{2\pi i\,(hx_i + ky_i + lz_i)} \tag{2.06}$$

where, f_n represents the atomic scattering factor of the n^{th} atom, and N_{total} is the number of atoms in the unit cell having fractional coordinates (x_i, y_i, z_i). Since the Heusler alloy crystal structure is composed of 4 interpenetrating face centred cubic (fcc) sublattices with a Wyckoff positions 4*a* (0.25, 0.25, 0.25), 4*b* (0.75, 0.75, 0.75), 4*c* (0.5, 0.5, 0.5), and 4*d* (0, 0, 0) as shown in Figure 1.04 (a) of Chapter 1, the typical structure factor of full Heusler alloys with a chemical formula X_2YZ is given by,

$$F_{hkl} = 4\left(f_X e^{i\frac{\pi}{2}(h+k+l)} + f_X e^{i\frac{3\pi}{2}(h+k+l)} + f_Y e^{i\pi(h+k+l)} + f_Z\right). \tag{2.07}$$

Here, the multiplication factor 4 corresponds to the number of atoms in the fcc structure, and f_X, f_Y, and f_Z represent the atomic scattering factor of X, Y, and Z atoms, respectively. Since the superlattices of Heusler alloys are made up of fcc structure, the reflections correspond to the Miller indices (*h k l*) are either all even or all odd. As a result, only reflections corresponding to the planes (1 1 1), (2 0 0), (2 2 0), (3 1 1), (2 2 2), (4 0 0), (3 3 1), (4 2 0), (3 3 3), (5 1 1) … will appear in the XRD patterns. From Equation (2.07), the structure factor of the first 3 reflections are

$$\left.\begin{aligned} F_{111} &= 4\,[f_Y - f_Z] \\ F_{200} &= 4\,[-2f_X + f_Y + f_Z] \\ F_{220} &= 4\,[2f_X + f_Y + f_Z] \end{aligned}\right\} \quad (2.08)$$

From the above equations, it is evident that the structure factor F_{220} remains unaffected by any type of disorder within the crystal structure. Consequently, the intensity of the (2 2 0) reflection (I_{220}) remains unaltered and is referred to as the fundamental Heusler alloy peak. In contrast, in the presence of *B*2-type partial disorder, where Y and Z atoms are completely intermixed, the structure factor F_{111} becomes zero, while F_{200} and F_{220} remain unaffected. As a result, the intensity of the (1 1 1) superlattice reflection (I_{111}) drops to zero, whereas I_{200} and I_{220} are not influenced by this disorder. In the case of an *A*2-type fully disordered structure, all the elements are equally distributed among all the Wyckoff positions, causing both structure factors F_{111} and F_{200} to become zero, which results in $I_{111} = I_{200} = 0$. From the above discussion, it is evident that the intensities of I_{111} and I_{200} provide insight into the *B2* and *A2* type disorder commonly observed in the system. The procedure of evaluating the degree of *B*2 and $L2_1$-type orders is discussed in Section 1.2.1.1 of this thesis.

XRD measurements are commonly performed using two primary geometries, namely, Bragg-Brentano (θ-2θ) geometry and grazing incident (2θ) geometry. In Bragg-Brentano geometry, the X-ray incident angle (θ) varies with the detector angle as shown in Figure 2.13 (a). On the other hand, in the grazing incident geometry, the incident angle is fixed at a small angle (typically in the range of 0.5° to 2°), while only the detector moves to vary the angle between the incident and diffracted beams as depicted in Figure 2.13 (b) [MCCA2005, MORA2009]. In the θ-2θ geometry, due to the movement of the X-ray source, there will be a high incident angle for the X-rays. This results in several micrometers of penetration of X-rays into the sample. Since the film's thickness is often less than the penetration depth of X-rays, the diffraction signal from the thin film becomes weaker, while the substrate generates more intense reflections. In this scenario, grazing incident XRD is preferred over Bragg-Brentano geometry for the thin films. The low incident angle minimizes X-ray penetration into the sample, ensuring that the diffraction pattern primarily originates from the thin film rather than from the substrate. Figure 2.13 (c) shows the photograph of the Rigaku SmartLab XRD instrument used in the present investigations.

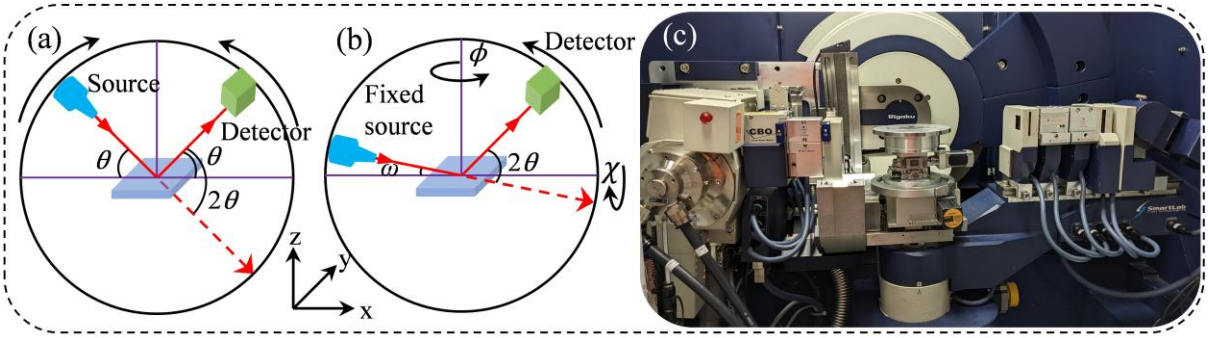

Figure 2.13. Schematic representation of (a) Bragg-Brentano and (b) grazing incident geometries. (c) Photograph of XRD instrument (Rigaku SmartLab) used in the study.

1-dimensional (1D) or 2-dimensional (2D) X-ray diffractometers use 1D and 2D detector, respectively. In both cases, the sample needs to be rotated around its χ-axis (sample rotates perpendicular to the incoming X-rays) and ϕ-axis (sample rotates within the sample plane) types if one desires to explore the epitaxial growth and alignment of crystalline orientations in the sample.

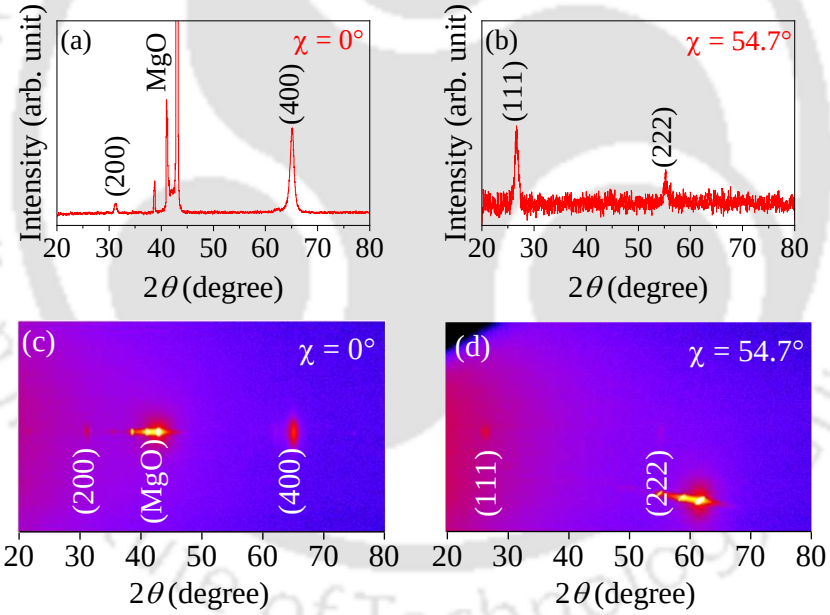

Figure 2.14. 1D XRD patterns from θ-2θ scans of CFGG samples at tilt angles (a) $\chi = 0°$ and (b) $\chi = 54.7°$. In (c) and (d), corresponding 2D XRD images at the same tilt angles.

A typical XRD pattern of CFGG Heusler alloy film on MgO (100) substrate, measured using 1D XRD in θ-2θ geometry at $\chi = 0°$, and $\chi = 54.7°$, is shown in Figures 2.14 (a and b), respectively. The corresponding 2D images from 2D XRD are shown in Figures 2.14 (c and d), respectively. The presence of (200) super lattice reflection at $\chi = 0°$, along with its absence at $\chi = 54.7°$, represents the epitaxial growth of the sample in the [100] direction. By examining the diffraction spots in the 2D XRD image, one can assess the crystalline quality and orientation

of the sample. Sharp and distinct diffraction spots indicate epitaxial growth, while a polycrystalline or non-epitaxial film will exhibit continuous or fragmented Debye-Scherrer rings due to the random orientation of the crystallites.

Structural details such as lattice constants, bond angles, bond lengths, and percentage of impurity phases present in the sample are determined by Rietveld refinement of the XRD patterns using software such as FullProf. The Rietveld refinement process involves the comparison of the experimental XRD pattern with the simulated pattern derived from the proposed crystal structure. The similarity between the two XRD patterns is quantitatively evaluated using a least-squares fitting method [CARV2000], where the refinement aims to minimize the goodness of fit parameter (χ^2) toward the ideal χ^2 value of unity to ensure an optimal match. A χ^2 value below 5 is generally considered as indicative of acceptably good fitting of the experimental pattern to the proposed model. Further information on the FullProf software, refinement methodology, and theoretical background can be found in the cited literature [CARV2000]. Figure 2.15 presents the Rietveld refined pattern of $Co_{1.5}FeTi_{0.5}Al$ alloy. The red data points represent the experimentally observed (Y_{obs}) XRD pattern, while the solid black line shows the evaluated XRD pattern (Y_{cal}) derived from the refinement process. The negligible difference between the two (Y_{cal}-Y_{obs}) is reflected in the nearly straight-line pattern in blue colour and a low χ^2 value (~1.3), which indicate a good fit of the experimental XRD pattern to the simulated pattern obtained for the proposed crystal structure.

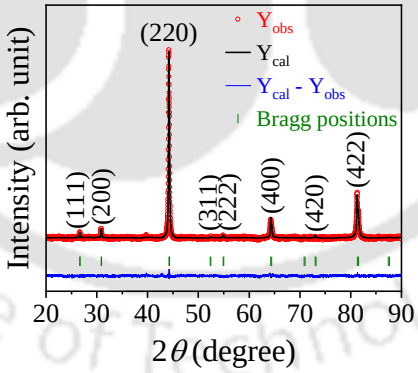

Figure 2.15. Typical Rietveld refinement of room temperature XRD pattern of $Co_{1.5}FeTi_{0.5}Al$ Heusler alloy for the proposed atomic arrangement with $L2_1$-type unit cell.

2.2.2.2. Transmission electron microscopy

Transmission electron microscopy is a widely used analytical technique for characterizing materials at the nanoscale. It employs a high energy electron beam transmitted through sample to generate highly magnified images. Due to the short wavelength of electrons, transmission electron microscopy offers much higher resolution, allowing for the direct observation of

atomic arrangements, crystal defects, grain boundaries, and interfaces. In addition to imaging, it can also provide information on crystal structure through a technique called selected area electron diffraction (SAED). In transmission electron microscopy, electrons generated by the electron gun are accelerated and projected on a thin sample with the aid of electromagnetic lenses. As electrons traverse the sample, electrons may experience several types of interactions: (a) some pass through without any deflection, (b) others may undergo elastic scattering, where they are deflected by the atomic or ionic potential fields without losing energy, contributing to the formation of electron diffraction patterns, and (c) some are inelastically scattered due to interactions with electrons in the material, imperfections, dislocations, or grain boundaries, leading to changes in their intensity [ZHAN2008b]. The transmitted electron beams are subsequently enlarged using a combination of intermediate and projector lenses before being visualized on a fluorescent screen. These transmitted electrons are used to extract various information about the specimen. Figure 2.16 (a) presents the schematic representation of the transmission electron microscope (TEM), while Figure 2.16 (b) shows the photograph of the TEM (FEI Titan G2 80-200) used in this study.

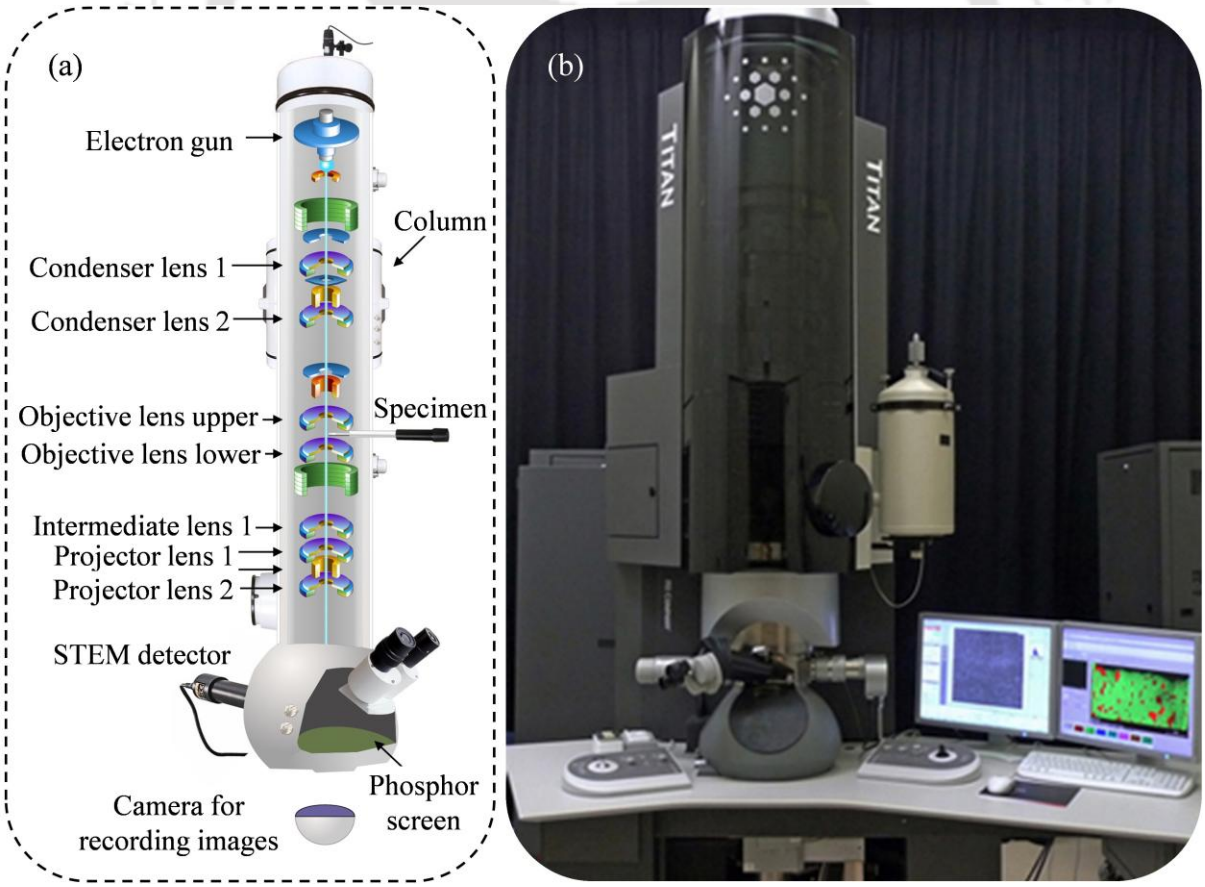

Figure 2.16. (a) Schematic diagram of a TEM. (b) Photograph of FEI Titan G2 80-200 TEM used for microstructural analysis.

In transmission electron microscopy, different imaging techniques provide unique insights into the specimen's structure. One common method is bright field imaging, where only the directly transmitted electrons that pass straight through the sample are allowed to form the image. This is done by placing an aperture in the objective lens's back focal plane to block all scattered beams except the central one. Conversely, dark field imaging is produced by selecting a specific diffracted beam while blocking the central transmitted beam and other diffracted beams. A third imaging technique relies on combining the primary transmitted beam with one or more diffracted beams after taking care to preserve both their phases and amplitudes. This method enables the generation of high-resolution transmission electron microscopy (HRTEM) images, which are essential for visualizing atomic arrangements and lattice planes. Figure 2.17 (a) presents the schematic diagram of the CFGG/Pt bilayer sample along with the corresponding cross-sectional HRTEM image, analyzed using ImageJ software. The analysis involves applying a fast Fourier transform (FFT) to a specific spot of the chosen HRTEM image. The resulting FFT pattern displays multiple bright spots, each corresponding to distinct crystallographic planes as shown in the inset of the HRTEM image. A particular spot of the FFT pattern is picked up to generate an inverse fast Fourier transform (iFFT) image. These images reveal lattice fringes that represent the chosen crystallographic plane. The interplanar spacing can be determined by measuring the distance between the two consecutive fringes using the line tool in ImageJ.

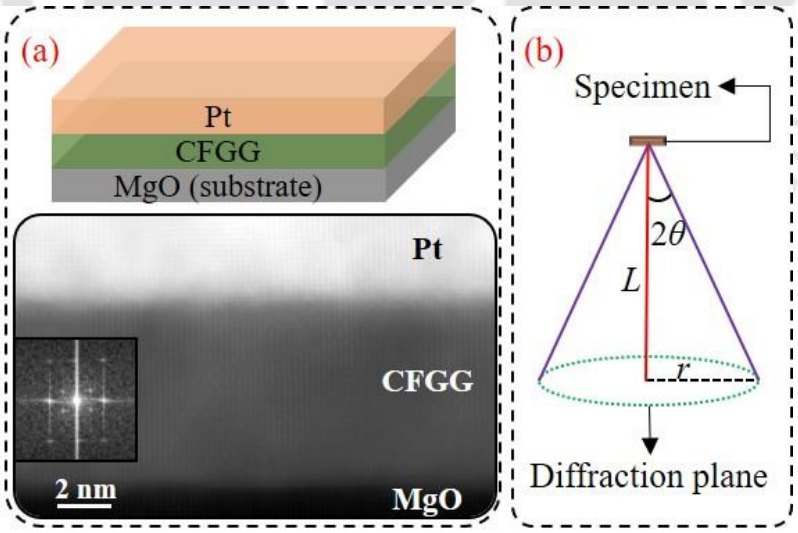

Figure 2.17. (a) Schematic diagram of CFGG/Pt bilayer and its cross-sectional HRTEM image. FFT of HRTEM image for CFGG layer is shown as an inset in the cross-sectional image. b) Geometry of SAED pattern of a specimen, detailing the parameters involved in the process.

On the other hand, SAED is obtained by blocking the central transmitted beam using a beam blocker and allowing only the diffracted beams to contribute to the formation of the diffraction pattern. In the case of single crystals, the SAED pattern displays well-defined spots due to the uniform crystal orientation. In polycrystalline materials, the SAED pattern appears as concentric rings formed by multiple randomly oriented crystallites [ZHAN2008b]. According to Bragg's law, when the diffraction angle θ is very small, $\sin\theta \approx \theta$. Considering the first-order diffraction (*i.e.*, for $n = 1$), Equation (2.01) simplifies to

$$2\theta_{\mathrm{hkl}} d_{\mathrm{hkl}} = \lambda. \tag{2.09}$$

The schematic geometry of the SAED pattern from a specimen is illustrated in Figure 2.17 (b). Here, *L,* the camera length, refers to the distance from the specimen to the screen and *r* is the radius of the circle connecting the diffraction spots arising from the same set of atomic planes with a particular interplanar spacing d_{hkl}. This radius corresponds to the separation between the transmitted and the specific diffracted beam. From Figure 2.17 (b), for small angle θ,

$$2\theta = r/L \tag{2.10}$$

On combining Equations (2.09) and (2.10),

$$d_{hkl} = \frac{1}{\left(\frac{r}{L\lambda}\right)} \tag{2.11}$$

For a TEM operated at 200 kV, the electron wavelength λ is ~0.0027 nm, which is a constant. Hence, *L* and *r* are interdependent, which means that modifying *L* directly influences the size of the diffraction pattern associated with a specific set of planes. By adjusting the camera length, one can tune the magnification of the diffraction pattern to optimize the visibility of a specific diffraction spot or ring. The length scale in a SAED image is expressed in units of nm^{-1}. By measuring the radius of the circle connecting the diffraction spots, the interplanar spacing d_{hkl} can be calculated.

2.2.3. Evaluation of magnetic properties

2.2.3.1. Vibrating sample magnetometry

Static magnetic behaviour of the samples was investigated using vibrating sample magnetometry. This technique works on the principle of Faraday's law of electromagnetic induction. According to this, a changing magnetic flux (ϕ) linked with the conducting coil induces electromotive force (ε), which is proportional to the rate at which the flux changes. *i.e.* [GRIF1999],

$$\varepsilon \propto -\frac{\mathrm{d}\phi}{\mathrm{d}t} \tag{2.12}$$

Figure 2.18 (a) shows the schematic diagram of the typical vibrating sample magnetometer (VSM). It consists of several integrated components, including: a vibration unit for oscillating the sample, a sample holding rod, an electromagnet with a power supply, a Hall probe for magnetic field measurement, detection coil pairs, a lock-in amplifier for signal extraction, and a computer interface. The magnetic sample being examined is placed in between the poles of an electromagnet. Then, the sample is made to vibrate at a constant frequency within the magnetic field by the vibration unit, causing a periodic variation of magnetic flux linked to the detection coils. This changing flux induces an electromotive force in the coils due to electromagnetic induction as specified by the Faraday's law. The resulting small sinusoidal voltage is then detected by the lock-in amplifier, which filters out noise and improves the signal clarity. The detected voltage magnitude is directly proportional to the magnetic moment of the sample and is influenced by the amplitude and frequency of the vibration. This voltage signal is converted into magnetization unit (*e.g.*, emu) and displayed on the monitor.

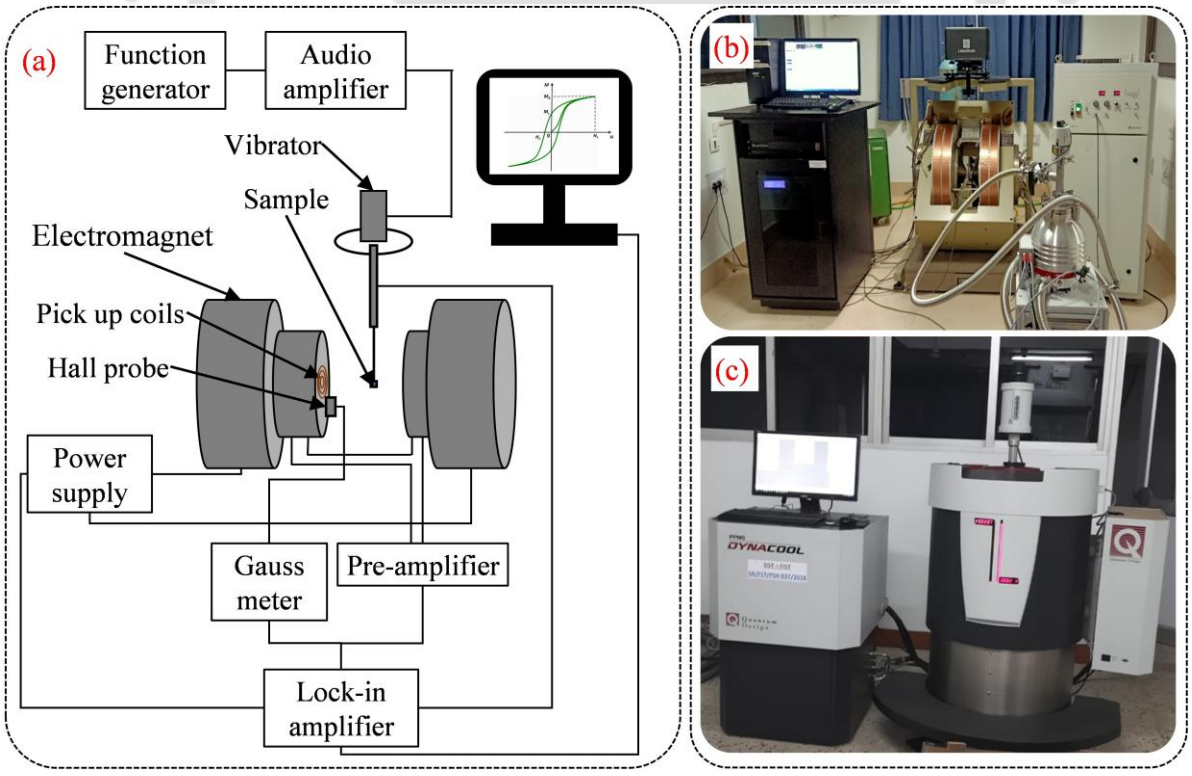

Figure 2.18. (a) Schematic diagram of a VSM. Photograph of (b) electromagnet-based VSM and (c) PPMS with a VSM module.

Magnetic measurements were typically performed using two types of VSM. The first one is a conventional electromagnet based VSM (Lakeshore 7410), dedicated solely to magnetic characterization. The second one is an integrated VSM module within a physical property measurement system (PPMS) (Quantum Design, Dynacool). PPMS enables measurement of both magnetic and other physical properties at fields up to 9 T. Figures 2.18 (b and c) show the image of conventional electromagnet based VSM and the integrated VSM in PPMS, respectively. Prior to the measurements, calibrating the VSM is essential. In the case of conventional VSM, calibration is carried out using a standard nickel sphere with a known magnetic moment M_s = 6.92 emu at 5000 Oe. To calibrate the PPMS, the magnetic susceptibility (χ) of palladium is evaluated and compared with its known reference value of 5.25×10^{-6} emu/Oe-g. If any discrepancies are observed, calibration adjustments can be made through the system's software to ensure accurate magnetization readings. In both conventional VSM and PPMS, a program sequence is defined by the user as per the requirements. The sequence is customized with optimum steps of magnetic fields (H), temperatures (T), and time (t) to gather the optimum number of data points to obtain the magnetic parameters with minimum error.

The PPMS is a major upgrade over conventional VSM systems in terms of magnetic field range. The conventional VSM is typically limited to around 2 T, while the PPMS can generate much stronger fields, reaching up to 9 T or even 14 T depending on the model. The samples studied in this thesis are soft magnetic materials, characterized by low coercivity and high magnetic permeability. Conventional electromagnet based VSM equipped with variable temperature sample holder is capable of measuring the magnetic hysteresis (M-H) loops and thermomagnetization (M-T) curves across various range of temperatures. Therefore, for M-H and M-T measurement, conventional VSM is utilized. To enable temperature variation during measurements, a closed cycle refrigerator was placed between the pole pieces for low-temperature measurements (10-300 K), and a high-temperature oven was used for the high-temperature range (300 – 1200 K). A quartz rod with a sample holder made of polychloro-trifluoro-ethylene and boron nitride was used for the low and high temperature ranges, respectively. During the low-temperature measurements, He gas is continuously purged in the cold stage of the cryostat to facilitate efficient cooling and to ensure proper thermal conduction between the sample holder and the cold stage of the cryostat, apart from ensuring that no moisture condensation occurs on the sample. On the other hand, a continuous flow of Ar gas into the oven prevented oxidation of the sample during the high-temperature measurements.

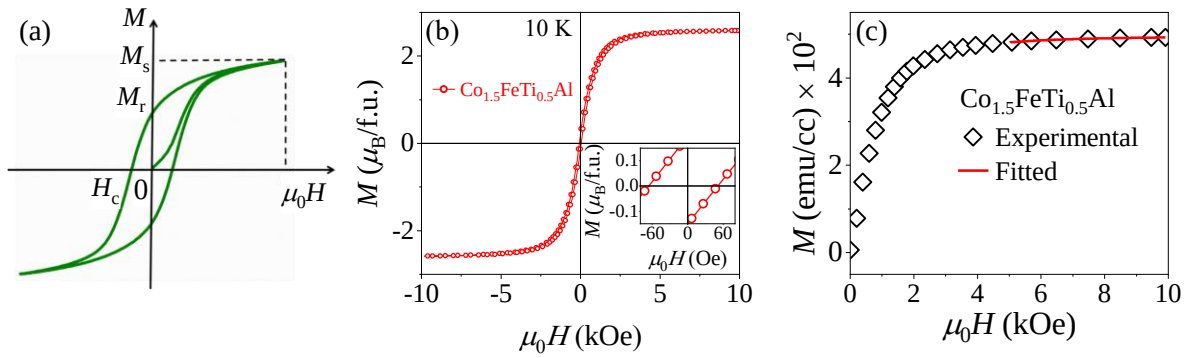

Figure 2.19. (a) Typical *M-H* loop of a ferromagnetic material. (b) *M-H* loop with inset shows the expanded view of data near to the origin, and (c) initial magnetization curve of bulk $Co_{1.5}FeTi_{0.5}Al$ alloy recorded at 10 K, fitted to Equation (2.14).

Figure 2.19 (a) shows the typical *M-H* loop of a ferromagnetic material. In this work, saturation magnetization (M_s), coercive field (H_c), magnetic remanence (M_r), and the effective anisotropy constant (K_{eff}) are the main parameters extracted from the *M-H* loops. Figure 2.19 (b) shows the magnetic hysteresis loop recorded at 10 K for $Co_{1.5}FeTi_{0.5}Al$ bulk Heusler alloy. The inset in the figure shows the expanded view of the data close to the origin. The value of H_c and M_r of the specimen were directly obtained from the *M-H* loop part shown in the inset. For evaluating M_s and K_{eff} of the sample, 1st quadrant (initial magnetization curve) of the *M-H* loop (*c. f.*, Figure 2.19 (c)) is used using the method of law of approach to saturation, which relates the variation of magnetization ($M(H)$) with the external magnetic field (H) as [KRON2003],

$$M(H) = M_s - \frac{a}{\sqrt{H}} + \frac{b}{H} + \frac{c}{H^{\frac{3}{2}}} + \frac{d}{H^2} + \alpha T\sqrt{H} + \chi_P.\mu_0 H. \qquad (2.13)$$

In this expression, $a/\sqrt{H}$ accounts for point-like defects and intrinsic magnetostatic fluctuations, b/H is linked with structural defects and $c/H^{3/2}$ is related to non-magnetic precipitations. The term d/H^2 arises partly from magnetoelastic interactions of quasi-dislocation poles and uniform magnetocrystalline anisotropy. The $\sqrt{H}$ dependence emerges from the energy gap in the spin wave spectrum caused by Zeeman energy. The linear term $\chi_p.H$ originates from the Pauli paramagnetism. Using the concept of minimizing the Gibbs' free energy in the presence of strong magnetic fields, Equation (2.13) can be simplified [PATH2022] to

$$M(H) = M_s\left(1 - \frac{d}{H^2}\right) \qquad (2.14)$$

M_s and d are evaluated by fitting Equation (2.14) to the initial magnetization curve and substituted in the following expression for the effective anisotropy constant [ANDR1997],

$$K_{\text{eff}} = \mu_0 M_s \left(\frac{105d}{8}\right)^{0.5} \tag{2.15}$$

Here, μ_0 represents the permeability of free space. The obtained values of M_s and K_{eff} are in terms of emu/cc and erg/cc, respectively.

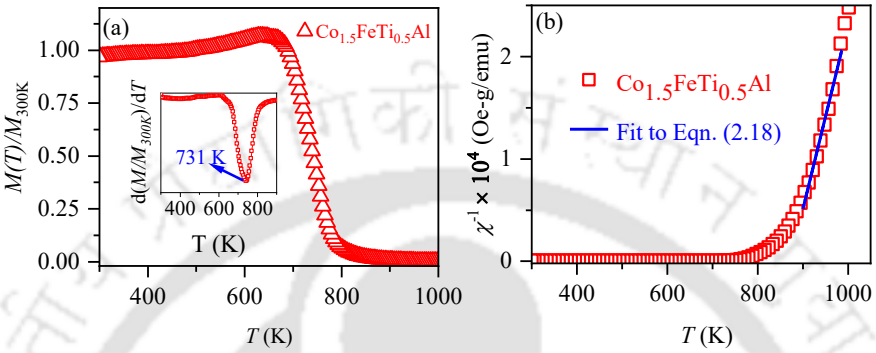

Figure 2.20. (a) *M-T* curves of bulk $Co_{1.5}FeTi_{0.5}Al$ alloy measured under an applied field of 500 Oe. Inset shows the first derivative of magnetization with respect to temperature near T_C. (b) Inverse magnetic susceptibility of $Co_{1.5}FeTi_{0.5}Al$ alloy plotted as a function of temperature.

Alongside magnetic hysteresis analysis, *M-T* measurements play a crucial role in characterizing magnetic materials, as they enable one to determine the T_C of a ferromagnetic material. Figure 2.20 (a) shows the *M-T* curve of bulk $Co_{1.5}FeTi_{0.5}Al$ alloy recorded in the temperature range of 300 K to 1000 K under an externally applied magnetic field of 500 Oe. The exact value of T_C was calculated from the temperature at which the derivative of the magnetization is minimum, as shown in the inset of Figure 2.20 (a).

M-T data can be used to infer the half-metallic nature of the samples from the value of the Rhodes-Wohlfarth ratio p_c/p_s [SHAM2019]. Here, p_c denotes the effective paramagnetic moment per atom, while p_s represents the magnetic moment of the sample at 0 K, evaluated by extrapolating temperature-dependent M_s to 0 K. $p_c/p_s = 1$ indicates that the magnetism in the sample arises from localized magnetic moments. If $p_c/p_s > 1$, the magnetism is attributed to itinerant magnetic moments. On the other hand, if $p_c/p_s < 1$, then the ferromagnetic material exhibits a half-metallic nature as proposed by Otto *et al.* [OTTO1989] and Katsnelson *et al.* [KATS2008]. p_c can be evaluated from the expression [SHAM2019],

$$p_c = \sqrt{1 + \mu_{\text{eff}}^2} - 1 \tag{2.16}$$

In Equation (2.16), μ_{eff}^2 is the effective magnetic moment, which is given by the relation,

$$\mu_{\text{eff}}^2 = \frac{3Mk_{\text{B}}C}{N_{\text{A}}} \tag{2.17}$$

where M, k_{B}, C, and N_{A} are the molecular weight, Boltzmann constant, Curie constant, and Avogadro's number, respectively. Curie constant can be obtained from a linear fit to the *M-T* data as depicted in Figure 2.20 (b) using the Curie-Weiss law [ZHER2015],

$$\chi^{-1} = \left(\frac{T - T_{\text{C}}}{C}\right) \tag{2.18}$$

where, χ^{-1} is the inverse of magnetic susceptibility. Using the evaluated p_{c} along with p_{s}, the Rhodes-Wohlfarth ratio was determined, which is utilized to assess the half-metallic nature of the materials.

2.2.3.2. Ferromagnetic resonance

Ferromagnetic Resonance (FMR) is a spectroscopic technique used to study the dynamic magnetic properties of ferromagnetic materials. The technique is based on the principle that, under a static magnetic field, magnetization begins to precess about the field direction at a natural frequency determined by effective magnetic field. Over time, the magnetization gradually aligns itself along the applied magnetic field direction. When an alternating magnetic field is applied perpendicular to the static field with its frequency matching the natural precession frequency of the magnetization, resonant absorption will occur. At the resonance condition, the magnetization absorbs energy from the microwave field, leading to sustained precession around the static field direction. There are two common practices to achieve the resonance condition in FMR. The first involves sweeping the magnetic field while keeping the frequency constant, and the second involves sweeping the frequency while maintaining the magnetic field constant.

FMR study can be performed using a microwave cavity-based FMR or a coplanar waveguide (CPW) based FMR. While both are employed to investigate magnetization dynamics, they differ considerably in terms of design, sensitivity, and measurement flexibility. Cavity-based FMR is a highly sensitive technique for probing the dynamic magnetic properties of materials. In this setup, the sample is placed inside a resonant microwave cavity, commonly operating at a fixed frequency of ~9.4 GHz available in most electron spin spectroscopy units. Even though cavity-based FMR is a highly sensitive technique, it is limited by its fixed

frequency operation. Therefore, the only possible way to achieve the resonance condition is by sweeping the magnetic field.

On the other hand, CPW-based FMR is a more flexible technique used to study the broadband (typically in the range of 1 to 40 GHz) magnetization dynamics. Additionally, its compatibility with variable temperature setups and ease of integration make it a widely adopted choice in contemporary magnetic materials research. In the case of thin films, the static magnetic field can be applied either parallel or perpendicular to the film surface. Depending on the field orientation, the measurement is termed in-plane FMR or out-of-plane FMR spectroscopy. Considering these factors, the present study has employed CPW based broadband FMR in in-plane configuration.

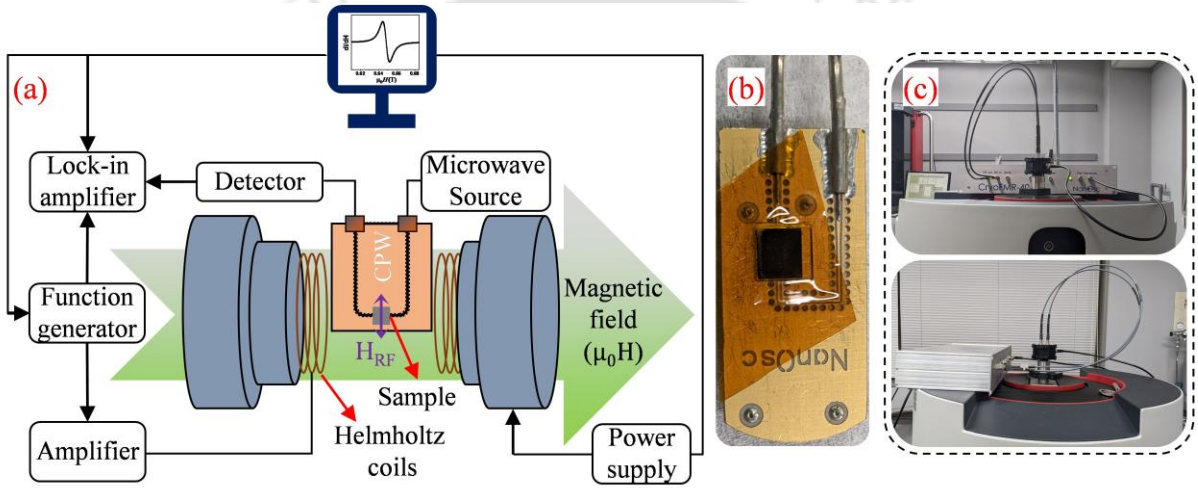

Figure 2.21. (a) Schematic of a broadband FMR spectrometer. Photograph of (b) CPW with the CFGG thin film placed for in-plane FMR measurement. (c) Phase FMR-40 spectrometer unit attached to the PPMS.

The schematic diagram of broadband in-plane FMR spectroscopy setup is shown in Figure 2.21 (a). In this configuration, the sample is placed directly on top of a CPW (*c.f.*, Figure 2.21 (b)) through which a microwave signal is transmitted. This microwave signal generates a microwave magnetic field (H_{RF}) in the vicinity of the sample. Since H_{RF} is confined to a small region near the CPW surface, it is important to place a thin film face-down on top of the CPW to enhance the coupling between H_{RF} and the sample, thereby improving the resulting signal strength. To prevent electrical short circuiting in CPW by the conducting thin film, a thin insulating layer is inserted between the CPW and the sample during measurements. For efficient and sustained magnetization precession, H_{RF} must be oriented perpendicular to the external static magnetic field ($\mu_0 H$). Hence, the setup is designed to ensure that H_{RF} remains

perpendicular to $\mu_0 H$. The photograph of the Phase FMR-40 spectrometer (Quantum Design) unit attached to the PPMS is shown in Figure 2.21 (c).

Measurements are typically performed at a fixed frequency while sweeping $\mu_0 H$ by 800 Oe across the resonance field ($\mu_0 H_r$) to eliminate the frequency-dependent background response that may mask the relatively weak FMR response of the sample. As $\mu_0 H$ is swept through the resonance condition (when the natural precession frequency of the sample's magnetization matches the frequency of H_{RF}), the magnetization undergoes resonant precession while absorbing energy from the applied microwave. This decreases the transmitted microwave signal while sweeping through the resonance field, and it is detected as a DC voltage using an RF diode. To improve the signal-to-noise ratio, lock-in detection technique is commonly employed, which requires a modulating signal at a known frequency. The modulation signal is generated by an additional set of Helmholtz coils powered by an alternating current source, producing a small (~1 Oe) modulation field. In this measurement configuration, one actually measures the derivative of the microwave absorption signal (dI/dH), with respect to the applied external magnetic field. In this work, the FMR spectra were recorded typically in the frequency range of 16 to 36 GHz. Figure 2.22 (a) presents the FMR spectrum obtained at 24 GHz for the CFGG thin film annealed at 600 °C. This spectrum is used to determine $\mu_0 H_r$ and the linewidth ($\mu_0 \Delta H$) by fitting it to the equation [KUMA2019],

$$\frac{dI}{dH} = K_1 \frac{[(\Delta H/2)^2 - (H - H_r)^2]}{[(\Delta H/2)^2 + (H - H_r)^2]^2} + K_2 \frac{2(H - H_r)(\Delta H/2)}{[(\Delta H/2)^2 + (H - H_r)^2]^2} \qquad (2.19)$$

where, K_1 and K_2 are coefficients corresponding to the symmetric and antisymmetric components of the FMR spectrum, respectively.

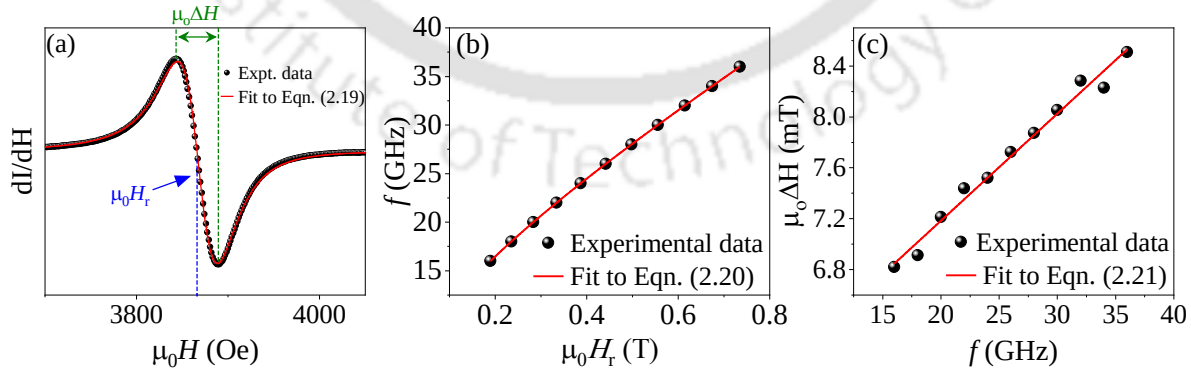

Figure 2.22. (a) FMR spectrum of a 16 nm thick CFGG film measured at 24 GHz fitted to Equation (2.19). (b) $\mu_0 H_r$ *versus* resonance frequency (f) data fitted to Equation (2.20). (c) $\mu_0 \Delta H$ *versus* f data fitted to Equation (2.21).

The evaluated $\mu_0 H_r$ is plotted with corresponding resonance frequency (f) as shown in Figure 2.22 (b), and the data is fitted to Kittel's equation [KALA2006],

$$f = \frac{\gamma \mu_0}{2\pi}\sqrt{\{(H_K + H_r)(H_K + H_r + M_{\text{eff}})\}} \tag{2.20}$$

Here, γ is the gyromagnetic ratio, and it is used to calculate the total Gilbert damping constant by fitting $\mu_0 \Delta H$ *versus* f plot as shown in Figure 2.22 (c), using equation [KUMA2017],

$$\mu_0 \Delta H = \frac{4\pi\alpha_{\text{total}}}{\gamma} f + \mu_0 \Delta H_0 \tag{2.21}$$

Here, $\mu_0 \Delta H_0$ corresponds to the line width due to inhomogeneity in the sample, and α_{total} is the total Gilbert damping constant obtained as a fitting parameter. Experimentally evaluated α_{total} contains both intrinsic (α_{int}) and extrinsic (α_{ext}) components. α_{ext} consists of contributions from spin pumping (α_{sp}), two-magnon scattering (α_{TMS}), radiative damping (α_{rad}), and eddy current (α_{eddy}) [HAIT2021]. Therefore, α_{int} is determined by subtracting all the extrinsic contributions from the α_{total}.

As discussed earlier in Section 1.2.3 of this thesis, efficient spin current transfer across the FM/NM interface is important for enabling magnetization switching of the free FM layer using the SOT mechanism in MRAM devices. Since $g_{\text{eff}}^{\downarrow\uparrow}$ is a parameter which quantitatively assesses the spin current transfer efficiency across the FM/NM interface, it is essential to evaluate it. In a bilayer (FM/NM) sample, the presence of an additional NM layer enhances the α_{sp} contribution by transferring the spin current from FM to the NM layer, leading to an increase in the α_{total}. Therefore, an enhancement of α_{total} ($\Delta\alpha$) in bilayer (FM/NM) sample in comparison to the corresponding single layer (FM) sample is expressed as [AKAN2018],

$$\Delta\alpha = \alpha_{\text{Bilayer}} - \alpha_{\text{Single layer}} \cong \alpha_{\text{sp}} \tag{2.22}$$

where, $\alpha_{\text{single layer}}$ and α_{Bilayer} are the α_{total} of single and bilayer samples, respectively. $\Delta\alpha$ is related to $g_{\text{eff}}^{\downarrow\uparrow}$ by the relation [AKAN2018],

$$\Delta\alpha = \frac{g\mu_{\text{B}}}{4\pi M_{\text{s}}} \frac{1}{t_{\text{FM}}} g_{\text{eff}}^{\uparrow\downarrow} \tag{2.23}$$

where g is Lande's g factor, while μ_{B}, M_{s}, and t_{FM} refer to the Bohr magneton, saturation magnetization, and thickness of the FM layer, respectively. To evaluate $g_{\text{eff}}^{\downarrow\uparrow}$, $\Delta\alpha$ is plotted as a function of t_{FM} and is fitted to Equation (2.23) as shown in Figure 2.23.

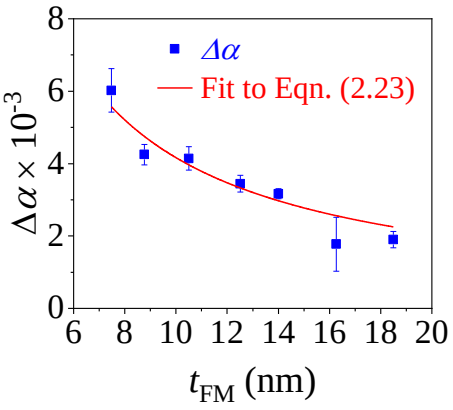

Figure 2.23. Variation of $\Delta\alpha$ with t_{FM}. The dotted red line represents the fit to Equation (2.23).

2.2.4. Electrical resistivity measurements

Electrical studies such as measurement of electrical resistivity as a function of temperature are useful in unravelling the intrinsic characteristics of spintronic materials as well as for assessing the device potential of Heusler alloy films, since the proposed devices involve flow of electric current. The influence of a magnetic field on the flow of electric current in these alloy films can be investigated using magnetoresistance measurements. These techniques, which have been exploited in this thesis work, will be discussed below:

2.2.4.1. Temperature dependent electrical resistivity measurements

Temperature dependent electrical resistivity measurements offer valuable information for assessing the half-metallic behavior of materials for spintronic applications. In general, the measured electrical resistivity of metallic ferromagnets can be decomposed into three components, *viz*. [BOMB2013, CHAT2023],

$$\rho(T) = \rho_R + \rho_P(T) + \rho_M(T) \qquad (2.24)$$

where ρ_R, $\rho_P(T)$, and $\rho_M(T)$ are the contributions to the resistivity from electron-defect, electron-phonon scattering, and electron-magnon scattering, respectively. Here, ρ_R is independent of temperature, whereas $\rho_P(T)$ and $\rho_M(T)$ increase linearly and quadratically with an increase in temperature, respectively. Considering these dependencies on temperature, Equation (2.24) can be rewritten as,

$$\rho(T) = \rho_R + \alpha T + \beta T^2 \qquad (2.25)$$

where, α and β are the coefficient of resistivity corresponding to $\rho_P(T)$ and $\rho_M(T)$, respectively. Since the contribution from $\rho_P(T)$ is negligible in the low temperature range, Equation (2.25) can be further simplified to,

$$\rho(T) = \rho_R + \beta T^2 \quad (2.26)$$

at low temperatures. Since $\rho_M(T) = \beta T^2$ is the contribution to the resistivity arising from the spin-flip scattering of majority electrons, a reduction or total absence of minority DOS at E_F in half-metallic materials, suppresses the spin-flip scattering process exponentially, thereby reducing βT^2. By incorporating this suppression factor into Equation (2.26), the modified expression for $\rho(T)$ turns out to be [BOMB2013],

$$\rho(T) = \rho_R + \beta T^2 \exp\left(-\Delta/k_B T\right) \quad (2.27)$$

Here, Δ is the minimum excitation energy required for the majority electrons to make a transition into empty minority conduction states *via* a spin-flip process, as shown in Figure 2.24 (a). As a consequence of Equation (2.27), considerable suppression of the βT^2 term is possible in the presence of a large Δ, serving as a clear indicator of half-metallic nature. At higher temperatures (typically, in the range of about 100 K and above), the contribution from $\rho_P(T)$ dominates over that of $\rho_M(T)$ due to significant amount of lattice vibrations, resulting in a linear relationship with temperature. *i.e.*,

$$\rho(T) \propto \alpha T \quad (2.28)$$

In the present work, temperature-dependent electrical resistivity was measured using a conventional linear four-probe method using a PPMS configured for resistivity studies.

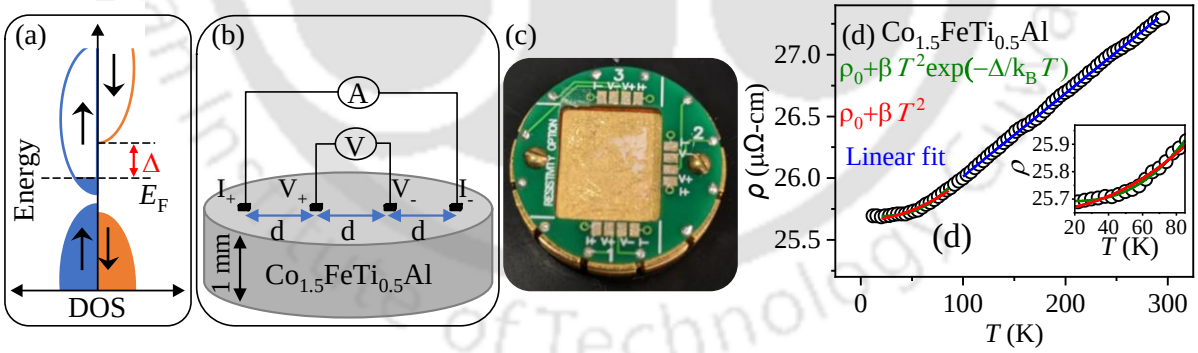

Figure 2.24. (a) Schematic of DOS *versus* energy plot of a half-metal. (b) The schematic diagram of a four-probe connection setup. (c) Photograph of a four-probe puck used in the temperature-dependent electrical resistivity measurement. (d) Variation of electrical resistivity with temperature in the range of 5 K to 300 K recorded for $Co_{1.5}FeTi_{0.5}Al$ alloy specimen.

The schematic diagram of the four-probe setup is shown in Figure 2.24 (b). For the measurement, a cylindrical sample slice with a 6 mm diameter and 1 mm thickness was used. To ensure a stable electrical connection, a standard four-probe puck (*c.f.*, Figure 2.24 (c))

supplied with the PPMS resistivity probe was employed. Electrical connections between the sample and the puck's gold pads were established using fine copper wires, with indium employed as a conductive bonding agent. During the measurement, a constant current of 5 mA was supplied, and the resistivity data were collected in the temperature range of 5 K to 300 K. Figure 2.24 (d) shows the temperature dependent electrical resistivity behaviour of $Co_{1.5}FeTi_{0.5}Al$ Heusler alloy measured in the range of 5 K to 300 K. Solid lines in red and green colour correspond to fits of low temperature data (~20 to 85 K) to Equations (2.26) and (2.27), respectively, while solid blue line represents to the fit of high temperature data (~100 to 300 K) using Equation (2.28).

2.2.4.2. Magnetoresistance measurement

Ordinary magnetoresistance measurement

Ordinary magnetoresistance (OMR) effect in any material refers to the change in electrical resistivity caused by the deflection of charge carriers by the Lorentz force when an external magnetic field is applied perpendicular to the current direction. This change in electrical resistance is quantified by the OMR ratio, defined as,

$$OMR \text{ ratio} = \frac{\Delta\rho_{OMR}}{\rho_0} = \frac{\rho_H - \rho_0}{\rho_0}. \qquad (2.29)$$

Here, ρ_H and ρ_0 are the electrical resistivity in the presence and absence of a magnetic field, respectively. As already pointed out through Equation (2.24), the measured electrical resistivity ($\rho(T)$) of metallic ferromagnet includes a contribution from temperature-independent ρ_R and temperature-dependent $\rho_P(T)$ and $\rho_M(T)$. $\rho_M(T)$ is sensitive to the magnetic field and decreases with increasing magnetic field due to the suppression of electron-magnon scattering, caused by a reduction in the number of magnons. This leads to a reduction in total resistivity under an applied magnetic field, resulting in a negative OMR ratio [PATR2019]. In half-metallic ferromagnets, the absence of minority DOS at E_F leads to an exponential suppression of $\rho_M(T)$, *i.e.*, $\rho_M(T)e^{-\Delta/k_BT}$ [BOMB2013, CHAT2023], where Δ represents the lowest excitation energy for spin-flip process of majority charge carriers, as depicted in Figure 2.24 (a). At low temperature, this additional factor largely suppresses $\rho_M(T)$. Additionally, lowering temperature reduces lattice vibration, and hence, diminishes $\rho_P(T)$. In this scenario, ρ_R becomes dominant, and the Lorentz force causes electrons to travel longer paths in a magnetic field, giving rise to an increase in $\rho(T)$ [BAKO2022], which results in a positive OMR ratio. Based on the above discussion, it is evident that the rise in the OMR ratio from negative to positive value is attributed to the suppression of $\rho_M(T)$ due to an increase in Δ and a decrease in T. Since

Δ is directly related to P, an increase in the OMR ratio signifies an enhancement in P. Thus, OMR ratio serves as a useful qualitative indicator for assessing changes in the P of a material.

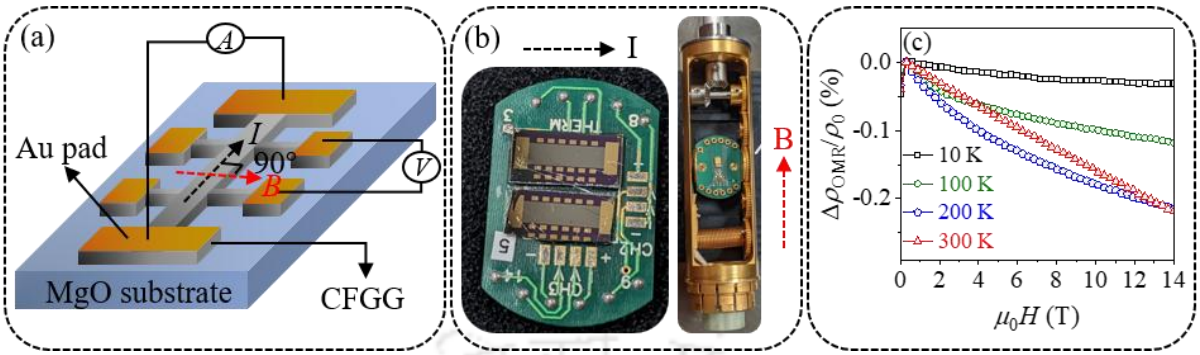

Figure 2.25. (a) Hall bar geometry for the OMR measurement. (b) Photograph of the CFGG film attached to the sample holder and the rotating puck used in the OMR measurement. (c) Variation of OMR ratio of the 600 °C annealed CFGG sample as a function of applied magnetic field measured at 10, 100, 200, and 300 K.

Figure 2.25 (a) depicts the schematic diagram of the DC four-probe Hall bar geometry used in the OMR measurement, with the magnetic field and current directions labelled. Figure 2.25 (b) shows the image of the sample patterned in Hall bar geometry attached to the sample holder used in the measurement. This sample holder is placed in the PPMS during the OMR measurement. During a typical measurement, 0.1 mA direct current was passed along the <110> direction of the sample, while the magnetic field was varied from 0 to 14 T. The primary criterion for observing a significant OMR effect is that the external magnetic field must be applied perpendicular to the current direction. Accordingly, the magnetic field was oriented perpendicular to the current direction, within a sample plane, although it is not strictly required to remain confined to the sample plane. The variations in OMR ratio of the CFGG sample annealed at 600 °C as a function of applied magnetic field at 10 K, 100 K, 200 K, and 300 K are shown in Figure 2.25 (c).

Anisotropic magnetoresistance measurement

Anisotropic magnetoresistance (AMR) in any ferromagnetic material refers to the change in electrical resistivity when the direction of magnetization changes relative to the direction of electric current. The variation in resistivity as a function of the angle between the magnetic field and the current is described by,

$$\rho(\phi) = \rho_{\perp} + (\rho_{\parallel} - \rho_{\perp})\cos^2\phi \qquad (2.30)$$

where ϕ is the angle between the magnetic field and current direction. $\rho_{\parallel}$ ($\rho_{\perp}$) represents the resistivity when the electrical current is parallel (perpendicular) to the magnetization direction. The origin of AMR is due to the spin-orbit interaction of the electrons, and is manifested through spin-dependent scattering mechanisms, particularly, *s*-*d* scattering. This spin dependent scattering results in the electrical resistivity exhibiting an angular dependence between the directions of the electric current and the magnetization. Quantitatively, the relative change in resistivity due to AMR is described in terms of the AMR ratio,

$$\text{AMR ratio} = \frac{\Delta\rho_{\text{AMR}}}{\rho} = \frac{\rho_{\phi} - \rho_{\perp}}{\rho_{\perp}} \tag{2.31}$$

where ρ_{ϕ} represents the resistivity when ϕ is the angle between electrical current and the magnetization directions. For the specific case with ϕ = 0°, $\rho_{\phi} = \rho_{\parallel}$. Under this condition,

$$\text{AMR ratio} = \frac{\rho_{\parallel} - \rho_{\perp}}{\rho_{\perp}} \tag{2.32}$$

By substituting the value of $\rho_{\parallel}$ and $\rho_{\perp}$ in Equation (2.32) [KOKA2012],

$$\frac{\Delta\rho_{\text{AMR}}}{\rho} = \gamma\left(D_{\uparrow}^{(d)} - D_{\downarrow}^{(d)}\right).\left(\frac{\rho_{\uparrow} - \rho_{\downarrow}}{\rho_{\uparrow}\,.\,\rho_{\downarrow}}\right) \tag{2.33}$$

where, $D_{\uparrow}^{(d)}\left(D_{\downarrow}^{(d)}\right)$ is/are the DOS of the *d* orbitals for the ↑ (↓) spin channels at E_F. $\rho_{\uparrow}$ and $\rho_{\downarrow}$ are the approximate resistivities of ↑ and ↓ spin channels, respectively, in a system without spin-orbit interaction.

According to the comprehensive theoretical model developed by Kokado *et al*., the sign of AMR ratio in ferromagnetic materials can provide information on its half-metallic nature. The sign of the AMR ratio depends on the type of the *s*-*d* scattering process involved. From the Equation (2.33), it is clear that the AMR ratio will be positive in the case of $\rho_{\uparrow} > \rho_{\downarrow}$ with $D_{\uparrow}^{(d)} > D_{\downarrow}^{(d)}$ or $\rho_{\uparrow} < \rho_{\downarrow}$ and $D_{\uparrow}^{(d)} < D_{\downarrow}^{(d)}$. Since $\rho_{\uparrow} > \rho_{\downarrow}$ ($\rho_{\uparrow} < \rho_{\downarrow}$) indicate that the down-spin (up-spin) electrons contribute dominantly to the transport, a positive AMR ratio arising from $\rho_{\uparrow} > \rho_{\downarrow}$ with $D_{\uparrow}^{(d)} > D_{\downarrow}^{(d)}$ is attributed to $s_{\downarrow} \rightarrow d_{\uparrow}$ scattering. Conversely, in the case of $\rho_{\uparrow} < \rho_{\downarrow}$ with $D_{\uparrow}^{(d)} < D_{\downarrow}^{(d)}$, the positive AMR ratio originates from $s_{\uparrow} \rightarrow d_{\downarrow}$ scattering. On the other hand, a negative AMR ratio can result from two scenarios, *viz*., when $\rho_{\uparrow} > \rho_{\downarrow}$ with $D_{\uparrow}^{(d)} < D_{\downarrow}^{(d)}$, or when $\rho_{\uparrow} < \rho_{\downarrow}$ with $D_{\uparrow}^{(d)} > D_{\downarrow}^{(d)}$. These two possibilities are attributed to $s_{\downarrow} \rightarrow d_{\downarrow}$ and $s_{\uparrow} \rightarrow d_{\uparrow}$ scatterings, respectively [KOKA2012].

From the above discussion, a positive AMR ratio results when the dominant $s \rightarrow d$ scattering occurs through a spin-flip process, such as $s_{\downarrow} \rightarrow d_{\uparrow}$ and $s_{\uparrow} \rightarrow d_{\downarrow}$. In contrast, when the scattering predominantly occurs without spin-flip, *i.e.*, by $s_{\uparrow} \rightarrow d_{\uparrow}$ and $s_{\downarrow} \rightarrow d_{\downarrow}$, a negative AMR ratio is observed. In half-metallic materials, the absence of a particular type of spin (either up or down) DOS at E_F (*c.f.*, Figure 1.02 (c)) prevents spin-flip scattering, while spin-conserving scatterings remain allowed. Consequently, the observation of a negative AMR ratio is generally considered as an indication of half-metallic behavior [CHEN2017, SAKU2014, YANG2012]. However, this is not conclusive evidence for 100% *P* [KUSH2022]. Therefore, the temperature dependence of $\Delta\rho_{AMR}$ was analyzed to assess the half-metallic nature of the sample. According to the two-current model, only $s_{\uparrow} \rightarrow d_{\downarrow}$ and $s_{\uparrow} \rightarrow d_{\uparrow}$ types of scattering processes need to be taken into consideration for evaluating $\Delta\rho_{AMR}$. So, the expression for $\Delta\rho_{AMR}$ reduces to [KUSH2022],

$$\Delta\rho_{AMR} \approx \gamma\left(\rho_{s,\uparrow\rightarrow d,\downarrow} - \rho_{s,\uparrow\rightarrow d,\uparrow}\right) \tag{2.34}$$

Here, $\rho_{s,\uparrow\rightarrow d,\downarrow}$ and $\rho_{s,\uparrow\rightarrow d,\uparrow}$ are the resistivities due to $s_{\uparrow} \rightarrow d_{\downarrow}$ and $s_{\uparrow} \rightarrow d_{\uparrow}$ scattering processes, respectively. On substituting the corresponding values to the above equation, $\Delta\rho_{AMR}$ becomes [KUSH2022],

$$\Delta\rho_{AMR} \propto D_{\uparrow}^{(d)}\left[1 - \frac{D_{\downarrow}^{(d)}}{D_{\uparrow}^{(d)}}\right] \tag{2.35}$$

where, $D_{\uparrow}^{(d)}$ and $D_{\downarrow}^{(d)}$ represent the *d*-orbital DOS at E_F for up and down spins, respectively. The temperature dependence of $\Delta\rho_{AMR}$ originates primarily from $D_{\downarrow}^{(d)}$, due to the thermally excited electrons governed by Fermi-Dirac distribution function. In the case of half-metallic materials, $D_{\downarrow}^{(d)}$ is nearly zero with E_F located near the middle of the gap. In this electronic structure, $D_{\downarrow}^{(d)}$ is robust against temperature increase. Therefore, $\Delta\rho_{AMR}$ is expected to be a remain unaffected with any variation in temperature. On the other hand, for a non-half-metallic material with substantial $D_{\downarrow}^{(d)}$ in the gap, Equation (2.35), does not hold because of the existence of other *s*-*d* scattering processes, such as $s_{\downarrow} \rightarrow d_{\downarrow}$ and $s_{\downarrow} \rightarrow d_{\uparrow}$ along with $s_{\uparrow} \rightarrow d_{\downarrow}$ and $s_{\uparrow} \rightarrow d_{\uparrow}$, which leads to a variation in $\Delta\rho_{AMR}$ with temperature. Hence, it is evident that this analysis aids in the identification of qualitative changes in *P*.

Figure 2.26 (a) depicts the schematic diagram of the DC four-probe Hall bar geometry used in the measurement, with the current and magnetic field directions shown. The photograph of the sample having a Hall bar geometry attached to the sample holder and rotating puck is shown in Figure 2.26 (b). The rotator unit attached to the PPMS is shown in Figure 2.26 (c). This rotating probe setup is used to change the relative direction of the external magnetic field

with respect to the current direction. The measurement was carried out in 50 K interval in the temperature range of 50 K to 300 K. During the measurement, 0.2 mA direct current was passed along the <110> direction of the sample, while changing the saturation magnetization direction within the sample plane over 360° by applying a 1 T external magnetic field. The strength of the magnetic field was sufficient to fully saturate the magnetization, ensuring its alignment with the field direction.

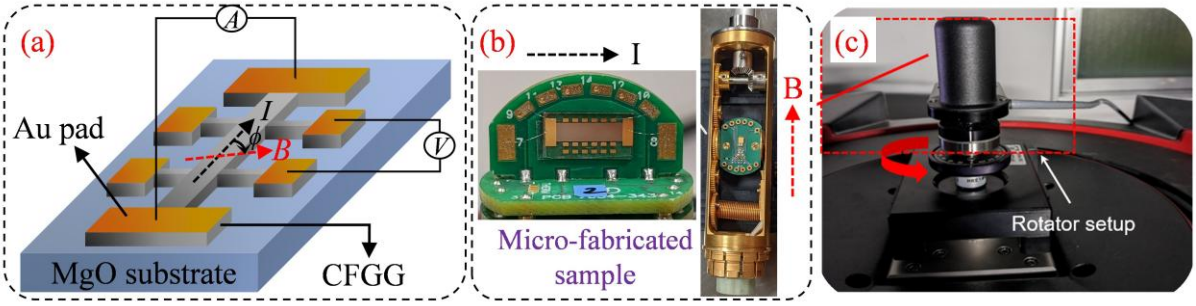

Figure 2.26. (a) Hall bar geometry of the sample used for the AMR measurement. (b) The sample attached to sample holder and rotating puck. (c) The rotator unit attached to the PPMS.

The angular dependence of the AMR ratio at 50 K, 100 K, 150 K, 200 K, 250 K, and 300 K, recorded for the 600 ℃ annealed CFGG film sample, is shown in Figure 2.27 (a). The observed negative AMR ratio indicates the dominance of $s_{\uparrow} \rightarrow d_{\uparrow}$ or $s_{\downarrow} \rightarrow d_{\downarrow}$ scatterings over $s_{\uparrow} \rightarrow d_{\downarrow}$ or $s_{\downarrow} \rightarrow d_{\uparrow}$ scatterings due to high P of the material. Figure 2.27 (b) shows the temperature dependence of $\Delta\rho_{AMR}$ ($\rho_{\parallel}$ - $\rho_{\perp}$) normalized by its value at T = 50 K for the specimens with and without minority DOS at E_F. The temperature dependence of $\Delta\rho_{AMR}$ in the as-deposited sample (denoted in black square) indicates the presence of minority DOS at E_F. In contrast, nearly temperature-independent behaviour of $\Delta\rho_{AMR}$ in the 600 ℃ annealed sample (denoted in red circle) indicates the absence of minority states at E_F.

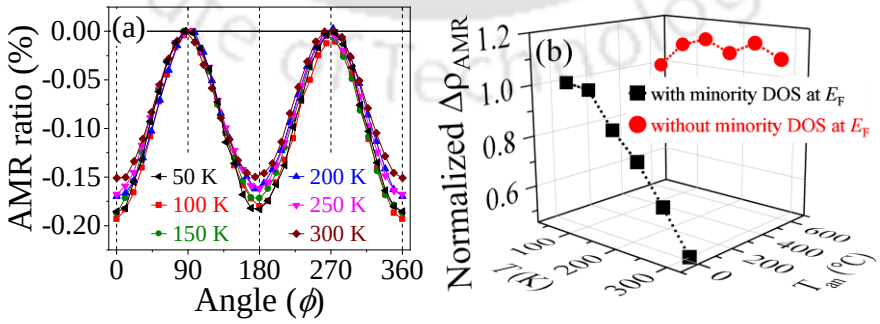

Figure 2.27. (a) Angular dependence of AMR ratio of measured at 50 K, 100 K, 150 K, 200 K, 250 K, and 300 K for the 600 ℃ annealed CFGG film sample. (b) Temperature dependence of the normalized $\Delta\rho_{AMR}$ (normalized by its value at T = 50 K).

2.2.5. Calculation of electronic properties

To complement and validate the experimental results, theoretical calculations were carried out. Density functional theory (DFT) [KOHN1965] has emerged as an effective tool for predicting the structural, electronic, and magnetic properties of materials. DFT is fundamentally based on the Hohenberg-Kohn theorem, which asserts that the ground-state properties of a many-electron system are uniquely determined by its electron density. The computational framework relies on the Born-Oppenheimer approximation [KRESS1999], the Kohn-Sham equations [KOHN1965], and suitable approximations for the exchange-correlation potential, which accounts for electron-electron interactions. Among the widely used approximations, the local density approximation (LDA) treats the exchange-correlation energy based on a uniform electron gas model evaluated at the local electron density. To improve accuracy for systems with varying electron densities, the generalized gradient approximation (GGA) [PERD1996], which includes gradient corrections, is commonly adopted. In this study, *ab initio* calculations were performed using the Vienna *ab initio* simulation package (VASP) [KRES1993]. The calculations incorporated the projector augmented wave (PAW) [BLOC1994, KRES1999] method along with spin-polarized DFT. The Perdew-Burke-Ernzerhof (PBE) functional within the GGA framework was used to model the exchange-correlation effects accurately.

The process of DOS calculation involves three main steps, *viz*., structural relaxation, self-consistent field (SCF) calculations, and finally, DOS calculations. These steps are executed using the VASP package, which requires four input files named as INCAR, POSCAR, POTCAR, and KPOINTS. Each computational step generates output files (CHGCAR, CONTCAR, DOSCAR, OSZICAR, OUTCAR, WAVECAR, *etc*.) required in subsequent steps. Comprehensive details of the input file formats and parameter settings are provided in the VASP manual [VASP2025]. A brief overview of the essential files and parameters associated with each computational step is given below:

2.2.5.1. Input files for computations using VASP

i. INCAR

The INCAR file serves as the central role in VASP, defining how a particular calculation will be carried out. It includes essential parameters, which can be fine-tuned depending on the type of analysis being performed to achieve accurate and efficient results. These parameters differ depending on the computational needs and change according to the calculation steps. The various parameters of INCAR file used in the relaxation, SCF, and DOS calculations of $Co_{1.5}FeTi_{0.5}Al$ alloy are listed in Table 2.01.

Table 2.01. Typical parameters of INCAR file utilized for relaxation, SCF, and DOS calculations performed on the $Co_{1.5}FeTi_{0.5}Al$ compound.

Relaxation	**SCF**	**DOS**
ISTART = 0	ISTART = 0	ISTART = 1
ISMEAR = 0	ISMEAR = 0	ISMEAR = -5
ICHARG = 2	ICHARG = 2	ICHARG = 11
SIGMA = 0.05	SIGMA = 0.05	SIGMA = 0.05
EDIFF = 0.00001	EDIFF = 0.00001	EDIFF = 0.00001
ENCUT = 520	ENCUT = 520	ENCUT = 520
ISPIN = 2	ISPIN = 2	ISPIN = 2
MAGMOM =	MAGMOM =	MAGMOM =
12*2.0 8*4.0 4*1.0 8*1.0	12*2.0 8*4.0 4*1.0 8*1.0	12*2.0 8*4.0 4*1.0 8*1.0
LORBIT = 11	LORBIT = 11	LORBIT = 11
LWAVE =. FALSE.	LWAVE = .FALSE.	LWAVE = .FALSE.
LCHARG =. FALSE.	LCHARG = .TRUE.	LCHARG = .FALSE.
PREC = Accurate	PREC = Accurate	PREC = Accurate
IBRION = 2		
ISIF = 2		
NSW = 500		
POTIM = 0.5		

A brief explanation of each parameter used in the INCAR files are provided below:

ISTART: This parameter determines whether the calculation starts from the scratch or uses a previously generated WAVECAR file. In the present case, for the relaxation and SCF steps, ISTART = 0 was used, indicating that the calculation starts from the scratch. In DOS calculations, ISTART=1 was employed to restart the calculation by considering the output CHARGECAR file from the previous SCF step.

ISMEAR: This parameter defines the smearing method used to assign fractional occupancies to electronic states. Gaussian smearing (ISMEAR = 0) was used during relaxation and SCF steps, while ISMEAR = -5 is applied in DOS calculations for higher total energy accuracy.

SIGMA: This parameter defines the smearing width in eV, which influences the occupation of electronic states near E_F. A value of 0.05 eV was used in the present calculations.

EDIFF: This parameter sets the energy convergence threshold for electronic iterations. A value of "EDIFF = $1E^{-5}$" was used, ensures the electronic iterations were continued until the total energy difference between successive steps dropped below 10^{-5} eV.

NSW: This parameter defines the maximum number of allowed relaxation steps. A value of "NSW = 500" was used to ensure structural convergence.

ENCUT: This parameter determines the kinetic energy cut-off for the plane-wave basis set. An "ENCUT = 520 eV" was chosen to ensure adequate accuracy in the calculations.

ISPIN: This parameter decides the spin resolved calculations. In this work, "ISPIN = 2" was used to obtain the spin-resolved DOS and spin magnetic moment.

ISIF: This parameter determines which ionic variables are allowed to change during the structural relaxation. In the present work, "ISIF = 2" is used, which permits only the adjustment of atomic coordinates while keeping the cell shape and volume fixed.

PREC: This parameter sets the accuracy level of input data and computational routines. For all calculations, "PREC = Accurate" was used to ensure high computational precision and reliable results.

LORBIT: This parameter determines how the projection onto angular momentum quantum numbers (*l* and *m*) is handled during DOS calculations. In this thesis, "LORBIT = 11" was used, which provides orbital-decomposed atomic orbitals of each element.

LWAVE: This parameter controls whether the calculated wavefunction is saved to the WAVECAR file or not. During the calculation, "LWAVE = .FALSE." was used to avoid storing the wavefunction data.

LCHARG: This parameter determines whether the charge density data is written to the CHGCAR file or not. During the relaxation process, "LCHARG = .FALSE." to skip generating the CHGCAR file. However, in SCF calculations, "LCHARG = .TRUE." was used to save the charge density, which is subsequently used for DOS analysis.

ICHARG: This parameter controls the treatment of initial charge density. For both relaxation and SCF steps, "ICHARG = 2" was used, while "ICHARG = 11" was used in the DOS step to read charge density from the previously generated CHGCAR file during the SCF step.

IBRION: This parameter controls how the crystal structure evolves during calculation. In this study, "IBRION = 2" was used to perform ionic relaxation.

POTIM: This parameter controls the step size used during ionic relaxation. Depending on the "IBRION = 2", a value of "POTIM = 0.5" was used in this study.

MAGMOM: This parameter sets the initial magnetic moments for each atomic element, defined as the product of the number of atoms and their estimated initial magnetic moments. For example, "MAGMOM = 12*2.0 8*4.0 4*1.0 8*1.0" assigns the initial moments to 12 Co, 8 Fe, 4 Ti, and 8 Al atoms.

ii. POSCAR

This input file provides details about the atomic arrangement and initial lattice parameters. A 32-atom supercell of $Co_{1.5}FeTi_{0.5}Al$ (12 Co, 8 Fe, 4 Ti, and 8 Al) was used in the present investigations. A typical POSCAR format is shown in Appendix appended at the end of this thesis. The first line is for comments, and the second line gives the scaling factor. Lines 3-5 define the unit cell dimensions in matrix format. The 6^{th} and 7^{th} lines list the constituent elements and the count of each element. The 8^{th} specifies the coordinate type (Cartesian or Direct), followed by 32 lines defining the atomic positions according to the sequence and quantity of elements given in the 6^{th} and 7^{th} lines.

iii. POTCAR

This file lists the pseudopotentials assigned to each element, containing essential information such as atomic mass, valence state, electronic configuration, *etc*.

iv. KPONTS

This file specifies the *k*-points (Bloch vectors) employed in the calculations. A Γ-centered Monkhorst-Pack grid with a resolution of up to 10×10×10 was used for Brillouin zone sampling. An example of a typical KPOINTS file is shown in Figure 2.28.

```
Automatic mesh
0
Gamma
10 10 10
 0  0  0
```

Figure 2.28. A typical KPOINTS file utilized in the calculations of $Co_{1.5}FeTi_{0.5}Al$ alloy.

2.2.5.2. Steps involved in DOS calculations

DOS calculations carried out using VASP generally proceed through the following three sequential steps:

Step 1: Structural relaxation

During the structural relaxation, all four aforementioned input files (INCAR, POSCAR, POTCAR, and KPOINTS), along with the execution (VASP) script, must be placed in the working directory before initiating the calculation. This step minimizes the total energy to find the stable atomic arrangement. The relaxed atomic positions are saved in the output CONTCAR file.

Step 2: SCF calculations

In this step, the CONTCAR file from the relaxation step is copied and renamed as a POSCAR, and placed in the same directory along with the updated INCAR, POTCAR, KPOINTS files, and the VASP script. With these input files, the SCF calculation can be started.

Step 3: DOS calculations

In this step, the CONTCAR file from the SCF calculation is used as the POSCAR input, along with the CHGCAR file for charge density information from the SCF step. The INCAR, POTCAR, and KPOINTS files are updated for DOS-specific settings, and the calculation is run using the VASP script. Once the calculation completes, the resulting data can be extracted and analyzed. An example of this output is shown in Figure 2.29, which illustrates the spin-resolved total density of states (TDOS) of the $Co_{1.5}FeTi_{0.5}Al$ compound.

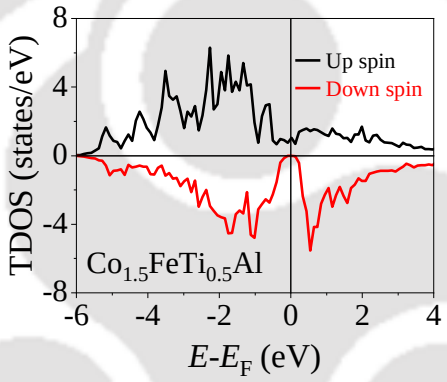

Figure 2.29. TDOS near E_F of Co_2FeGa obtained using *X*-type unit cell.

Chapter 3

Effect of V substitution for Co in Co_2MnAl alloy

3.1. Introduction

As mentioned in Chapter 1, Co_2MnZ-based ternary Heusler alloys are extensively studied by researchers due to their large M_s and relatively high P [YILG2005, YILG2012]. However, Co_2MnZ alloys fail in maintaining the high P exhibited at liquid He temperatures when raised to room temperature, as reflected in their lower MR ratio at ambient temperature [ISHI2006, SAKU2010]. This thermal degradation in half-metallic character is due to E_F being located very close to the valence (or conduction) band edge with a tendency to shift into the valence (or conduction) at finite temperatures. One way to mitigate this handicap is by identifying materials with a wide minority gap and ensuring that their E_F is located near the centre of this wide bandgap. 'Bandgap engineering' by substituting a suitable fourth element in the ternary Heusler alloy, which has E_F close to the minority conduction (or valence) band edge is an innovative way to achieve this [SHAM2019]. Co_2MnAl, is a compound in which E_F is close to the edge of the minority valence band [JUNG2009, RAMS2011], resulting in a substantial decrease in its P. On the other hand, the quaternary alloy CoMnVAl exhibits zero magnetic moment [BASI2011], and this semiconducting alloy has E_F near the middle of the minority gap [MARC2018b]. Thus, there is a possibility to reduce the minority DOS at E_F in Co_2MnAl by appropriate substitution of V for Co in the compound, thereby achieving 100% P without losing its ferromagnetic properties. Despite extensive work on Co_2MnAl, such studies have not been reported in $Co_{2-x}MnV_xAl$ alloys so far. In this chapter, a detailed study carried out on the structural, magnetic, and electronic properties of $Co_{2-x}MnV_xAl$ (x = 0.0, 0.25, 0.5) Heusler alloys to address this gap in the literature is presented.

3.2. Sample preparation and processing

$Co_{2-x}MnV_xAl$ (x = 0.0, 0.25, and 0.50) alloys were synthesized by arc melting appropriate amounts of high (≥ 99.9%) purity constituent elements under an argon atmosphere. The arc melted ingot was re-melted 5 to 6 times to improve the compositional homogeneity of the alloy ingot. Subsequently, each arc melted alloy ingot was encapsulated in a fused silica ampoule after evacuation to ~10^{-3} Pa, and the ampoule was heat treated at 1100 ℃ for 24 h in a rising

hearth furnace and then quenched in ice and water mixture. The bulk ingots were then gently ground into fine powder form and stored in a vacuum desiccator for further characterization.

3.3. Results and discussion

3.3.1. Composition analysis

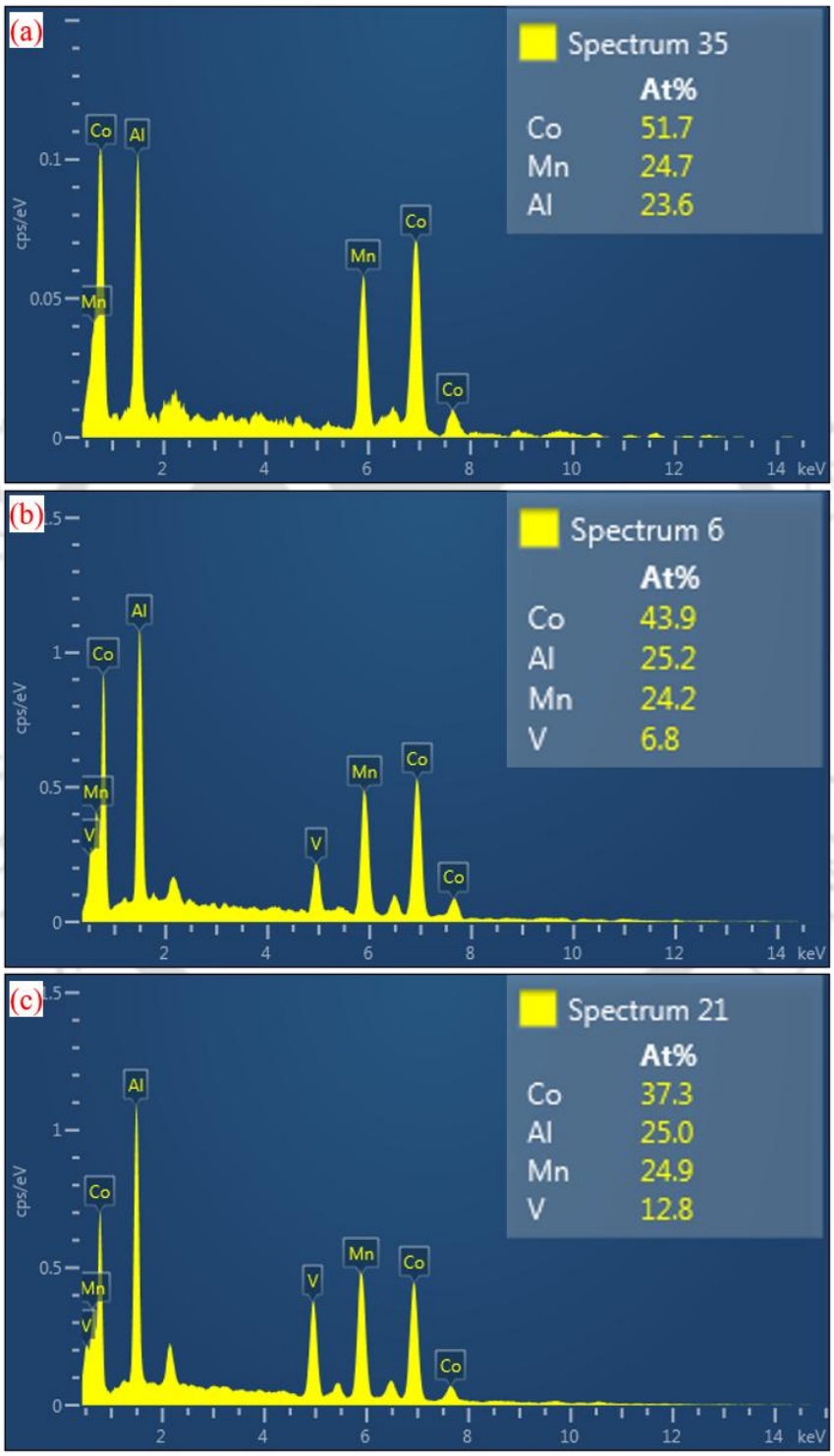

Figure 3.01. Reduced EDS spectrum of (a) Co_2MnAl, (b) $Co_{1.75}MnV_{0.25}Al$, and (c) $Co_{1.5}MnV_{0.5}Al$ Heusler alloys.

The overall chemical composition of the alloys was assessed using an EDS unit coupled with an FESEM. As described in Chapter 2. Figure 3.01 (a, b, and c) shows the typical EDS spectrum of the heat-treated Co_2MnAl, $Co_{1.75}MnV_{0.25}Al$, and $Co_{1.5}MnV_{0.5}Al$ alloy, respectively. In this reduced spectrum, only the characteristic peaks corresponding to the constituent elements (Co, Mn, V, and Al) are seen, since the peaks from the C tape and the Au, coating have been carefully subtracted using in-built software. The overall composition of the whole sample was determined by averaging the results from 10 such individual spectral scans taken at different regions of the sample. The overall elemental composition of $Co_{2-x}MnV_xAl$ Heusler alloys with x = 0.0, 0.25, and 0.50 is $Co_{51\pm1.3}Mn_{25\pm1.1}Al_{24\pm1.2}$, $Co_{44\pm1.3}Mn_{25\pm1.0}V_{6\pm0.5}Al_{25\pm1.2}$, and $Co_{37\pm1.2}Mn_{24\pm1.0}V_{13\pm0.7}Al_{26\pm1.1}$, respectively.

3.3.2. Structural analysis

Room temperature powder XRD measurements were carried out on all the heat-treated $Co_{2-x}MnV_xAl$ (x = 0.0, 0.25, and 0.50) Heusler alloys. Figure 3.02 (a-c) display XRD patterns of Co_2MnAl, $Co_{1.75}MnV_{0.25}Al$, and $Co_{1.5}MnV_{0.5}Al$, respectively, with insets highlighting the 25-33° range to clearly show the (111) and (200) superlattice reflections. The corresponding simulated patterns for $B2$ and $L2_1$-type structures are shown in Figure 3.02 (d-f).

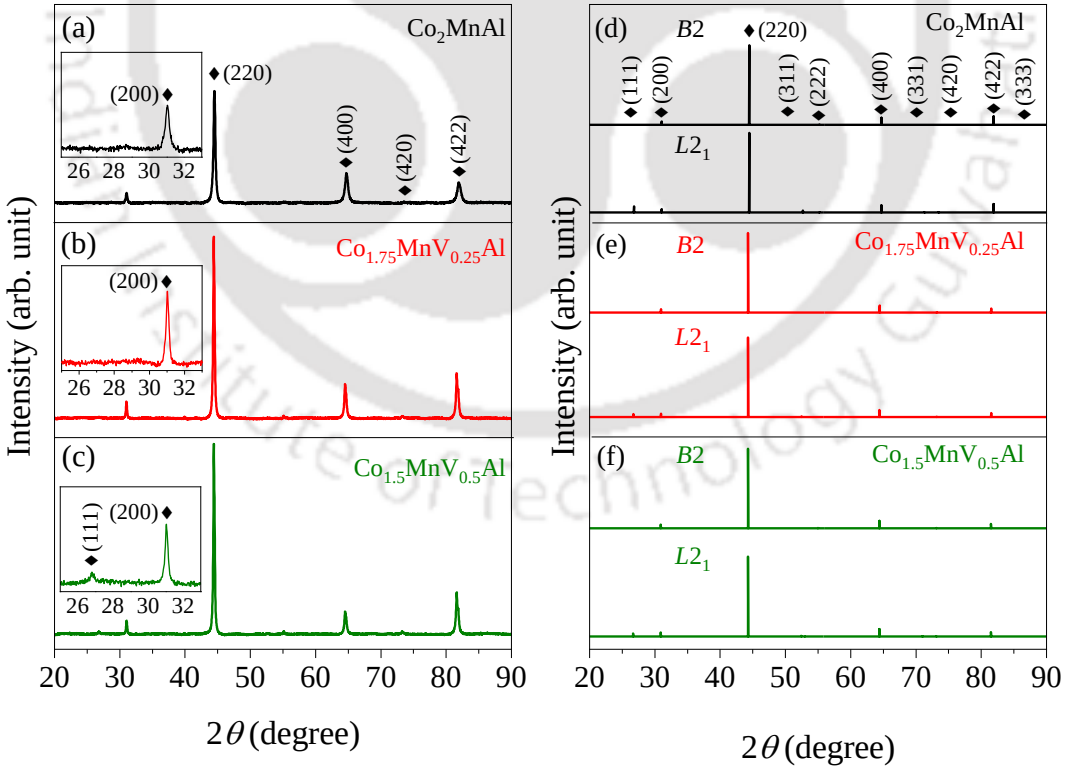

Figure 3.02. Room temperature XRD patterns of heat-treated (a) Co_2MnAl, (b) $Co_{1.75}MnV_{0.25}Al$, and (c) $Co_{1.5}MnV_{0.5}Al$ alloys. XRD patterns simulated using $B2$ and $L2_1$-type unit cells of (d) Co_2MnAl, (e) $Co_{1.75}MnV_{0.25}Al$, and (f) $Co_{1.5}MnV_{0.5}Al$ alloys.

Though the reflections corresponding to the Heusler alloy structure are visible in Figure 3.02 (a-c), the nature of the atomic disorder can be inferred only after comparing the intensity of experimentally observed (111) and (200) superlattice reflections with the corresponding reflection in the simulated XRD pattern. In the experimental XRD patterns of Co_2MnAl and $Co_{1.75}MnV_{0.25}Al$ alloys, the superlattice reflection of (111) is absent, while the (200) superlattice reflection is present, as seen from Figure 3.02 (a and b). These patterns match with the simulated XRD pattern of the alloys simulated with *B*2-type unit cell as portrayed in Figure 3.02 (d and e). This indicates the occurrence of *B*2-type partial disorder in Co_2MnAl and $Co_{1.75}MnV_{0.25}Al$ alloys. The presence of *B*2-type partial disorder is consistent with the previous studies [JUNG2009]. On the other hand, the emergence of both (111) and (200) superlattice reflections in $Co_{1.5}MnV_{0.5}Al$ alloy, consistent with the simulated XRD pattern of the $L2_1$-type ordered structure, as shown in Figure 3.02 (f), indicates the formation of a highly ordered structure in $Co_{1.5}MnV_{0.5}Al$ alloy.

As outlined in the Section 1.2.1.1, in X_2YZ Heusler alloys having 100% *B*2-type partial disorder, X atoms occupy the 4*a* (0.25, 0.25, 0.25) and 4*b* (0.75, 0.75, 0.75) atomic sites, while Y and Z atoms distribute equally at 4*c* (0.5, 0.5, 0.5) and 4*d* (0, 0, 0) sites. Accordingly, *B*2-type partially disordered Co_2MnAl has Co atoms at 4*a* (0.25, 0.25, 0.25) and 4*b* (0.75, 0.75, 0.75) atomic sites, while Mn and Al distribute equally in 4*c* (0.5, 0.5, 0.5) and 4*d* (0, 0, 0) sites. On the other hand, when 50 at.% of V substitutes for Co in Co_2MnAl to form CoMnVAl, V atoms displace Mn atoms to the vacant Co sites due to the concurrent reduction in Co content. Consequently, V takes over the 4*c* (0.5, 0.5, 0.5) site (rather than the 4*d* (0, 0, 0) site, to maintain the highly ordered structure), establishing a rock-salt-type arrangement with Al atoms positioned at 4*d* (0, 0, 0) [XION2014]. These modifications in the atomic site occupancy follow the Hume-Rothery criterion of phase stability [TSAI2004]. According to this rule, the larger the electronegativity difference between two elements, the higher is the probability of compound formation. So, it is expected that the substitution of V atoms for Co will lead to the relocation of Mn atoms to the unoccupied Co sites in the intermediate compositions of $Co_{2-x}MnV_xAl$ alloys.

To validate this stable atomic configuration, energy minimization of all possible atomic configurations of $Co_{1.75}MnV_{0.25}Al$ and $Co_{1.5}MnV_{0.5}Al$ alloys was carried out using a 32 atoms super unit cell. The atomic configuration with the lowest energy corresponds to the most stable structure. At absolute zero temperature, the total energy of an atomic system corresponds to its free energy. Table 3.01 and Table 3.02 list the computed free energy values associated with various atomic configurations in a 32 atoms super unit cell, along with the respective Wyckoff

positions of each element for $Co_{1.75}MnV_{0.25}Al$ and $Co_{1.5}MnV_{0.5}Al$ alloys, respectively. For $Co_{1.75}MnV_{0.25}Al$, atomic positions were assigned by considering 100% *B*2-type partial disorder, whereas for $Co_{1.5}MnV_{0.5}Al$, an $L2_1$-type ordered structure was considered, based on the XRD results. As indicated in Table 3.01, the Type 4 atomic configuration of the $Co_{1.75}MnV_{0.25}Al$ unit cell exhibits the lowest free energy. In this configuration, one V atom replaces a Mn atom at both the 4*c* (0.5, 0.5, 0.5) and 4*d* (0, 0, 0) sites, resulting in a total of two Mn atoms to relocate to the unoccupied Co sites at 4*b* (0.75, 0.75, 0.75). It may be noted that the Type 5 configuration with free energy very close to the Type 4 configuration is equivalent to Type 4 due to the symmetric atomic occupancies in the unit cell. Hence, Type 5 is equally probable as Type 4 despite its slightly higher energy value. This suggests that Type 4 and Type 5 atomic configurations are the most energetically favourable ones among all the examined possibilities.

Table 3.01. Diverse atomic arrangements possible in the 32 atoms super unit cell designed for $Co_{1.75}MnV_{0.25}Al$ and their associated free energy.

Configuration	Wyckoff positions				Free energy (eV)
	$4a\left(\frac{1}{4},\frac{1}{4},\frac{1}{4}\right)$	$4b\left(\frac{3}{4},\frac{3}{4},\frac{3}{4}\right)$	$4c\left(\frac{1}{2},\frac{1}{2},\frac{1}{2}\right)$	$4d(0,0,0)$	
Type 1	8Co	8Mn	3Co, 1V, 4Al	3Co, 1V, 4Al	-224.556
Type 2	4Co, 4Mn	4Co, 4Mn	3Co, 1V, 4Al	3Co, 1V, 4Al	-224.171
Type 3	8Co	6Co, 2V	4Mn, 4Al	4Mn, 4Al	-226.989
Type 4	8Co	6Co, 2Mn	3Mn, 1V, 4Al	3Mn, 1V, 4Al	-228.369
Type 5	7Co, 1Mn	7Co, 1Mn	3Mn, 1V, 4Al	3Mn, 1V, 4Al	-228.217
Type 6	8Co	4Co, 2Mn, 2V	1Co, 3Mn, 4Al	1Co, 3Mn, 4Al	-225.561
Type 7	6Co, 1Mn, 1V	6Co, 1Mn, 1V	1Co, 3Mn, 4Al	1Co, 3Mn, 4Al	-225.440

In the case of $Co_{1.5}MnV_{0.5}Al$, the lowest free energy was again observed for the Type 4 atomic configuration, where 4 V atoms replace 4 Mn atoms at the 4*c* (0.5, 0.5, 0.5) atomic site, causing Mn atoms to relocate to the unoccupied Co sites at 4*b* (0.75, 0.75, 0.75) (see Table

3.02). Just as in the case of $Co_{1.75}MnV_{0.25}Al$ alloy, the Type 5 configuration in $Co_{1.5}MnV_{0.5}Al$ exhibits a free energy value very close to the Type 4 configuration, and both are considered equivalent due to the symmetric atomic occupancies in the unit cell. Therefore, Type 5 atomic configuration is as favourable as Type 4, indicating that both represent the most stable configurations among all the examined possibilities. These aforementioned possible atomic configurations of $Co_{1.5}MnV_{0.5}Al$ and $Co_{1.75}MnV_{0.25}Al$ alloys align well with the reports in previous studies on Heusler alloys [SHAM2019, MAHA2022, MAHA2023].

Table 3.02. Diverse atomic arrangements possible in the 32 atoms super unit cell designed for $Co_{1.5}MnV_{0.5}Al$ and their associated free energy.

Configuration	Wyckoff positions				Free energy (eV)
	$4a\left(\frac{1}{4},\frac{1}{4},\frac{1}{4}\right)$	$4b\left(\frac{3}{4},\frac{3}{4},\frac{3}{4}\right)$	$4c\left(\frac{1}{2},\frac{1}{2},\frac{1}{2}\right)$	$4d(0,0,0)$	
Type 1	8Co	8Mn	4Co, 4V	8Al	-229.228
Type 2	4Co, 4Mn	4Co, 4Mn	4Co, 4V	8Al	-229.665
Type 3	8Co	4Co, 4V	8Mn	8Al	-230.498
Type 4	8Co	4Co, 4Mn	4Mn, 4V	8Al	-233.537
Type 5	6Co, 2Mn	6Co, 2Mn	4Mn, 4V	8Al	-233.290
Type 6	8Co	4Co, 2Mn, 2V	6Mn, 2V	8Al	-231.828
Type 7	6Co, 1Mn, 1V	6Co, 1Mn, 1V	6Mn, 2V	8Al	-231.627

Rietveld refinement was performed for all the samples by considering the most stable atomic configurations of $Co_{2-x}MnV_xAl$ (x = 0.0, 0.25, and 0.50) Heusler alloys. Figure 3.03 (a, b, and c) display room temperature XRD patterns along with the Rietveld refinement for the heat-treated Co_2MnAl, $Co_{1.75}MnV_{0.25}Al$, and $Co_{1.5}MnV_{0.5}Al$ Heusler alloys, respectively. The corresponding atomic arrangements used during the refinement process, having *B*2-type partial disorder for Co_2MnAl and the Type 4 atomic configurations for both $Co_{1.75}MnV_{0.25}Al$ and $Co_{1.5}MnV_{0.5}Al$, are shown in Figure 3.03 (d-f). The obtained lattice constant (a) from the refinement process was increased from 5.758±0.002 Å for Co_2MnAl to 5.782±0.003 Å for $Co_{1.5}MnV_{0.5}Al$. The observed lattice parameter increase is consistent with Vegard's law, which correlates atomic size differences with structural changes [DENT1991]. In this case, the larger radius of V (1.92 Å) relative to Co (1.67 Å) contributes to the increase in the values of a. The lattice constant of Co_2MnAl agrees with values reported in the literature [WEBS1971].

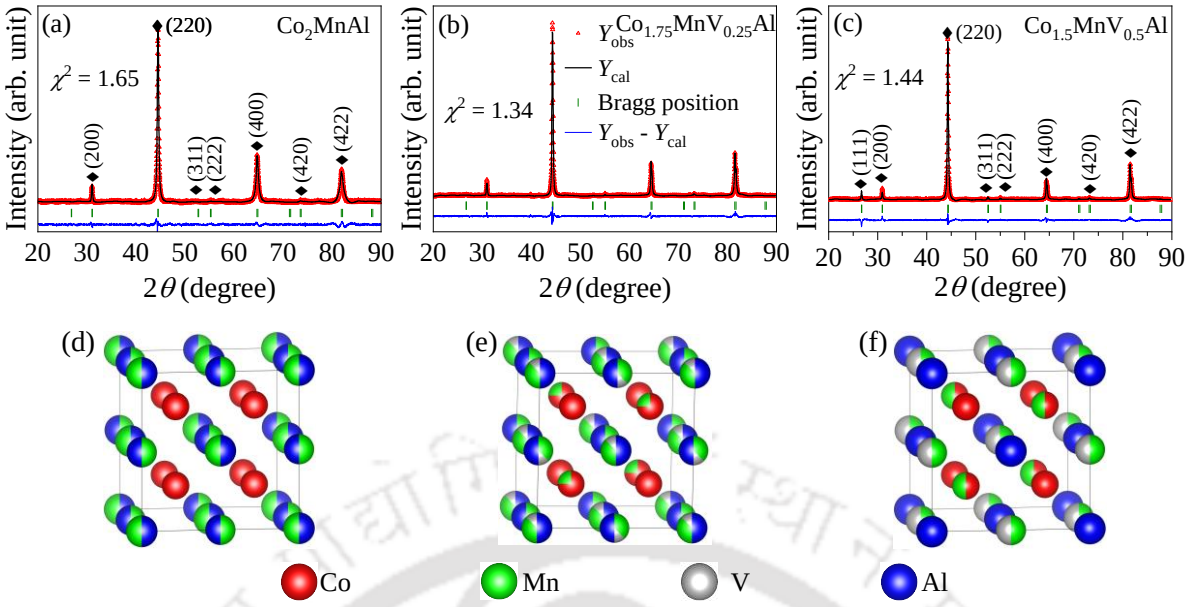

Figure 3.03. Rietveld refined XRD patterns of heat-treated (a) Co_2MnAl, (b) $Co_{1.75}MnV_{0.25}Al$, and (c) $Co_{1.5}MnV_{0.5}Al$ alloys. Unit cell of (d) Co_2MnAl with *B*2 disorder, (e) $Co_{1.75}MnV_{0.25}Al$ with Type 4 atomic configuration, and (f) $Co_{1.5}MnV_{0.5}Al$ with Type 4 atomic configuration, used in the Rietveld refinement.

3.3.3. Density of electronic states and magnetic moment

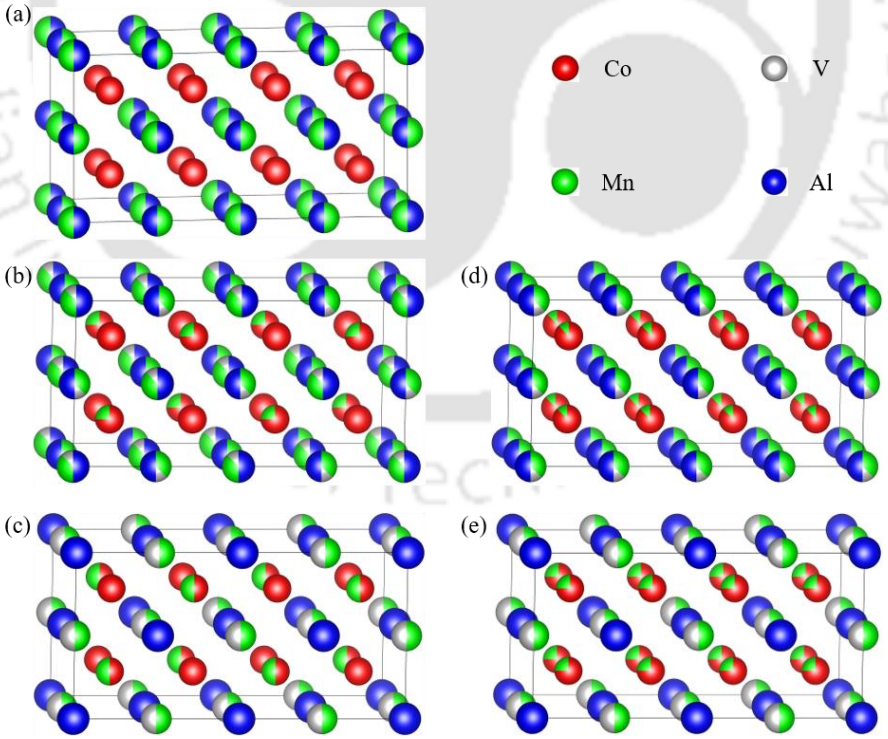

Figure 3.04. 32 atoms super unit cell of (a) Co_2MnAl alloy with *B*2-type disorder, (b and d) $Co_{1.75}MnV_{0.25}Al$ alloy with Type 4 and Type 5 atomic configurations, respectively. (c and e) $Co_{1.5}MnV_{0.5}Al$ alloy with Type 4 and Type 5 atomic configurations, respectively.

The procedure followed in calculating the electronic DOS of the alloys is discussed in Section 2.2.5. The spin-resolved total DOS and element-resolved density of states (EDOS) of $Co_{2-x}MnV_xAl$ (x = 0.0, 0.25, 0.5) Heusler alloys were determined using a super unit cell containing 32 atoms to accommodate the small variations in the elemental composition of each alloy with its distinct atomic ordering. The calculations were carried out using the Type 4 atomic configuration, which corresponds to the lowest energy arrangement. Its equivalence with the Type 5 configuration would be discussed later. Figure 3.04 (a, b, and c) depict the 32 atoms super unit cell of Co_2MnAl exhibiting *B*2-type disorder, and $Co_{1.75}MnV_{0.25}Al$ and $Co_{1.5}MnV_{0.5}Al$ alloys corresponding to the Type 4 atomic configurations, respectively. The Type 5 atomic configurations of $Co_{1.75}MnV_{0.25}Al$, and $Co_{1.5}MnV_{0.5}Al$ alloys are shown in Figure 3.04 (d and e), respectively. In the case of Co_2MnAl, the absence of V eliminates the possibility of different atomic configurations. Hence, two different atomic configurations for Co_2MnAl are not shown in Figure 3.04.

Table 3.03. Structural ordering and atomic site occupancies in $Co_{2-x}MnV_xAl$ Heusler alloys. SC and RR represent the Wyckoff positions in the designed 32 atoms super unit cell with Type 4 configuration and the corresponding atomic occupations derived from Rietveld refinement.

Heusler alloy composition	Atomic order	In SC/RR	Wyckoff positions			
			$4a\left(\frac{1}{4},\frac{1}{4},\frac{1}{4}\right)$	$4b\left(\frac{3}{4},\frac{3}{3},\frac{3}{4}\right)$	$4c\left(\frac{1}{2},\frac{1}{2},\frac{1}{2}\right)$	$4d(0,0,0)$
Co_2MnAl	*B*2	SC	8Co	8Co	4Mn, 4Al	4Mn, 4Al
		RR	0.99 Co	1.00 Co	0.52 Mn 0.49 Al	0.51 Mn 0.49 Al
$Co_{1.75}MnV_{0.25}Al$	*B*2	SC	8Co	6Co, 2Mn	3Mn, 1V, 4Al	3Mn, 1V, 4Al
		RR	1.01 Co	0.75 Co 0.25 Mn	0.37 Mn 0.13 V 0.50 Al	0.36 Mn 0.13 V 0.50 Al
$Co_{1.5}MnV_{0.5}Al$	$L2_1$	SC	8Co	4Co, 4Mn	4Mn, 4V	8Al
		RR	1.00 Co	0.5 Co 0.49 Mn	0.5 Mn 0.5 V	1.01 Al

To obtain $Co_{2-x}MnV_xAl$ (x = 0.0, 0.25, 0.5) alloy compositions, V was progressively substituted for Co in steps of 6.25 at.%, leading to a reduction in Co concentration from 50 at.% in Co_2MnAl (x = 0.0) to 37.5 at.% in $Co_{1.5}MnV_{0.5}Al$ (x = 0.50). Table 3.03 provides details of Type 4 atomic configuration in a 32 atoms super unit cell along with the corresponding (equivalent) atomic occupations obtained from the Rietveld refinement of experimental XRD pattern of each alloy composition and the respective atomic order used in the calculations.

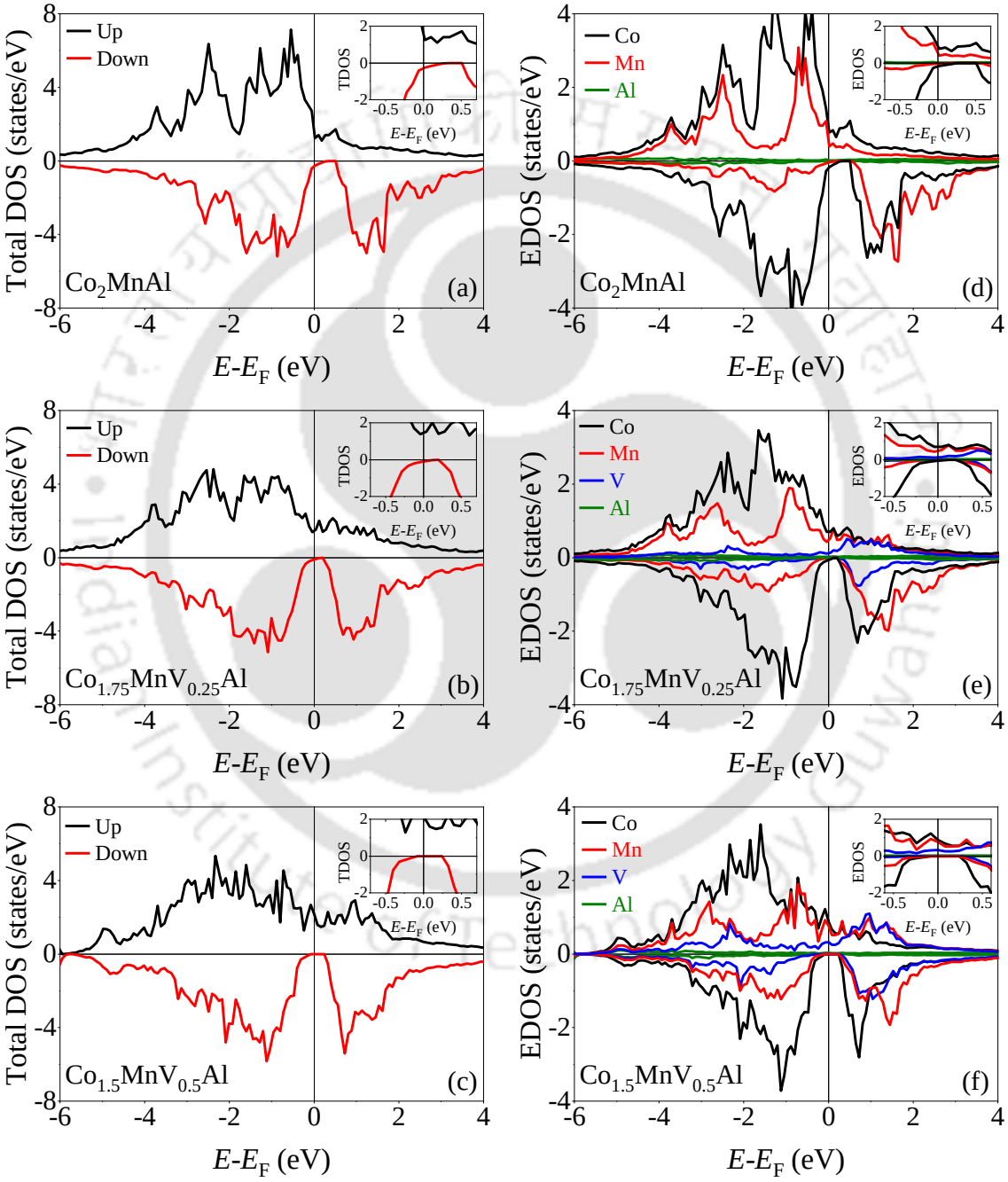

Figure 3.05. Spin-resolved total DOS at E_F computed for (a) Co_2MnAl, (b) $Co_{1.75}MnV_{0.25}Al$, and (c) $Co_{1.5}MnV_{0.5}Al$ alloys. EDOS computed for (d) Co_2MnAl, (e) $Co_{1.75}MnV_{0.25}Al$, and (f) $Co_{1.5}MnV_{0.5}Al$ alloys. Insets show the expanded view of the DOS close to E_F.

The computed total DOS for Co_2MnAl, $Co_{1.75}MnV_{0.25}Al$, and $Co_{1.5}MnV_{0.5}Al$ are shown in Figure 3.05 (a-c), with insets providing an enlarged view of the data near E_F. The corresponding EDOS is depicted in Figure 3.05 (d-f), where insets offer a magnified view of element-specific states near E_F for better visualization. Figure 3.05 (a) illustrates a clear minority gap in Co_2MnAl, resulting from strong *d-d* hybridizations between Co and Mn atoms [MEBS2013]. The inset of Figure 3.05 (a) reveals that the minority gap is located just above E_F at ~0.27 eV, leading to the presence of ~0.24 states/eV minority DOS at E_F. From the EDOS data of Co_2MnAl (*c.f.* Figure 3.05 (d)), it is evident that the minority DOS at E_F comprises ~81.4% contribution from Co, ~16.9% from Mn, and ~1.7% from Al. The presence of these minority states at E_F lowers P to ~69%, with a corresponding M_t of 4.08 μ_B/f.u. [KAND2007]. In an attempt to improve P, 6.25 at.% V was incorporated for Co in Co_2MnAl forming the $Co_{1.75}MnV_{0.25}Al$ alloy. Figure 3.05 (b) shows a minority gap in $Co_{1.75}MnV_{0.25}Al$. The inset of this figure clearly illustrates the shift of the minority gap toward E_F, positioning the minority gap ~0.12 eV away from E_F. As a result, the minority DOS at E_F was reduced to ~0.08 states/eV, which is notably smaller than that of Co_2MnAl. The EDOS for $Co_{1.75}MnV_{0.25}Al$ is shown in Figure 3.05 (e), which indicates a significantly reduced minority DOS at E_F for each element, with the individual contribution of 75.5% from Co, 16.7% from Mn, 5.5% from V, and 2.3% from Al. Thus, there is a relative decrease in Co contribution to the minority DOS at E_F (from 81.4% to 75.5%) upon 6.25 at.% V substitution. However, the relative contributions from Mn and Al remain approximately the same through this substitution. Thus, the overall effect of 6.25 at.% V substitution leads to a reduction of minority states at E_F, thereby enhancing P to ~87%, with a simultaneous reduction in M_t to 3.02 μ_B/f.u.. Upon further increase in V to 12.5 at.%, the resulting $Co_{1.5}MnV_{0.5}Al$ Heusler alloy exhibits a clear minority gap with a width of ~0.34 eV, as shown in Figure 3.05 (c). The inset of this figure reveals that E_F is positioned near the center of the minority gap, resulting in 100% P. The corresponding EDOS shown in Figure 3.05 (f) confirms that the valence band edge of each element has shifted towards the left side of E_F and is positioned at ~0.08 eV below E_F. As a consequence, there are no states corresponding to any of the elements at E_F. Hence, the overall effect of 12.5 at.% of V substitution is the total reduction of minority states due to all elements at E_F, thereby enhancing P to 100%, with a simultaneous reduction in M_t to 2.00 μ_B/f.u.. The substantial enhancement in P can be attributed to the compositional change caused by decreasing the Co concentration, which results in structural evolution from a partially disordered *B*2-type to a highly ordered structure (refer to Section 3.3.2).

The impact of V substitution for Co on P and M_t of the alloys has been compared between Type 4 and Type 5 configurations, which are structurally equivalent. Figure 3.06 (a-c) show the spin-resolved total DOS at E_F for Co_2MnAl, $Co_{1.75}MnV_{0.25}Al$, and $Co_{1.5}MnV_{0.5}Al$ alloys, respectively. The black and red lines correspond to Type 4 and Type 5 atomic configurations, respectively. In the case of Co_2MnAl, there is no V. Therefore, Type 4 and Type 5 configurations are exactly identical for this alloy, as reflected in their respective spin-resolved total DOS (*c.f.* Figure 3.06 (a)) and M_t. However, in the quaternary alloy, the total DOS corresponding to the two configurations shows some small differences, mainly in the majority spin channel. P and M_t of $Co_{1.75}MnV_{0.25}Al$ and $Co_{1.5}MnV_{0.5}Al$ corresponding to Type 4 and Type 5 configurations are tabulated in Table 3.04. It can be noticed that although these two atomic configurations are structurally equivalent, very small differences in P and M_t values are observed, which may be due to computational limitations.

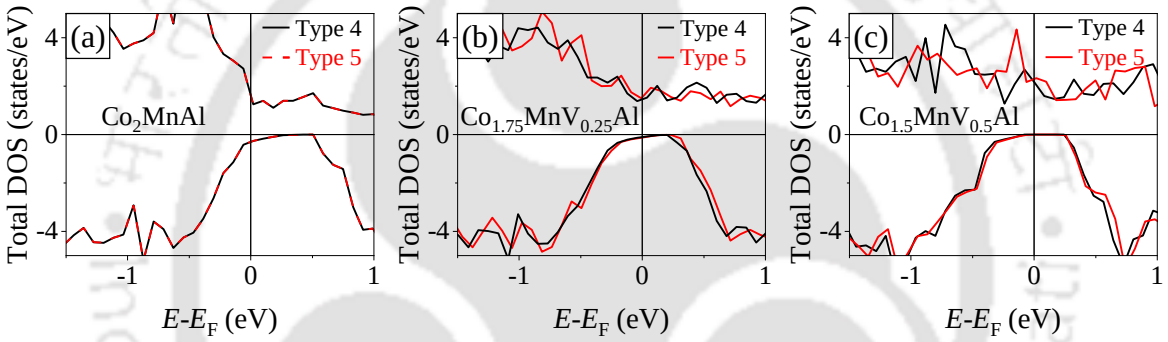

Figure 3.06. Comparison of spin-resolved total DOS at E_F between the Type 4 (black line) and the Type 5 (red line) atomic configurations, computed for (a) Co_2MnAl, (b) $Co_{1.75}MnV_{0.25}Al$, and (c) $Co_{1.5}MnV_{0.5}Al$ alloys.

Table 3.04. P and M_t of $Co_{1.75}MnV_{0.25}Al$ and $Co_{1.5}MnV_{0.5}Al$ alloys for Type 4 and Type 5 configurations.

Heusler alloy composition	Configuration	P (%)	M_t (μ_B/f.u.)
$Co_{1.75}MnV_{0.25}Al$	Type 4	87	3.02
	Type 5	86	3.03
$Co_{1.5}MnV_{0.5}Al$	Type 4	100	2.00
	Type 5	100	2.00

3.3.4. Magnetic and half-metallic properties

Figure 3.07 (a-b) show the *M-H* loop of Co_2MnAl (x = 0.0), $Co_{1.75}MnV_{0.25}Al$ (x = 0.25), and $Co_{1.5}MnV_{0.5}Al$ (x = 0.50) alloys at 10 K and 300 K, respectively. It is observed that M_s at 10 K is 3.91±0.04, 2.45±0.04, and 1.48±0.03 μ_B/f.u. for alloys with x = 0.0, 0.25, and 0.50, while at

300 K, the M_s values are 3.84±0.04, 2.40±0.03, and 1.32±0.04 μ_B/f.u., respectively. M_s of Co_2MnAl is consistent with reports in the literature [BALK2010]. The insets of both figures display the zoomed view of the loops in the vicinity of the origin, revealing a H_c of ~55 Oe and soft magnetic nature. M_s decreases with an increase in V substitution for Co, which is consistent with the trend in the theoretically calculated spin magnetic moment. However, the experimentally obtained M_s shows a slight deviation from the theoretical predictions with an increase in V concentration, which has also been noticed earlier [SHAM2024]. A slight decrease in M_s with an increase in the measurement temperature from 10 K to 300 K is observed, and the extent of decrease in M_s is more pronounced in the samples with higher V concentration. This behaviour could be attributed to the decrease in T_C with reduction in Co, making the sample more vulnerable to thermal demagnetization. Along with M_s and H_c, K_{eff} has been determined from the initial magnetization curve using the law of approach to saturation as already discussed in Section 2.2.3.1. K_{eff} of $Co_{2-x}MnV_xAl$ alloys was evaluated at 10 K to be 3.67×10^6, 1.85×10^6, and 0.89×10^6 erg/cc for alloys with x = 0.0, 0.25, and 0.50, respectively. The corresponding K_{eff} values at 300 K are 3.64×10^6, 1.80×10^6, and 0.72×10^6 erg/cc. Subsequent decrease in K_{eff} at higher temperatures has also been reported earlier [PATH2022]. Further, the decrease in K_{eff} with increasing V concentration is attributed to the corresponding decrease in M_s in this series of alloys.

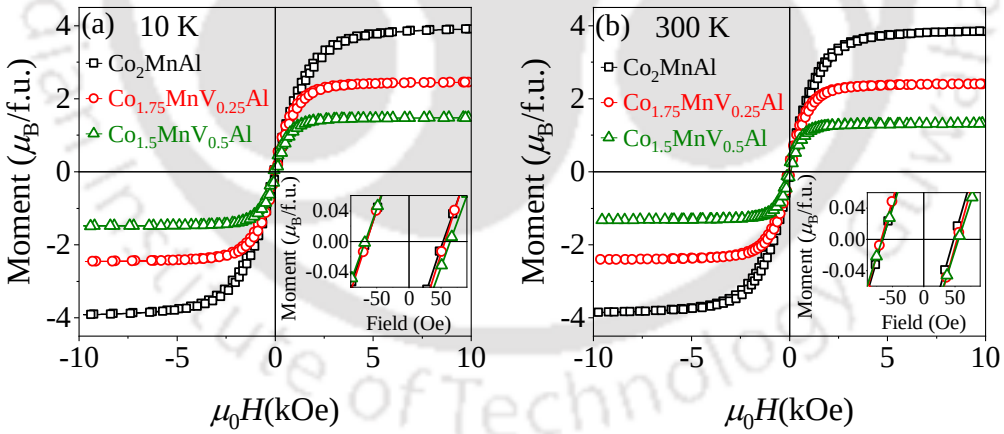

Figure 3.07. Variation in magnetization of Co_2MnAl, $Co_{1.75}MnV_{0.25}Al$, and $Co_{1.5}MnV_{0.5}Al$ alloys with applied magnetic field at (a) 10 and (b) 300 K. Inset shows a magnified view of data points in the vicinity of the origin.

Figure 3.08 (a) shows the *M-T* curves measured from 300 K to 1000 K by applying 500 Oe external magnetic field. These curves show the second-order magnetic phase transition from the ferromagnetic state to the paramagnetic state in all the samples. The T_C values evaluated from the thermal derivative of magnetization (d*M*/d*T*) curves (*c.f.* inset of Figure

3.08 (a)) are 690 K for Co_2MnAl (for x = 0.0), 680 K for $Co_{1.75}MnV_{0.25}Al$ (for x = 0.25), and 533 K for $Co_{1.5}MnV_{0.5}Al$ (for x = 0.50), indicating a decrease T_C with increased substitution of V for Co in Co_2MnAl alloy. T_C of Co_2MnAl is in close agreement with the earlier reports [BALK2010, MARC2014, UMET2008].

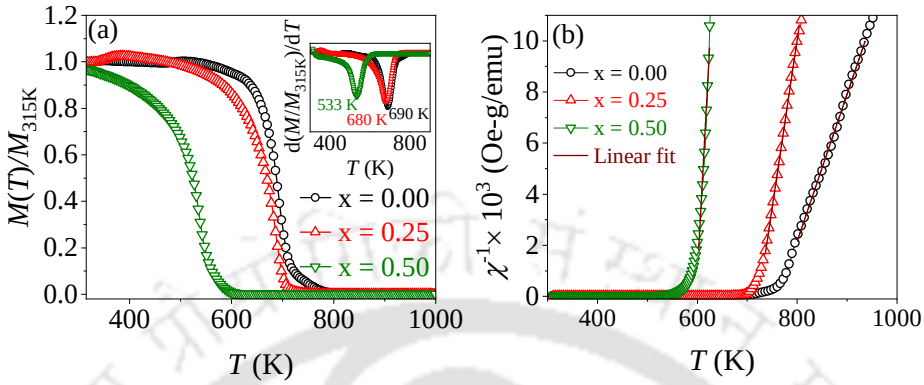

Figure 3.08. (a) *M-T* curves of $Co_{2-x}MnV_xAl$ alloys with x = 0.0, 0.25, and 0.50. Inset depicts d*M*/d*T* *vs* *T* plots close to the magnetic phase transition. (b) The inverse of magnetic susceptibility plotted against temperature for $Co_{2-x}MnV_xAl$ alloys with x = 0.0, 0.25, and 0.50.

Figure 3.08 (b) shows the high-temperature linear *M-T* data fitted to the Curie-Weiss law (Equation (2.18)). This fitting provides an estimate of the Curie constant, which can be used to evaluate p_c in the Rhodes-Wohlfarth ratio (p_c/p_s), as discussed in Section 2.2.3.1. The Rhodes-Wohlfarth ratio for Co_2MnAl, $Co_{1.75}MnV_{0.25}Al$, and $Co_{1.5}MnV_{0.5}Al$ is 1.11, 1.07, and 0.89, respectively. $p_c/p_s > 1$ for Co_2MnAl and $Co_{1.75}MnV_{0.25}Al$, which indicates that they are non half-metallic in nature. In contrast, $p_c/p_s < 1$ for $Co_{1.5}MnV_{0.5}Al$, which validates its half-metallic nature predicted in the first-principles calculations.

3.4. Summary

Systematic experimental and theoretical investigations have been conducted to explore the structural, magnetic, and electronic properties of bulk $Co_{2-x}MnV_xAl$ (x = 0.0, 0.25, and 0.5) Heusler alloys. The key findings from this study are summarized below.

- Structural investigation confirmed that Co_2MnAl and $Co_{1.75}MnV_{0.25}Al$ alloys exhibited the partially disordered *B*2-type structure, whereas $Co_{1.5}MnV_{0.5}Al$ alloy exhibited the ordered $L2_1$-type structure.
- First-principles calculations predicted a shift in the minority bandgap towards E_F, thereby raising P from ~69% to 100% as the composition was progressively changed from Co_2MnAl to $Co_{1.5}MnV_{0.5}Al$.

- *M-H* loop measured at 10 K and 300 K revealed a decrease in M_s and K_{eff} with an increase in V content at the expense of Co. Furthermore, *M-T* curves showed a change in T_C from 690 K to 533 K with the compositional change from Co_2MnAl to $Co_{1.5}MnV_{0.5}Al$.
- The Rhodes-Wohlfarth ratio exceeding unity for Co_2MnAl and $Co_{1.75}MnV_{0.25}Al$ alloys indicated itinerant ferromagnetic behavior. In contrast, the ratio of 0.89 obtained for $Co_{1.5}MnV_{0.5}Al$ alloy validated its half-metallic nature predicted by first-principles calculations.

In conclusion, this investigation into the impact of V substitution for Co in $Co_{2-x}MnV_xAl$ Heusler alloys demonstrates a viable approach to attain 100% *P* by tuning the minority spin bandgap at E_F, thereby escalating the potential applications of these alloys.

Chapter 4

Effect of Ti substitution for Co in Co_2FeAl alloy

4.1. Introduction

As mentioned in Chapter 1, some Heusler alloys fail to maintain their high *P* observed at liquid He temperature when raised to room temperature, which is usually reflected as a decrease in the ambient MR ratio [ISHI2006, LIST2013, MARU2007]. This thermal degradation in half-metallic character is due to the location of E_F very close to the valence or conduction band edges. One way to mitigate this problem is by choosing materials with a wide minority gap and ensuring the E_F is located near its center. In Chapter 3, it was demonstrated that *P* can be enhanced in Co_2MnAl alloy from ~69% to 100% by progressive substitution of V for Co up to 0.5 mol.%. However, it was noticed that improvement in *P* is accompanied by a decrease in T_C, which drops from 690 K to 533 K due to 0.5 mol.% V substitution. Additionally, having Mn as a constituent element, it may hinder its application as an electrode material in spin-valves with an Ag spacer layer, due to the tendency of Mn atoms to diffuse into the Ag spacer layer at elevated temperatures [SAKU2011]. To overcome these challenges in Co_2MnZ-based Heusler alloy, Co_2FeZ-based ternary Heusler alloys, such as Co_2FeAl, exhibiting high T_C can be explored [KUMA2017]. However, the E_F in Co_2FeAl also lies near the edge of the valence band [BALK2008], leading to reduced *P* and increased sensitivity to thermal disorder. An interesting report points out that in the quaternary alloy CoFeTiAl, E_F is positioned in the minority spin gap but exhibits semiconducting nature with zero magnetic moment [XION2014]. This report makes one speculate that partial substitution of Ti for Co in Co_2FeAl could suppress the minority density of states at the E_F, potentially enabling 100% *P*, while still preserving its ferromagnetic behavior. Although Co_2FeAl has been widely investigated, systematic studies on $Co_{2-x}FeTi_xAl$ alloys remain largely unexplored. This chapter presents investigations on the structural, magnetic, and electronic properties of $Co_{2-x}FeTi_xAl$ (x = 0.0, 0.25, 0.5, 0.75, and 1.0) Heusler alloys, aimed at addressing the gap in the literature as well as achieving a ferromagnetic half-metallic alloy.

4.2. Sample preparation and processing

Bulk $Co_{2-x}FeTi_xAl$ (x = 0.00, 0.25, 0.50, 0.75, and 1.00) alloy ingots were prepared by arc melting the constituent elements (>99.9% purity) under an argon atmosphere as described in

Chapter 2. Weighed amounts of the elements corresponding to each composition of $Co_{2-x}FeTi_xAl$ alloys were melted 5 to 6 times to ensure compositional homogeneity of the alloy ingots. After melting, the weight loss of the ingots was found to be <1% in all the ingots. The arc melted ingots were individually sealed in fused silica ampoules at ~10^{-3} Pa, heat treated at 1100 °C for 24 hours in a rising hearth furnace, and quenched in ice water.

4.3. Results and discussion

4.3.1. Composition analysis

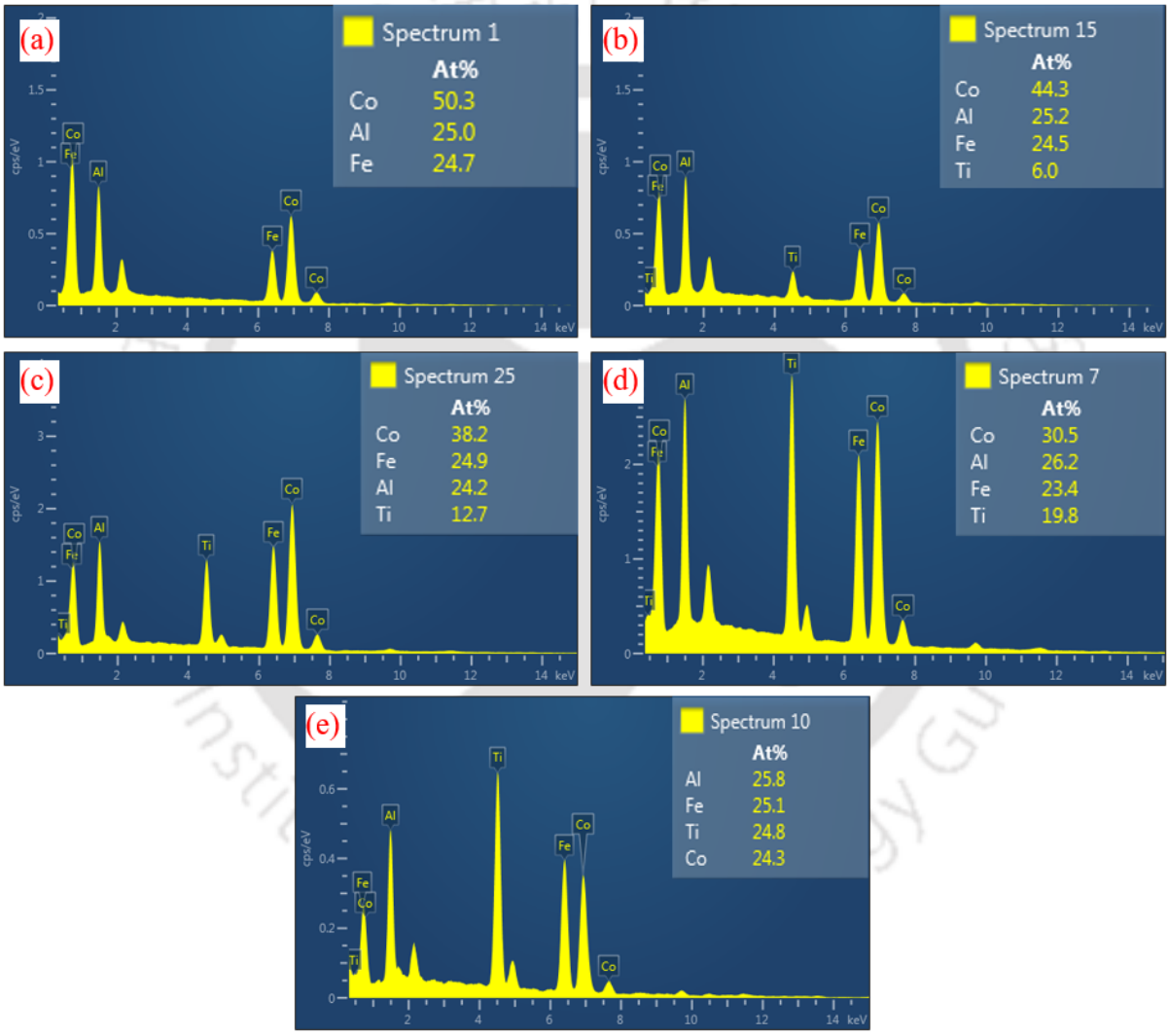

Figure 4.01. Typical reduced EDS spectrum of (a) Co_2FeAl, (b) $Co_{1.75}FeTi_{0.25}Al$, (c) $Co_{1.5}FeTi_{0.5}Al$, (d) $Co_{1.25}FeTi_{0.75}Al$, and (e) CoFeTiAl Heusler alloys.

The elemental composition of the heat-treated alloys was deduced using an EDS unit integrated with an FESEM, as outlined in Chapter 2. Representative EDS spectra of the heat-treated $Co_{2-x}FeTi_xAl$ Heusler alloys with (x = 0.00, 0.25, 0.50, 0.75, and 1.00) alloys are presented in

Figures 4.01 (a–e). This reduced spectrum displays characteristic peaks associated with the constituent elements Co, Fe, Ti, and Al. While processing the composition, the peaks from the C tape and Au coating were not considered by carefully eliminating the corresponding content using the built-in software. The average chemical composition of each sample was obtained from averaging 10 separate EDS spectra collected from different parts of the sample surface. The resulting overall composition of the $Co_{2-x}FeTi_xAl$ Heusler alloys with x = 0.00, 0.25, 0.50, 0.75, and 1.00 were found to be $Co_{50.6\pm1.4}Fe_{24.8\pm1.3}Al_{24.6\pm1.5}$, $Co_{44.5\pm1.2}Fe_{24.4\pm1.2}Ti_{5.8\pm0.3}Al_{25.3\pm1.4}$, $Co_{38.4\pm1.3}Fe_{24.6\pm1.3}Ti_{12.3\pm0.5}Al_{24.7\pm1.4}$, $Co_{30.8\pm1.2}Fe_{24.5\pm1.4}Ti_{18.4\pm1.4}Al_{26.3\pm1.3}$, and $Co_{24.6\pm1.2}Fe_{25.5\pm1.3}Ti_{24.5\pm1.1}Al_{25.4\pm1.4}$, respectively.

4.3.2. Structural analysis

Structural analyses of all the heat-treated $Co_{1-x}FeTi_xAl$ (x = 0.00, 0.25, 0.50, 0.75, and 1.00) alloys were performed as already described in Chapter 2. The XRD patterns of Co_2FeAl, $Co_{1.75}FeTi_{0.25}Al$, $Co_{1.5}FeTi_{0.5}Al$, $Co_{1.25}FeTi_{0.75}Al$, and CoFeTiAl alloys are shown in Figures 4.02 (a–e), respectively. To emphasize the presence of the (111) and (200) superlattice reflections, the 2θ region between 25° and 33° is enlarged and shown as an inset in each figure. The corresponding simulated XRD patterns obtained using $B2$ and $L2_1$-type unit cells are portrayed in Figures 4.02 (f–j) and 4.02 (k–o), respectively. To assess the degree of atomic disorder in the samples, the intensities of (111) and (200) reflections observed in the experimental XRD patterns were compared with those from simulated XRD patterns of $B2$ and $L2_1$-type structures. Figures 4.02 (a–b), showcasing the XRD patterns of Co_2FeAl and $Co_{1.75}FeTi_{0.25}Al$, clearly show the presence of the (200) reflection, whereas the (111) reflection is not detected in either composition. Thus, the XRD patterns of Co_2FeAl and $Co_{1.75}FeTi_{0.25}Al$ closely resemble the simulated patterns generated using $B2$-type unit cells, as seen in Figure 4.02 (f) and 4.02 (g). This confirms the presence of $B2$-type partial disorder in both alloys. On the other hand, Figures 4.02 (c, d, and e) displaying the XRD patterns of $Co_{1.5}FeTi_{0.5}Al$, $Co_{1.25}FeTi_{0.75}Al$, and CoFeTiAl alloys exhibit (111) and (200) reflections and closely resemble the XRD patterns simulated with $L2_1$-type unit cells (Figures 4.02 (m, n, and o)). This indicates the formation of a fully ordered structure in these three alloy compositions. The observed $B2$-type partial disorder in Co_2FeAl [HUSA2017] and the fully ordered structure in CoFeTiAl [BASI2011] are consistent with previous reports in the literature.

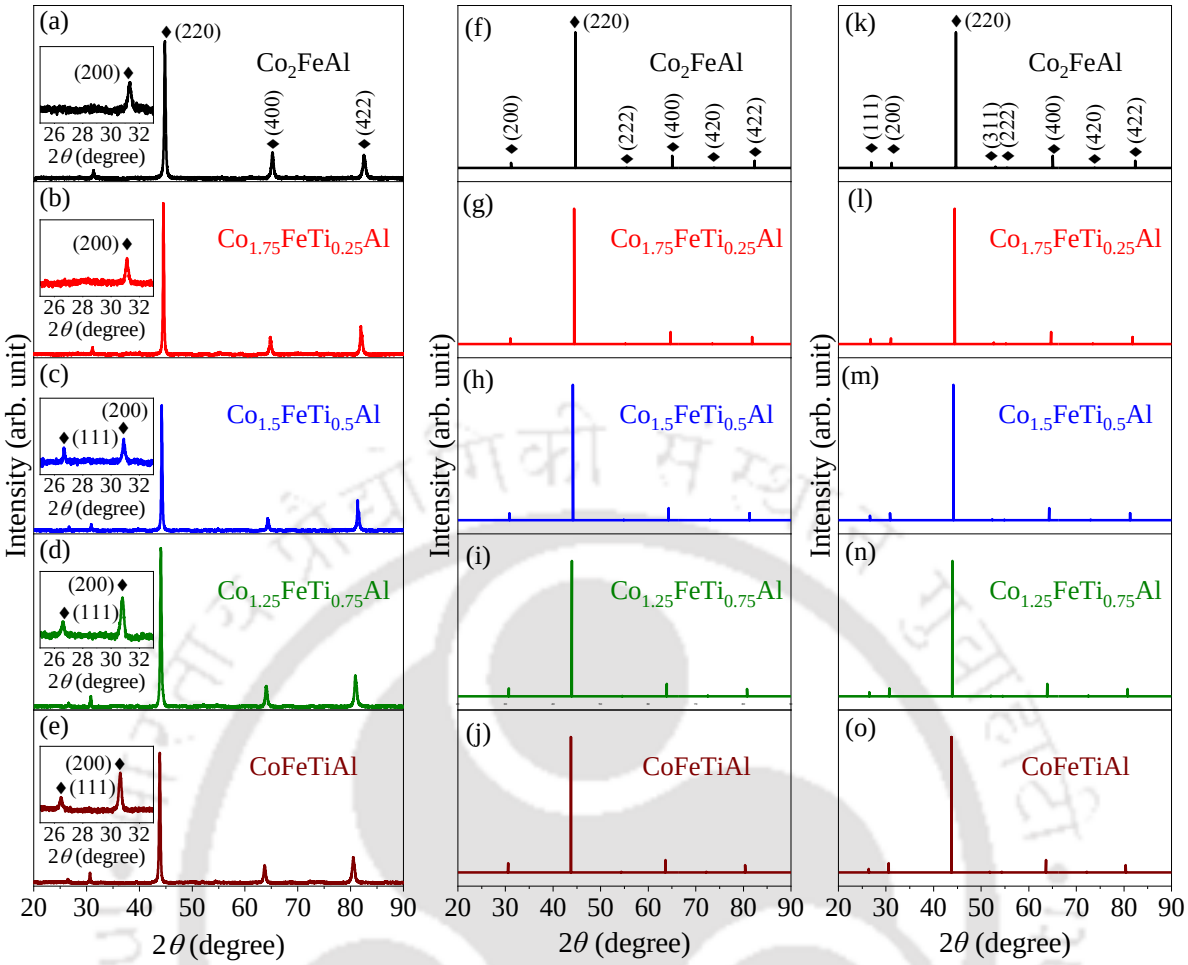

Figure 4.02. XRD patterns of heat-treated (a) Co_2FeAl, (b) $Co_{1.75}FeTi_{0.25}Al$, (c) $Co_{1.5}FeTi_{0.5}Al$, (d) $Co_{1.25}FeTi_{0.75}Al$, and (e) CoFeTiAl alloys. Insets show an enlarged view of data in a 2θ range of 25° to 33°. XRD patterns of (f) Co_2FeAl, (g) $Co_{1.75}FeTi_{0.25}Al$, (h) $Co_{1.5}FeTi_{0.5}Al$, (i) $Co_{1.25}FeTi_{0.75}Al$, and (j) CoFeTiAl alloys simulated using *B*2-type unit cell. (k–o) Corresponding XRD patterns simulated using $L2_1$-type unit cell.

As described in Section 1.2.1.1, in X_2YZ Heusler alloys with complete *B*2-type disordered structure, X atoms are located at the 4*a* (0.25, 0.25, 0.25) and 4*b* (0.75, 0.75, 0.75) Wyckoff positions, whereas the Y and Z atoms randomly occupy the 4*c* (0.50, 0.50, 0.50) and 4*d* (0, 0, 0) lattice sites in equal proportion. Accordingly, *B*2-type disordered Co_2FeAl alloy, Co atoms occupy the 4*a* (0.25, 0.25, 0.25) and 4*b* (0.75, 0.75, 0.75) Wyckoff positions, whereas Fe and Al atoms are equally distributed among the 4*c* (0.5, 0.5, 0.5) and 4*d* (0, 0, 0) positions, respectively. However, wshen 50 at.% Ti is substituted for Co in Co_2FeAl to form CoFeTiAl alloy, Fe atoms are displaced by Ti atoms to the vacated Co sites, resulting from the simultaneous decrease in Co concentration. As a result, the substituted Ti occupies the 4*c* (0.5, 0.5, 0.5) site, rather than the 4*d* (0, 0, 0) position, in order to preserve the high structural order, and form the rock-salt-type structure with Al atoms located at the 4*d* (0, 0, 0) sites [XION2014].

This change in the site occupancy is consistent with the Hume-Rothery rule of phase stability, which states that the larger the difference in electronegativity between two elements, the higher is the tendency to form compounds [TSAI2004]. Accordingly, it is anticipated that the substitution of Ti atoms will displace Fe atoms to the vacated Co sites in intermediate compositions of $Co_{2-x}FeTi_xAl$ (*i.e.*, for x = 0.25, 0.50, and 0.75) alloys.

To confirm the above speculation on the stable atomic configuration, energy minimization of $Co_{2-x}FeTi_xAl$ (with x = 0.25, 0.50, and 0.75) alloys was performed for different atomic configurations in a 32 atoms super unit cell. Since the most stable atomic configuration of a system corresponds to the one with the lowest total energy, it is a standard procedure to evaluate the total energy of all the possible atomic configurations and identify the one with the lowest energy [BISW2024]. At absolute zero temperature, the total energy of an atomic system corresponds to its free energy [VASP2025]. Therefore, the free energy is determined for different atomic configurations of $Co_{2-x}FeTi_xAl$ (x = 0.25, 0.50, and 0.75) alloys. The atomic sites of each element in 32 atoms super unit cells representing each of the different atomic configurations are listed in Tables 4.01, 4.02, and 4.03 for $Co_{1.75}FeTi_{0.25}Al$, $Co_{1.5}FeTi_{0.5}Al$, and $Co_{1.25}FeTi_{0.75}Al$, respectively, along with their corresponding free energy value. In the case of $Co_{1.75}FeTi_{0.25}Al$, atomic arrangements were configured by considering 100% *B*2-type partial disorder. On the other hand, for $Co_{1.5}FeTi_{0.5}Al$, and $Co_{1.25}FeTi_{0.75}Al$, an $L2_1$-type ordered structure was considered, based on the corresponding XRD results. According to Table 4.01, the atomic configuration of $Co_{1.75}FeTi_{0.25}Al$ super unit cell designated as Type 1, in which 1 Ti atom displace Fe atom from both 4*c* (0.5, 0.5, 0.5) and 4*d* (0, 0, 0) sites, resulting in a total of two Fe atoms to relocate to the vacated Co sites at 4*b* (0.75, 0.75, 0.75), has the lowest free energy. Notably, the free energy of the Type 2 configuration is very close to that of Type 1. Given the symmetrical nature of atomic site occupancies in the unit cell, Type 2 can be regarded as structurally equivalent to Type 1, making it an equally probable configuration despite its slightly elevated energy value.

In the case of $Co_{1.5}FeTi_{0.5}Al$ alloy, the most energetically favourable structure corresponds to the Type 1 configuration, wherein 4 Ti atoms occupy the 4c (0.5, 0.5, 0.5) positions by replacing 4 Fe atoms. The displaced Fe atoms subsequently shift to the unoccupied 4*b* (0.75, 0.75, 0.75) sites originally designated for Co, as detailed in Table 4.02. As seen in the case of $Co_{1.75}FeTi_{0.25}Al$ alloy, the Type 2 configuration demonstrates a free energy almost identical to the Type 1 configuration, owing to the symmetry in atomic site distributions in the unit cell. Hence, the structural symmetry between the two makes Type 2 as probable as Type 1.

Table 4.01. Different atomic configurations possible in the 32 atoms super unit cell of $Co_{1.75}FeTi_{0.25}Al$ alloy and their corresponding free energy.

Configuration	Wyckoff positions				Free Energy (eV)
	4*a* $\left(\frac{1}{4},\frac{1}{4},\frac{1}{4}\right)$	4*b* $\left(\frac{3}{4},\frac{3}{4},\frac{3}{4}\right)$	4*c* $\left(\frac{1}{2},\frac{1}{2},\frac{1}{2}\right)$	4*d* (0,0,0)	
Type 1	8Co	6Co, 2Fe	3Fe, 1Ti, 4Al	3Fe, 1Ti, 4Al	-221.199
Type 2	7Co, 1Fe	7Co, 1Fe	3Fe, 1Ti, 4Al	3Fe, 1Ti, 4Al	-221.105
Type 3	8Co	4Co, 2Fe, 2Ti	1Co, 3Fe, 4Al	1Co, 3Fe, 4Al	-217.851
Type 4	6Co, 1Fe, 1Ti	6Co, 1Fe, 1Ti	1Co, 3Fe, 4Al	1Co, 3Fe, 4Al	-217.782
Type 5	8Co	6Co, 2Ti	4Fe, 4Al	4Fe, 4Al	-218.805
Type 6	8Co	8Fe	3Co, 1Ti, 4Al	3Co, 1Ti, 4Al	-217.949
Type 7	4Co, 4Fe	4Co, 4Fe	3Co, 1Ti, 4Al	3Co, 1Ti, 4Al	-217.603

Table 4.02. Different atomic configurations possible in the 32 atoms super unit cell of $Co_{1.5}FeTi_{0.5}Al$ alloy and their corresponding free energy.

Configuration	Wyckoff positions				Free Energy (eV)
	4*a* $\left(\frac{1}{4},\frac{1}{4},\frac{1}{4}\right)$	4*b* $\left(\frac{3}{4},\frac{3}{4},\frac{3}{4}\right)$	4*c* $\left(\frac{1}{2},\frac{1}{2},\frac{1}{2}\right)$	4*d* (0,0,0)	
Type 1	8Co	4Co, 4Fe	4Fe, 4Ti	8Al	-225.40
Type 2	6Co, 2Fe	6Co, 2Fe	4Fe, 4Ti	8Al	-225.33
Type 3	8Co	4Co, 2Fe, 2Ti	6Fe, 2Ti	8Al	-221.76
Type 4	6Co, 1Fe, 1Ti	6Co, 1Fe, 1Ti	6Fe, 2Ti	8Al	-221.82
Type 5	8Co	4Co, 4Ti	8Fe	8Al	-219.98
Type 6	8Co	8Fe	4Co, 4Ti	8Al	-222.28
Type 7	4Co, 4Fe	4Co, 4Fe	4Co, 4Ti	8Al	-222.28

Following the trend observed in $Co_{1.75}FeTi_{0.25}Al$ and $Co_{1.5}FeTi_{0.5}Al$ alloys, the Type 1 configuration exhibits the lowest free energy for $Co_{1.25}FeTi_{0.75}Al$ composition also. In this atomic configuration, 6 Ti atoms replace 6 Fe atoms at the 4*c* (0.5, 0.5, 0.5) site, causing Fe atoms to relocate to the vacated Co sites at 4*b* (0.75, 0.75, 0.75) (see Table 4.03). Additionally, the Type 2 atomic configuration in $Co_{1.25}FeTi_{0.75}Al$ shows nearly identical free energy value to

that of the Type 1 configuration due to their structural symmetry. Hence, both configurations are equally stable and energetically favourable for this alloy too. These proposed stable atomic configurations of $Co_{1.75}FeTi_{0.25}Al$, $Co_{1.5}FeTi_{0.5}Al$, and $Co_{1.25}FeTi_{0.75}Al$ alloys are consistent with the findings reported in earlier studies on other Heusler alloys [SHAM2019, MAHA2022].

Table 4.03. Different atomic configurations possible in the 32 atoms super unit cell of $Co_{1.25}FeTi_{0.75}Al$ alloy and their corresponding free energy.

Configuration	Wyckoff positions				Free Energy
	4a $\left(\frac{1}{4},\frac{1}{4},\frac{1}{4}\right)$	*4b* $\left(\frac{3}{4},\frac{3}{4},\frac{3}{4}\right)$	*4c* $\left(\frac{1}{2},\frac{1}{2},\frac{1}{2}\right)$	*4d* (0,0,0)	(eV)
Type 1	8Co	2Co, 6Fe	2Fe, 6Ti	8Al	-228.751
Type 2	5Co, 3Fe	5Co, 3Fe	2Fe, 6Ti	8Al	-228.845
Type 3	8Co	2Co, 2Fe, 4Ti	6Fe, 2Ti	8Al	-221.900
Type 4	5Co, 1Fe, 2Ti	5Co, 1Fe, 2Ti	6Fe, 2Ti	8Al	-222.197
Type 5	8Co	2Co, 6Ti	8Fe	8Al	-220.568
Type 6	8Co	8Fe	2Co, 6Ti	8Al	-227.142
Type 7	4Co, 4Fe	4Co, 4Fe	2Co, 6Ti	8Al	-227.080

Rietveld refinement of the XRD patterns of heat-treated $Co_{2-x}FeTi_xAl$ alloys with x = 0.00, 0.25, 0.50, 0.75, and 1.00 was performed using the most stable atomic configuration. Figures 4.03 (a−e) depict the Rietveld refined XRD patterns of Co_2FeAl, $Co_{1.75}FeTi_{0.25}Al$, $Co_{1.5}FeTi_{0.5}Al$, $Co_{1.25}FeTi_{0.75}Al$, and CoFeTiAl alloys. Figures 4.03 (f–j) illustrate the atomic configurations used in the Rietveld refinement of Co_2FeAl and $Co_{1.75}FeTi_{0.25}Al$ alloys with *B*2-type partial disorder, whereas the Type 1 configuration was employed to refine the XRD data of $Co_{1.5}FeTi_{0.5}Al$, $Co_{1.25}FeTi_{0.75}Al$, and CoFeTiAl alloys. The lattice constant obtained from the refinement shows an increasing trend with Ti substitution, as shown in Table 4.04. This increase in lattice constant with Ti substitution is due to the larger atomic radius of Ti (176 pm) compared to Co (167 pm) and is in line with Vegard's law [DENT1991].

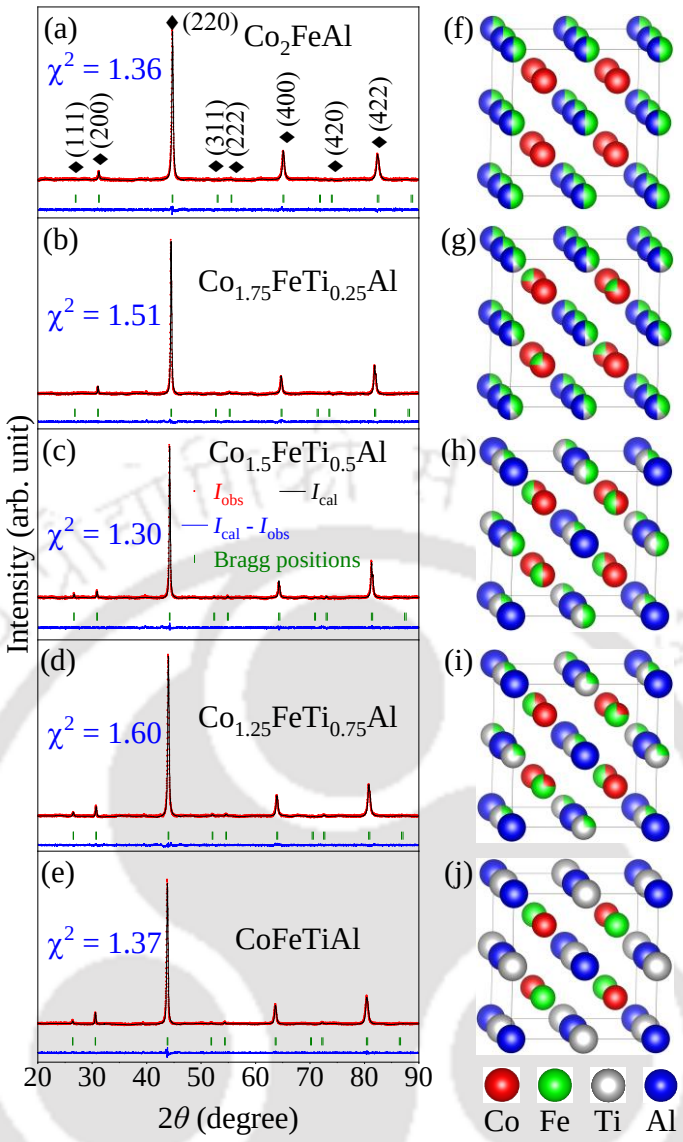

Figure 4.03. Rietveld refined XRD patterns of heat-treated (a) Co_2FeAl, (b) $Co_{1.75}FeTi_{0.25}Al$, (c) $Co_{1.5}FeTi_{0.5}Al$, (d) $Co_{1.25}FeTi_{0.75}Al$, and (e) CoFeTiAl alloys. *B*2-type unit cell corresponding to (f) Co_2FeAl, (g) $Co_{1.75}FeTi_{0.25}Al$ alloys, and unit cell with Type 1 atomic configuration corresponding to (h) $Co_{1.5}FeTi_{0.5}Al$, (i) $Co_{1.25}FeTi_{0.75}Al$, and (j) CoFeTiAl alloys used in the Rietveld refinement.

4.3.3. Density of electronic states and magnetic moment

The procedure followed for evaluating the electronic DOS of the alloys is detailed in Section 2.2.5. To calculate the spin-resolved total DOS in $Co_{2-x}FeTi_xAl$ Heusler alloys, a larger unit cell of 32 atoms was utilized to enable incorporation of small changes in the elemental composition with specific type of ordering.

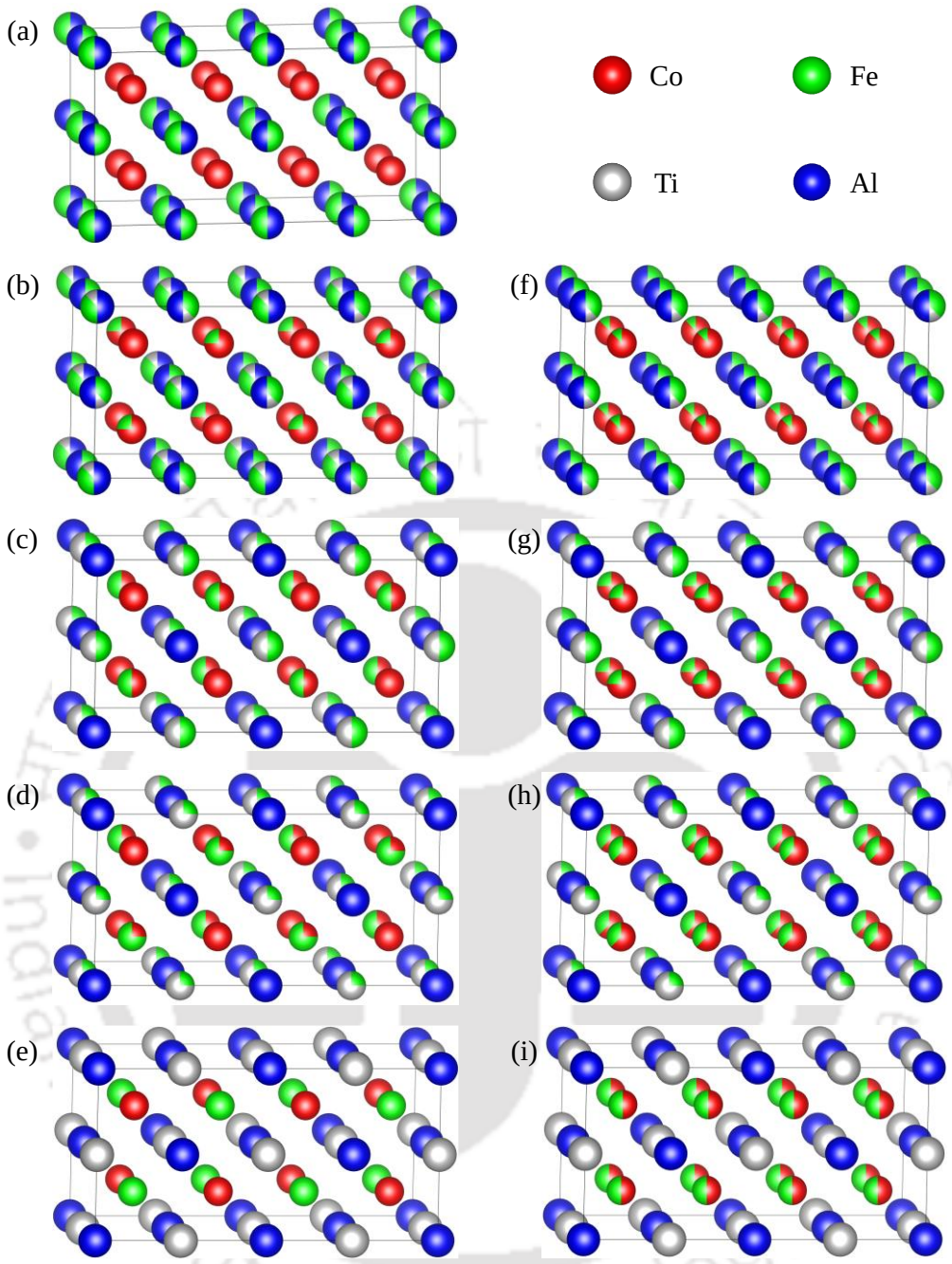

Figure 4.04. 32 atoms super unit cell of (a) Co_2FeAl alloy with *B*2-type disorder. Type 1 atomic configurations of (b) $Co_{1.75}FeTi_{0.25}Al$, (c) $Co_{1.5}FeTi_{0.5}Al$, (d) $Co_{1.25}FeTi_{0.75}Al$, and (e) CoFeTiAl alloys. The corresponding Type 2 atomic configurations of (f) $Co_{1.75}FeTi_{0.25}Al$, (g) $Co_{1.5}FeTi_{0.5}Al$, (h) $Co_{1.25}FeTi_{0.75}Al$, and (i) CoFeTiAl alloys.

The calculations were performed by considering structural details, including the lattice constant and atomic ordering deduced from the XRD data analysis, along with the lowest-energy atomic configuration (Type 1). A comparison with the structurally similar Type 2 configuration will be made in subsequent discussions. For better visualization, the 32 atoms super unit cell of Co_2FeAl and $Co_{1.75}FeTi_{0.25}Al$ exhibiting *B*2-type disorder, and $Co_{1.5}FeTi_{0.5}Al$,

$Co_{1.25}FeTi_{0.75}Al$, and CoFeTiAl alloys with the Type 1 atomic configuration are depicted in Figures 4.04 (a−e), respectively. The Type 2 atomic configurations of $Co_{1.75}FeTi_{0.25}Al$, $Co_{1.5}FeTi_{0.5}Al$, $Co_{1.25}FeTi_{0.75}Al$, and CoFeTiAl alloys are shown in Figures 4.04 (f−i), respectively. In the case of Co_2FeAl, the absence of Ti eliminates the possibility of different atomic configurations. Hence, two different atomic configurations for Co_2FeAl are not shown in the Figure 4.04. Atomic site preferences of 32 atoms super unit cell with Type 1 atomic configuration, along with the equivalent atomic occupations obtained from Rietveld refinement of each composition, with the corresponding atomic ordering and the lattice constant used in the calculations, are listed in Table 4.04.

Table 4.04. Type of structural order, atomic arrangements, and lattice constant (*a*) of all $Co_{2-x}FeTi_xAl$ Heusler alloys. SC and RR refer to the Wyckoff positions in the designed 32 atoms super unit cell and the results obtained from Rietveld refinement, respectively.

Heusler alloy composition	Type of order	Wyckoff positions					Lattice constant (Å)
		In SC/RR	4*a* $(\frac{1}{4}, \frac{1}{4}, \frac{1}{4})$	4*b* $(\frac{3}{4}, \frac{3}{4}, \frac{3}{4})$	4*c* $(\frac{1}{2}, \frac{1}{2}, \frac{1}{2})$	4*d* (0, 0, 0)	
Co_2FeAl	*B*2	SC	8Co	8Co	4Fe, 4Al	4Fe, 4Al	5.731 ± 0.004
		RR	0.97 Co	1.02 Co	0.5 Fe, 0.49 Al	0.49 Fe, 0.53 Al	
$Co_{1.75}FeTi_{0.25}Al$	*B*2	SC	8Co	6Co, 2Fe	3Fe, 1Ti, 4Al	3Fe, 1Ti, 4Al	5.761 ± 0.005
		RR	1.02 Co	0.74 Co 0.24 Fe	0.37 Fe 0.12 Ti 0.50 Al	0.38 Fe 0.12 Ti 0.51 Al	
$Co_{1.5}FeTi_{0.5}Al$	$L2_1$	SC	8Co	4Co, 4Fe	4Fe, 4Ti	8Al	5.793 ± 0.003
		RR	1.01 Co	0.49 Co 0.53 Fe	0.48 Fe 0.49 Ti	1.00 Al	
$Co_{1.75}FeTi_{0.75}Al$	$L2_1$	SC	8Co	2Co, 6Fe	2Fe, 6Ti	8Al	5.824 ± 0.002
		RR	1.00 Co	0.25 Co 0.76 Fe	0.24 Fe 0.73 Ti	1.02 Al	
CoFeTiAl	$L2_1$	SC	8Co	8Fe	8Ti	8Al	5.848 ± 0.014
		RR	0.98 Co	1.01 Fe	1.00 Ti	1.01 Al	

The transition from 50 at.% Co in Co_2FeAl (x = 0.00) to 25 at.% Co in CoFeTiAl (x = 1.00) was achieved by incrementally increasing the Ti content at the cost of Co in steps of 6.25 at.%. The calculated spin-resolved total DOS of $Co_{2-x}FeTi_xAl$ alloys are shown in Figures 4.05(a−e), with insets in each figure providing magnified views of the DOS near E_F for better visualization. Figures 4.05 (f–j) illustrate the respective EDOS, with the insets highlighting the magnified view of element-specific states in the vicinity of E_F. Figure 4.05 (a) shows the presence of a small amount of minority DOS (0.208 states/eV) in Co_2FeAl at E_F. Analysis of the EDOS of Co_2FeAl (*c.f.* Figure 4.05 (f)) indicates that at E_F, the minority spin states are predominantly contributed by Co atoms (~61.8%), with Fe and Al atoms contributing ~37.5% and ~0.7%, respectively. The presence of minority DOS results in a reduced P of ~54%, and a magnetic moment of 5.15 μ_B/f.u.. In an attempt to improve P, 6.25 at.% Ti was incorporated for Co in Co_2FeAl to form the $Co_{1.75}FeTi_{0.25}Al$ alloy, and the corresponding total DOS plot is shown in Figure 4.05 (b). The inset of Figure 4.05 (b) reveals the presence of ~0.207 states/eV minority DOS at E_F, indicating a very small reduction in the minority DOS at E_F upon Ti substitution. From the EDOS data of $Co_{1.75}FeTi_{0.25}Al$ (*c.f.* Figure 4.05 (g)), it is evident that the minority DOS at E_F comprises ~63.4% contribution from Co, ~32.6% from Fe, ~3.4% from Ti, and ~0.6% from Al, indicating a small change in relative contributions from constituent elements. The presence of these minority states at E_F lowers P to ~67%, with a corresponding reduced M_t of 3.92 μ_B/f.u..

On further increase of Ti concentration to 12.5 at.%, the resulting $Co_{1.5}FeTi_{0.5}Al$ Heusler alloy displays a clear half-metallic gap at E_F, demonstrating 100% P as shown in Figure 4.05 (c). The inset highlights a minority spin bandgap of ~ 0.10 eV with the valence band edge shifting towards the left side of E_F and positioning at ~0.08 eV below E_F. The corresponding EDOS shown in Figure 4.05 (h) confirms that there are no states corresponding to any of the elements at E_F, thereby resulting in 100% P. This significant increase in P can be correlated with the transition of the $B2$-type partially disordered alloy to a fully ordered $L2_1$-type structure with a change in composition, as already revealed in the XRD patterns. With a decrease in Co concentration, the magnetic moment of $Co_{1.5}FeTi_{0.5}Al$ alloy further decreases to 2.56 μ_B/f.u.. As the Ti concentration is increased to 18.75 at.% in $Co_{1.25}FeTi_{0.75}Al$, the half-metallic gap remains intact, as shown in Figure 4.05 (d). From the inset of this figure, it is evident that E_F is positioned at ~0.08 eV above the valence band edge, and the half-metallic gap has a width of ~0.21 eV. It is also to be noted that $L2_1$-type ordering is preserved in this alloy. The associated EDOS of $Co_{1.25}FeTi_{0.75}Al$, shown in Figure 4.05 (i), confirms that there

are no states corresponding to any of the elements at E_F, thereby resulting in 100% *P*. However, the magnetic moment continues to decrease, reaching a low value of 1.29 μ_B/f.u..

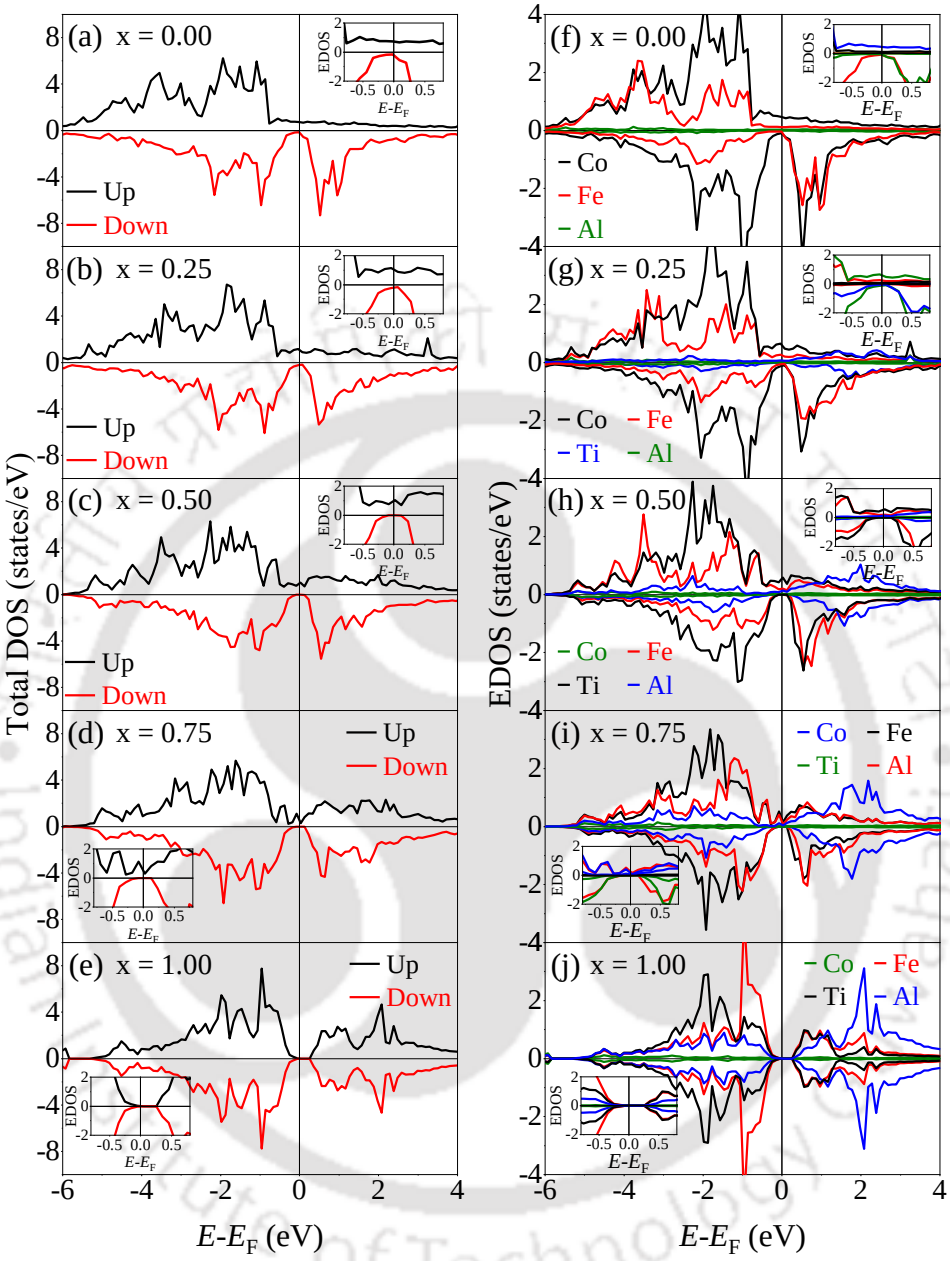

Figure 4.05. Spin-resolved total DOS at E_F computed for $Co_{2-x}FeTi_xAl$ alloys with (a) x = 0.00, (b) 0.25, (c) 0.50, (d) 0.75, and (e) 1.00. Corresponding EDOS of the alloys with (f) x = 0.00, (g) 0.25, (h) 0.5, (i) 0.75, and (j) 1.00. Insets in all figures show an enlarged view of DOS near E_F.

Finally, with 25 at.% of Ti substitution, *i.e.*, in CoFeTiAl, the absence of both majority and minority DOS results in a semiconducting nature with zero *P*, as depicted in Figure 4.05 (e). From the inset of the figure, it is evident that the energy gap of 0.203 eV between the valence and conduction bands in both the majority and minority spin bands indicates the

semiconducting nature of the CoFeTiAl alloy, which is consistent with an earlier report [XION2014]. The corresponding EDOS is shown in Figure 4.05 (j), which confirms that there are no states corresponding to any of the elements for both minority and majority spins at E_F. Magnetic moment continues to decrease with the Ti substitution and ultimately reaches zero μ_B/f.u. in CoFeTiAl.

The effect of Ti substitution for Co on P and M_t of $Co_{2-x}FeTi_xAl$ alloys with structurally equivalent Type 1 and Type 2 configurations can be compared. Figures 4.06 (a−c) illustrate the spin-resolved total DOS at E_F for Co_2FeAl, $Co_{1.5}FeTi_{0.5}Al$, and CoFeTiAl alloys, respectively. In these figures, the total DOS associated with Type 1 and Type 2 configurations are represented by black and red lines, respectively. Since Co_2FeAl does not contain any Ti atoms, both Type 1 and Type 2 configurations are structurally indistinguishable, leading to identical spin-polarized total DOS profiles (*c.f.* Figure 4.06 (a)) and magnetic moments. However, in Ti-substituted quaternary alloys, slight differences are observed in the total DOS between the two configurations. Table 4.05 presents the calculated P and M_t of $Co_{1.75}FeTi_{0.25}Al$, $Co_{1.5}FeTi_{0.5}Al$, $Co_{1.25}FeTi_{0.75}Al$, and CoFeTiAl alloys with Type 1 and Type 2 atomic configurations. Despite their structural similarity, minor discrepancies in the P values are evident, which may stem from the computational limitations.

Table 4.05. P and M_t of $Co_{1.75}FeTi_{0.25}Al$, $Co_{1.5}FeTi_{0.5}Al$, $Co_{1.25}FeTi_{0.75}Al$, and CoFeTiAl alloys for Type 1 and Type 2 configurations.

Heusler alloy composition	Configuration	P (%)	M_t (μ_B/f.u.)
$Co_{1.75}FeTi_{0.25}Al$	Type 1	67	3.92
	Type 2	57	3.92
$Co_{1.5}FeTi_{0.5}Al$	Type 1	100	2.56
	Type 2	100	2.56
$Co_{1.25}FeTi_{0.75}Al$	Type 1	100	1.29
	Type 2	100	1.29
CoFeTiAl	Type 1	0	0.00
	Type 2	0	0.00

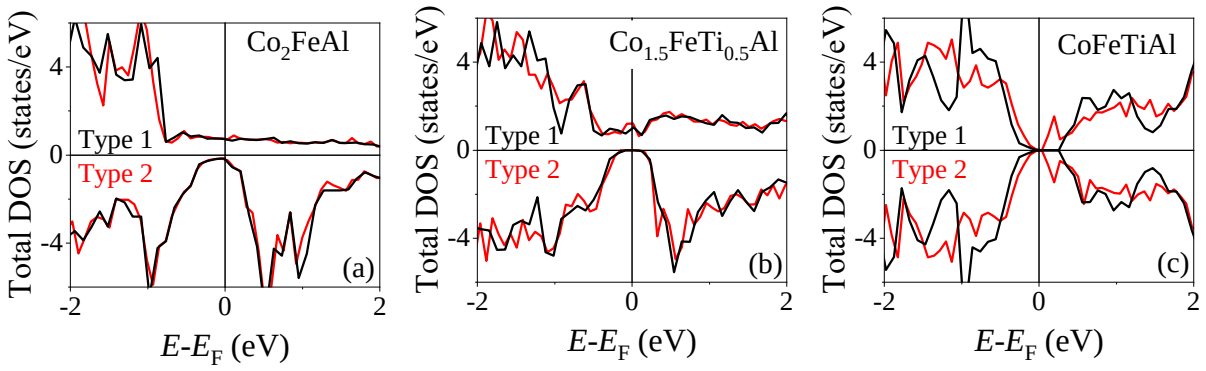

Figure 4.06. Comparison of spin-resolved total DOS at E_F of Type 1 (black line) and Type 2 (red line) atomic configurations of (a) Co_2FeAl, (b) $Co_{1.5}FeTi_{0.5}Al$, and (c) CoFeTiAl alloys.

4.3.4. Magnetic and half-metallic properties

M-H loops of heat-treated $Co_{2-x}FeTi_xAl$ alloys with x = 0.00, 0.25, 0.50, 0.75, and 1.00 recorded at 10 K and 300 K are depicted in Figure 4.07 (a and b), respectively. The changes in the experimental magnetic moment measured at 10 K and 300 K for different compositions, along with the theoretically calculated spin magnetic moments, are listed in Table 4.06. The experimentally observed reduction in the magnetic moment with increasing Ti substitution is consistent with the theoretical predictions. A relatively small reduction in the magnetic moment with increasing temperature from 10 K to 300 K is observed in Co_2FeAl, $Co_{1.75}FeTi_{0.25}Al$, and $Co_{1.5}FeTi_{0.5}Al$, as compared to the pronounced decrease in $Co_{1.25}FeTi_{0.75}Al$. This significant reduction of magnetic moment in $Co_{1.25}FeTi_{0.75}Al$ at room temperature could be attributed to its relatively low T_C, which makes it more susceptible to thermal demagnetization.

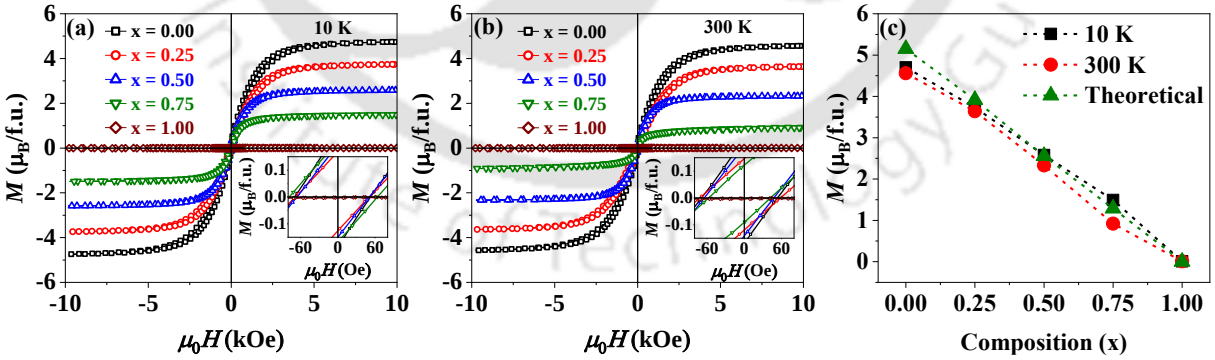

Figure 4.07. Variation in magnetization of $Co_{2-x}FeTi_xAl$ alloys with x = 0.00, 0.25, 0.50, 0.75, and 1.00 as a function of applied magnetic field recorded at (a) 10 K, and (b) 300 K. (c) Variation of M_s at 10 K and 300 K, along with the theoretically calculated spin magnetic moment as a function of Ti concentration.

Table 4.06. M_s (at 10 kOe) recorded at 10 K and 300 K, along with the theoretical estimate of $Co_{2-x}FeTi_xAl$ (x = 0.00, 0.25, 0.50, 0.75, and 1.00) Heusler alloys.

Composition	Experimental magnetic moment (μ_B/f.u.)		Spin magnetic moment (μ_B/f.u.)
	10 K	300 K	
Co_2FeAl	4.70 ± 0.04	4.56 ± 0.04	5.15
$Co_{1.75}FeTi_{0.25}Al$	3.73 ± 0.04	3.64 ± 0.04	3.92
$Co_{1.5}FeTi_{0.5}Al$	2.58 ± 0.03	2.33 ± 0.03	2.56
$Co_{1.25}FeTi_{0.75}Al$	1.49 ± 0.03	0.92 ± 0.03	1.29
CoFeTiAl	0.01 ± 0.01	0.01 ± 0.01	0

All the ferromagnetic samples exhibit soft ferromagnetic behavior, as indicated by the low coercivity values (~60 Oe) displayed in the insets of Figure 4.07 (a and b). Figure 4.07 (c) shows the variation in experimentally determined M_s at 10 kOe measured at 10 K and 300 K, along with the theoretically calculated spin magnetic moment as a function of Ti concentration. In addition to evaluating M_s and H_c, K_{eff} was evaluated from the initial magnetization data by applying the law of approach to saturation, as outlined earlier in Section 2.2.3.1. The evaluated K_{eff} of $Co_{2-x}FeTi_xAl$ Heusler alloys with x = 0.00, 0.25, 0.50, and 0.75 at 300 K are 4.29×10^6, 2.97×10^6, 1.37×10^6, and 0.93×10^6 erg/cc, respectively. The corresponding K_{eff} values measured at 10 K for x = 0.00, 0.25, 0.50, and 0.75 are 4.3×10^6, 3.12×10^6, 1.58×10^6, and 0.94×10^6 erg/cc, respectively. The increase in K_{eff} observed at low temperature is consistent with reports in the literature [PATH2022]. Additionally, K_{eff} decreases as the Ti content increases from 0 at.% to 18.75 at.% (x = 0.00 to x = 0.75). This decrease in K_{eff} is due to the corresponding reduction in M_s with increased Ti substitution for Co.

M-T curves were recorded in the temperature range of 300 K - 1200 K under an external magnetic field of 500 Oe to evaluate the T_C of $Co_{2-x}FeTi_xAl$ alloys. The *M-T* curves are shown in Figure 4.08 (a). The complete transition from the ferromagnetic to the paramagnetic phase in the Co_2FeAl sample was not observed up to 1200 K [AHMA2021], indicating that the T_C of this composition is above our measurement limit of 1200 K. T_C of $Co_{1.75}FeTi_{0.25}Al$ (with x = 0.25), $Co_{1.5}FeTi_{0.5}Al$ (with x = 0.50), and $Co_{1.25}FeTi_{0.75}Al$ (with x = 0.75) are 1030 K, 731 K, and 351 K, respectively. T_C was evaluated from the temperature derivative curves of magnetization depicted as an inset in Figure 4.08 (a). Temperature-dependent magnetization data can also be used to assess the half-metallic nature of the samples through the estimation of the Rhodes-Wohlfarth ratio (p_c/p_s) [SHAM2019].

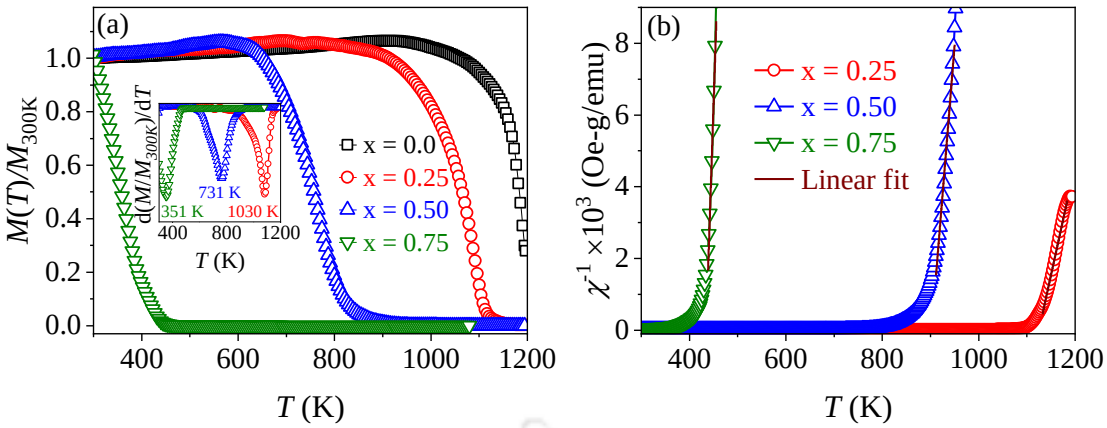

Figure 4.08. (a) *M*-*T* curves of $Co_{2-x}FeTi_xAl$ (x = 0.0, 0.25, 0.5, and 0.75) alloys. The inset shows the first derivative of magnetization with respect to temperature near T_C for alloys with x = 0.25, 0.5, and 0.75. (b) χ^{-1} *versus* temperature plots of alloys with x = 0.25, 0.5, and 0.75.

Using the evaluated value of p_c along with p_s, the Rhodes-Wohlfarth ratio (p_c/p_s) was determined for $Co_{1.75}FeTi_{0.25}Al$ (with x = 0.25), $Co_{1.5}FeTi_{0.5}Al$ (with x = 0.50), and $Co_{1.25}FeTi_{0.75}Al$ (with x = 0.75) alloys to be 1.12, 0.86, and 0.80, respectively. $p_c/p_s < 1$ for $Co_{1.5}FeTi_{0.5}Al$, and $Co_{1.25}FeTi_{0.75}Al$ alloys indicates their half-metallic nature. On the other hand, $p_c/p_s > 1$ for $Co_{1.75}FeTi_{0.25}Al$ alloy shows that it is not half-metallic. Thus, the Rhodes-Wohlfarth ratio estimated for the alloys validates the theoretical prediction on the half-metallic character of the three alloys. Since the evaluation of p_c requires χ^{-1} *versus* T data for $T > T_C$, p_c/p_s could not be evaluated for Co_2FeAl Heusler alloy as its T_C was beyond the measurement range of our instrument.

4.4. Summary

Systematic experimental and theoretical investigations have been conducted to explore the structural, magnetic, and electronic properties of bulk $Co_{2-x}FeTi_xAl$ (x = 0.00, 0.25, 0.5, 0.75, and 1.00) Heusler alloys. The key findings from this study are summarized below.

- Structural analysis showed that Co_2FeAl and $Co_{1.75}FeTi_{0.25}Al$ alloys exhibit the partially disordered *B*2-type structure, whereas, $Co_{1.5}FeTi_{0.5}Al$, $Co_{1.25}FeTi_{0.75}Al$, and CoFeTiAl alloys exhibited the ordered $L2_1$-type structure.
- Rietveld refinement of the XRD data revealed a gradual increase in lattice constant from 5.731±0.004 Å in Co_2FeAl to 5.848±0.001 Å in CoFeTiAl, which can be attributed to the larger atomic radius of Ti compared to Co.
- First-principles calculations predicted a shift in the minority bandgap towards E_F, thereby increasing P from ~54% in Co_2FeAl to 100% in $Co_{1.5}FeTi_{0.5}Al$ and $Co_{1.25}FeTi_{0.75}Al$,

indicating an increase in half-metallic character when Ti is progressively substituted for Co.

- M_s and K_{eff} decreased with an increase in Ti content at the expense of Co in $Co_{2-x}FeTi_xAl$ alloys. Furthermore, T_C decreases from >1200 K to 351 K as the alloy composition is changed from Co_2FeAl to $Co_{1.25}FeTi_{0.75}Al$.
- The Rhodes-Wohlfarth ratio exceeding unity for $Co_{1.75}FeTi_{0.25}Al$ alloy indicated itinerant ferromagnetic behavior. In contrast, the ratio being lower than unity, *i.e.*, 0.86 for $Co_{1.5}FeTi_{0.5}Al$, and 0.80 for $Co_{1.25}FeTi_{0.75}Al$ alloys, validated their half-metallic nature predicted by first-principles calculations.

In conclusion, this investigation on the impact of Ti substitution for Co in $Co_{2-x}FeTi_xAl$ Heusler alloys demonstrated a viable approach to attain 100% *P* by tuning the minority spin bandgap about E_F and achieve ferromagnetic half-metals in this quaternary alloy system.

Chapter 5

Effect of atomic disorder on off-stoichiometric $Co_2FeGa_{0.5}Ge_{0.5}$ alloy films

5.1. Introduction

As discussed in Chapter 1, materials with low damping constant (α) are essential for the development of energy-efficient spintronic devices [FANY2024]. Since the intrinsic contribution to the α is directly related to the total DOS at E_F [KUBO2009, MIZU2009, SHAW2018], half-metallic materials with only one type of electronic spin DOS at E_F are expected possess a smaller number of electronic states at E_F, leading to a low α. Additionally, half-metallic materials are advantageous for realizing a larger MR ratio. In this regard, extensive studies on the potential of half-metallic character for spintronic applications have been carried out on various Heusler alloys, particularly on stoichiometric $Co_2FeGa_{0.5}Ge_{0.5}$ (CFGG), due to its high P of 75%, low α of ~0.008, and high T_C of 1080 K [VARA2012]. However, in 2019, Goto *et al*. [GOTO2020] reported that Co-Fe type disorder in stoichiometric CFGG results in minority spin states at E_F, thereby decreasing its spin polarization. To address this, Chen *et al*. [CHEN2022] proposed that the observed Co-Fe disorder in stoichiometric CFGG could be suppressed in Co-deficient and Fe-rich off-stoichiometric CFGG compositions, thereby reducing the minority DOS at E_F. They also demonstrated this hypothesis with AMR studies. Based on these findings, α is expected to be lower in Co-deficient and Fe-rich off-stoichiometric CFGG compositions. However, only the bulk α value of stoichiometric CFGG is available in the literature [VARA2012], leading to a demand for detailed studies on α in off-stoichiometric CFGG thin films. In this chapter, a detailed study on the variation of α with the half-metallicity, associated with the change in atomic ordering in Co-deficient and Fe-rich off-stoichiometric CFGG Heusler alloys, is presented.

5.2. Thin film deposition, processing, and basic characterizations

Off-stoichiometric CFGG epitaxial thin films were deposited on single-crystal MgO (100) substrates using a high (>99.9%) purity alloy target of composition $Co_{1.86}Fe_{0.96}Ga_{0.55}Ge_{0.63}$. The deposition was carried out at room temperature using an ultra-high vacuum RF magnetron sputtering system with a deposition rate of ~1.2 nm/min. Prior to the deposition, the process of substrate cleaning and the procedure followed in the film deposition are described in detail in

Section 2.1.2. During the deposition, a target-to-substrate distance of 100 mm was maintained. The as-deposited thin films were annealed *in situ* in the vacuum chamber at 400, 500, and 600 ℃ for 30 minutes each to improve the atomic ordering. A 2 nm aluminium (Al) capping layer was deposited on the annealed films after cooling down to ambient temperature. All the CFGG thin films were deposited under the same sputtering conditions. The overall composition estimated by X-ray fluorescence spectroscopy was in the range of $Co_{1.77\pm0.03}Fe_{1.23\pm0.05}Ga_{0.56\pm0.01}Ge_{0.44\pm0.01}$, indicating the small composition variation among the samples. The sample thickness and surface roughness of the films were determined by X-ray reflectivity (XRR) measurements. Figure 5.01 shows the XRR patterns of as-deposited, 400, 500, and 600 ℃ annealed samples. From the fitting to the XRR data, the average thickness and roughness of the samples were found to be ~24±1 nm and ~0.7 nm, respectively.

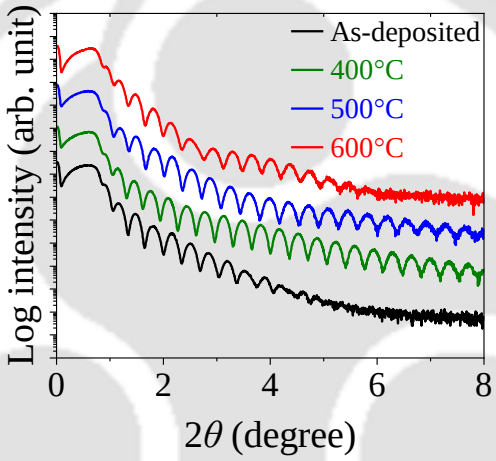

Figure 5.01. XRR data of as-deposited and annealed $Co_{1.77}Fe_{1.23}Ga_{0.56}Ge_{0.44}$ thin films deposited on MgO (100) substrate having Al capping layer.

5.3. Results and discussion

5.3.1. Crystal structure

Figures 5.02 (a) and 5.02 (b) show the out-of-plane (χ = 0°) and <111>-direction (χ = 54.7°) 2θ-ω XRD patterns of the as-deposited and annealed samples, respectively. The presence of the (200) and (400) reflections in the out-of-plane XRD patterns indicates epitaxial growth along the [100] direction in all the samples. The as-deposited and 400 ℃-annealed films exhibit *B*2-type partially disordered structure as evidenced by the presence of (200) and the absence of (111) superlattice reflections. However, the films annealed at T_{an} = 500 ℃ reveal $L2_1$-ordered structure as evidenced by the appearance of (111) superlattice reflection. The degree of *B*2 (S_{B2}) and $L2_1$ (S_{L2_1}) ordering was evaluated using Equations (1.02) and (1.03), respectively. The variation of S_{B2} and S_{L2_1} with change in annealing temperature (T_{an}) is shown in Figure 5.02 (c).

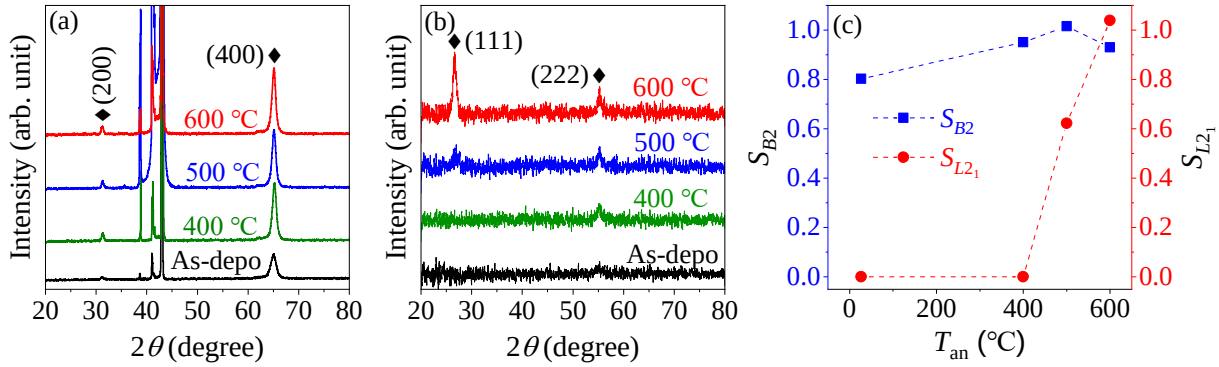

Figure 5.02. XRD patterns of 2θ-ω scans of as-deposited and annealed films at tilt angles (a) χ = 0° and (b) χ = 54.7°. (c) Variation of S_{B2} and S_{L2_1} of the films with annealing temperature T_{an}.

Since the surface roughness is small (~0.7 nm), its influence on the experimentally observed XRD peak intensity is assumed to be negligible while doing the analysis of ordering parameters. A high S_{B2} of ~0.8 already obtained in the as-deposited film increases slightly upon increasing T_{an}. On the other hand, S_{L2_1}, which appears after annealing at T_{an} = 500 °C, increases close to unity in films annealed at T_{an} = 600 °C. It may be noted that the presence of Co-Fe disorder is difficult to identify from standard XRD data because of the close atomic form factors (f_{atom}) of Co and Fe. XRD using high intensity and resolution X-rays generated in synchrotrons can help in detecting disorder between the elements with close f_{atom} through the change in anomalous dispersion term of atomic form factor at the absorption edges of the constituent elements. This method is called anomalous XRD. A previous study of anomalous XRD on CFGG reported that substantial Co-Fe disorder existed in the as-deposited sample, and the amount of disorder decreased with increasing T_{an} up to 500 °C [GOTO2020]. Based on this report, one can presume that Co-Fe disorder exists in films annealed at $T_{an} \leq$ 400 °C. Moreover, it can be presumed from Chen *et al*. [CHEN2022] that the $Co_{1.77}Fe_{1.23}Ga_{0.56}Ge_{0.44}$ thin film annealed at $T_{an} \geq$ 500 °C is free of Co-Fe disorder.

5.3.2. First-principles calculations

To illustrate the potential advantages of off-stoichiometric $Co_{1.77}Fe_{1.23}Ga_{0.56}Ge_{0.44}$ over stoichiometric CFGG as a half-metallic material, its electronic properties were evaluated and compared with those of stoichiometric CFGG. The details of the procedure followed in the evaluation of electronic properties are mentioned in Section 2.2.5. Figure 5.03 (a and b) shows the unit cell used for stoichiometric and off-stoichiometric CFGG, respectively. In the stoichiometric CFGG with $L2_1$ structure, the unit cell consists of four face-centered cubic sublattices with four atomic positions (refer to the Section 1.2.1.1.): two Co atoms at 4*a* (0.25,

0.25, 0.25) and 4*b* (0.75, 0.75, 0.75), one Fe atom at 4*c* (0.5, 0.5, 0.5), and Ga and Ge atoms in a 50:50 ratio at 4*d* (0, 0, 0). On the other hand, for the off-stoichiometric $Co_{1.77}Fe_{1.23}Ga_{0.56}Ge_{0.44}$ alloy, the atomic site occupancies were modified as follows: Co and Fe occupied the (0.25, 0.25, 0.25) and (0.75, 0.75, 0.75) sites in an 88.6%:11.4% ratio, Fe occupied the (0.5, 0.5, 0.5) site, and Ga and Ge occupied the (0, 0, 0) site in a 55.6%:44.4% ratio.

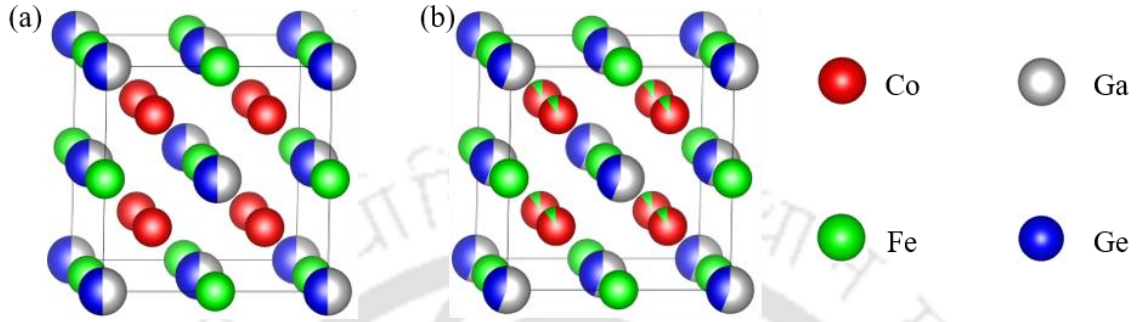

Figure 5.03. Unit cell of (a) stoichiometric $Co_2FeGa_{0.5}Ge_{0.5}$ and (b) off-stoichiometric $Co_{1.77}Fe_{1.23}Ga_{0.56}Ge_{0.44}$.

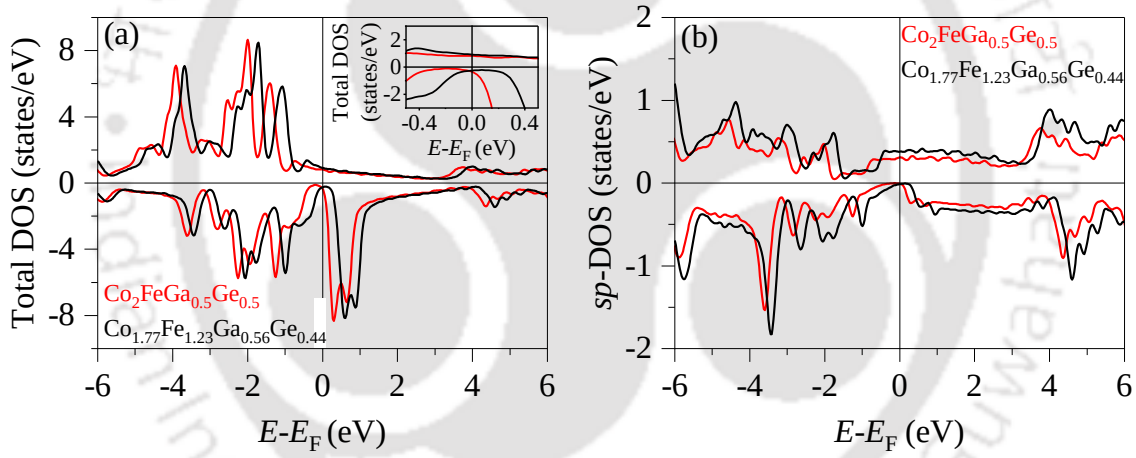

Figure 5.04. (a) Spin-resolved total DOS of $Co_2FeGa_{0.5}Ge_{0.5}$ and $Co_{1.77}Fe_{1.23}Ga_{0.56}Ge_{0.44}$ alloys. Inset in figure provides an expanded view of DOS near E_F. (b) *sp*-DOS corresponding to $Co_2FeGa_{0.5}Ge_{0.5}$ and $Co_{1.77}Fe_{1.23}Ga_{0.56}Ge_{0.44}$ alloy compositions.

Figure 5.04 (a) shows the calculated spin-resolved total DOS for $Co_2FeGa_{0.5}Ge_{0.5}$ and $Co_{1.77}Fe_{1.23}Ga_{0.56}Ge_{0.44}$ alloys. In the off-stoichiometric composition, the DOS shifts horizontally with respect to the DOS of the stoichiometric CFGG, positioning E_F closer to the middle of the gap, while the overall DOS shape remains similar. As a result, the spin polarization increased from ~35% to ~58%. Additionally, *sp*-partial DOS was calculated, as shown in Figure 5.04 (b), because the electrons in the *s* and *p* bands are the primary contributors to electric conduction due to their high Fermi velocities. The estimated spin polarization of the *sp*-partial DOS is high, being ~96% for stoichiometric CFGG and ~94% for off-stoichiometric

$Co_{1.77}Fe_{1.23}Ga_{0.56}Ge_{0.44}$. But the sum of majority and minority DOS at E_F, which is related to α, is the same (= 1.166 states/eV) for both stoichiometric and off-stoichiometric CFGG. Nevertheless, Co-Fe disorder, which is expected to occur in stoichiometric CFGG, is known to give rise to in-gap states in the minority band at E_F [GOTO2020, KUSH2022]. These in-gap states can increase α by increasing the sum of majority and minority DOS at E_F and disturbing the half-metallicity of the alloy. So, it can be expected that off-stoichiometric CFGG with Co-Fe disorder can exhibit lower α.

Figures 5.05 (a) and 5.05 (b) show the spin-resolved band structures for $Co_2FeGa_{0.5}Ge_{0.5}$ and $Co_{1.77}Fe_{1.23}Ga_{0.56}Ge_{0.44}$ alloy compositions, respectively. In both the compositions, a pseudo-gap is observed in the minority-spin channel around E_F, characterized by a substantial reduction in band dispersion and absence of band crossings near E_F. In contrast, the majority-spin bands are metallic, with several bands crossing E_F, indicating metallic conduction in that channel. This behavior is consistent with that observed in the spin-resolved total DOS of these alloys. However, since the band structure does not exhibit a complete gap in the minority-spin channel, 100% half-metallicity is not achieved. The presence of a pseudo-gap implies that the system lies near the half-metallic regime, but small perturbations such as atomic disorder can introduce states at E_F and significantly degrade the spin polarization. Notably, the off-stoichiometric composition exhibits a more pronounced separation of minority-spin bands near E_F, suggesting enhanced spin polarization. This also indicates that it is much easier to achieve half-metallicity in this alloy composition, as predicted in the DOS analysis.

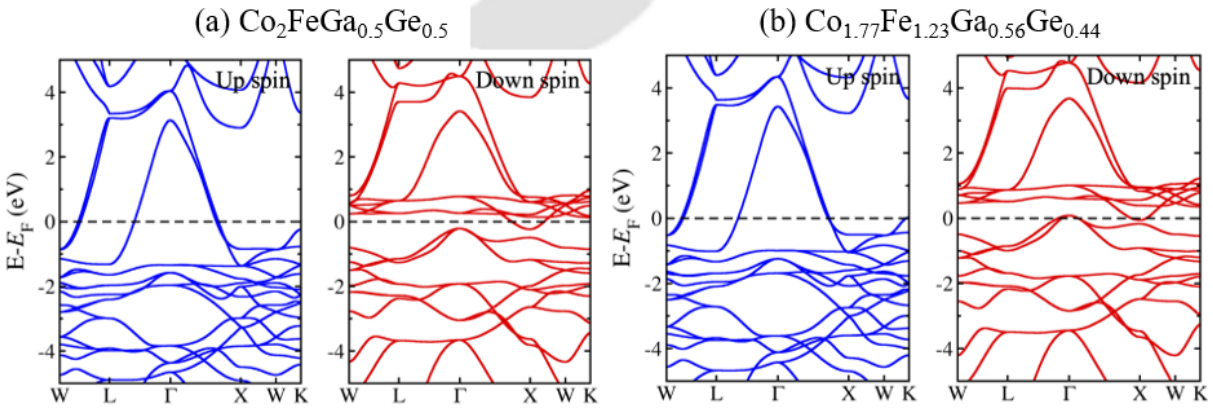

Figure 5.05. Spin-resolved band structures of (a) $Co_2FeGa_{0.5}Ge_{0.5}$ and (b) $Co_{1.77}Fe_{1.23}Ga_{0.56}Ge_{0.44}$ alloy compositions. A pseudo-gap near E_F is evident in the minority-spin channel, consistent with the features observed in the DOS (see Figure 5.04 (a)).

5.3.3. Magneto-dynamic properties

In the case of off-stoichiometric CFGG composition, reduced Co-Fe disorder leads to a lower minority DOS, resulting in decreased total DOS at E_F. Given that intrinsic α (α_{int}) is directly proportional to the total DOS, it is expected to observe a lower α in the off-stoichiometric CFGG. In order to understand the variation of α with changes in half-metallicity induced by heat-treatment at different T_{an}, FMR measurements were carried out at room temperature on as-deposited and annealed off-stoichiometric $Co_{1.77}Fe_{1.23}Ga_{0.56}Ge_{0.44}$ thin films to determine α_{int}. The underlying mechanism behind FMR is explained in Section 1.2.1.2.3, while the experimental procedures followed to record FMR spectra and analyse them are detailed in Section 2.2.3.2. FMR spectra were recorded by fixing the frequency while sweeping the magnetic field by 800 Oe across the resonance field $\mu_0 H_r$. The same procedure was repeated for frequencies in 2 GHz interval in the range of 16 to 36 GHz. Figure 5.06 shows the representative FMR spectra of the as-deposited $Co_{1.77}Fe_{1.23}Ga_{0.56}Ge_{0.44}$ film recorded at 16, 20, 24, 28, 32, and 36 GHz in in-plane geometry. A systematic shift in resonance field towards higher fields can be observed as the frequency is increased from 16 to 36 GHz. The in-plane FMR spectrum recorded at each frequency is then fitted to Equation (2.19) to elucidate $\mu_0 H_r$ and $\mu_0 \Delta H$. The good fit obtained for each spectrum to the theoretically expected profile can be seen in Figure 5.06. $\mu_0 H_r$ evaluated at each frequency was used to create plots of measurement frequency (resonance frequency *f*) *versus* $\mu_0 H_r$, as illustrated in Figure 5.07 (a–d) for the as-deposited film, and those annealed at different T_{an}. These plots were fitted to Kittel's equation [KALA2006] to determine the gyromagnetic ratio (γ) associated with each film. The estimated γ values, as listed in Table 5.01, were subsequently used to evaluate α_{total} by fitting the $\mu_0 \Delta H$ *versus f* plot (shown in Figure 5.07 (e)) to Equation (2.21).

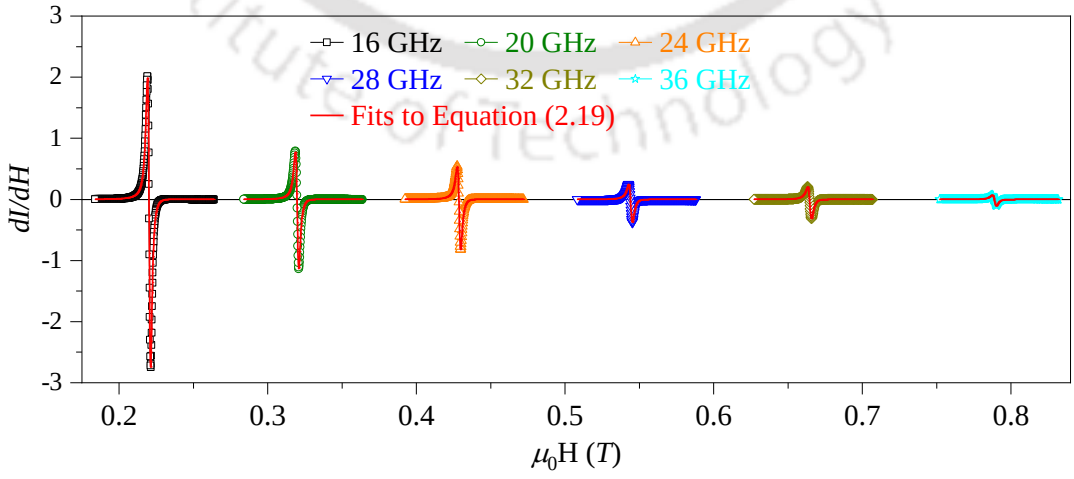

Figure 5.06. Typical in-plane FMR spectra of as-deposited $Co_{1.77}Fe_{1.23}Ga_{0.56}Ge_{0.44}$ film for the frequencies 16, 20, 24, 28, 32, and 36 GHz.

Table 5.01. γ, α_{total}, and α_{int} of as-deposited and annealed $Co_{1.77}Fe_{1.23}Ga_{0.56}Ge_{0.44}$ films.

Type of film	γ (GHz/T)	α_{total}	α_{int}
As-deposited	182.19	~5.36×10^{-3}	~4.98×10^{-3}
Annealed at 400 °C	182.15	~1.74×10^{-3}	~1.36×10^{-3}
Annealed at 500 °C	179.74	~0.76×10^{-3}	~0.38×10^{-3}
Annealed at 600 °C	179.57	~0.73×10^{-3}	~0.35×10^{-3}

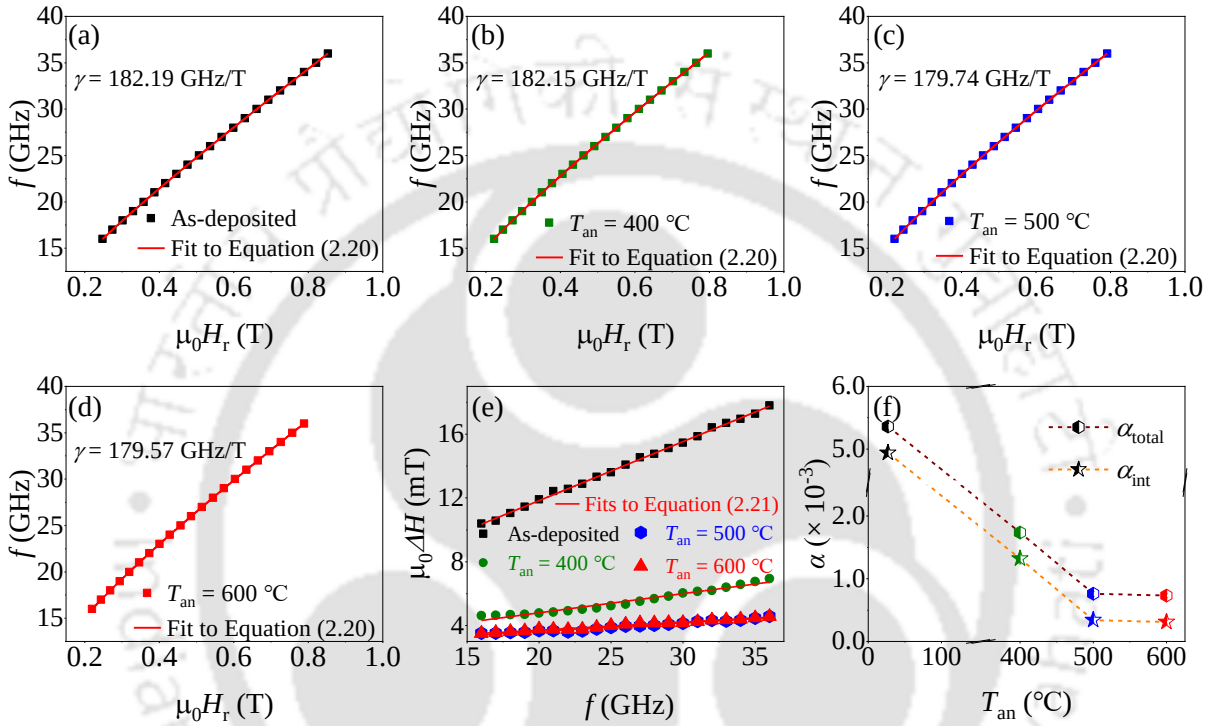

Figure 5.07. Variation of μ_0H_r with resonance frequency of (a) as-deposited film and films annealed at (b) T_{an} = 400 °C, (c) T_{an} = 500 °C, and (d) T_{an} = 600 °C. (e) Variation of $\mu_0\Delta H$ as a function of resonance frequency of all the films. (f) Variation of estimated α_{total} and α_{int} of $Co_{1.77}Fe_{1.23}Ga_{0.56}Ge_{0.44}$ films as a function of annealing temperature T_{an}.

As discussed in Section 2.2.3.2, the experimentally obtained α_{total} contains both α_{int} and α_{ext} components. In turn, α_{ext} has contributions from α_{TMS}, α_{sp}, α_{rad}, and α_{eddy} [HAIT2021]. Here, α_{TMS} is neglected because this factor is negligibly small at the high frequencies used in the FMR measurements [MIZU2009]. α_{sp}, which arises due to spin pumping, is also neglected by considering the low spin-orbit coupling of the Al capping layer whose thickness (~2 nm) is very much lower than the spin diffusion length (~350 nm) [COST2006]. The third contribution α_{rad}, arising from the interaction between magnetization precession and the co-planar waveguide, is estimated to be ~3.7×10^{-4}, following the report by Schoen *et al.* [SCHO2015]. The last contribution arises from the eddy current induced by an alternating magnetic field,

which is estimated to be ~1×10^{-5} [HAIT2021]. After subtracting all the extrinsic contributions from α_{total}, α_{int} was determined for each sample. The evaluated values of α_{total} and α_{int} of as-deposited and annealed $Co_{1.77}Fe_{1.23}Ga_{0.56}Ge_{0.44}$ films are listed in Table 5.01. Figure 5.07 (f) shows the T_{an} dependence of α_{total} and α_{int}. It can be seen that α_{int} decreases almost linearly with increasing T_{an} up to 500 ℃ and then decreases slightly upon further increase in T_{an} to 600 ℃, thereby reaching a very low value of $(3.5\pm0.3)\times10^{-4}$.

In comparison, non-conducting yttrium iron garnet ($Y_3Fe_5O_{12}$) exhibits much lower α_{total} of $(8.58\pm0.21)\times10^{-5}$ [CHAN2014]. However, this comparison is not relevant here since charge-based spintronic devices require conducting materials. Hence, one should restrict the comparison to conducting materials only. Among conducting materials, $Co_{25}Fe_{25}$ shows α_{int} of 5.0×10^{-4} and α_{total} ranging from ~1.4×10^{-3} to 2.1×10^{-3} [EDWA2019, LEEA2017, SCHO2016], while NiFe and CoFeB exhibited α_{total} of ~4.6×10^{-3} to 5.5×10^{-3} and 4.2×10^{-3}, respectively [CONC2013, DONG2021]. These reported values are higher than the obtained α of 600 ℃ annealed $Co_{1.77}Fe_{1.23}Ga_{0.56}Ge_{0.44}$ films in this study, highlighting its superiority over the rest for spintronic device applications.

5.3.4. Transport properties

The above discussion on crystal structure and magneto-dynamic properties shows that increasing T_{an} enhances atomic ordering in off-stoichiometric CFGG films, which is accompanied by a reduction in α. To understand the qualitative variation in half-metallicity due to improved atomic order in these CFGG films, transport properties such as ordinary and anisotropic magnetoresistance of the films were evaluated.

5.3.4.1. Ordinary magnetoresistance

The experimental and theoretical details of ordinary MR (OMR) are discussed in Section 2.2.4.2. The OMR ratio ($\Delta\rho_{OMR}/\rho_0$) is evaluated using the relation, $\Delta\rho_{OMR} = \rho_H - \rho_0$, where ρ_H and ρ_0 represent the electrical resistivity in the presence and absence of a magnetic field, respectively. Figures 5.08 (a−d) show the variation of the OMR ratio of the as-deposited and annealed off-stoichiometric $Co_{1.77}Fe_{1.23}Ga_{0.56}Ge_{0.44}$ thin films as a function of external magnetic field. In all the samples, the OMR ratio exhibits a negative slope with respect to the magnetic field, and the slope increases with a decrease in measurement temperature. This slope increases with an increase in T_{an}.

In general, the electrical resistivity of a ferromagnetic material can be expressed by Equation (2.24) as $\rho(T) = \rho_R + \rho_P(T) + \rho_M(T)$, where ρ_R, $\rho_P(T)$, and $\rho_M(T)$ are resistivities due to temperature-independent electron-defect scattering, temperature-dependent scattering of

electrons by phonons, and temperature-dependent scattering of electrons by magnons, respectively. Here, $\rho_M(T)$ is sensitive to the magnetic field and decreases with increasing magnetic field due to the suppression of electron-magnon scattering. This manifests as a negative magnetoresistance [CHAT2023]. In half-metallic ferromagnets, the absence of minority DOS at E_F results in an exponential suppression of $\rho_M(T)$, *i.e.*, $\rho_M(T)e^{-\Delta/k_BT}$ [BOMB2013, CHAT2023], where Δ represents the lowest excitation energy for spin-flip process of majority charge carriers, as depicted in Figure 5.08 (e). At low temperatures, this additional factor suppresses $\rho_M(T)$. Additionally, at low temperatures, lattice vibrations are greatly reduced, diminishing $\rho_P(T)$. In this scenario, ρ_R becomes dominant, and the Lorentz force causes electrons to travel longer paths in a magnetic field, leading to an increase in $\rho(T)$ [BAKO2022]. Therefore, the OMR ratio increases with a decrease in measurement temperature. The OMR ratio at 10 K (300 K) increases with increasing T_{an}, as shown in Figure 5.08 (f). This increase is attributed to the increase in Δ and resultant higher suppression of $\rho_M(T)$. As Δ is directly linked to half-metallicity, the increase in OMR ratio signifies improved half-metallicity of the material annealed at higher T_{an}.

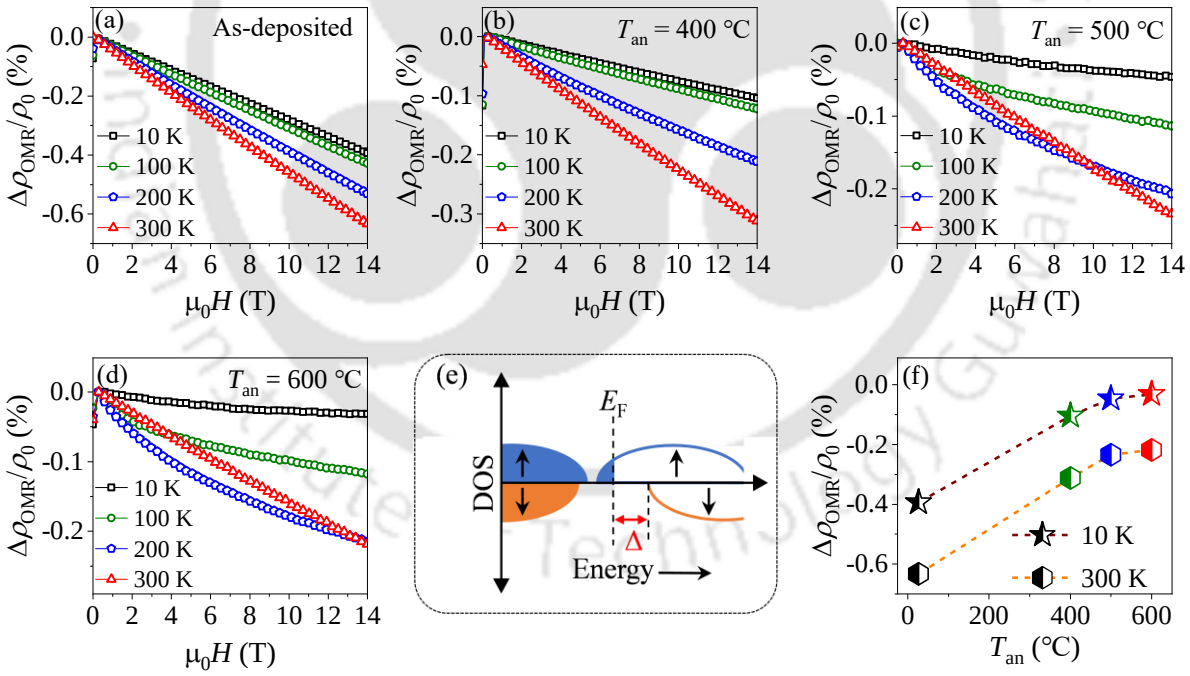

Figure 5.08. Variation of OMR ratio with applied magnetic field measured at 10, 100, 200, and 300 K for off-stoichiometric $Co_{1.77}Fe_{1.23}Ga_{0.56}Ge_{0.44}$ thin films (a) as-deposited, and annealed at (b) T_{an} = 400 °C, (c) T_{an} = 500 °C, and (d) T_{an} = 600 °C. (e) Schematic diagram of DOS *versus* energy plot of a half-metal. (f) T_{an} dependence of OMR ratio measured under an applied field of 14 T at 10 and 300 K.

5.3.4.2. Anisotropic magnetoresistance

To investigate the variation in half-metallicity with improvement in atomic order achieved by annealing off-stoichiometric $Co_{1.77}Fe_{1.23}Ga_{0.56}Ge_{0.44}$ thin films, the anisotropic MR (AMR) ratio was measured at measurement temperatures (T) from 50 to 300 K, in 50 K intervals. The experimental and theoretical details of AMR are discussed in Section 2.2.4.2. Figures 5.09 (a−f) show the angular variation in AMR ratio measured at T = 50, 100, 150, 200, 250, and 300 K, respectively, for the as-deposited and annealed off-stoichiometric $Co_{1.77}Fe_{1.23}Ga_{0.56}Ge_{0.44}$ thin films. All the samples show negative AMR, and the amplitude of the negative AMR ratio increases with an increase in T_{an} at each measurement temperature. The negative AMR ratio is considered as a signature of half-metallicity [CHEN2017, SAKU2014, YANG2012], though it is not conclusive evidence [KUSH2022]. Therefore, the temperature dependence of $\Delta\rho_{AMR}$ was analyzed to confirm the half-metallic nature of the samples.

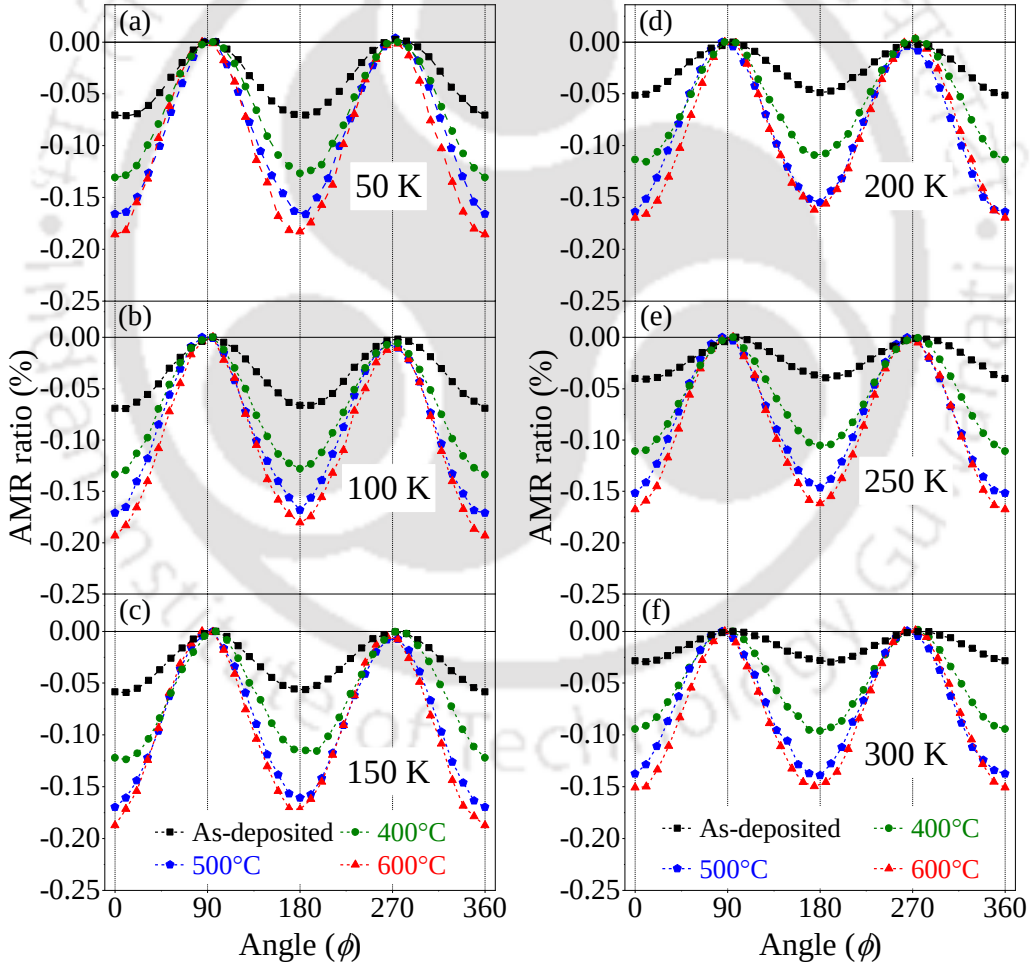

Figure 5.09. Angular dependence of AMR ratio of all $Co_{1.77}Fe_{1.23}Ga_{0.56}Ge_{0.44}$ films recorded at (a) 50 K, (b) 100 K, (c) 150 K, (d) 200 K, (e) 250 K, and (f) 300 K.

Figure 5.10 (a) shows the temperature dependence of $\Delta\rho_{AMR}$ normalized by the value at T = 50 K. Here, $\Delta\rho_{AMR}$ is defined as the difference in the electrical resistivity of a sample when the magnetic field and current directions are applied parallel and perpendicular to each other [KUSH2022]. The as-deposited $Co_{1.77}Fe_{1.23}Ga_{0.56}Ge_{0.44}$ film shows the largest reduction in the normalized $\Delta\rho_{AMR}$ as the measurement temperature T is increased. The annealed films do not show such a large reduction with T, and $\Delta\rho_{AMR}$ becomes nearly constant at T_{an} = 500 and 600 °C.

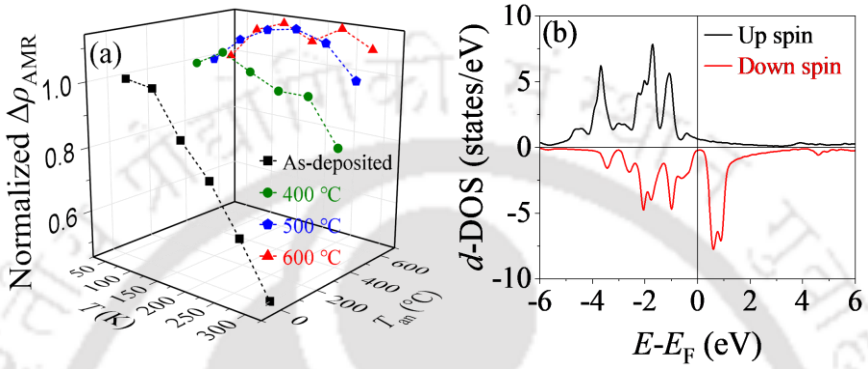

Figure 5.10. (a) Measurement temperature dependence of normalized $\Delta\rho_{AMR}$ of off-stoichiometric CFGG films annealed at different T_{an}. (b) d-orbital DOS of off-stoichiometric CFGG with $L2_1$ ordered structure.

Temperature dependence of $\Delta\rho_{AMR}$ can be interpreted using the two-current model [KUSH2022]. As outlined in Section 2.2.4.2, the two-current model describes $\Delta\rho_{AMR}$ in half-metallic ferromagnetic materials by considering only $s_\uparrow \rightarrow d_\downarrow$ and $s_\uparrow \rightarrow d_\uparrow$ types of scattering mechanisms. Hence, $\Delta\rho_{AMR}$ can be expressed as [KUSH2022]

$$\Delta\rho_{AMR} \approx \gamma\left(\rho_{s,\uparrow\rightarrow d,\downarrow} - \rho_{s,\uparrow\rightarrow d,\uparrow}\right) \propto D_\uparrow^{(d)}(E_F)\left[1 - \frac{D_\downarrow^{(d)}(E_F)}{D_\uparrow^{(d)}(E_F)}\right]. \qquad (5.01)$$

Here, $D_\uparrow^{(d)}(E_F)$ and $D_\downarrow^{(d)}(E_F)$ represent the d-orbital DOS at E_F for up and down spins, respectively. The temperature dependence of $\Delta\rho_{AMR}$ observed in Figure 5.10 (a) originates primarily from the $D_\downarrow^{(d)}(E_F)$ due to thermally excited electrons governed by the Fermi-Dirac distribution function. In the case of $L2_1$-ordered off-stoichiometric $Co_{1.77}Fe_{1.23}Ga_{0.56}Ge_{0.44}$, $D_\downarrow^{(d)}(E_F)$ is nearly zero with E_F located near the middle of the gap, as seen in the calculated d-orbital DOS in Figure 5.10 (b). This electronic structure indicates that near-zero $D_\downarrow^{(d)}(E_F)$ is robust against temperature increase. Therefore, $\Delta\rho_{AMR}$ is expected to remain constant, as observed in the $L2_1$-ordered film annealed at $T_{an} \geq$ 500 °C. On the other hand, a substantial $D_\downarrow^{(d)}(E_F)$ in the gap is expected due to the Co-Fe disorder in the as-deposited and 400 °C-annealed films [GOTO2020, KUSH2022]. In this scenario, Equation (5.01) does not hold

because of the existence of other types of *s-d* scattering processes, such as $s_\downarrow \rightarrow d_\downarrow$ and $s_\downarrow \rightarrow d_\uparrow$ along with $s_\uparrow \rightarrow d_\downarrow$ and $s_\uparrow \rightarrow d_\uparrow$, which explains the large temperature dependence of $\Delta\rho_{AMR}$. The above analysis qualitatively confirms an enhancement in half-metallicity associated with an improvement in the atomic order in the films attained by increasing T_{an}.

The results of both OMR and AMR measurements confirm an increase in half-metallicity in off-stoichiometric CFGG films upon increase in T_{an} due to improved atomic order. From the previous studies reported by Goto *et al*. [GOTO2020], it is known that an improvement in half-metallicity is expected in CFGG as the atomic ordering improves from *B*2 to $L2_1$ type. Based on this report, the enhancement in $L2_1$ order achieved by increasing T_{an} from 400 to 600 ℃ explains the improved half-metallicity in the films. However, the improvement in the half-metallicity between the as-deposited and 400 ℃-annealed samples cannot be explained on this basis because neither samples exhibit $L2_1$ ordering. In such a situation, one can attribute the difference to the change in the Co-Fe disorder in both films. As reported in an anomalous XRD study, the Co-Fe disorder gives rise to the minority DOS at E_F, deteriorating the half-metallicity [GOTO2020, KUSH2022]. The amount of Co-Fe disorder decreases continuously with increasing T_{an} and ultimately vanishes at $T_{an} \geq 500$ ℃. So, the improvement in half-metallicity of the 400 ℃-annealed film over the as-deposited film is expected due the lower Co-Fe disorder in the annealed film.

5.4. Summary

The effect of improvement in atomic ordering on the half-metallicity and α_{int} of off-stoichiometric Co-deficient and Fe-rich $Co_{1.77}Fe_{1.23}Ga_{0.56}Ge_{0.44}$ Heusler alloy thin films was systematically investigated by studying films heat treated at different T_{an}. Further, the correlation between α, atomic ordering, and half-metallicity was also examined. The key findings from this study are summarized below.

- Off-stoichiometric CFGG thin films were prepared by magnetron sputtering and annealed *in situ* at T_{an} = 400, 500, and 600 ℃ to improve the atomic ordering. Structural analysis confirmed the presence of *B*2-type disordered structure in the as-deposited film and the film annealed at T_{an} = 400 ℃. $L2_1$ ordering appeared in the film annealed at T_{an} = 500 ℃, which improved as T_{an} was increased to 600 ℃.
- First-principles calculations reveal an increase in *P* from 35% in stoichiometric CFGG to 58% in off-stoichiometric Co-deficient and Fe-rich $Co_{1.77}Fe_{1.23}Ga_{0.56}Ge_{0.44}$ Heusler alloy, highlighting its greater potential for spintronic applications as a half-metallic material.

- α_{int} decreased significantly in films annealed at T_{an} up to 500 ℃. Further increase in T_{an} to 600 ℃ slightly decreased α_{int}, achieving a remarkably low α_{int} of $(3.5\pm0.3)\times10^{-4}$.
- The effect of atomic ordering on the half-metallicity was explored through OMR and AMR measurements, which indicated an improvement in half-metallicity with an increase in T_{an} due to the improvement in atomic ordering.
- This enhanced half-metallicity in annealed off-stoichiometric CFGG films revealed from the OMR and AMR measurements is supported by the decreasing trend of α_{int} observed in FMR studies.

In conclusion, this investigation clarifies that atomic disorder significantly influences α in off-stoichiometric $Co_{1.77}Fe_{1.23}Ga_{0.56}Ge_{0.44}$ alloy films. A remarkably low intrinsic α was achieved in the film with a fully ordered $L2_1$-type structure, making it a promising candidate to reduce the critical current density and pave the way for the realization of highly energy-efficient spintronic devices.

Chapter 6

Spin mixing conductance of $Co_2FeGa_{0.5}Ge_{0.5}$/Pt bilayers

6.1. Introduction

As discussed in Chapter 1, developing high-performance, non-volatile magnetoresistive random access memory requires MTJs with energy-efficient magnetization switching of the free (or unpinned) FM layer [IKEG2020]. This need propels the adoption of the SOT mechanism, in which spin current injection occurs from a nonmagnetic (NM) layer to the free FM layer [LUQL2019]. In this method of magnetization switching, spin mixing conductance $g_{\text{eff}}^{\downarrow\uparrow}$ is a key parameter for quantifying the spin current flowing from the NM to the FM layer. Moreover, to achieve high SOT efficiency, an FM/NM interface with high $g_{\text{eff}}^{\downarrow\uparrow}$ (~ 10^{19} to 10^{20} m^{-2}) is essential. Since $g_{\text{eff}}^{\downarrow\uparrow}$ depends on the spin-orbit coupling of the NM layer, heavy metals such as Pt, Ta, W, Ir, or Hf, which can serve as effective spin-current sources, are recommended as the NM layer. These heavy metals are characterized by a large spin-orbit coupling (SOC), an entity which scales as Z^4 (where Z is the atomic number of the element) [CHUN2014, TSER2002]. Another crucial factor required for efficient magnetization switching of the free FM layer is its α, which should be extremely low [FANY2024]. Since α is proportional to the total DOS at E_F, a half-metallic material can exhibit low α, as highlighted in Chapter 5 [BHAT2025b, KUBO2009, MIZU2009]. Additionally, half-metallic nature minimizes spin-flip scattering, leading to a reduced α [SHAW2018], and simultaneously helps in realizing a higher MR ratio due to its higher P [BARW2024]. Considering these factors, Co_2Fe-based $Co_2FeGa_{0.5}Ge_{0.5}$ (CFGG) Heusler alloy with high P of 75% and a low α of ~0.008 appears to be a promising free FM layer [VARA2012]. Motivated by these inputs from the literature and utilizing the low α of CFGG and strong SOC of Pt, $g_{\text{eff}}^{\downarrow\uparrow}$ across a CFGG/Pt bilayer has been studied to investigate the spin current injection efficiency of this device.

6.2. Thin film deposition, processing, and basic characterizations

Figures 6.01 (a, b, and c) illustrate the schematic structure of the samples prepared and used in this study, *viz*., CFGG (8–20 nm) film on MgO (100) substrate, CFGG (8–20 nm)/Pt (10 nm) bilayer on MgO (100) substrate, and CFGG (16 nm)/Pt (0.5–10 nm) bilayer on MgO (100) substrate. All the samples were deposited on MgO (100) substrate at room temperature using an ultra-high vacuum RF magnetron sputtering as described in Section 2.1.2. The CFGG layers

were deposited using a high (>99.9%) purity alloy target of $Co_{1.95}Fe_{0.89}Ga_{0.48}Ge_{0.68}$ composition and subsequently annealed *in situ* at 600 °C for 30 minutes to improve the atomic order. These processed films were used in the following study. During the deposition, a target-to-substrate distance of 100 mm was maintained. The overall composition of the CFGG layer was estimated to be $Co_{2.06\pm0.01}Fe_{0.99\pm0.01}Ga_{0.53\pm0.01}Ge_{0.42\pm0.01}$ by XRR measurements. A 2 nm Al capping layer was deposited on the CFGG film to avoid oxidation (not shown in Figure 6.01 (a)). A Pt layer was deposited over the heat-treated and cooled $Co_{2.06}Fe_{0.99}Ga_{0.53}Ge_{0.42}$ layers, which served as both a spin sink and a capping layer (*c.f.* Figure 6.01 (a and b)).

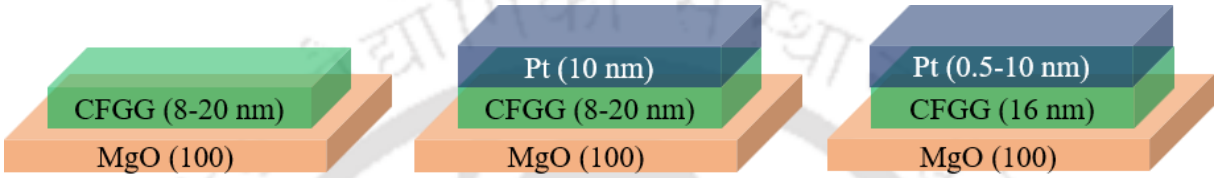

(a) Single layer (b) Bilayer with different t_{CFGG} (c) Bilayer with different t_{Pt}

Figure 6.01. Schematic representation of the thin film stack of (a) CFGG (8-20 nm) single layer, (b) CFGG (8-20 nm)/Pt (10 nm), and (c) CFGG (16 nm)/Pt (0.5-10 nm) bilayer, deposited on MgO (100) substrate.

6.3. Results and discussion

6.3.1. Crystal structure

Figures 6.02 (a) and 6.02 (b) show the 2θ-ω XRD patterns of $Co_{2.06}Fe_{0.99}Ga_{0.53}Ge_{0.42}$ single-layer samples with thickness (t_{CFGG}) of 8, 10, 12, 14, 16, 18, and 20 nm, recorded along the out-of-plane direction for $\chi = 0°$ and along the <111> direction for $\chi = 54.7°$, respectively. The corresponding XRD patterns of $Co_{2.06}Fe_{0.99}Ga_{0.53}Ge_{0.42}$ (t_{CFGG})/Pt (10 nm) bilayer samples are shown in Figures 6.03 (a) and 6.03(b), while Figures 6.04 (a) and 6.04 (b) present the XRD patterns of bilayer samples of $Co_{2.06}Fe_{0.99}Ga_{0.53}Ge_{0.42}$ (16 nm)/Pt (0.5, 1, 2, 3, and 5 nm). In all the samples, the observed reflections of CFGG (400) and Pt (200) for $\chi = 0°$ confirm epitaxial growth along the [100] direction. Additionally, the presence of CFGG (200) and CFGG (111) superlattice reflections confirms the $L2_1$-type ordered crystal structure in $Co_{2.06}Fe_{0.99}Ga_{0.53}Ge_{0.42}$. Due to the proximity of the atomic scattering factors of Co and Fe, the conventional XRD technique cannot ascertain the presence of Co-Fe disorder as already discussed in the previous chapter. Nonetheless, Co-Fe disorder is expected to be suppressed in these CFGG films due to the heat treatment given at 600 °C [GOTO2020].

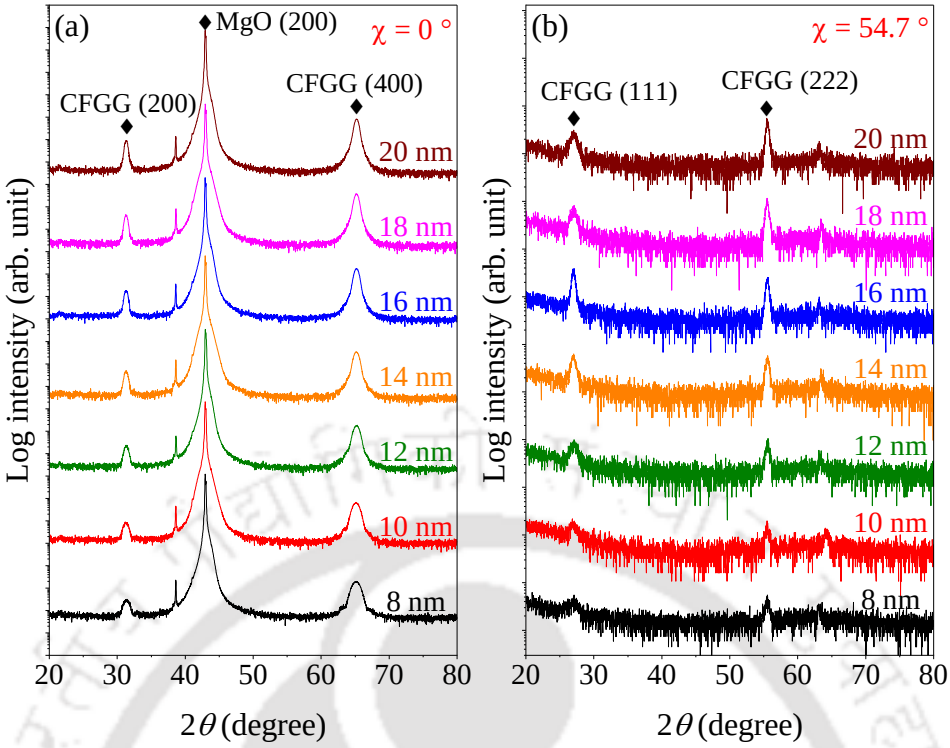

Figure 6.02. XRD patterns of 2θ-ω scans of $Co_{2.06}Fe_{0.99}Ga_{0.53}Ge_{0.42}$ (8, 10, 12, 14, 16, 18, and 20 nm) single layer samples recorded at (a) χ = 0° and (b) χ = 54.7°.

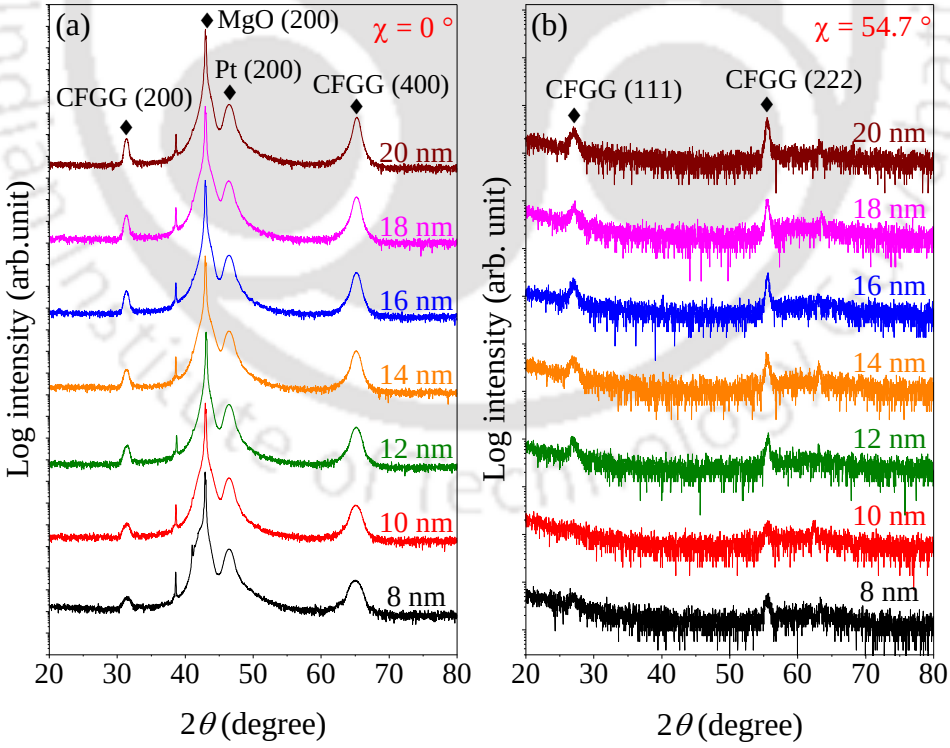

Figure 6.03. XRD patterns of 2θ-ω scans of $Co_{2.06}Fe_{0.99}Ga_{0.53}Ge_{0.42}$ (8, 10, 12, 14, 16, 18, and 20 nm)/Pt (10 nm) bilayer samples recorded at (a) χ = 0° and (b) χ = 54.7°.

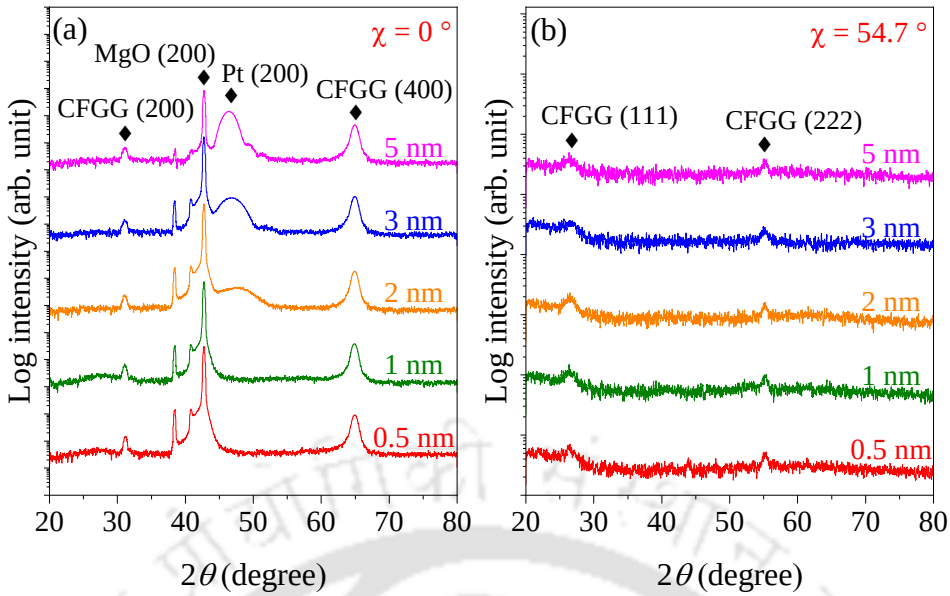

Figure 6.04. XRD patterns of 2θ-ω scans of $Co_{2.06}Fe_{0.99}Ga_{0.53}Ge_{0.42}$ (16 nm)/Pt (0.5, 1, 2, 3, and 5 nm) bilayer samples recorded at (a) $\chi = 0°$ and (b) $\chi = 54.7°$.

6.3.2. Magneto-dynamic properties

To evaluate $g_{eff}^{\uparrow\downarrow}$ across the $Co_{2.06}Fe_{0.99}Ga_{0.53}Ge_{0.42}$/Pt interface, α of single layer $Co_{2.06}Fe_{0.99}Ga_{0.53}Ge_{0.42}$ (8–20 nm), and bilayer $Co_{2.06}Fe_{0.99}Ga_{0.53}Ge_{0.42}$ (8–20 nm)/Pt (10 nm) samples were evaluated from in-plane broadband FMR spectra. The underlying mechanism behind FMR is explained in Section 1.2.1.2.3, while the experimental procedures followed to record FMR spectra are detailed in Section 2.2.3.2.

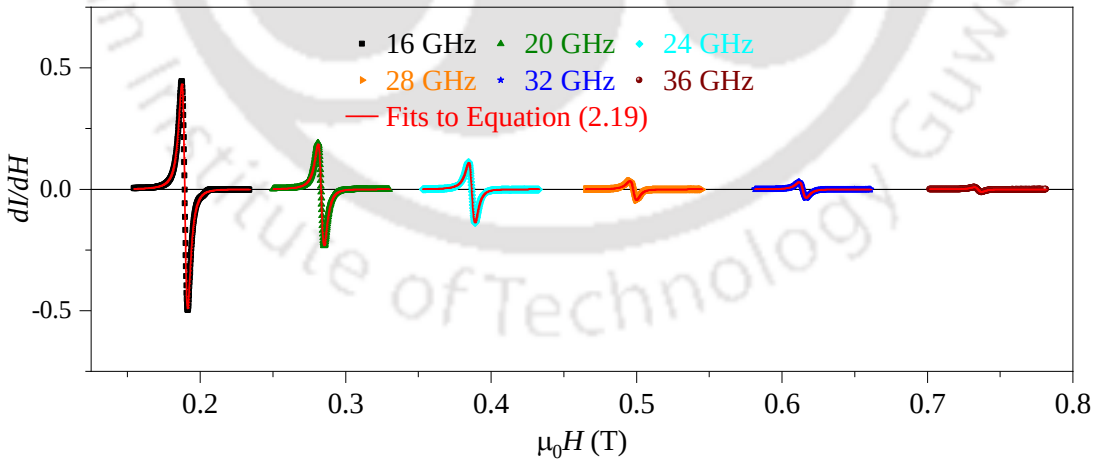

Figure 6.05. Typical in-plane FMR spectra of a 16 nm thick $Co_{2.06}Fe_{0.99}Ga_{0.53}Ge_{0.42}$ film. Only spectra recorded at 16, 20, 24, 28, 32, and 36 GHz are displayed for the sake of clarity.

FMR spectra of the films were recorded by fixing the frequency (say, at 16 GHz) while sweeping the magnetic field by 800 Oe across the resonance field $\mu_0 H_r$. The same procedure was repeated for frequencies in a 2 GHz interval in the range of 16 to 36 GHz. Figure 6.05

shows the representative FMR spectra of a 16 nm $Co_{2.06}Fe_{0.99}Ga_{0.53}Ge_{0.42}$ film. Only spectra recorded at six frequencies (16, 20, 24, 28, 32, and 36 GHz) in in-plane geometry are shown out of the 11 spectra recorded for each film for the sake of visual clarity. A systematic shift in resonance field towards higher fields can be observed as the frequency is increased from 16 to 36 GHz. The in-plane FMR spectrum recorded at each frequency was then fitted to Equation (2.19) to elucidate $\mu_0 H_r$ and $\mu_0 \Delta H$. The good fit obtained for each spectrum to the theoretically expected profile (represented by solid lines) can be seen. $\mu_0 H_r$ evaluated at each frequency was used to create plots of measurement frequency (resonance frequency f) *versus* $\mu_0 H_r$, as illustrated in Figures 6.06 (a–g) for the $Co_{2.06}Fe_{0.99}Ga_{0.53}Ge_{0.42}$ films with thicknesses of 8, 10, 12, 14, 16, 18, and 20 nm, respectively. These plots were fitted to Kittel's equation [KALA2006] to determine the gyromagnetic ratio (γ) associated with each film. The estimated γ values, listed in Table 6.01, were subsequently used to evaluate α_{total} by fitting the $\mu_0 \Delta H$ *versus* f plot (shown in Figure 6.06 (h)) to Equation (2.21). The evaluated values of α_{total} of $Co_{2.06}Fe_{0.99}Ga_{0.53}Ge_{0.42}$ (8-20 nm) films are listed in Table 6.01.

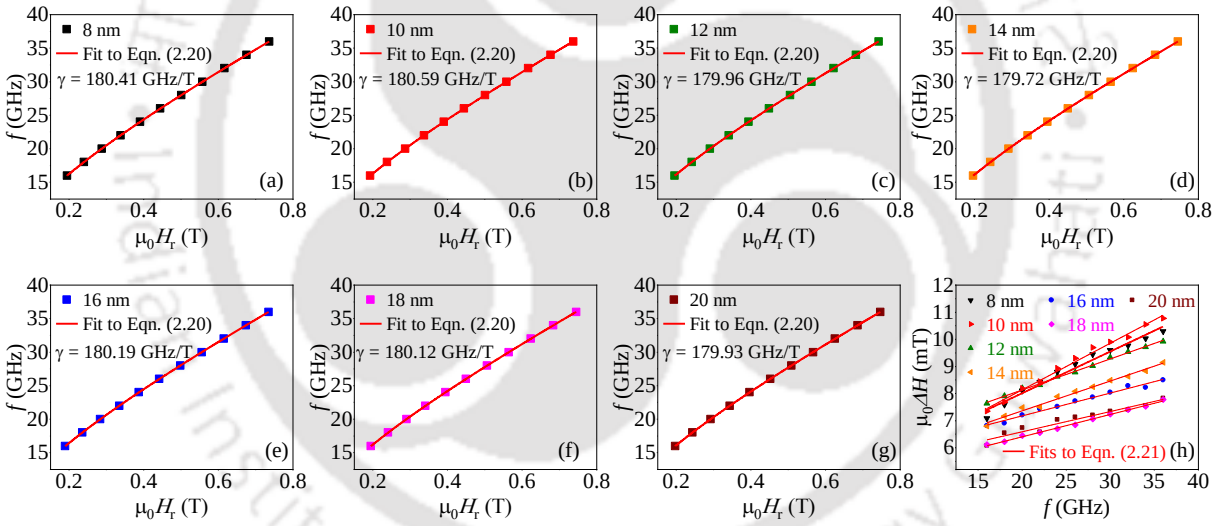

Figure 6.06. Variation of $\mu_0 H_r$ with resonance frequency of $Co_{2.06}Fe_{0.99}Ga_{0.53}Ge_{0.42}$ single layer films with thickness of (a) 8 nm, (b) 10 nm, (c) 12 nm, (d) 14 nm, (e) 16 nm, (f) 18 nm, and (g) 20 nm. (h) $\mu_0 \Delta H$ as a function of the resonance frequency of all the films.

Following the same procedure, the $\mu_0 H_r$ *versus* f plot recorded for the bilayer $Co_{2.06}Fe_{0.99}Ga_{0.53}Ge_{0.42}$ (8–20 nm)/Pt (10 nm) samples (Figures 6.07 (a–g)) were fitted to Kittel's equation [SING2021] to evaluate the gyromagnetic ratio (γ) corresponding to each film. The estimated γ values, listed in Table 6.01, were subsequently used to evaluate α_{total} by fitting the $\mu_0 \Delta H$ *versus* f plot (shown in Figure 6.07 (h)) to Equation (2.21). The evaluated α_{total} values of $Co_{2.06}Fe_{0.99}Ga_{0.53}Ge_{0.42}$ (8–20 nm)/Pt (10 nm) films are listed in Table 6.01.

Table 6.01. γ and α_{total} of $Co_{2.06}Fe_{0.99}Ga_{0.53}Ge_{0.42}$ (8–20 nm) single layer and $Co_{2.06}Fe_{0.99}Ga_{0.53}Ge_{0.42}$ (8–20 nm)/Pt (10 nm) bilayer films.

Type of film	γ (GHz/T)	α_{total}
CFGG (8 nm)	180.41	~2.21×10^{-3}
CFGG (10 nm)	180.59	~2.47×10^{-3}
CFGG (12 nm)	179.96	~1.64×10^{-3}
CFGG (14 nm)	179.72	~1.57×10^{-3}
CFGG (16 nm)	180.19	~1.21×10^{-3}
CFGG (18 nm)	180.12	~1.18×10^{-3}
CFGG (20 nm)	179.93	~1.07×10^{-3}
CFGG (8 nm)/Pt (10 nm)	181.58	~8.23×10^{-3}
CFGG (10 nm)/Pt (10 nm)	181.17	~6.72×10^{-3}
CFGG (12 nm)/Pt (10 nm)	180.67	~5.78×10^{-3}
CFGG (14 nm)/Pt (10 nm)	180.13	~5.02×10^{-3}
CFGG (16 nm)/Pt (10 nm)	180.22	~4.37×10^{-3}
CFGG (18 nm)/Pt (10 nm)	188.04	~2.95×10^{-3}
CFGG (20 nm)/Pt (10 nm)	180.79	~2.97×10^{-3}

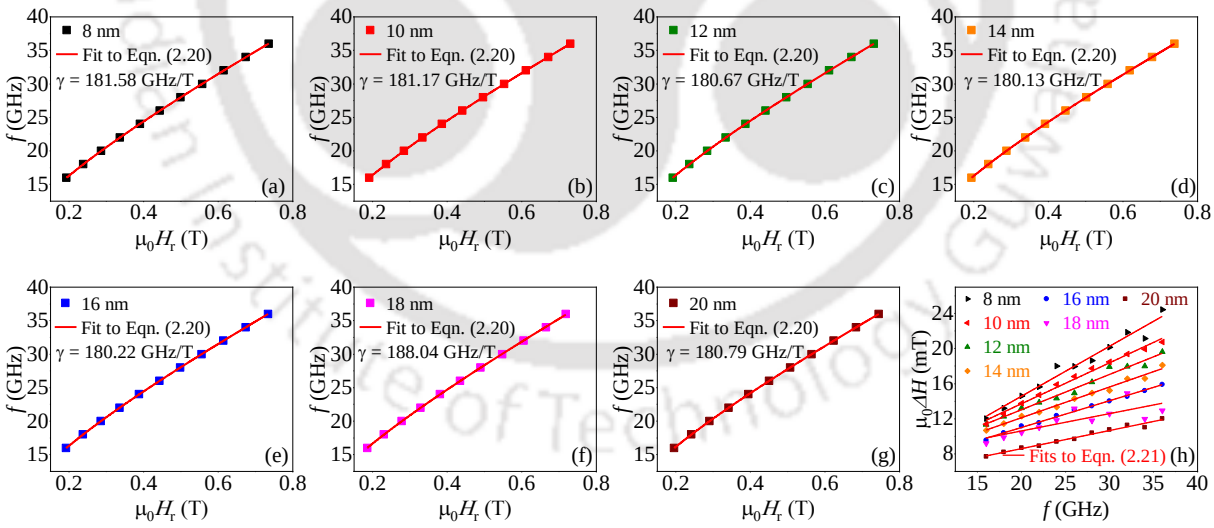

Figure 6.07. Variation of $\mu_0 H_r$ with resonance frequency of $Co_{2.06}Fe_{0.99}Ga_{0.53}Ge_{0.42}$ (t_{CFGG})/Pt (10 nm) bilayer films with t_{CFGG} of (a) 8 nm, (b) 10 nm, (c) 12 nm, (d) 14 nm, (e) 16 nm, (f) 18 nm, and (g) 20 nm. (h) $\mu_0 \Delta H$ as a function of the resonance frequency of all the films.

The dependence of evaluated α_{total} on the thickness of $Co_{2.06}Fe_{0.99}Ga_{0.53}Ge_{0.42}$ in both single layer and bilayer samples is depicted in Figure 6.08 (a). In the case of single layer films,

α_{total} exhibits a minimum value of ~1.07×10^{-3} for the film with ~20 nm thickness, followed by a slight increase with further decrease in t_{CFGG}. In bilayer samples, α_{total} is significantly higher when compared to the single layer samples. As discussed in Section 2.2.3.2, the experimentally obtained α_{total} contains both intrinsic and extrinsic components. Here, the extrinsic components include the contributions from spin pumping (α_{sp}), two-magnon scattering, radiative damping, and eddy current [HAIT2021]. But, the Pt layer present in $Co_{2.06}Fe_{0.99}Ga_{0.53}Ge_{0.42}$($t_{CFGG}$)/Pt bilayer samples selectively increase α_{sp} by spin pumping, thereby significantly increasing the α_{total}. Therefore, the enhancement in α_{total} of the bilayer samples as compared to the single layer samples is, $\Delta\alpha = \alpha_{Bilayer} - \alpha_{Single\ layer} \cong \alpha_{sp}$ (*c.f.*, Equation (2.22)).

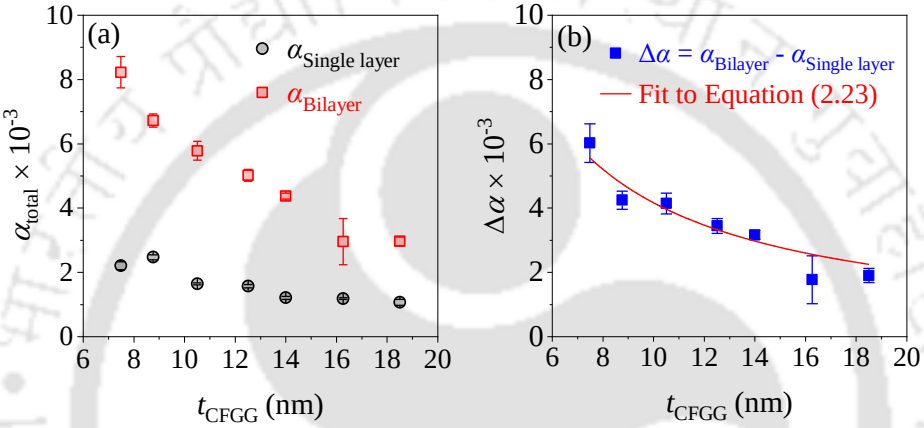

Figure 6.08. Variations of (a) α_{total} with t_{CFGG} in single and bilayer samples, and (b) $\Delta\alpha$ with t_{CFGG}.

Figure 6.08 (b) shows a decrease in $\Delta\alpha$ with the increase in t_{CFGG}. By fitting the data in this Figure to Equation (2.23), $g_{eff}^{\uparrow\downarrow}$ was evaluated to be $(2.78\pm0.09)\times10^{19}$ m^{-2}. The estimated value of $g_{eff}^{\uparrow\downarrow}$ is relatively high in comparison with the previously reported values for conventional FM/Pt bilayer samples such as Co/Pt, CoFe/Pt, and Py/Pt [TAOX2018]. It may be noted that $g_{eff}^{\uparrow\downarrow}$ varies with the Pt layer thickness because of the contribution from spin back flow from the Pt layer to the $Co_{2.06}Fe_{0.99}Ga_{0.53}Ge_{0.42}$ layer. In this analysis, during the evaluation of $g_{eff}^{\uparrow\downarrow}$, the effect of spin back flow was neglected because the Pt layer thickness is sufficiently larger than its reported spin diffusion length (λ_{Pt}) [ZHAN2013].

To quantitatively assess the contribution of spin backflow to the $g_{eff}^{\uparrow\downarrow}$, the variation of $\Delta\alpha$ was investigated as a function of Pt layer thickness (t_{Pt}). For this purpose, α_{total} of various bilayer $Co_{2.06}Fe_{0.99}Ga_{0.53}Ge_{0.42}$ (16 nm)/Pt (0–10 nm) samples was determined. A relatively higher thickness of 16 nm $Co_{2.06}Fe_{0.99}Ga_{0.53}Ge_{0.42}$ was chosen to minimize the influence of surface disorder, which tends to enhance α_{total}.

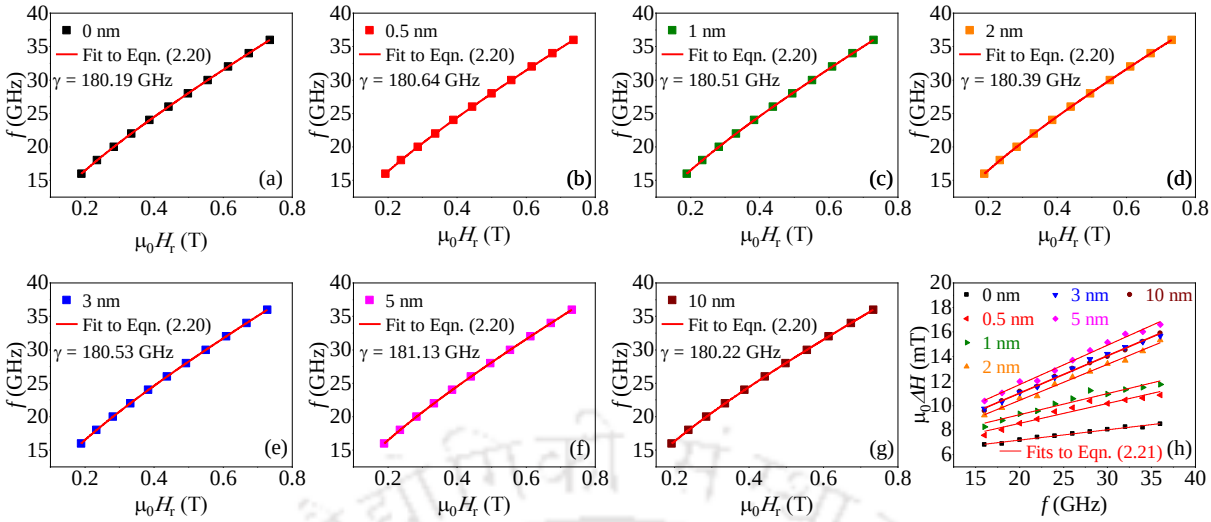

Figure 6.09. Variation of $\mu_0 H_r$ with resonance frequency of $Co_{2.06}Fe_{0.99}Ga_{0.53}Ge_{0.42}$ (16 nm)/Pt (t_{Pt}) bilayer films with t_{Pt} of (a) 0 nm, (b) 0.5 nm, (c) 1 nm, (d) 2 nm, (e) 3 nm, (f) 5 nm, and (g) 10 nm. (h) $\mu_0 \Delta H$ as a function of the resonance frequency of all the films.

Figures 6.09 (a–g) show the $\mu_0 H_r$ *versus* f plot of $Co_{2.06}Fe_{0.99}Ga_{0.53}Ge_{0.42}$ (16 nm)/Pt (0–10 nm), used to evaluate γ corresponding to each film. The estimated γ values, listed in Table 6.02, were utilized to determine α_{total} by fitting the $\mu_0 \Delta H$ *versus* f plot (shown in Figure 6.09 (h)) to Equation (2.21). The evaluated α_{total} and $\Delta\alpha$ values of the films of different Pt thicknesses are listed in Table 6.02.

Table 6.02. γ, α_{total}, and $\Delta\alpha$ of $Co_{2.06}Fe_{0.99}Ga_{0.53}Ge_{0.42}$ (16 nm)/ Pt (0–10 nm) bilayer films.

Type of film	γ (GHz/T)	α_{total}	$\Delta\alpha$
CFGG (16 nm)/Pt (0 nm)	180.19	~1.21×10^{-3}	~$(0\pm0.10)\times10^{-3}$
CFGG (16 nm)/Pt (0.5 nm)	180.64	~2.33×10^{-3}	~$(1.13\pm0.25)\times10^{-3}$
CFGG (16 nm)/Pt (1 nm)	180.51	~2.47×10^{-3}	~$(1.27\pm0.24)\times10^{-3}$
CFGG (16 nm)/Pt (2 nm)	180.39	~4.21×10^{-3}	~$(3.01\pm0.17)\times10^{-3}$
CFGG (16 nm)/Pt (3 nm)	180.53	~4.38×10^{-3}	~$(3.18\pm0.16)\times10^{-3}$
CFGG (16 nm)/Pt (5 nm)	181.13	~4.63×10^{-3}	~$(3.42\pm0.21)\times10^{-3}$
CFGG (16 nm)/Pt (10 nm)	180.22	~4.37×10^{-3}	~$(3.17\pm0.15)\times10^{-3}$

Figure 6.10 represents the variation of $\Delta\alpha$ as a function of t_{Pt} for $Co_{2.06}Fe_{0.99}Ga_{0.53}Ge_{0.42}$ (16 nm)/Pt (0–10 nm) bilayer sample. It can be seen that $\Delta\alpha$ decreases sharply in the lower t_{Pt} range (*i.e.*, for $t_{Pt} \leq 4$ nm). This reduction is attributed to spin current reflection at the Pt/air interface.

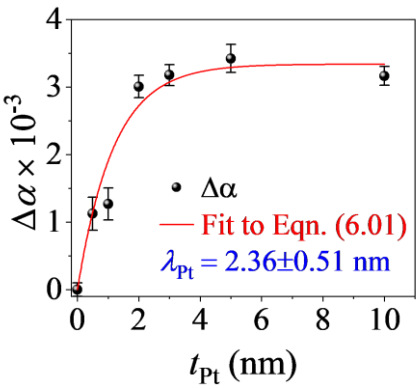

Figure 6.10. Variation of $\Delta\alpha$ with the Pt layer thickness in $Co_{2.06}Fe_{0.99}Ga_{0.53}Ge_{0.42}$ (16 nm)/Pt (0–10 nm) bilayers.

When the Pt layer thickness is comparable to its spin diffusion length, the reflected spin current flows back into the $Co_{2.06}Fe_{0.99}Ga_{0.53}Ge_{0.42}$ layer, thereby reducing $\Delta\alpha$. As a result, Equation (2.23) is modified to [SHAW2012],

$$\Delta\alpha = \frac{g\mu_B}{4\pi M_s}\frac{1}{t_{CFGG}}\, g_{eff}^{\uparrow\downarrow}\left(1-\exp\left(\frac{-2t_{Pt}}{\lambda_{Pt}}\right)\right) \qquad (6.01)$$

The terms within the bracket on the right side represent perfect spin current reflection at the Pt/air interface. Thus, the factor of 2 in the exponential term represents the total distance travelled by the spin current as it returns to the $Co_{2.06}Fe_{0.99}Ga_{0.53}Ge_{0.42}$ layer. By fitting the data in Figure 6.10 to Equation (6.01), λ_{Pt} was estimated to be 2.36±0.51 nm, which falls near the previously reported value [CAST2012]. This validates the assumption made in the earlier analysis of $g_{eff}^{\uparrow\downarrow}$ that it is unaffected by the spin current reflection since λ_{Pt} is much smaller than t_{Pt}.

6.4. Summary

$g_{eff}^{\uparrow\downarrow}$ across the interface of $Co_{2.06}Fe_{0.99}Ga_{0.53}Ge_{0.42}$/Pt bilayers was evaluated to assess the potential of the SOT mechanism for achieving energy-efficient switching of the free FM layer. The key findings from this study are summarized below.

- In the case of single layer $Co_{2.06}Fe_{0.99}Ga_{0.53}Ge_{0.42}$ film, α_{total} exhibits a minimum value of ~1.07×10^{-3} for the ~20 nm film, indicating its low intrinsic damping and highlighting its potential as a free FM layer in MTJs.
- A significant increase of α_{total} was observed in $Co_{2.06}Fe_{0.99}Ga_{0.53}Ge_{0.42}$/Pt bilayers as compared to single-layer samples, suggesting efficient spin pumping across the interface.

- The observed enhancement in α_{total} led to the estimation of high $g_{eff}^{\uparrow\downarrow}$ of (2.78±0.09)×10^{19} m^{-2}, confirming significant spin current transfer across the bilayer interface.
- The spin diffusion length of Pt was found to be 2.36±0.51 nm, which is considerably shorter than the Pt layer thickness used in the analysis of $g_{eff}^{\uparrow\downarrow}$. As a result, the contribution from spin backflow can be considered to be negligible.

In conclusion, this study shows the relatively high $g_{eff}^{\uparrow\downarrow}$ in $Co_{2.06}Fe_{0.99}Ga_{0.53}Ge_{0.42}$/Pt in comparison with the previously reported values for conventional FM/Pt bilayer samples.

Chapter 7

Effect of various insertion layers on $Co_2FeGa_{0.5}Ge_{0.5}$/Pt bilayer interface

7.1. Introduction

As already pointed out in the previous chapter, energy-efficient magnetization switching in the free FM layer in MTJs is crucial for realizing high-performance non-volatile magnetoresistive random access memory [IKEG2020]. This requirement has spurred interest in exploiting the SOT mechanism [DOLU2020, LUQL2019]. A critical factor governing the efficiency of the spin current transfer in this mechanism is $g_{\text{eff}}^{\downarrow\uparrow}$, which quantifies the interfacial spin transparency between the NM and FM layers. For achieving high SOT efficiency, an FM/NM interface with a large $g_{\text{eff}}^{\downarrow\uparrow}$ is essential [AKAN2018, KUMA2019, SING2021]. In this regard, Chapter 6 provides a comprehensive study of bilayer film, which demonstrates achievement of a notably high $g_{\text{eff}}^{\downarrow\uparrow}$ value of $(2.78\pm0.09)\times10^{19}$ m^{-2} in $Co_{2.06}Fe_{0.99}Ga_{0.53}Ge_{0.42}$/Pt. The value of $g_{\text{eff}}^{\downarrow\uparrow}$ strongly depends on the various interfacial properties at the FM/NM interface, including interface roughness [ZHAN2011] and the crystallographic nature of both layers at the junction [TOKA2015]. It has been pointed out that an ultrathin insertion layer at the FM/NM interface can alter $g_{\text{eff}}^{\downarrow\uparrow}$ [SWIN2021, SWIN2022]. Prior studies have explored the effect of insertion layer on $g_{\text{eff}}^{\downarrow\uparrow}$ from the viewpoints of proximity-induced magnetization and interface transparency of spin current. However, these reports do not provide a detailed structural analysis of the NM overlayer at the FM/NM interface, making it difficult to separate the effects solely due to the insertion layer (X) from the overall changes in the NM layer structure in a FM/X/NM film stack. To address this gap in the literature, the effect of ultrathin insertion layers of Cu, Ni, Ru, Ta, or Cr on $g_{\text{eff}}^{\downarrow\uparrow}$ of $Co_2FeGa_{0.5}Ge_{0.5}$/Pt bilayer has been studied by focusing on the possible changes in Pt overlayer at the $Co_2FeGa_{0.5}Ge_{0.5}$/X/Pt interface.

7.2. Thin film deposition, processing, and basic characterizations

To investigate the impact of ultrathin insertion layers of Cu, Ni, Ru, Ta, or Cr on $g_{\text{eff}}^{\uparrow\downarrow}$, ~0.2 nm thin insertion layer was introduced between CFGG and Pt layers. Trilayers (bilayers with an insertion layer) having CFGG layer thicknesses of 8 nm and a Pt layer of thickness 10 nm were

prepared. Choice of the CFGG layer thickness was based on the findings in Chapter 6, which showed that α_{total} of a thinner CFGG layer is more sensitive to variations in spin pumping. Figures 7.01 (a and b) illustrate the schematic structure of the samples used in this study, *viz*., CFGG (8 nm)/Pt (10 nm) film on MgO (100) substrate and CFGG (8 nm)/X (~ 0.2 nm)/Pt (10 nm) film on MgO (100) substrate with insertion of X (Cu, Ni, Ru Ta, or Cr) layers. All the samples were deposited on MgO (100) substrate at room temperature using an ultra-high vacuum RF magnetron sputtering as described in Section 2.1.2. During the deposition, a target-to-substrate distance of 100 mm was maintained. The CFGG layers were deposited using a high (>99.9%) purity alloy target of $Co_{1.95}Fe_{0.89}Ga_{0.48}Ge_{0.68}$ composition and subsequently annealed *in situ* at 600 °C for 30 minutes. This heat treatment process was followed for all the films in this study to ensure enhanced atomic order. In the case of the CFGG (8 nm)/Pt (10 nm) bilayer film, a 10 nm thick Pt layer was deposited over the heat-treated and cooled CFGG layer, which served as both a spin sink and a capping layer. In the case of bilayer samples with an insertion layer, ~0.2 nm thick layer of Cu, Ni, Ru, Ta, or Cr was deposited before the deposition of the Pt layer. The overall composition of the CFGG layer was estimated to be $Co_{2.06\pm0.01}Fe_{0.99\pm0.01}Ga_{0.53\pm0.01}Ge_{0.42\pm0.01}$ by XRR measurements.

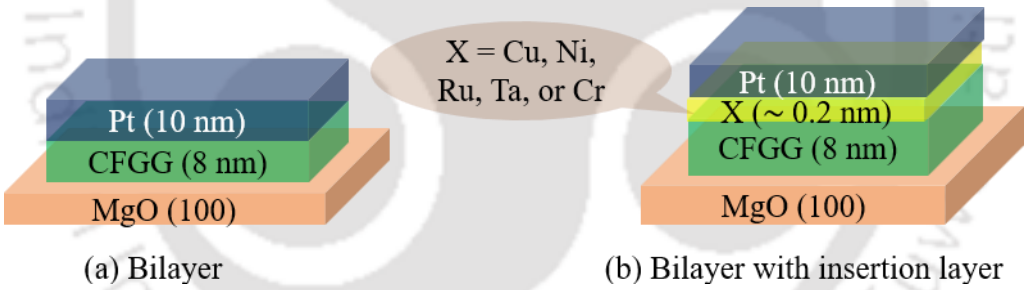

Figure 7.01. Schematic representation of the thin film stack of (a) bilayer CFGG (8 nm)/Pt (10 nm) and (b) CFGG (8 nm)/X (~ 0.2 nm)/Pt (10 nm) bilayer samples with insertion of X (Cu, Ni, Ru Ta, or Cr) layers, deposited on MgO (100) substrate.

7.3. Results and discussion

7.3.1. Crystal structure

To examine the possible modifications in the atomic structure of the Pt layer due to different insertion layers, XRD patterns were recorded on all the samples. Figures 7.02 (a and b) show the 2θ-ω scans of $Co_{2.06}Fe_{0.99}Ga_{0.53}Ge_{0.42}$ (8 nm)/X (~ 0.2 nm)/Pt (10 nm) samples with various insertion layers (X = Cu, Ni, Ru, Ta, or Cr) along the <100> (χ = 0°) and <110> (χ = 45°) directions, respectively.

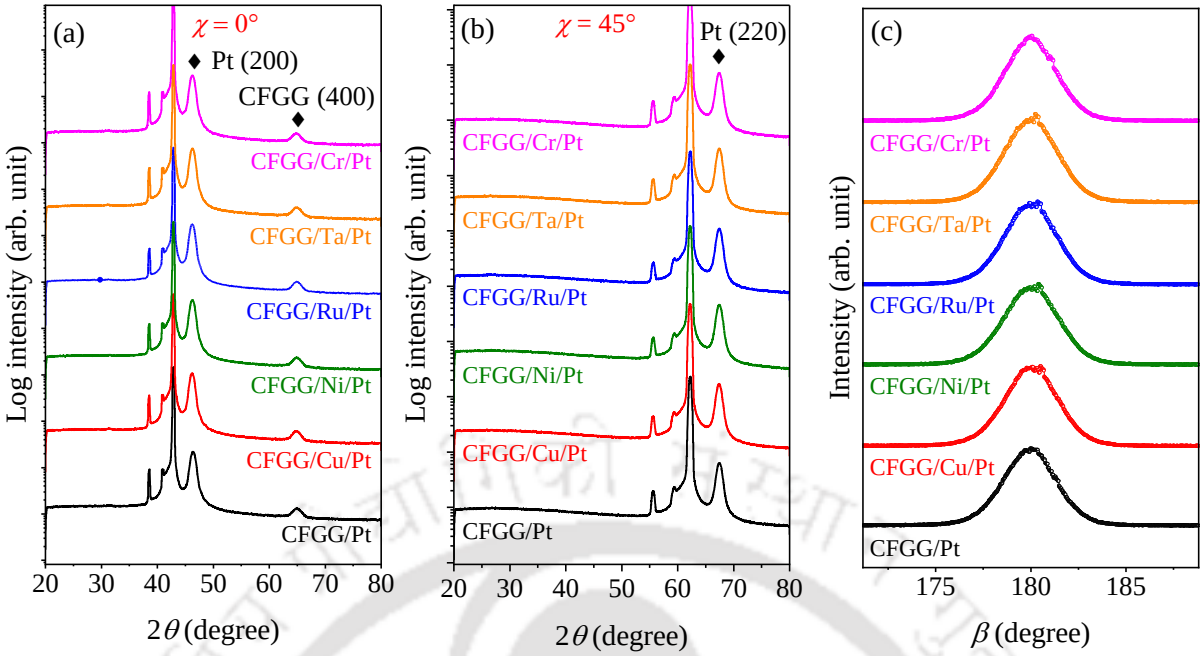

Figure 7.02. XRD patterns of CFGG (8 nm)/X (~ 0.2 nm)/Pt (10 nm) samples recorded at (a) $\chi = 0°$ and (b) $\chi = 45°$. (c) Corresponding rocking curves recorded about the Pt (220) reflection.

In all the samples, the observed reflections of CFGG (400) and Pt (200) for $\chi = 0°$ confirm epitaxial growth along the [100] direction. It can be noted that the CFGG (200) reflection is not visible in Figure 7.02 (a). However, this reflection is clearly visible in the XRD patterns of $Co_{2.06}Fe_{0.99}Ga_{0.53}Ge_{0.42}$ (8 nm) and $Co_{2.06}Fe_{0.99}Ga_{0.53}Ge_{0.42}$ (8 nm)/Pt (10 nm) films recorded with a 0D-mode detector as shown in Figures 6.02 (a) and 6.03 (a), respectively. Therefore, the reduced intensity of the CFGG (200) refection in Figure 7.02 (a) is attributed to the limitation of the 2D-mode XRD detector in capturing low-intensity reflection peaks. Despite this limitation, the 2D-mode XRD detector is still employed to perform rocking curve measurements, as discussed later in this chapter. Given that the deposition and annealing conditions of $Co_{2.06}Fe_{0.99}Ga_{0.53}Ge_{0.42}$ are identical to those used in the 6th chapter, it is reasonable to presume that the prepared $Co_{2.06}Fe_{0.99}Ga_{0.53}Ge_{0.42}$ films possess an $L2_1$-type ordered crystal structure. Due to the proximity of the atomic scattering factors of Co and Fe, conventional XRD technique cannot be ascertain the presence of Co-Fe disorder as already discussed in the previous chapter. Nonetheless, Co-Fe disorder is expected to be suppressed in these CFGG films due to the heat treatment given at 600 °C [GOTO2020]. The XRD patterns for the samples with insertion layer closely resemble that of the $Co_{2.06}Fe_{0.99}Ga_{0.53}Ge_{0.42}$/Pt bilayer film. This indicates that the [100]-oriented epitaxial growth of both $Co_{2.06}Fe_{0.99}Ga_{0.53}Ge_{0.42}$ and Pt layers is preserved, and the insertion layers have a negligible impact on the crystal structure of both layers.

To study the structure of the Pt layer in more detail, rocking curves were recorded for the Pt (220) reflection, as shown in Figure 7.02 (c). Pt (220) reflection was chosen because of its larger angular separation from the MgO reflection peak than the Pt reflection in the <100> direction scan. The Pt (220) rocking curves show identical shape and intensity. The full-width at half-maximum (FWHM) values of these reflections for all the samples with different insertion layers are shown in Figure 7.03. The nearly identical FWHM values confirm that the atomic structure of the Pt epitaxial layer remains largely unaffected by the insertion layers.

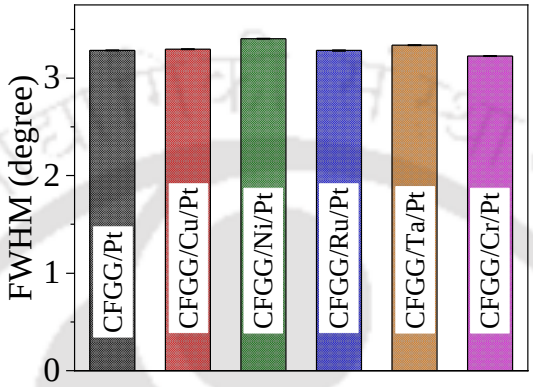

Figure 7.03. FWHM of rocking curves about the Pt (220) reflection for $Co_{2.06}Fe_{0.99}Ga_{0.53}Ge_{0.42}$ (8 nm)/X (~ 0.2 nm)/Pt (10 nm) samples (X = Cu, Ni, Ru, Ta, or Cr).

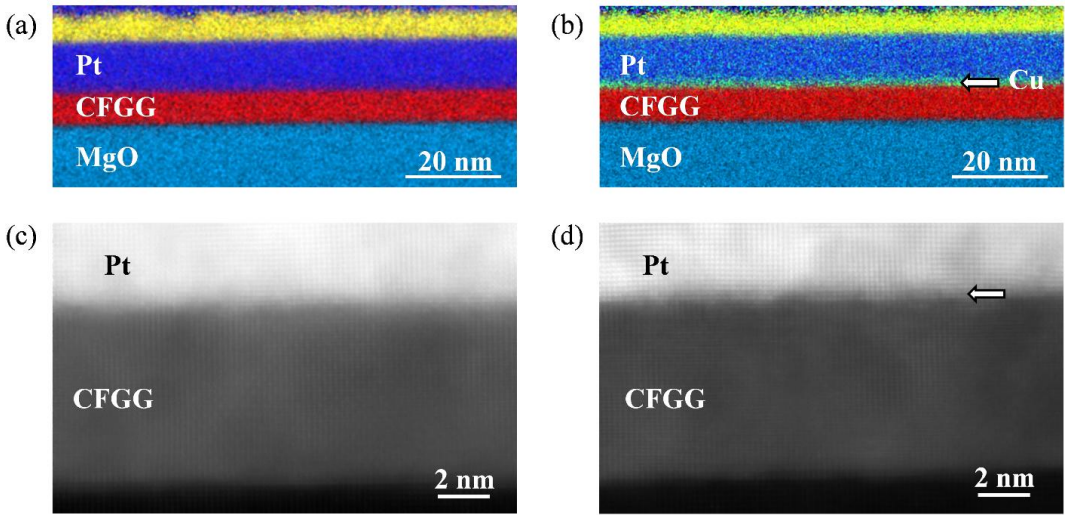

Figure 7.04. Cross-sectional elemental maps of (a) $Co_{2.06}Fe_{0.99}Ga_{0.53}Ge_{0.42}$ (8 nm)/Pt (10 nm), and (b) $Co_{2.06}Fe_{0.99}Ga_{0.53}Ge_{0.42}$ (8 nm)/Cu (~ 0.2 nm)/Pt (10 nm) films. (c and d) Corresponding high magnification cross-sectional TEM images. The arrows in the figures indicate the position of Cu insertion.

Cross-sectional TEM analysis was carried out to confirm the presence of the ultrathin insertion layer and to examine any possible changes in the Pt layer due to the introduction of the insertion layer. For this purpose, specific samples such as $Co_{2.06}Fe_{0.99}Ga_{0.53}Ge_{0.42}$ (8 nm)/Pt

(10 nm) and $Co_{2.06}Fe_{0.99}Ga_{0.53}Ge_{0.42}$ (8 nm)/Cu (~ 0.2 nm)/Pt (10 nm) films were chosen since Cu insertion layer modifies $g_{\text{eff}}^{\uparrow\downarrow}$ the most, as discussed later. Figures 7.04 (a and b) show the cross-sectional TEM images with elemental mapping of the $Co_{2.06}Fe_{0.99}Ga_{0.53}Ge_{0.42}$ (8 nm)/Pt (10 nm) and $Co_{2.06}Fe_{0.99}Ga_{0.53}Ge_{0.42}$ (8 nm)/Cu (~ 0.2 nm)/Pt (10 nm) samples, respectively. The corresponding high magnification cross-sectional TEM images are shown in Figures 7.04 (c and d). Elemental mapping performed using energy dispersive X-ray spectroscopy confirms the presence of Cu insertion layer (indicated by an arrow) at the $Co_{2.06}Fe_{0.99}Ga_{0.53}Ge_{0.42}$/Pt interface, as depicted in Figure 7.04 (b). Furthermore, comparison of high magnification cross-sectional TEM images shown in Figures 7.04 (c and d) confirms that the Cu layer does not disrupt the epitaxial growth of the Pt layer.

7.3.2. Magneto-dynamic properties

To investigate the influence of insertion layers on $g_{\text{eff}}^{\downarrow\uparrow}$, α_{total} of $Co_{2.06}Fe_{0.99}Ga_{0.53}Ge_{0.42}$ (8 nm)/Pt (10 nm) bilayers without and with an insertion layer of Cu, Ni, Ru, Ta, or Cr was evaluated through in-plane broadband FMR spectroscopy. The underlying mechanism behind FMR is explained in Section 1.2.1.2.3, while the experimental procedures followed to record FMR spectra are detailed in Section 2.2.3.2.

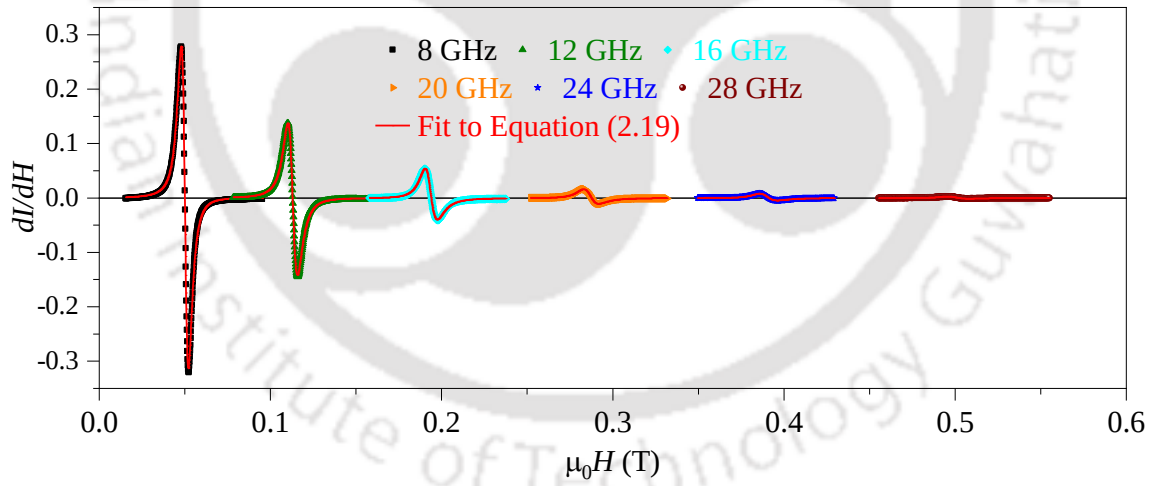

Figure 7.05. Typical in-plane FMR spectra of $Co_{2.06}Fe_{0.99}Ga_{0.53}Ge_{0.42}$ (8 nm)/Pt (10 nm) film. For the sake of clarity, only spectra recorded at 8, 12, 16, 20, 24, and 28 GHz are displayed.

FMR spectra of the films were recorded by fixing the frequency (say, at 8 GHz) while sweeping the magnetic field by 800 Oe across the resonance field $\mu_0 H_r$. The same procedure was repeated for frequencies in a 2 GHz interval in the range of 8 to 28 GHz. Figure 7.05 shows the representative FMR spectra of $Co_{2.06}Fe_{0.99}Ga_{0.53}Ge_{0.42}$ (8 nm)/Pt (10 nm) film. Only spectra recorded at six frequencies (8, 12, 16, 20, 24, and 28 GHz) in in-plane geometry are shown out

of the 11 spectra recorded for each film to avoid clutter. A systematic shift in resonance field towards higher fields can be observed as the frequency is increased from 8 to 28 GHz. The in-plane FMR spectrum recorded at each frequency was then fitted to Equation (2.19) to elucidate $\mu_0 H_r$ and $\mu_0 \Delta H$. The good fit obtained for each spectrum to the theoretically expected profile (represented by solid lines) can be seen. $\mu_0 H_r$ evaluated at each frequency was used to create plots of measurement frequency (resonance frequency f) *versus* $\mu_0 H_r$, as illustrated in Figures 7.06 (a–f) for the $Co_{2.06}Fe_{0.99}Ga_{0.53}Ge_{0.42}$/Pt bilayer without and with insertion of Cu, Ni, Ru, Ta, or Cr insertion layers.

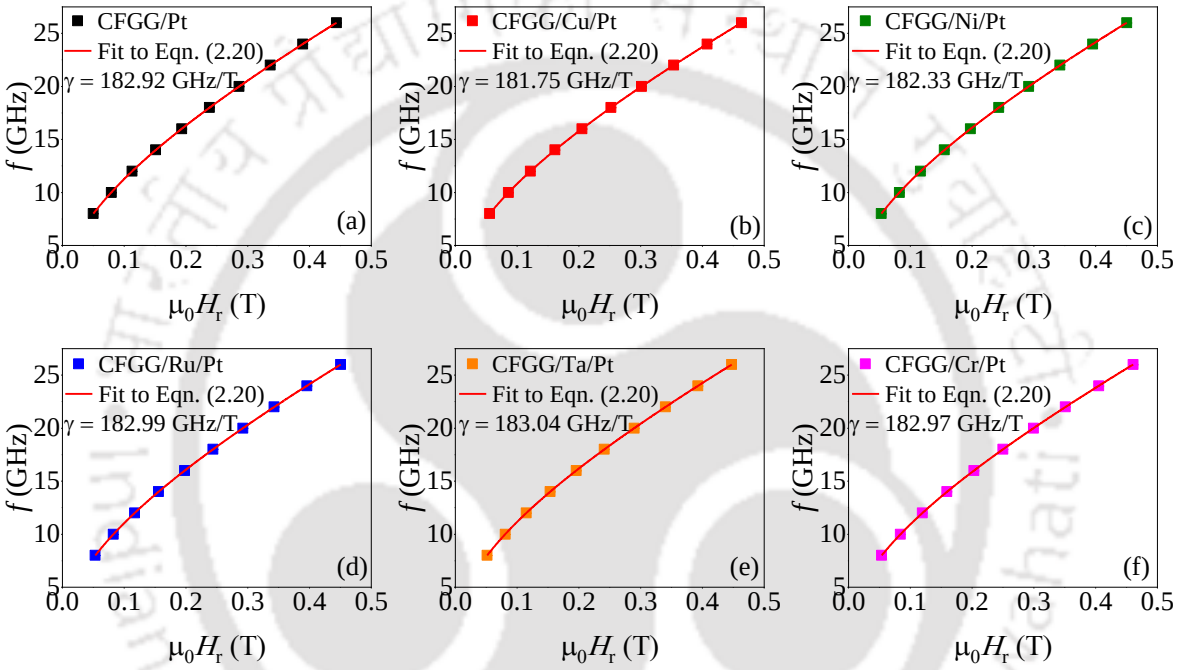

Figure 7.06. Variation of $\mu_0 H_r$ with resonance frequency of $Co_{2.06}Fe_{0.99}Ga_{0.53}Ge_{0.42}$ (8 nm)/Pt (8 nm) bilayer films (a) without insertion layer, and with ~0.2 nm thick (b) Cu, (c) Ni, (d) Ru, (e) Ta, and (f) Cr insertion layers.

These plots were fitted to Kittel's equation [SING2021] to determine the gyromagnetic ratio (γ) associated with each film. The estimated γ values, listed in Table 7.01, were subsequently used to evaluate α_{total} by fitting the $\mu_0 \Delta H$ *versus* f plot (shown in Figures 7.07 (a–f) to Equation (2.21). The evaluated α_{total} of $Co_{2.06}Fe_{0.99}Ga_{0.53}Ge_{0.42}$/Pt and $Co_{2.06}Fe_{0.99}Ga_{0.53}Ge_{0.42}$/X/Pt (X = Cu, Ni, Ru, Ta, or Cr) films are listed in Table 7.01. As discussed in Section 2.2.3.2, the experimentally obtained α_{total} contains both intrinsic and extrinsic components. Here, the extrinsic components include the contributions from spin pumping (α_{sp}), two-magnon scattering, radiative damping, and eddy current [HAIT2021].

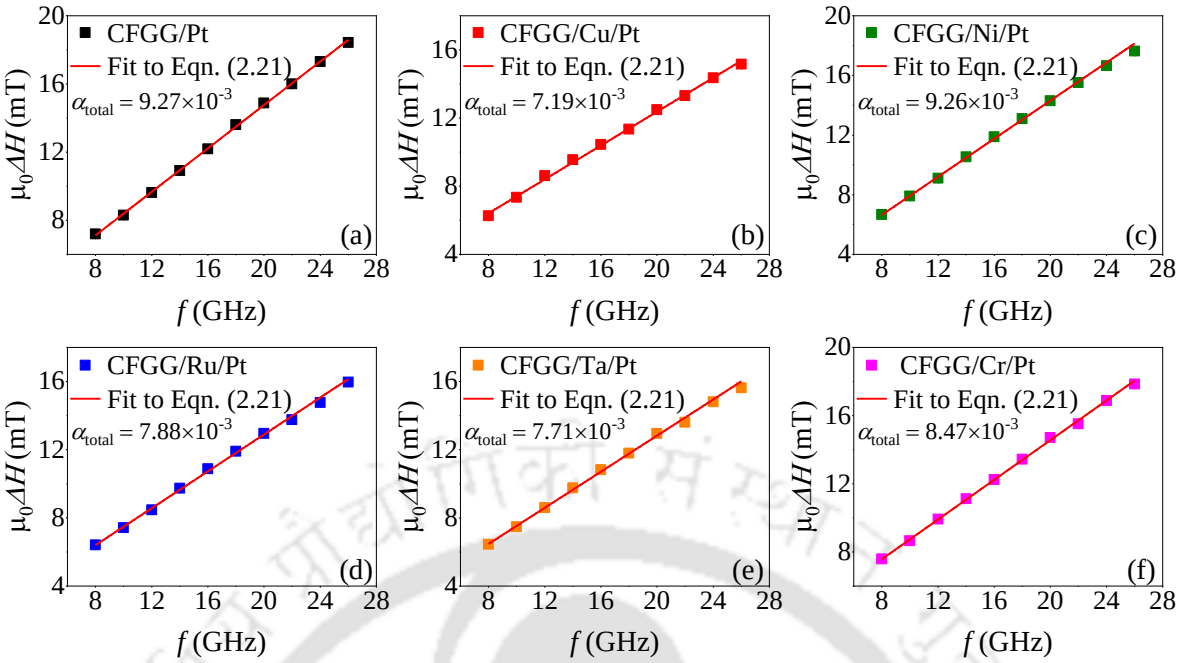

Figure 7.07. Variation of $\mu_0\Delta H$ as a function of resonance frequency of $Co_{2.06}Fe_{0.99}Ga_{0.53}Ge_{0.42}$ (8 nm)/Pt (8 nm) bilayer films (a) without insertion layer, and with ~0.2 nm thick (b) Cu, (c) Ni, (d) Ru, (e) Ta, and (f) Cr layers.

Table 7.01. γ, α_{total}, and $g_{eff}^{\uparrow\downarrow}$ of $Co_{2.06}Fe_{0.99}Ga_{0.53}Ge_{0.42}$ (8 nm)/Pt (10 nm), and $Co_{2.06}Fe_{0.99}Ga_{0.53}Ge_{0.42}$ (8 nm)/X (~ 0.2 nm)/Pt (10 nm) bilayers with X = Cu, Ni, Ru, Ta, or Cr layer.

Type of film	γ (GHz/T)	α_{total}	$g_{eff}^{\uparrow\downarrow}$ (m^{-2})
CFGG (8 nm)/Pt (10 nm)	182.92	9.27×10^{-3}	(2.85±0.08)×10^{19}
CFGG (8 nm)/Cu/Pt (10 nm)	181.75	7.19×10^{-3}	(1.93±0.10)×10^{19}
CFGG (8 nm)/Ni/Pt (10 nm)	182.33	9.26×10^{-3}	(2.84±0.09)×10^{19}
CFGG (8 nm)/Ru/Pt (10 nm)	182.99	7.88×10^{-3}	(2.23±0.10)×10^{19}
CFGG (8 nm)/Ta/Pt (10 nm)	183.04	7.71×10^{-3}	(2.16±0.10)×10^{19}
CFGG (8 nm)/Cr/Pt (10 nm)	182.97	8.47×10^{-3}	(2.49±0.09)×10^{19}

The Pt layer present in $Co_{2.06}Fe_{0.99}Ga_{0.53}Ge_{0.42}$ (8 nm)/Pt (10 nm) and $Co_{2.06}Fe_{0.99}Ga_{0.53}Ge_{0.42}$ (8 nm)/X (~0.2 nm)/Pt (8 nm) (X = Cu, Ni, Ru, Ta, or Cr) samples selectively increases α_{sp} by spin pumping, thereby significantly increasing α_{total}. The enhancement in α_{total} ($\Delta\alpha$) as compared to the $Co_{2.06}Fe_{0.99}Ga_{0.53}Ge_{0.42}$ (8 nm) single layer film (refer to Table 6.01) is evaluated using Equation (2.22). Furthermore, by substituting the corresponding $\Delta\alpha$ value into

Equation (2.23), $g_{eff}^{\uparrow\downarrow}$ is calculated for bilayers with and without an insertion layer. The resulting $g_{eff}^{\uparrow\downarrow}$ values of all samples are listed in Table 7.01.

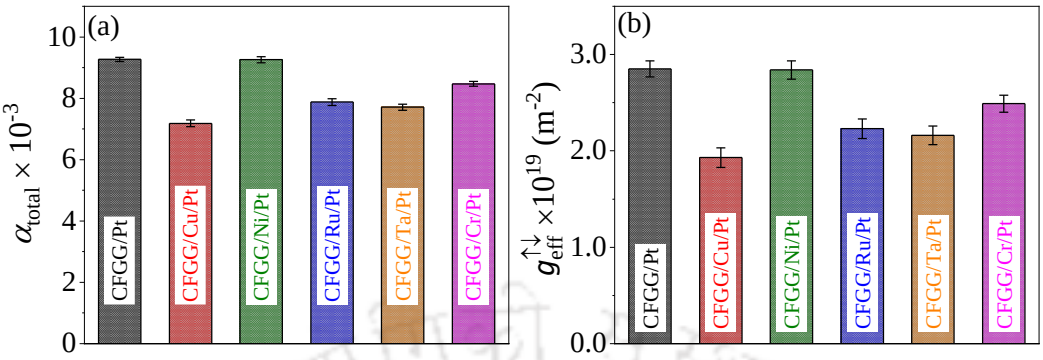

Figure 7.08. (a) α_{total} and (b) $g_{eff}^{\uparrow\downarrow}$ of bilayers without and with Cu, Ni, Ru, Ta, or Cr insertion layers.

Figures 7.08 (a and b) show the comparison of α_{total} and $g_{eff}^{\uparrow\downarrow}$ estimated for the bilayer samples without and with an insertion layer. The sample without an insertion layer exhibits the highest $g_{eff}^{\uparrow\downarrow}$ because direct contact of $Co_{2.06}Fe_{0.99}Ga_{0.53}Ge_{0.42}$ with Pt facilitates efficient spin current transfer across the $Co_{2.06}Fe_{0.99}Ga_{0.53}Ge_{0.42}$/Pt interface. The most pronounced decrease in α_{total} is noted in the case of the Cu insertion layer. Such adverse effect of Cu insertion layer has been reported in the previous studies [KUMA2019], which is attributed to a reduction of proximity-induced magnetization in the Pt layer resulting from the diamagnetic property of the Cu insertion layer. On the other hand, no noticeable change in α_{total}, and consequently in $g_{eff}^{\uparrow\downarrow}$, is observed in the sample with Ni insertion layer, primarily owing to its similar magnetic property as the $Co_{2.06}Fe_{0.99}Ga_{0.53}Ge_{0.42}$ layer. A direct contact between FM and the Pt layer enables the formation of proximity-induced magnetization in the Pt layer [CAMI2016, SWIN2021, WILH2000]. In the case of non-magnetic Ru and Ta insertion layers, a relatively smaller reduction in $g_{eff}^{\uparrow\downarrow}$ is observed in comparison to the Cu insertion layer. This difference in $g_{eff}^{\uparrow\downarrow}$ might originate from the relatively high spin-orbit coupling of Ru and Ta, which results in a larger spin Hall angle (θ_H), indicating it as an effective spin sink compared to the Cu insertion layer [WANG2014a]. In the case of the Cr insertion layer, despite its low spin-orbit coupling due to its lower atomic number, it exhibits a relatively high θ_H (half of that of Pt) due to its *d*-electron configuration [CHUN2014]. This makes Cr a relatively better spin sink, leading to a slight reduction in $g_{eff}^{\uparrow\downarrow}$ when Cr is inserted. Previous studies on $Y_3Fe_5O_{12}$ (YIG)/NM bilayers by Chunhui *et al*. [CHUN2014] and Wang *et al*. [WANG2014a] reported that Cr (~ 0.051) has a smaller θ_H than Ta (~ 0.071). Therefore, $g_{eff}^{\uparrow\downarrow}$ is expected to be lower for

the Cr insertion layer compared to Ta, which is contrary to the obtained result shown in Figure 7.08 (b). This discrepancy suggests that the antiferromagnetic property of the Cr insertion layer could affect spin current transfer between the $Co_{2.06}Fe_{0.99}Ga_{0.53}Ge_{0.42}$ and Pt layer [KHYM2016, WANG2014b].

Based on the above discussion, it is apparent that the interfacial modification by ultrathin (~ 0.2 nm) insertion layers leads to a noticeable change in $g_{\text{eff}}^{\uparrow\downarrow}$ while not affecting the structure of the Pt layer. This highlights the role of material characteristics at the interface on $g_{\text{eff}}^{\uparrow\downarrow}$ in CFGG/Pt bilayers.

7.4. Summary

A detailed investigation was carried out to assess the effect of ultrathin Cu, Ni, Ru, Ta, and Cr insertion layers on $g_{\text{eff}}^{\uparrow\downarrow}$ of $Co_{2.06}Fe_{0.99}Ga_{0.53}Ge_{0.42}$/Pt bilayer film by eliminating the insertion-layer-induced changes in the Pt layer structure. The key findings from this study are summarized below.

- In-depth structural analysis confirmed that the Pt layer structure was unaffected by the ultrathin Cu, Ni, Ru, Ta, and Cr insertion layers, thereby excluding structural modifications in Pt as a contributing factor to the observed change in $g_{\text{eff}}^{\downarrow\uparrow}$ in the $Co_{2.06}Fe_{0.99}Ga_{0.53}Ge_{0.42}$/Pt bilayers with different insertion layers.
- The $Co_{2.06}Fe_{0.99}Ga_{0.53}Ge_{0.42}$/Pt bilayer without an insertion layer exhibits the highest $g_{\text{eff}}^{\uparrow\downarrow}$ because of direct contact between $Co_{2.06}Fe_{0.99}Ga_{0.53}Ge_{0.42}$ and Pt, which facilitates efficient spin current transfer across the interface.
- The most pronounced decrease in $g_{\text{eff}}^{\uparrow\downarrow}$ is observed in the case of the Cu insertion layer. It is attributed to a reduction of proximity-induced magnetization in the Pt layer, resulting from the NM property of the Cu insertion layer.
- The bilayer with Ni insertion layer shows no significant change in $g_{\text{eff}}^{\uparrow\downarrow}$, primarily due to its similarity with the $Co_{2.06}Fe_{0.99}Ga_{0.53}Ge_{0.42}$ layer in magnetic properties. This has resulted in the formation of proximity-induced magnetization in the Pt layer in both cases, leading to similar $g_{\text{eff}}^{\uparrow\downarrow}$ values.
- In the case of NM Ru and Ta insertion layers, the reduction in $g_{\text{eff}}^{\uparrow\downarrow}$ is smaller compared to that of the bilayer with a Cu insertion layer. This difference might be due to the relatively high spin-orbit coupling of Ru and Ta, which makes them more effective spin sinks as compared to the bilayer with Cu.

- In the case of the Cr insertion layer, despite its low spin-orbit coupling, it acts as a good spin sink due to its *d*-electron configuration, which results in a slight reduction in $g_{\text{eff}}^{\uparrow\downarrow}$ when Cr is inserted.

In conclusion, this study highlights the critical role of interface properties on which $g_{\text{eff}}^{\uparrow\downarrow}$ in $Co_{2.06}Fe_{0.99}Ga_{0.53}Ge_{0.42}$/Pt bilayer depends upon and provides insights into interface engineering to tune $g_{\text{eff}}^{\uparrow\downarrow}$ with appropriate ultrathin insertion layers.

Chapter 8

Summary and scope for future work

This chapter summarizes the key findings and conclusions drawn on the research work presented in this thesis. Structural, electronic, and magnetic properties of arc-melted Co-Mn and Co-Fe based bulk Heusler alloys were first discussed. This was followed by the assessment of α in off-stoichiometric CFGG films, the evaluation of $g_{\text{eff}}^{\uparrow\downarrow}$ at the CFGG/Pt interface, and the impact of insertion layer on $g_{\text{eff}}^{\uparrow\downarrow}$ of the bilayer films. The key outcomes of these investigations are presented below, along with potential directions for future research in these topics.

8.1. Summary of key results

Systematic experimental and theoretical investigations have been conducted to explore the structural, magnetic, and electronic properties of bulk $Co_{2-x}MnV_xAl$ (x = 0.0, 0.25, and 0.5) and $Co_{2-x}FeTi_xAl$ (x = 0.00, 0.25, 0.50, 0.75, and 1.00) Heusler alloys. These investigations explored the impact of V and Ti substitution for Co in $Co_{2-x}MnV_xAl$ and $Co_{2-x}FeTi_xAl$ Heusler alloys, respectively. These studies demonstrated a viable approach to attain 100% P by tuning the minority spin bandgap at E_F while retaining the ferromagnetic character. After achieving high P, the next step was to comprehend impact of P on α to ascertain the efficiency of the free FM layer in MR devices. In this regard, off-stoichiometric compositions of the promising CFGG Heusler alloy was considered. Off-stoichiometric $Co_{1.77}Fe_{1.23}Ga_{0.56}Ge_{0.44}$ Heusler alloy thin film was heat treated films at different T_{an} to improve its atomic ordering. Effect of improvement in atomic ordering on α_{int} and its correlation with P was then analysed. This investigation revealed remarkably low α in the $Co_{1.77}Fe_{1.23}Ga_{0.56}Ge_{0.44}$ film annealed at T_{an} = 600 °C. It also clarified that atomic disorder significantly influences α, and α decreases with increasing P resulting from improved atomic ordering. To assess the potential of the SOT mechanism for achieving energy-efficient switching of the magnetization in the free FM layer, $g_{\text{eff}}^{\uparrow\downarrow}$ across the interface of $Co_{2.06}Fe_{0.99}Ga_{0.53}Ge_{0.42}$/Pt bilayers was evaluated. Furthermore, a detailed investigation was carried out to assess the effect of ultrathin Cu, Ni, Ru, Ta, and Cr insertion layers on $g_{\text{eff}}^{\uparrow\downarrow}$ of $Co_{2.06}Fe_{0.99}Ga_{0.53}Ge_{0.42}$/Pt bilayer film after ensuring that there are no insertion-layer-induced changes in the atomic structure of the Pt layer.

Bulk $Co_{2-x}MnV_xAl$ (x = 0.0, 0.25, and 0.50) and $Co_{2-x}FeTi_xAl$ (*x* = 0.0, 0.25, 0.50, 0.75, and 1.00) alloys were prepared using arc melting method, followed by annealing at 1100 ℃ for 24 hours to realize high degree of atomic ordering in the synthesized Heusler alloys. Structural analysis confirmed that the heat treated Co_2MnAl and $Co_{1.75}MnV_{0.25}Al$ alloys crystallized in partially disordered *B*2-type structure, whereas a well ordered $L2_1$-type structure was achieved in $Co_{1.5}MnV_{0.5}Al$ alloy. First-principles calculations predicted a progressive shift of the minority bandgap towards E_F with increasing V content, leading to an enhancement in *P* from ~69% for Co_2MnAl to 100% for $Co_{1.5}MnV_{0.5}Al$. A decrease in M_s, K_{eff}, and T_C was noticed as Co was progressively substituted by V. Evaluation of the Rhodes-Wohlfarth ratio of the alloys revealed that the itinerant ferromagnetic nature of Co_2MnAl and $Co_{1.75}MnV_{0.25}Al$ alloys changed to half-metallic nature in $Co_{1.5}MnV_{0.5}Al$ alloy which supported the predictions of the first-principles calculations. In the case of $Co_{2-x}FeTi_xAl$ (*x* = 0.0, 0.25, 0.50, 0.75, and 1.00) alloys, structural characterization revealed a similar transition in atomic ordering with increasing Ti substitution. Co_2FeAl and $Co_{1.75}FeTi_{0.25}Al$ alloys were found to crystallize in partially disordered *B*2-type structure, while $Co_{1.5}FeTi_{0.5}Al$, $Co_{1.25}FeTi_{0.75}Al$, and CoFeTiAl alloys exhibited a well ordered $L2_1$-type structure. First-principles calculations predicted that Ti substitution shifts the minority bandgap towards E_F, enhancing *P* from ~54% in Co_2FeAl to 100% in $Co_{1.5}FeTi_{0.5}Al$ and $Co_{1.25}FeTi_{0.75}Al$, signalling the inducement of half-metallic behaviour. Magnetic measurement revealed a decreasing trend in both M_s and K_{eff} with an increasing Ti content at the expense of Co in $Co_{2-x}FeTi_xAl$ alloys. Additionally, T_C was observed to drop significantly from >1200 K in Co_2FeAl to ~351 K in $Co_{1.25}FeTi_{0.75}Al$ alloy. The Rhodes-Wohlfarth ratio indicated that the itinerant ferromagnetism in $Co_{1.75}FeTi_{0.25}Al$ alloy changed to half-metallic nature in $Co_{1.5}FeTi_{0.5}Al$ and $Co_{1.25}FeTi_{0.75}Al$ alloys as predicted by first-principles calculations. These studies performed on bulk $Co_{2-x}MnV_xAl$ and $Co_{2-x}FeTi_x$ Al Heusler alloys demonstrate a promising strategy to achieve 100% *P* in ternary Heusler alloys compounds by tailoring their minority-spin bandgap near E_F by atomic substitution, and leading to the development of ferromagnetic half-metallic quaternary Heusler alloys.

To investigate how *P* influences *α,* and to assess the material's potential as a free FM layer in MR devices, off-stoichiometric $Co_{1.77}Fe_{1.23}Ga_{0.56}Ge_{0.44}$ thin films were deposited using magnetron sputtering. These films were annealed *in situ* at T_{an} = 400, 500, and 600 ℃ to enhance atomic ordering. As-deposited and the film annealed at 400 ℃ exhibited *B*2-type disordered structure. The onset of $L2_1$ ordering was observed in the film annealed at T_{an} = 500 ℃, which improved further in the film annealed at T_{an} = 600 ℃. First-principles calculations

indicated that *P* increases from 35% in stoichiometric $Co_2FeGa_{0.5}Ge_{0.5}$ alloy to 58% in the off-stoichiometric $Co_{1.77}Fe_{1.23}Ga_{0.56}Ge_{0.44}$ alloy, highlighting the latter's superior potential for spintronic applications as compared to the stoichiometric alloy. A notable reduction in α_{int} was observed upon annealing the off-stoichiometric film up to 500 °C. A further increase in T_{an} to 600 °C slightly decreased α_{int}, resulting in a remarkably low α_{int} of $(3.5\pm0.3)\times10^{-4}$. The relationship between atomic ordering and half metallic character was examined by AMR and OMR measurements, which showed a gradual enhancement in half-metallic nature with increase in T_{an}, which is attributed to improvement of atomic order with T_{an}. This enhancement in half-metallic nature in the annealed off-stoichiometric $Co_{1.77}Fe_{1.23}Ga_{0.56}Ge_{0.44}$ films correlates with the decreasing trend in α_{int} with T_{an} observed in FMR studies. To assess the potential of achieving energy-efficient switching of the magnetization in the free FM layer, $g_{eff}^{\uparrow\downarrow}$ across the interface of $Co_{2.06}Fe_{0.99}Ga_{0.53}Ge_{0.42}$/Pt bilayers was evaluated. This involved the determination of α_{total} of $Co_{2.06}Fe_{0.99}Ga_{0.53}Ge_{0.42}$ (8-20 nm) single layer and $Co_{2.06}Fe_{0.99}Ga_{0.53}Ge_{0.42}$ (8-20 nm)/Pt (10 nm) bilayer films. A minimum value of $\alpha_{total} \approx 1.07\times10^{-3}$ obtained in single layer $Co_{2.06}Fe_{0.99}Ga_{0.53}Ge_{0.42}$ film of 20 nm thickness, indicates low intrinsic damping and affirming its potential as a free FM layer in MTJs. In comparison, a significant increase in α_{total} was observed in $Co_{2.06}Fe_{0.99}Ga_{0.53}Ge_{0.42}$/Pt bilayers, suggesting efficient spin pumping across the interface. The observed enhancement in α_{total} led to high $g_{eff}^{\uparrow\downarrow}$ of $(2.78\pm0.09)\times10^{19}$ m^{-2}, signifying efficient spin current transfer across the bilayer interface.

To investigate the effect of insertion layers on the $g_{eff}^{\uparrow\downarrow}$ of this bilayer, $Co_{2.06}Fe_{0.99}Ga_{0.53}Ge_{0.42}$ (8 nm)/Pt (10 nm) and $Co_{2.06}Fe_{0.99}Ga_{0.53}Ge_{0.42}$ (8 nm)/X (~0.2 nm)/Pt (10 nm) (X = Cu, Ni, Ru, Ta, and Cr) bilayer films were prepared. Introduction of ultrathin insertion layers of Cu, Ni, Ru, Ta, and Cr did not alter the Pt layer structure, thereby excluding structural changes in Pt as a factor contributing to the observed change in $g_{eff}^{\uparrow\downarrow}$ in the $Co_{2.06}Fe_{0.99}Ga_{0.53}Ge_{0.42}$/Pt bilayers with different insertion layers. Among all the samples, $Co_{2.06}Fe_{0.99}Ga_{0.53}Ge_{0.42}$/Pt bilayer without any insertion layer exhibits the highest $g_{eff}^{\uparrow\downarrow}$, likely due to direct contact between $Co_{2.06}Fe_{0.99}Ga_{0.53}Ge_{0.42}$ and Pt layers, which facilitates efficient spin current transfer across the interface. The insertion of Cu layer led to the most substantial decrease in $g_{eff}^{\uparrow\downarrow}$, due to the suppression of proximity-induced magnetization in the Pt layer, on account of the NM nature of the Cu insertion layer. In contrast, the Ni inserted sample showed a negligible change in $g_{eff}^{\uparrow\downarrow}$, primarily because of the similarity between the magnetic properties of $Co_{2.06}Fe_{0.99}Ga_{0.53}Ge_{0.42}$ and Ni. In the case of NM Ru and Ta insertion layers, a moderate

reduction in $g_{\text{eff}}^{\uparrow\downarrow}$ is observed, which is smaller compared to that of the bilayer with Cu insertion layer. This could be due to the relatively high spin-orbit coupling of Ru and Ta, enabling more effective spin absorption. The Cr insertion layer, despite its low spin-orbit coupling, acts as a good spin sink due to its *d*-electron configuration, which results in a slight reduction in $g_{\text{eff}}^{\uparrow\downarrow}$. Thus, this study concludes that atomic disorder has a significant impact on α and reveals a notably high $g_{\text{eff}}^{\uparrow\downarrow}$ in CFGG/Pt bilayers, which is strongly influenced by the interface characteristics. These findings also demonstrate that the strategic insertion of ultrathin layers in FM/Pt bilayers can effectively modulate $g_{\text{eff}}^{\uparrow\downarrow}$ through interface engineering.

8.2. Scope for future work

The first two chapters of the thesis explain an important advancement towards realizing compositionally optimized quaternary Heusler alloys having robust half-metallic ferromagnetic character in $Co_{1.5}MnV_{0.5}Al$ and $Co_{1.5}FeTi_{0.5}Al$ alloys through strategic elemental substitution. It would be interesting to prepare these bulk Heusler alloys in thin-film form, where factors like interface quality and strain effects play a critical role in device performance. In particular, exploring these materials as free FM electrodes in CPP-GMR based spin valves and TMR based MTJs could accelerate their integration into practical device platforms. Moreover, addressing scalability and fabrication stability could bridge the gap between lab-scale materials design and industrial-level deployment.

The last three chapters of the thesis focus on evaluating α_{int} in off-stoichiometric CFGG and report very low α_{int} value of $(3.5\pm0.3)\times10^{-4}$. In this context, it is natural to explore the potential of off-stoichiometric CFGG as a free FM layer in CPP-GMR based spin-valves and TMR based MTJs, as low α_{int} enables easier and more energy efficient switching the magnetization of free FM layer. Moreover, analysis of $g_{\text{eff}}^{\uparrow\downarrow}$ in CFGG/Pt has yielded a high value of $\sim2.78\times10^{19}$ m^{-2}, which is largely influenced by the interface characteristics. It would be worthy to find out if this high $g_{\text{eff}}^{\uparrow\downarrow}$ indeed enables efficient switching of the magnetization in the free FM layer of MTJs. Since the value of $g_{\text{eff}}^{\uparrow\downarrow}$ is primarily governed by the interface characteristic, one can explore the possibility of further enhancement of $g_{\text{eff}}^{\uparrow\downarrow}$ by interface engineering. The present studies have used CFGG films and CFGG/Pt bilayers deposited on MgO substrates. Although MgO enables high-quality film growth, its cost and scalability limitations highlight the need to investigate more affordable substrate alternatives for industrial applications. In this context, future research should explore these properties using films deposited on low-cost Si substrates to evaluate their potential for practical applications.

References

[AHMA2021] Ahmad A., Mitra S., Srivastava S. K., Das A. K., Giant magnetocaloric effect in Co_2FeAl Heusler alloy nanoparticles, J. Phys. D: Appl. Phys., **54**(38) 385001 (8pp) (2021).

[AKAN2018] Akansel S., Kumar A., Behera N., Husain S., Brucas R., Chaudhary S., Svedlindh P., Thickness-dependent enhancement of damping in Co_2FeAl/β-Ta thin films, Phys. Rev. B, **97**(13) 134421 (2018).

[ANDR1997] Andreev S. V., Bartashevich M. I., Pushkarsky V. I., Maltsev V. N., Pamyatnykha L. A., Tarasov E. N., Kudrevatykh N. V., Goto T., Law of approach to saturation in highly anisotropic ferromagnets application to Nd-Fe-B melt-spun ribbons, J. Alloys Compd., **260** 196-200 (1997).

[ANDR2016] Andrieu S., Neggache A., Hauet T., Devolder T., Hallal A., Chshiev M., Bataille A. M., Le Fèvre P., Bertran F., Direct evidence for minority spin gap in the Co_2MnSi Heusler compound, Phys. Rev. B, **93**(9) 094417 (2016).

[BAIB1988] Baibich M. N., Broto J. M., Fert A., Van Dau F. N., Petroff F., Eitenne P., Creuzet G., Friederich A., Chazelas J., Giant magnetoresistance of (001)Fe/(001)Cr magnetic superlattices, Phys. Rev. Lett., **61**(21) 2472 (1988).

[BAKO2022] Bakonyi I., Czeschka F. D., Kiss L. F., Isnaini V. A., Krupp A. T., Palotás K., Zsurzsa S., Péter L., High-field magnetoresistance of microcrystalline and nanocrystalline Ni metal at 3 K and 300 K, Eur. Phys. J. Plus, **137**(7) 871 (2022).

[BALK2008] Balke B., Wurmehl S., Fecher G. H., Felser C., Kübler J., Rational design of new materials for spintronics: Co_2FeZ (Z=Al, Ga, Si, Ge), Sci. and Technol. Adv. Mater., **9** 014102(13pp) (2008).

[BALK2010] Balke B., Ouardi S., Graf T., Barth J., Blum C. G. F., Fecher G. H., Shkabko A., Weidenkaff A., Felser C., Seebeck coefficients of half-metallic ferromagnets, Solid State Commun., **150**(11-12) 529-532. (2010).

[BARW2024] Barwal V., Suto H., Toyama R., Simalaotao K., Sasaki T., Miura Y., Sakuraba Y., Large magnetoresistance and high spin-transfer torque efficiency of

$Co_2Mn_xFe_{1-x}Ge$ ($0 \leq x \leq 1$) Heusler alloy thin films obtained by high-throughput compositional optimization using combinatorially sputtered composition-gradient film, APL Mater., **12**(11) 111114 (2024).

[BASI2011] Basit L., Fecher G. H., Chadov S., Balke B., Felser C., Quaternary Heusler compounds without inversion symmetry: $CoFe_{1+x}Ti_{1-x}Al$ and $CoMn_{1+x}V_{1-x}Al$, Eur. J. Inorg. Chem., **26** 3950–3954 (2011).

[BHAT2017] Bhatti S., Sbiaa R., Hirohata A., Ohno H., Fukami S., Piramanayagam S. N., Spintronics based random access memory: a review, Materials Today **20**(9) 530 (2017).

[BHAT2025a] Bhat M. M., Alagarsamy P., Srinivasan A., Effect of Ti substitution for Co on structural, magnetic, and electronic properties of Co_2FeAl Heusler alloy, Intermetallics, **182** 108783 (2025).

[BHAT2025b] Bhat M. M., Simalaotao K., Suto H., Perumal A., Srinivasan A., Sakuraba Y., Atomic order induced reduction of Gilbert damping constant and enhancement of half-metallicity in off-stoichiometric $Co_2FeGa_{0.5}Ge_{0.5}$ Heusler alloy thin films, J. Appl. Phys., **138**(4) 043904 (2025).

[BINA1989] Binasch G., Griinberg P., Saurenbach F., Zinn W., Enhanced magnetoresistance in layered magnetic structures with antiferromagnetic interlayer exchange, Phys. Rev. B, **39**(7) 4828 (1989).

[BISW2024] Biswas S., Alagarsamy P., Srinivasan A., Influence of atomic substitution on the structural stability and half-metallicity of $Fe_{2-x}Cr_xCoSi$ (x = 0 to 1) alloys, J. Magn. Magn. Mater, **612** 172648 (2024).

[BLOC1994] Blochl P. E., Projector augmented-wave method, Phys. Rev. B, **50** 17953 (1994).

[BOMB2013] Bombor D., Blum C. G. F., Volkonskiy O., Rodan S., Wurmehl S., Hess C., Büchner B., Half-metallic ferromagnetism with unexpectedly small spin splitting in the Heusler compound Co_2FeSi, Phys. Rev. Lett., **110**(6) 066601 (2013).

[BRAD1933] Bradley A. J., Rodgers, J. W., The crystal structure of the Heusler alloys, (1933).

[BRAT2006] Bratton D., Yang D., Dai J., Ober C. K., Recent progress in high resolution lithography, Polym. Adv. Technol., **17** 94-103 (2006).

[BUSC1981] Buschow K. H. J., Van Engen P. G., magnetic and magneto-optical properties of Heusler alloys based on aluminium and gallium, J. Magn. Magn. Mater., **25** 90-96 (1981).

[CAMI2016] Caminale M., Ghosh A., Auffret S., Ebels U., Ollefs K., Wilhelm F., Rogalev A., Bailey W. E., Spin pumping damping and magnetic proximity effect in Pd and Pt spin-sink layers, Phys. Rev. B, **94**(1) 014414 (2016).

[CARV2000] Carvajal J. R., Fullprof-A program for Rietveld, profile matching and integrated intensities refinement of X-ray and/or neutron data, Laboratoire Leon Brillouin: CEA-Saclay, France, (2000).

[CAST2012] Castel V., Vlietstra N., Youssef J. B., van Wees B. J., Platinum thickness dependence of the inverse spin-Hall voltage from spin pumping in a hybrid yttrium iron garnet/platinum system, Appl. Phys. Lett. **101** 132414 (2012).

[CHAN2014] Chang H., Li P., Zhang W., Liu T., Hoffmann A., Deng L., Wu M., Nanometer-thick yttrium iron garnet films with extremely low damping, IEEE Magn. Lett., **5** 6700104 (2014).

[CHAP2007] Chappert C., Fert A., Van Dau F. N., The emergence of spin electronics in data storage, Review articles | insight., **6** 813 (2007).

[CHAT2023] Chatterjee S., Samanta S., Ghosh B., Mandal K., Half-metallic ferromagnetism and intrinsic anomalous Hall effect in the topological Heusler compound Co_2MnGe, Phys. Rev. B, **108**(20) 205108 (2023).

[CHEN2017] Chen J., Sakuraba Y., Masuda K., Miura Y., Li S., Kasai S., Furubayashi T., Hono K., Enhancement of $L2_1$ order and spin-polarization in Co_2FeSi thin film by substitution of Fe with Ti, Appl. Phys. Lett., **110**(24) 242401 (2017).

[CHEN2022] Chen Z., Sakuraba Y., Miura Y., Li Z., Sasaki T., Suto H., Kushwaha V. K., Nakatani T., Mitani S., Hono K., Phase stability and half-metallic character of off-stoichiometric $Co_2FeGa_{0.5}Ge_{0.5}$ Heusler alloys, J. Appl. Phys., **132**(18) 183902 (2022).

[CHUN2014] Chunhui D., Wang H., Yang F., Hammel P. C., Systematic variation of spin-orbit coupling with *d*-orbital filling: Large inverse spin Hall effect in 3*d* transition metals, Phys. Rev. B, **90**(14) 140407(R) (2014).

[CONC2013] Conca A., Greser J., Sebastian T., Klingler S., Obry B., Leven B., Hillebrands B., Low spin-wave damping in amorphous $Co_{40}Fe_{40}B_{20}$ thin films, J. Appl. Phys., **113**(21) 213909 (2013).

[COST2006] Costache M. V., Zaffalon M., van Wees B. J., Spin accumulation probed in multiterminal lateral all-metallic devices, Phys. Rev. B, **74** 012412 (2006).

[CULL2014] Cullity B. D., Stock S. R., Elements of X-ray diffraction, Pearson education limited, Harlow, **3** 656 (2014).

[DEGR1983] De Groot R. A., Mueller F. M., Van Engen P. G., Buschow K. H. J., New class of materials: Half-metallic ferromagnets, Phys. Rev. Lett., **50**(25) 2024 (1983).

[DENT1991] Denton A. R., Ashcroft N. W., Vegard's law, Phys. Rev. A, **43**(6) 3161-3164 (1991).

[DOLU2020] Dolui K., Bajpai U., Nikolić B. K., Effective spin-mixing conductance of topological-insulator/ferromagnet and heavy-metal/ferromagnet spin-orbit-coupled interfaces: A first-principles Floquet-nonequilibrium Green function approach, Phys. Rev. Mater., **4**(12) 121201(R) (2020).

[DONG2021] Dong K. F., Jiao Y. Y., Yuan Z. Y., Sun C., He K. H., Jin F., Mo W. Q., Song J. L., Low magnetic damping of epitaxial NiFe (100) thin films grown on different substrate, J. Magn. Magn. Mater., **523** 167615 (2021).

[EDWA2019] Edwards E. R. J., Nembach H. T., Shaw J. M., $Co_{25}Fe_{75}$ thin films with ultralow total damping of ferromagnetic resonance, Phys. Rev. Appl., **11**(5) 054036 (2019).

[FANY2024] Fan Y., Wang J., Chen A., Yu K., Zhu M., Han Y., Zhang S., Lin X., Zhou H., Zhang X., Lin Q., Thickness-dependent Gilbert damping and soft magnetism in metal/Co-Fe-B/metal sandwich structure, Nanomater., **14**(7) 596 (2024).

[FELS2015] Felser C., Wollmann L., Chadov S., Fecher G. H., Parkin S. S. P., Basics and prospective of magnetic Heusler compounds, APL Mater., **3**(4) 041518 (2015).

[FELS2022] Felser C., Parkin S., Topology, skyrmions, and Heusler compounds, MRS Bulletin, **47** 600-608 (2022).

[GALA2002a] Galanakis I., Dederichs P. H., Papanikolaou N., Origin and properties of the gap in the half-ferromagnetic Heusler alloys, Phys. Rev. B, **66**(13) 134428(1–10) (2002).

[GALA2002b] Galanakis I., Dederichs P. H., Papanikolaou N., Slater-Pauling behavior and origin of the half-metallicity of the full-Heusler alloys, Phys. Rev. B, **66**(17) 174429(1–9) (2002).

[GALA2006] Galanakis I., Mavropoulos P., Dederichs P. H., Electronic structure and Slater–Pauling behaviour in half-metallic Heusler alloys calculated from first principles, J. Phys. D: Appl. Phys., **39** 765–775 (2006).

[GALA2023] Galanakis I., Slater–Pauling behavior in half-metallic Heusler compounds, Nanomaterials (MDPI), **13**, 2010 (2023).

[GILB2004] Gilbert T. L., A phenomenological theory of damping in ferromagnetic materials, IEEE Trans. Magn., **40**(6) 3443–3449 (2004).

[GOTO2020] Goto K., Kumara L. S. R., Sakuraba Y., Miura Y., Kurniawan I., Yasui A., Tajiri H., Fujita Y., Chen Z., Hono K., Effects of the atomic order on the half-metallic electronic structure in the $Co_2Fe(Ga_{0.5}Ge_{0.5})$ Heusler alloy thin film, Phys. Rev. Mater., **4**(11) 114406 (2020).

[GRAF2009] Graf T., Casper F., Winterlik J., Balke B., Fecher G. H., Felser C., Crystal structure of new Heusler compounds, Z. Anorg. Allg. Chem., **635**(6–7) 976–981 (2009).

[GRAF2011] Graf T., Felser C., Parkin S. S. P., Simple rules for the understanding of Heusler compounds, Progress in Solid State Chemistry **39** 1-50 (2011).

[GRIF1999] Griffiths D. J., Inglefield C., Introduction to electrodynamics, Prentice-Hall, Inc., New Jersey, **73** 562 (1999).

[GROV1980] Grover A. K., Pillay R. G., Nagarajan V., Tandon P. N., Site preference and local environment effects in ferromagnetic ternary alloys, J. Magn. Magn. Mater., **15-18** 699-700 (1980).

[GUIL2019] Guillemard C., Petit-Watelot S., Pasquier L., Pierre D., Ghanbaja J., Rojas-Sánchez J. C., Bataille A., Rault J., Le Fèvre P., Bertran F., Andrieu S., Ultralow magnetic damping in Co_2Mn-based Heusler compounds: Promising materials for spintronics, Phys. Rev. Appl., **11**(6) 064009 (2019).

[GURE1996] Gurevich A. G., Melkov G. A., Magnetization Oscillations and Waves, CRC Press, Boca Raton (1996).

[HAIT2021] Hait S., Husain S., Barwal V., Gupta N. K., Pandey L., Svedlindh P., Chaudhary S., Comparison of high temperature growth versus post-deposition *in situ* annealing in attaining very low Gilbert damping in sputtered Co_2FeAl Heusler alloy films, J. Magn. Magn. Mater., **519** 167509 (2021).

[HEUS1934] Heusler V. O., Kristallstruktur und Ferromagnetismus der Mangan–Aluminium–Kupferlegierungen, Annalen der Physik. **19**(5) (1934).

[HUSA2017] Husain S., Kumar A., Akansel S., Svedlindh P., Chaudhary S., Anomalous Hall effect in ion-beam sputtered Co_2FeAl full Heusler alloy thin films, J. Magn. Magn. Mater, **442** 288–294 (2017).

[IKEG2020] Ikegawa S., Mancoff F. B., Janesky J., Aggarwal S., Magnetoresistive random access memory: Present and future, IEEE Trans. Electron Devices, **67**(4) 1407–1419 (2020).

[INOU2019] Inoue M., Inubushi K., Mouri D., Tanimoto T., Nakada K., Kondo K., Yamamoto M., Uemura T., Origin of biquadratic interlayer exchange coupling in Co_2MnSi-based current-perpendicular-to-plane pseudo spin valves, Appl. Phys. Lett., **114**(6) 062401 (2019).

[ISHI1982] Ishida S., Akazawa S., Kubo Y., Ishida J., Band theory of Co_2MnSn and Co_2TiAl, J. Phys. F: Met. Phys., **12** 1111-22 (1982).

[ISHI2006] Ishikawa T., Marukame T., Kijima H., Matsuda K. I., Uemura T., Arita M., Yamamoto M., Spin-dependent tunneling characteristics of fully epitaxial

magnetic tunneling junctions with a full-Heusler alloy Co_2MnSi thin film and a MgO tunnel barrier, Appl. Phys. Lett., **89**(19) 192505 (2006).

[JAGG1978] Jaggi N. K., Rao K. R. P. M., Grover A. K., Gupta L. C., Vijayaraghavan R., Khoi L. D., Mossbauer and NMR study of site preference and local environment effects in Co_2FeGa and Fe_2CoGa, Hyperfine Interactions, **4** 402-406 (1978).

[JUNG2009] Jung V., Fecher G. H., Balke B., Ksenofontov V., Felser C., Electronic structure, magnetic properties and order-disorder phenomena in $Co_2Mn_{1-x}Fe_xAl$, J. Phys. D: Appl. Phys., **42**(8) 084007(15pp) (2009).

[KALA2006] Kalarickal S. S., Krivosik P., Wu M., Patton C. E., Schneider M. L., Kabos P., Silva T. J., Nibarger J. P., Ferromagnetic resonance linewidth in metallic thin films: Comparison of measurement methods, J. Appl. Phys., **99**(9) 093909 (2006).

[KAND2007] Kandpal H. C., Fecher G. H., Felser C., Calculated electronic and magnetic properties of the half-metallic, transition metal based Heusler compounds, J. Phys. D: Appl. Phys., **40**(6) 1507–1523 (2007).

[KATS2008] Katsnelson M. I., Irkhin V. Y., Chioncel L., Lichtenstein A. I., De Groot R. A., Half-metallic ferromagnets: From band structure to many-body effects, Rev. Mod. Phys., **80**(2) 315–378 (2008).

[KAUF2006] Kaufmann M. D., Magnetization dynamics in all-optical pump-probe experiments: spin-wave modes and spin-current damping, (2006).

[KHYM2016] Khymyn R., Lisenkov I., Tiberkevich V. S., Slavin A. N., Ivanov B. A., Transformation of spin current by antiferromagnetic insulators, Phys. Rev. B, **93**(22) 224421 (2016).

[KOHN1965] Kohn W., Sham L. J., Self-consistent equations including exchange and correlation effects, Phys. Rev., **140**(4A) 1133 (1965).

[KOKA2012] Kokado S., Tsunoda M., Harigaya K., Sakuma A., Anisotropic magnetoresistance effects in Fe, Co, Ni, Fe_4N, and half-metallic ferromagnet: A systematic analysis, J. Phys. Soc. Jpn., **81** 024705 (2012).

[KOUS2024] Koushik P., Mukherjee K., Unveiling the structure-property relationship in a disordered inverse Heusler alloy Ti_2MnAl, Phys. Lett. A, **514–515** 129628 (2024).

[KRES1993] Kresse G., Hafner J., *Ab initio* molecular dynamics for liquid metals, Phys. Rev. B, **47** 558 (1993).

[KRES1999] Kresse G., Joubert D., From ultrasoft pseudopotentials to the projector augmented-wave method, Phys. Rev. B, **59** 1758 (1999).

[KRIS2002] Krishna S., Handbook of thin-film deposition processes and techniques: principles, methods, equipment and applications, Noyes Publications/William Andrew Pub. (2002).

[KRIZ2022] Krizakova V., Perumkunnil M., Couet S., Gambardella P., Garello K., Spin-orbit torque switching of magnetic tunnel junctions for memory applications, J. Magn. Magn. Mater., **562** 169692 (2022).

[KRON2003] Kronmüller H., Fähnle M., Micromagnetism and the microstructure of ferromagnetic solids, Cambridge university press, (2003).

[KSEN2006] Ksenofontov V., Melnyk G., Wojcik M., Wurmehl S., Kroth K., Reiman S., Blaha P., Felser C., Structure and properties of CoMnSb in the context of half-metallic ferromagnetism, Phys. Rev. B, **74**(13) 134426 (2006).

[KUBO2009] Kubota T., Tsunegi S., Oogane M., Mizukami S., Miyazaki T., Naganuma H., Ando Y, Half-metallicity and Gilbert damping constant in $Co_2Fe_xMn_{1-x}Si$ Heusler alloys depending on the film composition, Appl. Phys. Lett., **94**(12) 122504 (2009).

[KUMA2017] Kumar A., Pan F., Husain S., Akansel S., Brucas R., Bergqvist L., Chaudhary S., Svedlindh P., Temperature-dependent Gilbert damping of Co_2FeAl thin films with different degree of atomic order, Phys. Rev. B, **96**(22) 224425 (2017).

[KUMA2019] Kumar A., Gupta R., Husain S., Behera N., Hait S., Chaudhary S., Brucas R., Svedlindh P., Spin pumping and spin torques in interfacially tailored Co_2FeAl/β -Ta layers, Phys. Rev. B, **100**(21) 214433 (2019).

[KUSH2022] Kushwaha V. K., Kokado S., Kasai S., Miura Y., Nakatani T., Kumara R., Tajiri H., Furubayashi T., Hono K., Sakuraba Y., Prediction of half-metallic gap formation and Fermi level position in Co-based Heusler alloy epitaxial thin films through anisotropic magnetoresistance effect, Phys. Rev. Mater., **6**(6) 064411 (2022).

[LAND1935] Landau L. D. and Lifshitz E. M., Phys. Z. Sowietunion 8, 153 (1935).

[LEEA2017] Lee A. J., Brangham J. T., Cheng Y., White S. P., Ruane W. T., Esser B. D., McComb D. W., Hammel P. C., Yang F., Metallic ferromagnetic films with magnetic damping under 1.4×10^{-3}, Nat. Commun., **8**(1) 234 (2017).

[LINT2016a] Lin T. T., Dai X. F., Wang L. Y., Wang X. T., Liu X. F., Cui Y. T., Liu G. D., Anti-site-induced diluted magnetism in semiconductive CoFeTiAl alloy, J. Alloys Compd., **657** 519–525 (2016).

[LINT2016b] Lin T. T., Dai X. F., Zhao J. X., Wang L. Y., Wang X. T., Cui Y. T., Liu G. D., The structural, electronic and magnetic properties for the transition process between nonmagnetic and magnetic states in $CoFe_{1+x}Ti_{1-x}Al$, J. Alloys Compd., **684** 143–150 (2016).

[LINT2018] Lin T. T., Dai X. F., Zhang X. M., Zhang H. P., Chen G. F., Liu G. D., Nonmagnetic element induced novel ferromagnetism in CoFeTiAl quaternary Heusler alloy, Superlattices Microstruct., **122** 471–475 (2018).

[LIST2013] Li S., Takahashi Y. K., Furubayashi T., Hono K., Enhancement of giant magnetoresistance by $L2_1$ ordering in $Co_2Fe(Ge_{0.5}Ga_{0.5})$ Heusler alloy current-perpendicular-to-plane pseudo spin valves, Appl. Phys. Lett., **103**(4) 042405 (2013).

[LIUT2024] Liu T., Li X., An H., Chen S., Zhao Y., Yang S., Xu X., Zhou C., Zhang H., Zhou Y., Reconfigurable spintronic logic gate utilizing precessional magnetization switching, Scientific Reports, **14**(1) 14796 (2024).

[LUQL2019] Lu Q., Li Y., Peng B., Tang H., Zhang Y., He Z., Wang L., Li C., Su W., Yang Q., Zhou Z., Liu M., Enhancement of the spin-mixing conductance in Co-Fe-B/W bilayers by interface engineering, Phys. Rev. Appl., **12**(6) 064035 (2019).

[MAHA2021a] Mahat R, Shambhu K., Karki U., Regmi S., Law J. Y., Franco V., Galanakis I., Gupta A., LeClair P., Structural, electronic, magnetic, transport and mechanical properties of the half-metal-type quaternary Heusler alloy $Co_2Fe_{1-x}V_xGe$, J. Magn. Magn. Mater., **539** 168352 (2021).

[MAHA2021b] Mahat R., Shambhu K., Karki U., Law J. Y., Franco V., Galanakis I., Gupta A., LeClair P., Possible half-metallic behavior of Heusler alloys: Theory and experiment, Phys. Rev. B, **104**(1) 014430 (2021).

[MAHA2022] Mahat R., Karki U., Shambhu K., Law J. Y., Franco V., Galanakis I., Gupta A., Leclair P., Effect of mixing the low-valence transition metal atoms Y = Co, Fe, Mn, Cr, V, Ti, or Sc on the properties of quaternary Heusler compounds $Co_{2-x}Y_xFeSi$ ($0 \leq x \leq 1$), Phys. Rev. Mater., **6**(6) 064413 (2022).

[MAHA2023] Mahat R., Karki U., Shambhu K., Law J. Y., Franco V., Gupta A., LeClair P., Experimental study of the structural, magnetic, electrical, and mechanical properties of possible half-metallic $Co_{2-x}V_xFeGe$ Heusler alloys, J. Phys. Chem. Solids., **172** 110988 (2023).

[MARC2014] Marchenkov V. V., Kourov N. I., Belozerova K. A., Emelyanova S. M., Dyakina V. P., Marchenkova E. B., Eisterer M., Weber H. W., Electronic transport in Co-based half-metallic ferromagnetic Heusler alloys, J. Phys. Conf. Ser., **568** 052019 (2014).

[MARC2018a] Marchenkov V. V., Perevozchikova Y. A., Kourov N. I., Irkhin V. Y., Eisterer M., Gao T., Peculiarities of the electronic transport in half-metallic Co-based Heusler alloys, J. Magn. Magn. Mater., **459** 211–214 (2018).

[MARC2018b] Marco I. D., Held A., Keshavarz S., Kvashnin Y. O., Chioncel L., Half-metallicity and magnetism in the Co_2MnAl/CoMnVAl heterostructure, Phys. Rev. B, **97**(3) 03510 (2018).

[MARU2007] Marukame T., Yamamoto M., Tunnel magnetoresistance in fully epitaxial magnetic tunnel junctions with a full-Heusler alloy thin film of $Co_2Cr_{0.6}Fe_{0.4}Al$ and a MgO tunnel barrier, J. Appl. Phys., **101** 083906 (2007).

[MARU2007] Marukame T., Yamamoto M., Tunnel magnetoresistance in fully epitaxial magnetic tunnel junctions with a full-Heusler alloy thin film of $Co_2Cr_{0.6}Fe_{0.4}Al$ and a MgO tunnel barrier, J. Appl. Phys., **101**(8) 083906 (2007).

[MATS2017] Matsushita Y. I., Madjarova G., Dewhurst J. K., Shallcross S., Felser C., Sharma S., Gross E. K. U., Large magnetocrystalline anisotropy in tetragonally distorted Heuslers: A systematic study, J. Phys. D: Appl. Phys., **50**(9) 095002 (2017).

[MCCA2005] Mccandless B. E., Glancing incidence X-Ray diffraction of polycrystalline thin films, Mater. Res. Soc. Symp. Proc., **865** (2005).

[MEBS2013] Mebsout R., Amari S., Méçabih S., Abbar B., Bouhafs B., Spin-polarized calculations of magnetic and thermodynamic properties of the full-Heusler Co_2MnZ (Z = Al, Ga), Int. J. Thermophys., **34**(3) 507-520 (2013).

[MIRS2020] Mir S. A., She A. Q., Gupta D. C., New ferromagnetic half-metallic perovskites for spintronic applications: $BaMO_3$(M = Mg and Ca), RSC Adv, **10**(60) 36241–36252 (2020).

[MIUR2004] Miura Y., Nagao K., Shirai M., Atomic disorder effects on half-metallicity of the full-Heusler alloys $Co_2(Cr_{1-x}Fe_x)$A1: A first-principles study, Phys. Rev. B, **69**(14) 144413 (2004).

[MIYA1995] Miyazaki T., Tezuka N., Giant magnetic tunneling effect in Fe/Al_2O_3/Fe junction, J. Magn. Magn. Mater., **139** L231-L234 (1995).

[MIZU2009] Mizukami S., Watanabe D., Oogane M., Ando Y., Miura Y., Shirai M., Miyazaki T., Low damping constant for Co_2FeAl Heusler alloy films and its correlation with density of states, J. Appl. Phys., **105**(7) 07D306 (2009).

[MIZU2022] Mizuno H., Modak R., Hirai T., Takahagi A., Sakuraba Y., Iguchi R., Uchida K. I., Deposition temperature dependence of thermo-spin and magneto-thermoelectric conversion in Co_2MnGa films on $Y_3Fe_5O_{12}$ and $Gd_3Ga_5O_{12}$, Appl. Phys. Lett., **120**(20) 202401 (2022).

[MODA2021] Modak R., Goto K., Ueda S., Miura Y., Uchida K. I., Sakuraba Y., Combinatorial tuning of electronic structure and thermoelectric properties in $Co_2MnAl_{1-x}Si_x$Weyl semimetals, APL Mater., **9**(3) 031105 (2021).

[MOOD1995] Moodera J. S., Kinder L. R., Wong T. M., Meservey R., Large magnetoresistance at room temperature in ferromagnetic thin film tunnel junctions, Phys. Rev. Lett., **74**(16) 3273-3276 (1995).

[MOOR1965] Moore G. E., Cramming more components onto integrated circuits, **38**(8) (1965).

[MORA2009] Moram M. A., Vickers M. E., X-ray diffraction of III-nitrides, Rep. Prog. Phys., **72**(3) 036502 (40pp) (2009).

[OOGA2018] Oogane M., McFadden A. P., Fukuda K., Tsunoda M., Ando Y., Palmstrøm C. J., Low magnetic damping and large negative anisotropic magnetoresistance in half-metallic $Co_{2-x}Mn_{1+x}Si$ Heusler alloy films grown by molecular beam epitaxy, Appl. Phys. Lett., **112**(26) 262407 (2018).

[OTTO1989] Otto M. J., Woerden R. A. M. van, Valk P. J. van der, Wijngaard J., Bruggen C. F. van, Haas C., Buschow K. H. J., Half-metallic ferromagnets: I. Structure and magnetic properties of NiMnSb and related inter-metallic compounds, J. Phys.: Condens. Matter, **1**(13) 2341-2350 (1989).

[PATH2022] Pathak P., Bisht G. S., Srinivasan A., Enhanced Magnetic Properties of Electrodeposited Co_2FeSn film with high structural order, J. Electrochem. Soc., **169**(9) 092508 (2022).

[PATR2019] Patra A., Maity K. P., Prasad V., Influence of orbital two-channel Kondo effect on anomalous Hall effect in ferrimagnetic composites of $LaNiO_3$ and $CoFe_2O_4$, J. Phys.: Condens. Matter, **31**(25) 255702 (8pp) (2019).

[PERD1996] Perdew J. P., Burke K., Ernzerhof M., Generalized Gradient Approximation Made Simple, Phys. Rev. Lett., **77** 3865 (1996).

[PERI2020] Peria W. K., Peterson T. A., Mcfadden A. P., Qu T., Liu C., Palmstrøm C. J., Crowell P. A., Interplay of large two-magnon ferromagnetic resonance linewidths and low Gilbert damping in Heusler thin films, Phys. Rev. B, **101**(13) 134430 (2020).

[RAMS2011] Ram S., Chauhan M. R., Agarwal K., Kanchana V, *Ab initio* study of Heusler alloys Co_2XY (X = Cr, Mn, Fe; Y = Al, Ga) under high pressure, Philos. Mag. Lett., **91**(8) 545–553 (2011).

[SAKU2010] Sakuraba Y., Izumi K., Iwase T., Bosu S., Saito K., Takanashi K., Miura Y., Futatsukawa K., Abe K., Shirai M., Mechanism of large magnetoresistance in Co_2MnSi/Ag/Co_2MnSi devices with current perpendicular to the plane, Phys. Rev. B., **82**(9) 094444 (2010).

[SAKU2011] Sakuraba Y., Izumi K., Bosu S., Saito K., Takanashi K., Temperature dependence of spin-dependent transport properties of Co_2MnSi-based current-perpendiculartо-plane magnetoresistive devices, J. Phys. D: Appl. Phys., **44**(6) 064009(6pp) (2011).

[SAKU2014] Sakuraba Y., Kokado S., Hirayama Y., Furubayashi T., Sukegawa H., Li S., Takahashi Y. K., Hono K., Quantitative analysis of anisotropic magnetoresistance in Co_2MnZ and Co_2FeZ epitaxial thin films: A facile way to investigate spin-polarization in half-metallic Heusler compounds, Appl. Phys. Lett., **104**(17) 172407 (2014).

[SCHO2015] Schoen M. A. W., Shaw J. M., Nembach H. T., Weiler M., Silva T. J., Radiative damping in waveguide-based ferromagnetic resonance measured via analysis of perpendicular standing spin waves in sputtered permalloy films, Phys. Rev. B, **92**(18) 184417 (2015).

[SCHO2016] Schoen M. A. W., Thonig D., Schneider M. L., Silva T. J., Nembach H. T., Eriksson O., Karis O., Shaw J. M., Ultra-low magnetic damping of a metallic ferromagnet, Nat. Phys., **12**(9), 839–842 (2016).

[SHAM2019] Shambhu K., Mahat R., Regmi S., Mukherjee A., Padhan P., Datta R., Butler W. H., Gupta A., Leclair P., Tunable properties and potential half-metallicity in $(Co_{2-x}Ti_x)FeGe$ Heusler alloys: An experimental and theoretical investigation, Phys. Rev. Mater., **3**(11) 114406 (2019).

[SHAM2024] Shamardin A., Cichoň S., Rameš M., de Prado E., Volfová L., Kmječ T., Fekete L., Kopeček J., Kos P., Nowak L., Heicl J., Zázvorka J., Hamrle J., Veis M., Heczko O., Lančok J., Growth and properties of full Heusler Co_2TiSn epitaxial thin films. J. Alloys Compd., **1002** 175296 (2024).

[SHAR2007] Sharma V. K., Chattopadhyay M. K., Kumar R., Ganguli T., Tiwari P., Roy S. B., Magnetocaloric effect in Heusler alloys $Ni_{50}Mn_{34}In_{16}$ and $Ni_{50}Mn_{34}Sn_{16}$, J. Phys.: Condens. Matter., **19**(49) 496207(12pp) (2007).

[SHAW2012] Shaw J. M., Nembach H. T., Silva T. J., Determination of spin pumping as a source of linewidth in sputtered $Co_{90}Fe_{10}$/Pd multilayers by use of broadband ferromagnetic resonance spectroscopy, Phys. Rev. B, **85** 054412 (2012).

[SHAW2018] Shaw J. M., Delczeg-Czirjak E. K., Edwards E. R. J., Kvashnin Y., Thonig D., Schoen M. A. W., Pufall M., Schneider M. L., Silva T. J., Karis O., Rice K. P., Eriksson O., Nembach H. T., Magnetic damping in sputter-deposited Co_2MnGe Heusler compounds with *A*2, *B*2, and $L2_1$ orders: Experiment and theory, Phys. Rev. B, **97**(9) 094420 (2018).

[SING2021] Singh B. B., Roy K., Gupta P., Seki T., Takanashi K., Bedanta S., High spin mixing conductance and spin interface transparency at the interface of a $Co_2Fe_{0.4}Mn_{0.6}Si$ Heusler alloy and Pt, NPG Asia Materials, **13**(1) 9 (2021).

[SKAF2013] Skaftouros S., Özdoğan K., Şaşioğlu E., Galanakis I., Generalized Slater-Pauling rule for the inverse Heusler compounds, Phys. Rev. B, **87**(2) 024420 (2013).

[SONG2021] Song C., Zhang R., Liao L., Zhou Y., Zhou X., Chen R., You Y., Chen X., Pan F., Spin-orbit torques: Materials, mechanisms, performances, and potential applications, Prog. Mater. Sci., **118** 100761 (2021).

[SWIN2021] Swindells C., Głowiński H., Choi Y., Haskel D., Michałowski P. P., Hase T., Kuświk P., Atkinson D., Proximity-induced magnetism and the enhancement of damping in ferromagnetic/heavy metal systems, Appl. Phys. Lett., **119**(15) 152401 (2021).

[SWIN2022] Swindells C., Glowinski H., Choi Y., Haskel D., Michalowski P. P., Hase T., Stobiecki F., Kuswik P., Atkinson D., Magnetic damping in ferromagnetic/heavy-metal systems: The role of interfaces and the relation to proximity-induced magnetism, Phys. Rev. B, **105**(9) 094433 (2022).

[SZOT2004] Szotek Z., Temmerman W. M., Svane A., Petit L., Stocks G. M., Winter H., Half-metallic transition metal oxides, J. Magn. Magn. Mater., **272–276** 1816–1817 (2004).

[TANG2022] Tang Q., Zhu X., Half-metallic double perovskite oxides: recent developments and future perspectives, J. Mater. Chem. C, **10** 15301 (2022).

[TAOX2018] Tao X., Liu Q., Miao B., Yu R., Feng Z., Sun L., You B., Du J., Chen K., Zhang S., Zhang L., Yuan Z., Wu D., Ding H., Self-consistent determination of spin Hall angle and spin diffusion length in Pt and Pd: The role of the interface spin loss, Sci. Adv., **4** 1670 (2018).

[TAPA2024] Taparia D., Sasaki T., Nakatani T., Suto H., Miura Y., Li Z., Kushwaha V. K., Inubushi K., Ichikawa S., Nakada K., Sasaki T, Mitani S., Sakuraba Y, Improvement in CPP-GMR read head sensor performance using [001]-oriented polycrystalline half-metallic Heusler alloy $Co_2FeGa_{0.5}Ge_{0.5}$ and CoFe bilayer electrode, **25**(1) 2388503 (2024).

[TOKA2015] Tokaç M., Bunyaev S. A., Kakazei G. N., Schmool D. S., Atkinson D., Hindmarch A. T., Interfacial structure dependent spin mixing conductance in cobalt thin films, Phys. Rev. Lett., **115**(5) 056601 (2015).

[TRUD2010] Trudel S., Gaier O., Hamrle J., Hillebrands B., Magnetic anisotropy, exchange and damping in cobalt-based full-Heusler compounds: An experimental review, J. Phys. D: Appl. Phys., **43**(19) 193001 (2010).

[TSAI2004] Tsai A. P., A test of Hume-Rothery rules for stable quasicrystals, J. Non-Cryst. Solids., **334-335** 317-322 (2004).

[TSER2002] Tserkovnyak Y., Brataas A., Bauer G. E. W., Enhanced Gilbert damping in thin ferromagnetic films, Phys. Rev. Lett., **88**(11) 117601(4) (2002).

[UMET2008] Umetsu R. Y., Kobayashi K., Fujita A., Kainuma R., Ishida K., Phase stability and magnetic properties of $L2_1$ phase in $Co_2Mn(Al_{1-x}Si_x)$ Heusler alloys, Scr. Mater., **58**(9) 723–726 (2008).

[VARA2012] Varaprasad B. S. D. C. S., Srinivasan A., Takahashi Y. K., Hayashi M., Rajanikanth A., Hono K., Spin polarization and Gilbert damping of $Co_2Fe(Ga_xGe_{1-x})$ Heusler alloys, Acta Mater., **60**(18), 6257–6265 (2012).156

[VASP2025] VASP manual, https://www.vasp.at/wiki (2025).

[WALD2016] Waldrop m. m., More than Moore, Nature feature news, **530** 144 (2016).

[WALO2008] Walowski J., Kaufmann M. D., Lenk B., Hamann C., McCord J., Munzenberg M., Intrinsic and non-local Gilbert damping in polycrystalline nickel studied

by Ti: sapphire laser fs spectroscopy, J. Phys. D: Appl. Phys., **41** 164016(10pp) (2008).

[WANG2014a] Wang H. L., Du C. H., Pu Y., Adur R., Hammel P. C., Yang F. Y., Scaling of spin hall angle in 3*d*, 4*d*, and 5*d* metals from $Y_3Fe_5O_{12}$/metal spin pumping, Phys. Rev. Lett., **112**(19) 197201 (2014).

[WANG2014b] Wang H., Du C., Hammel P. C., Yang F., Antiferromagnonic spin transport from $Y_3Fe_5O_{12}$ into NiO, Phys. Rev. Lett., **113**(9) 097202 (2014).

[WEBE2019] Weber R., Han D. S., Boventer I., Jaiswal S., Lebrun R., Jakob G, Kläui M., Gilbert damping of CoFe-alloys, J. Phys. D: Appl. Phys., **52** 325001(7pp) (2019).

[WEBS1971] Webster P. J., Magnetic and chemical order in Heusler alloys containing cobalt and manganese, J. Phys. Chem. Solids, **32** 1221-1231 (1971).

[WEDE2024] Wederni A., Daza J., Ben Mbarek W., Saurina J., Escoda L., Suñol J. J., Crystal structure and properties of Heusler Alloys: A comprehensive review, Metals (MDPI), **14** 688 (2024).

[WENZ2011] Wen Z., Sukegawa H., Mitani S., Inomata K., Tunnel magnetoresistance in textured Co_2FeAl/MgO/CoFe magnetic tunnel junctions on a Si/SiO_2 amorphous substrate, Appl. Phys. Lett., **98**(19) 192505 (2011).

[WILH2000] Wilhelm F., Poulopoulos P., Ceballos G., Wende H., Baberschke K., Srivastava P., Benea D., Ebert H., Angelakeris M., Flevaris N. K., Niarchos D., Rogalev A., Brookes N. B., Layer-resolved magnetic moments in Ni Pt multilayers, Phys. Rev. Lett., **85**(2) 413-416 (2000).

[WOLF2001] Wolf S. A., Awschalom D. D., Buhrman R. A., Daughton J. M., Von Molnár S., Roukes M. L., Chtchelkanova A. Y., Treger D. M., Spintronics: A spin-based electronics vision for the future, Science, **294** 1488 (2001).

[WOLL2017] Wollmann L., Nayak A. K., Parkin S. S. P., Felser C., Heusler 4.0: Tunable materials, Annu. Rev. Mater. Res., **47** 247–70 (2017).

[WORL2024] Worledge D. C., Hu G., Spin-transfer torque magnetoresistive random access memory technology status and future directions, Nat. Rev. Electr. Eng., **1**(11) 730–747 (2024).

[WUSS2022] Wu S., Smith D. A., Nakarmi P., Rai A., Clavel M., Hudait M. K., Zhao J., Michel F. M., Mewes C., Mewes T., Emori S., Room-temperature intrinsic and extrinsic damping in polycrystalline Fe thin films, Phys. Rev. B, **105** 174408 (2022).

[XION2014] Xiong L., Yi L., Gao G. Y., Search for half-metallic magnets with large half-metallic gaps in the quaternary Heusler alloys CoFeTiZ and CoFeVZ (Z=Al, Ga, Si, Ge, As, Sb), J. Magn. Magn. Mater., **360** 98–103 (2014).

[YANG2012] Yang F. J., Sakuraba Y., Kokado S., Kota Y., Sakuma A., Takanashi K., Anisotropic magnetoresistance in Co_2(Fe,Mn)Si Heusler epitaxial films: A fingerprint of half-metallicity, Phys. Rev. B, **86**(2) 020409(R) (2012).

[YILG2005] Yilgin R., Oogane M., Yakata S., Ando Y., Miyazaki T., Intrinsic Gilbert damping constant in Co_2MnAl Heusler alloy films, IEEE Trans. Magn., **41**(10) 2799-2801 (2005).

[YILG2012] Yilgin R., Sakuraba Y., Oogane M., Ando Y., Miyazaki T., Magnetic properties of single crystalline Co_2MnAl Heusler alloy thin films, J. Supercond. Nov. Magn., **25**(8) 2659-2663 (2012).

[YUGH2015] Yu G. H., Xu Y. L., Liu Z. H., Qiu H. M., Zhu Z. Y., Huang X. P., Pan L. Q., Recent progress in Heusler-type magnetic shape memory alloys, Rare Met., **34**(8) 527–539 (2015).

[ZHAN2008a] Zhang C. W., Half-metallic ferromagnetism in zinc-blende Ca*M* (*M*=C, N), J. Appl. Phys., **103**(4) 043715 (2008).

[ZHAN2008b] Zhang S., Li L., Kumar A., Materials characterization techniques. CRC Press, Taylor & Francis Group, Boca Raton, **1** 319 (2008).

[ZHAN2011] Zhang Q., Hikino S. I., Yunoki S., First-principles study of the spin-mixing conductance in Pt/$Ni_{81}Fe_{19}$ junctions, Appl. Phys. Lett., **99**(17) 172105 (2011).

[ZHAN2013] Zhang W., Vlaminck V., Pearson J. E., Divan R., Bader S. D., Hoffmann A., Determination of the Pt spin diffusion length by spin-pumping and spin Hall effect, Appl. Phys. Lett., **103**(24) 242414 (2013).

[ZHER2015] Zhernovoi A. I., Dyachenko S. V., On the fulfillment of Curie's law in magnetic fluids, Russ. Phys. J., **58**(1) 133–137 (2015).

[ZIEB1974] Ziebeck K. R. A., Webster P. J., A neutron diffraction and magnetization study of Heusler alloys containing Co and Zr, Hf, V or Nb, J. Phys. Chem. Solids, **35** 1-7 (1974).

[ZUTI2004] Zutic I., Fabian J., Sarma S. D., Spintronics: Fundamentals and applications, Rev. Mod. Phys., **76**(2) 323-410 (2004).

Appendix

A typical POSCAR file for 32 atoms super unit cell of $Co_{1.5}FeTi_{0.5}Al$ Heusler alloy (consisting of 12 Co, 8 Fe, 4 Ti, and 8 Al atoms) is given below. This file provides inputs on the atomic arrangement and initial lattice parameters. The 1st line is for title (CFTA_44), the 2nd line specifies the scaling factor (1.0). Lines 3-5 define the unit cell dimensions in matrix format. The 6th and 7th lines list the constituent elements and their count. The 8th line specifies the coordinate type. Subsequent 32 lines define the atomic positions as per the sequence and quantity of elements given in 6th and 7th lines. VASP manual [VASP2025] provides full details.

```
CFTA_44
1.0
       11.6000003815         0.0000000000         0.0000000000
        0.0000000000         5.8000001907         0.0000000000
        0.0000000000         0.0000000000         5.8000001907
   Co   Fe   Ti   Al
   12    8    4    8
Direct
     0.125000000         0.250000000         0.250000000
     0.625000000         0.250000000         0.250000000
     0.375000000         0.750000000         0.250000000
     0.875000000         0.750000000         0.250000000
     0.375000000         0.250000000         0.750000000
     0.875000000         0.250000000         0.750000000
     0.125000000         0.750000000         0.750000000
     0.625000000         0.750000000         0.750000000
     0.375000000         0.750000000         0.750000000
     0.875000000         0.750000000         0.750000000
     0.125000000         0.250000000         0.750000000
     0.625000000         0.250000000         0.750000000
     0.125000000         0.750000000         0.250000000
     0.625000000         0.750000000         0.250000000
     0.375000000         0.250000000         0.250000000
     0.875000000         0.250000000         0.250000000
     0.250000000         0.500000000         0.500000000
     0.750000000         0.500000000         0.500000000
     0.250000000         0.000000000         0.000000000
     0.750000000         0.000000000         0.000000000
     0.000000000         0.500000000         0.000000000
     0.500000000         0.500000000         0.000000000
     0.000000000         0.000000000         0.500000000
     0.500000000         0.000000000         0.500000000
     0.000000000         0.000000000         0.000000000
     0.500000000         0.000000000         0.000000000
     0.000000000         0.500000000         0.500000000
     0.500000000         0.500000000         0.500000000
     0.250000000         0.000000000         0.500000000
     0.750000000         0.000000000         0.500000000
     0.250000000         0.500000000         0.000000000
     0.750000000         0.500000000         0.000000000
```

Publications/Presentations

List of publications from the thesis work:

[1] M. M. Bhat, A. Perumal, A. Srinivasan, Effect of Ti substitution for Co on structural, magnetic, and electronic properties of Co_2FeAl Heusler alloy, Intermetallics, **182** 108783 (2025). https://doi.org/10.1016/j.intermet.2025.108783.

[2] M. M. Bhat, A. Perumal, A. Srinivasan, Enhancement in structural order and half-metallicity by V substitution for Co in Co_2MnAl alloy, J. Magn. Magn. Mater. **629** 173308 (2025). https://doi.org/10.1016/j.jmmm.2025.173308.

[3] M. M. Bhat, K. Simalaotao, H. Suto, A. Perumal, A. Srinivasan, Y. Sakuraba, Atomic order induced reduction of Gilbert damping constant and enhancement of half-metallicity in off-stoichiometric $Co_2FeGa_{0.5}Ge_{0.5}$ Heusler alloy thin films, J. Appl. Phys. **138**, 043904 (2025). https://doi.org/10.1063/5.0268776.

[4] M. M. Bhat, H. Suto, T. Sasaki, A. Perumal, A. Srinivasan, Y. Sakuraba, Evaluation of spin mixing conductance in $Co_2FeGa_{0.5}Ge_{0.5}$/Pt bilayer and the effect of ultrathin Cu, Ni, Ru, Ta, or Cr insertion layers, Physical Review Materials, Under review – MK10427.

Presentations in conferences:

1. M. M. Bhat, H. Suto, T. Sasaki, A. Perumal, A. Srinivasan, Y. Sakuraba, Evaluation of spin mixing conductance in ordered $Co_2FeGa_{0.5}Ge_{0.5}$/Pt bilayer system, Japan Society of Applied Physics (JSAP-84), 19-23 Septmber 2023, (Oral).

2. M. M. Bhat, K. Simalaotao, H. Suto, A. Perumal, A. Srinivasan, Y. Sakuraba, Enhancement of half-metallicity in polycrystalline $Co_{1.77}Fe_{1.23}Ga_{0.56}Ge_{0.44}$ film deposited on Si substrate by systematic heat treatment, International Conference on Magnetic Materials and Applications (ICMAGMA-2023), 4-6 December 2023, Hyderabad (poster).

***